FUNCTIONALIZED TITANIA NANOTUBE ARRAYS-BASED SENSORS FOR ELECTROCHEMICAL DETECTION OF VOLATILE ORGANIC BIOMARKERS

by

Dhiman Bhattacharyya

A dissertation submitted to the faculty of
The University of Utah
in partial fulfillment of the requirements for the degree of

Doctor of Philosophy

Department of Metallurgical Engineering

The University of Utah

May 2016

The University of Utah Graduate School

STATEMENT OF DISSERTATION APPROVAL

The dissertation of **Dhiman Bhattacharyya**

has been approved by the following supervisory committee members:

Manoranjan Misra	, Chair	**February 25, 2016** Date Approved
Swomitra K. Mohanty	, Member	**February 25, 2016** Date Approved
Michael L. Free	, Member	**February 25, 2016** Date Approved
Sivaraman Guruswamy	, Member	**February 25, 2016** Date Approved
Bruce K. Gale	, Member	**February 25, 2016** Date Approved

and by **Manoranjan Misra** , Chair/Dean of

the Department/College/School of **Metallurgical Engineering**

and by David B. Kieda, Dean of The Graduate School.

ABSTRACT

Currently, all over the world, a lot of money is being pumped into the healthcare domain to facilitate development of rapid, point-of-care disease diagnostic platforms, which are relatively cheap with enhanced ease-of-use capabilities that can be deployed in low-resource settings which have higher prevalence of disease infected cases. Volatile organic compounds (VOCs) represent one class of biomarkers that has been less explored but possesses immense potential from a disease diagnostic standpoint. Tuberculosis (TB) has been a cause of significant health concern affecting a large population of people in Africa and Asia and recently, researchers have identified four specific TB VOCs from the breath of infected patients, through GC-MS analysis techniques. Rapid, accurate diagnosis is critical for timely initiation of treatment and, ultimately, control of the disease. Lack of access to appropriate diagnostic tools is caused, in part, by shortcomings as currently available diagnostics are often ill-adapted to resource-limited settings or specific patient needs, or may be priced out of reach.

Although many countries still rely on basic tools such as smear microscopy, new diagnostics are changing the TB diagnostics landscape. Some groups have previously attempted to develop breath-based TB detection techniques utilizing evanescent wave technology and colorimetry-based pattern detection techniques, but no sensors exist for detection of the four methyl ester-based VOCs. In the research presented in this dissertation, we have attempted to develop a low-cost, metal functionalized titania

nanotubular array-based sensor platform for electrochemical detection of the four major TB volatile organic biomarkers (VOBs). TiO_2 or titania nanotubes is an easy-to-synthesize, robust, wide bandgap (~3.2 eV) semiconductor material with excellent vectorial charge transport properties. In addition, the nanotubular morphology presents a large surface-area-to-volume ratio with sufficient metal bound active sites which facilitates efficient binding with the VOBs of interest. Titania nanotubes with an optimized morphology and stoichiometry and functionalized with cobalt through the incipient wetting impregnation, and an in-situ lattice functionalization method for electrochemical detection of the four TB VOBs and their subsequent integration into a sensor hardware, has been investigated. The potential light assisted, plasmonic-based sensing capabilities of gold nanoparticle functionalized TiO_2 nanotubes have been illustrated as well. In the end, a similar but slightly tweaked sensing platform has been tested for the detection of nonpulmonary colorectal cancer as well, extending the detection capabilities of the fabricated sensor substrate and leaving room for further research for screening of other life-threatening diseases. Improved access to better TB screening and diagnostics may present potential opportunities that may include efforts to accelerate market entry and/or scale-up of the innovative sensing platform that addresses unmet needs.

“I'D MADE IT THIS FAR AND REFUSED TO GIVE UP BECAUSE

ALL MY LIFE I HAD ALWAYS FINISHED THE RACE.”

- *Louis Zamperini*

Dedicated to my parents **Kalyan Kumar Bhattacharyya** and **Gargi Bhattacharyya,** who have always put the extra into ordinary, and taught me to become a good human being. A special feeling of gratitude towards my brother **Anirban** and my wife **Sreya** for putting up with me and having always encouraged me to stay motivated.

TABLE OF CONTENTS

LIST OF TABLES

ACKNOWLEDGEMENTS

I would first like to acknowledge the financial institutions that have supported my research endeavors. This research was supported by NSF-STTR Award # IIP-1321530 subcontracted from NanoSynth Materials and Sensors LLC, and Utah Government of Economic Development funds. This work made use of University of Utah USTAR shared facilities supported, in part, by the MRSEC Program of the NSF under Award No. DMR-1121252. Financial support through the Cooper-Hansen Graduate Research Fellowship, University of Utah, for 2014-2016 is also greatly appreciated.

I would sincerely like to express my heartfelt gratitude to Prof. Mano Misra for providing me with such a wonderful opportunity to work on this project. His guidance, persistence, and words of encouragement have been a constant source of inspiration for me, throughout my research. I have always tried to imbibe maximum knowledge on this subject through our scientific research discussions.

Also a great deal of thanks goes to Dr. Swomitra K. Mohanty and Dr. York R. Smith for their valuable input. Dr. Mohanty's unending enthusiasm helped in development of the first prototypes while Dr. Smith's expertise in semiconductor electrochemistry resulted in a few publications. I would also like to thank other members of my supervisory committee, Drs. Michael L. Free, Sivaraman Guruswamy, and Bruce K. Gale, for their valuable input.

I would like to thank the entire faculty, staff, and my colleagues and friends in the

department for helping me in some way or the other during my doctoral research. Last but not the least, I would like to express my love and appreciation towards my parents, in-laws, brother, and my wife for believing in my abilities, and for the endless support I received from them throughout my research work.

CHAPTER 1

INTRODUCTION AND BACKGROUND

Every year, the world spends billions of dollars on low-cost, innovative disease diagnostics to upgrade the existing healthcare infrastructure in an effort to make it more efficient. Of this, over US$ 1 billion is spent on diagnostics for tuberculosis (TB)[1]. This number is staggering given the fact that the amount might be greater than the GDP of several countries combined and also indicates the serious threat the disease possess. One third of this money is spent outside the established market economies, where 73% of TB diagnostic testing takes place.[1] In the developing world, where the vast majority of TB patients live, higher-performance but more complex and expensive tests, such as culture and nucleic acid testing, have not been widely implemented, and sputum microscopy and chest radiography remain the mainstay of diagnosis. Although relatively inexpensive on a per-test basis, these traditional methods result in considerable delay, repeat testing, and misdiagnosis, with significant attendant costs. Therefore, there is an enormous demand for new and better diagnostics that are more suitably adapted to the needs of developing countries.

Available reports illustrate that a very large global market exists for tuberculosis (TB) diagnostics and provides industry with a sound basis for decision-making in relation to developing better diagnostics that are suitable both for industrialized and developing

countries at various levels of the health system.[2] In the search for new tools to fight the global burden of disease, the world's attention has until now been focused on the need for new and better medicines. However, without effective diagnostics, health workers are unable to identify the true cause of disease for most of their patients, and are therefore forced to try out various treatments in the hope of finding the right one. Such mistreatment not only inflicts a huge health and financial cost on the patient, but also results in an unnecessary waste of scarce public resources. Simpler, more effective diagnostics that are designed for use in disease-endemic settings will be a key resource in the fight against the scourge of TB. Although the problems surrounding the existing tests are known, this work aims to explains the need for improved diagnostic tools with maximum impact.

1.1 Tuberculosis Overview

TB is an infectious disease caused by various strains of mycobacteria. It typically infects the lungs and is spread through the air when an infected patient sneezes, coughs, or spits. When this occurs, the TB bacilli are propelled into the air in droplets that can remain suspended for long periods of time. An individual simply needs to inhale a small amount of bacilli to become infected.

Every year, there are ~8.8 – 9 million new active TB cases and nearly 2 million TB deaths worldwide – 5,000 every day – mostly in the poorest communities of the developing world.[1,2] One third of the world's population has latent TB which may later develop into an active form of the disease. TB has also become the leading cause of death among people with HIV. Multidrug-resistance is also a growing problem. A key challenge for the public health community is to be able to effectively diagnose or screen

patients so that valuable resources and medicines are not wasted on misdiagnosis and repeat treatments.

Despite huge advances in technology, most countries around the world are still using the same microscopy examination of sputum that was used over 100 years ago. With only 40-60% test sensitivity under field conditions,[3,4] this falls as low as 20% when patients are co-infected with HIV. Preventive therapy effectively reduces progression to active disease, but today, there is no way to predict who is at greatest risk and who could gain the most from treatment.

The lack of accurate diagnosis leads to an unacceptable burden of human suffering and to a waste of precious resources in poor countries. Without the right diagnostic tools, it is difficult to control the TB epidemic. Developing new and rapid diagnostic tools is one of the critical elements required to execute a global plan to stop TB outbreaks. This presents immense potential for future markets to adopt a range of diagnostics in major testing areas, developed and tested for use in resource-poor settings.

World leaders, public health officials, and international donors have taken action against TB and financial resources for control and research have increased dramatically in recent years. Public-private partnerships like the Foundation for Innovative New Diagnostics (FIND) have emerged to bring together key players in these sectors to move research and development forward for the needs of patients.[1] In countries, years of running DOTS (directly observed therapy short-course) control programs have built a strong basis to further develop TB detection and treatment.[1] There is clearly a need, and organizations are looking for quality-assured tests that will help them manage the TB epidemic. Encouraged by the potential opportunities, we look forward to explore and

develop a new diagnostic tool that can result in an electrochemical sensor capable of screening TB patients based on their breath biomarkers.[5,6]

1.2 Current TB Diagnostic Scenario

While considering the TB diagnostic scenario, both latent and active TB should be taken into account. For latent TB diagnostics, generally in low-incidence settings, WHO guidelines advocate exclusion of active tuberculosis and then recommend chemoprophylaxis on the basis of results of immunodiagnostic tests such as tuberculin skin test [TST], interferon gamma release assay [IGRA], or TST followed by IGRA.[7-10]

As for active TB diagnostics, conventional methods for TB detection are traditionally performed in laboratories or hospitals. For example, the most common method for diagnosis of TB is the acid fast staining[11] of a sputum sample which is then followed by a sputum smear microscopy test.[3,4] However, a disadvantage with the sputum smear test is its poor sensitivity, which is estimated to be at 70%. Additionally, the sensitivity of sputum smear spectroscopy in field settings has been shown to be much lower (35%), especially in populations that have high rates of TB and HIV co-infection.[12,13] Culturing of mycobacterium from sputum samples is a more sensitive technique. Sputum samples are collected and cultured in either solid media or liquid media looking for the presence of the mycobacterium.[14,15] However, this methodology takes time to conduct (3-4 weeks for solid cultures, and 10-14 days for liquid cultures), which makes it difficult to employ in low-resource settings that are typically far from testing facilities. Recently, other technologies have been developed, including fluorescence microscopy[16] for smear tests (10% more sensitive than light microscopy),

LED fluorescent microscopy[17] for inexpensive imaging equipment that can be used in the field without the need for a darkroom, and rapid culturing techniques to reduce incubation time.[18] Despite all the improvements that have been made in TB diagnosis, no simple, inexpensive POC test for screening is currently available.[19] The techniques mentioned above either focus on variations of microscopy or culture technique. In either case, these methods require lab facilities and highly trained personnel that typically are not available in many rural or low-resource areas.

Access to diagnosis is particularly challenging in people with multidrug-resistant (MDR) TB and in children with TB.[2] In addition, some of the progress in the detection of drug-resistant TB has been attributed to the use of rapid molecular diagnostics such as line probe assays (LPAs)[20] and Gene Xpert® MTB/RIF.[21] Although TB diagnosis in many countries is still reliant on older tools, new diagnostics are changing the landscape. Stimulated, in part, by the success and rollout of Xpert® MTB/RIF, there is now considerable interest in new technologies.[21,22] The landscape looks promising with a robust pipeline of new tools, particularly molecular diagnostics or nucleic acid amplification test (NAAT) technologies, and well over 50 companies actively engaged in product development. The Determine urine lipoarabinomannan (LAM) point-of-care lateral flow assay is a low-cost useful rule-in test in people with HIV, especially in those who are sputum scarce or smear negative.[23-25] However, new diagnostics are yet to reach scale, and there needs to be greater convergence between diagnostics development and development of shorter TB drug regimens. Another concern is the relative absence of non-sputum-based diagnostics in the pipeline for children.[2] While many manufacturers remain interested in developing biomarker-based assays for point-of-care (POC) testing

or triaging (screening) patients for TB infection, they face significant challenges with identifying optimal biomarkers and specimen types and establishing cut-off values. The detection of volatile organic compounds is an area of increasing interest.

Recent research has shown that various strains of the mycobacteria produce distinct gaseous volatile biomarkers that can be used as a methodology for detecting and identifying the mycobacterium.[26-29] Specifically, Syhre and Chambers found that Mycobacterium tuberculosis and Mycobacterium bovis cultures give off four specific volatile organic biomarkers (VOBs): methyl phenylacetate, methyl p-anisate, methyl nicotinate, and o-phenylanisole.[28,29] These compounds were detectable before the visual appearance of colonies, which could have implications in detection of latent TB infection. Syhre *et al*. were able to detect statistically significant differences of methyl nicotinate in the breath of smear positive TB patients when compared to healthy (smear negative) subjects (Figure 1.1).[29] Analyses in these studies were done using gas chromatography/mass spectroscopy (GC-MS) analysis tools.

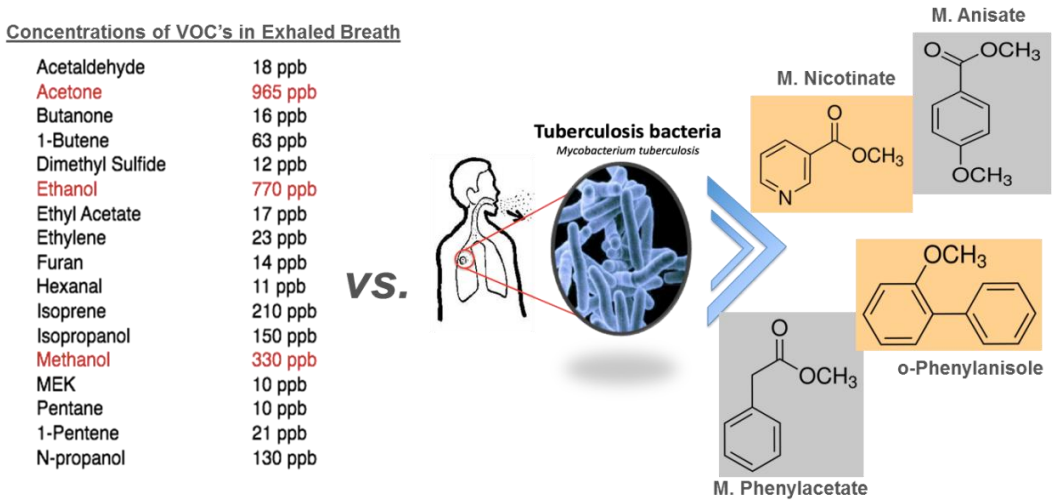

Figure 1.1. A comparison of the commonly found VOCs in exhaled breath of a health human (left) against the four specific VOCs found in the breath of TB patients (right).

While they are effective in identifying and quantifying complex gas samples, they are expensive, bulky, and not appropriate for point-of-care (POC) diagnostics. Therefore, it is evident that there are several challenges associated with the development of a rapid, low-cost, POC TB diagnostic device.

These challenges associated with the diagnosis of TB are significant as TB is the second leading cause of death due to a single infectious organism and is responsible for 1.3 million deaths annually (over 3,500 every day), according to the WHO. Overall, an estimated 2 billion people are currently infected worldwide with 8.6 million new active infections occurring each year.[30] Each of these individuals can transmit the disease to 10 to 15 people per year and face a mortality rate of 50% if untreated.[31] The economic burden of TB is staggering as the World Bank estimates that high-burden countries can lose up to 7% of GDP due to productivity losses from TB patients and their caretakers.[32] It is so critical that the World Bank committed $100 million to testing for and treating TB in India in 2014 alone.[1,2]

Of the 8.6 million new active TB cases that occur annually, the WHO estimates that roughly 3 million of these patients are 'missed' and do not receive the diagnosis or care they need. One of the primary reasons for this gap is delays in accessing TB-related care or long lead times for diagnostic tests. As a result, developing new large-scale screening tests (also known as triage or 'rule-out' tests) are particularly needed due to the fact that up to 80% of people tested for TB do not have active disease, stretching the limited and valuable resources that are devoted for diagnostic testing. As a result, FIND, a world leader in guiding and coordinating research and development for diseases such as TB, ranked the development of new screening tests as one of the top 3 priorities in the

fight against TB.[33]

1.2.1 VOCs-Based TB Diagnostic Approach

Rapid, point-of-care (POC) disease diagnostics present several challenges, including cost, detection time, equipment portability, and performance. Detection of volatile organic compounds (VOCs)-based disease biomarkers from the breath provides a potential solution to the aforementioned problems.[34] The clinical use of VOCs identification for improved and accurate diagnoses of pulmonary[35,36] and non-pulmonary[37-40] diseases possesses a significant potential for rapid screening of such diseases. Tuberculosis (TB) is a major pulmonary disease of concern, which can potentially be diagnosed via breath analysis. In a recent report, world health organization (WHO) states that almost 9.6 million people worldwide are infected with TB each year, while ~3 million people do not get the basic care they need and ~1.5 million people die of the disease, causing TB to be the leading cause of death worldwide alongside HIV.[41] Dheda *et al.*[12] had presented that VOCs detection-based approach falls under the "moderate complexity assays" group for TB diagnostics. In addition to the capability of giant African pouch rats (apopo) for sniffing TB, the technologies enlisted for the VOC-based approach include TB Breathalyzer (Rapid Biosensor Systems), Breathlink (Menssana), Aeonose (The eNose Company), Breath analysis instrument (Metabolomx), and Prototype Breathalyzer (Next Dimensions Tech). The TB Breathalyzer utilizes the evanescent wave technology leading to reduction in fluorescent signal when the TB antigen displaces fluorescently coated analogues and bonds to the antibody in the device.[42] Breathlink identifies markers of oxidative stress and disease using proprietary

algorithms where alveolar breath VOC samples are separated by gas chromatography and detected with flame ionization (GC-FID) or surface acoustic wave detection (GC-SAW) with high sensitivity.[27] The Aeonose utilizes the basic concept of an electronic nose, or machine olfaction, where a measurement generates complex multidimensional data for each measurement combined with a pattern recognition technique that interprets the complex data and relates them to a target value or class.[43] Metabolomx uses a colorimetric sensor array and breath analysis instrument. The colorimetric sensor helps to capture the chemical signature pattern of the complex mixture of VOCs present in breath, thereby helping in identifying tuberculosis, colon cancer, and lung cancer detection.[44] As stated previously, Syhre *et al.*[28,29] have successfully detected the prominent volatile organic biomarkers (VOBs) in the breath of smear positive tuberculosis patients using solid phase microextraction fibers with GC-MS analysis. It is evident that although the aforementioned technologies fall under the VOC-based detection category, none of them quintessentially detects the specific VOCs found in the exhaled breath of TB patients.

To overcome the challenges and present an affordable healthcare diagnostic platform, we have successfully demonstrated, through the research presented in this dissertation, our attempt to develop an inexpensive metal functionalized titania (TiO_2) nanotubular array-based semiconductor sensor for electrochemical detection of the predominate TB volatile organic biomarkers (VOBs) (Table 1.1).[45] Its important to note that these VOBs are very specific to the concerned disease and are found in tuberculosis only. This eliminates the specificity concern as the designed sensor will be highly selective and specific towards the VOBs of interest. Table 1.1 compares the gold-standard (smear) and the PCR-based technique against our proposed sensing technique.

Table 1.1. A comparison of the currently available common TB diagnostic techniques facing several drawbacks, which can be overcome using TNA based sensor.

	X-Ray	Smear	PCR	Culture	TNA Based Sensor
Sensitivity	**77%**	**20% - 70%**	<88%	80%	*Pending Trial*
Specificity	--	> 95%	<98%	> 95%	*Pending Trial*
Specimen	None	Sputum	Sputum	Sputum	**Breath**
Time Required	1 hour	>2 hours	90 minutes	**2-8 weeks**	**< 10 minutes**
Training Required	Yes	Yes	Yes	Yes	**No**
Patient Visits	1	1-2	1-2	2+	**POC**
Cost (per test)	$5	$4	**$10+**	**$15**	$3-5
Infrastructure Required	**Yes**	**Yes**	**Yes**	**Yes**	**No**
Other considerations	**Radiation exposure**	**Low sensitivity - children, HIV**	**Expensive instrument ($17,000)**	**Considered the 'gold standard'**	

1.3 Role of TiO_2 Nanotubes in Sensing Applications

Electrochemical gas sensors can be classified as amperometric, potentiometric, and conductometric based on their mode of operation.[46] Fine *et al.*[47] has discussed sensor response mechanisms in metal oxide semiconductor sensors, applying band theory to explain the n-type and p-type sensor response to oxidizing and reducing gases based on changes in resistance. In addition, one-dimensional (1D) nanostructured metal oxides have been studied extensively for their applications in sensors (chemical and biological) and catalysis.[48,49] 1D nanostructured metal oxides present a high surface-area-to-volume ratio[48,50] and are advantageous in sensing applications due to enhanced chemical and thermal stability, in addition to low power consumption. Kolmakov and Moskovits[49] emphasized the role of metal oxide nanowires in the sensitivity and selectivity of

chemical and biological sensors. They also stated that based on the application, a nanowire morphology can be utilized as a resistor whose conductivity will be affected by the charge transfer caused by the adsorbate on the sensor substrate, or as a transistor where the properties can be controlled by the application of a constant bias, thereby affecting the sensor's charge carrier density.

Synthesis of 1D self-organizing titania nanotube arrays (TNAs) via electrochemical anodization is a robust method to obtain highly ordered 1D nanostructures with good control of the morphology over large length scales.[51,52] These materials have demonstrated their use in numerous technical applications from catalysis to biomedics.[51,53] One distinct advantage of using this morphology for gas sensing is the high surface-area-to-volume ratio. Varghese *et al.*[54] reported the use of titania nanotubes for hydrogen sensing at elevated temperatures. Chen *et al.*[55] devised a room temperature hydrogen sensor based on TNA using platinum electrodes. Sennik *et al.*[56] synthesized a highly ordered titania nanotubes array for application as a hydrogen sensor, both at room temperature and elevated temperature. Further, Wen and Tian-mo demonstrated improved hydrogen[57] and formaldehyde[58] sensing of nanosize TiO2 doped with silver, through experimentation and DFT simulation. In addition to hydrogen sensing, low-temperature oxygen sensors have been fabricated using amorphous TiO2 nanotube arrays.[59] Perillo and Rodriguez[60] demonstrated gas sensing properties of titania nanotubes through electrochemical response to ethanol and ammonia at room temperatures. Ethanol sensing properties of TNAs have also been demonstrated by Kwon and coworkers[61] to be superior to most 1D nanostructured oxides reported in the literature. They described the ethanol gas sensing mechanism of the titania nanotube sensor based on the surface

depletion model. A SnO2–TiO2 composite oxide sensor doped with silver has been used for sensing VOC gases such as ethanol, methanol, acetone, and formaldehyde.[62] Previous investigations by our group have demonstrated the successful detection of triacetone triperoxide (TATP)[63] and trichloroethylene[64] vapors using functionalized TNA. We have recently utilized DFT simulation to understand the principle interaction of TATP vapor with metal sensitized TNA and demonstrated the results experimentally.[65] Hence, it is evident that TNA is a versatile substrate, which has been used extensively for various sensing applications. Consequentially, functionalized 1D TNA has been used in this study for electrochemical detection of the TB biomarkers.

1.4 Research Objectives

There are two major aspects of a smart sensor system: sensor element development; and element integration into sensor hardware, and subsequent testing of the resultant sensor system in application environment. Therefore, the two-fold objective of this research was to develop a novel, low-cost, solid state metal functionalized titania nanotube array (TNA)-based sensor, with:

- high sensitivity and specificity with significantly reduced detection time (when compared to current available technologies).
- which can be integrated into a hand-held device that will be portable and non-invasive and perfect for POC use.

In the process of development of the sensor element, the morphology and the functionalization methods will evolve through the stages to yield a sensor with optimized geometry and maximum signal response. In addition to the development of the proposed

sensor element, a crude lab-based prototype of the sensing platform housing the element will be prepared for the study. This study conducted will determine if the newly developed sensing methodology for screening TB at the POC based on volatile biomarkers is feasible through the use of a solid-state sensor using functionalized 1D TiO_2 nanotube arrays that bind and oxidize the volatile biomarkers. When the volatile biomarkers bind to the functionalized nanotubes, a large change in current is measured using a simple potentiostat. The readout for the end-user will be a simple yes/no answer for additional confirmatory testing based on the change in current. If the clinical sensitivity is sufficient, this technology could provide a means for identifying many of the 'missed' TB patients and allow testing resources and efforts to be focused on those at the highest risk of having the disease.

Additionally, to verify the validity of the sensing methodology and platform, sensor response upon exposure to volatile organic biomarkers from other diseases such as colorectal cancer (a non-pulmonary disease) will be investigated as well.

1.5 Dissertation Organization

The research presented in this dissertation aims to explore the feasibility of the fabricated 1D TNA-based sensors in healthcare diagnostics. Tuberculosis is arguably one of the major life-threatening diseases prevalent in the world, and hence the focus on this disease to find a rapid screening solution.

Chapter 1 provides an overview of the severity of the tuberculosis disease and the current diagnostic scenario involving molecular- and culture-based detection techniques, enzymatic, antigen-antibody, cellular response, and microscopy and imaging detection

techniques. In addition, some of the prevalent breath biomarker-based detection techniques were discussed, as they pertain to the present research interests. A brief review of the various sensing applications of titania nanotubes was also presented. Chapters 2-7 cover the first research objective, i.e., development of the sensor element.

Chapter 2 aims to optimize the geometry and stoichiometry of the 1D titania nanotubular array in order to maximize the sensor response to the TB biomarkers. The variation in the anodization voltage (change in nanotube diameter) and time (change in nanotube length) did not have a significant impact on the sensor response and has not been reported. The water content of the anodization electrolyte was varied, resulting in stoichiometrically different nanotubes with various concentrations of oxygen vacancy. Further, the anodization was carried out at different temperatures, resulting in change in nanotube wall thickness, which impacts the width of the depletion region and subsequent charge transfer. As a result, the sensor response is significantly affected by the electrolyte water content and temperature of the anodization bath used during fabrication of the sensor element.

Chapter 3 and 4 utilize the optimized titania nanotube sensor element, which is functionalized with cobalt by an incipient wetting impregnation method (Co-TNA), to examine the sensor response to the four predominate tuberculosis biomarkers. A predicted reaction mechanism for the electrochemical interaction of methyl nicotinate with Co-TNA will be illustrated based on experimental and characterization evidences. This mechanism can be extended to explain the interaction of the other three biomarkers with Co-TNA as well. Further, the experimental and theoretical limit of detection of the sensor will be determined. The specificity of the Co-TNA sensor will also be investigated

by exposing the sensor to other organic vapors commonly found in human breath. Lastly, the chapter will be wrapped up by examining the electrochemical reaction kinetics of Co-TNA with the four TB biomarkers by invoking the Butler Volmer equation.

Chapter 5 explores the development of an alternate synthesis method which allows for in situ functionalization of titania nanotubes with oxygen containing metal species (i.e., $Co(OH)_2$) during anodization. Amperometric detection of volatile organic biomarkers with various concentrations using next-generation titania nanotubes functionalized with $Co(OH)_2$ (*i*Co-TNA) were compared with $Co(OH)_2$ functionalized titania nanotubes via the wet incipient method (Co-TNA), discussed in the previous chapter. Improved sensor response and sensitivity was observed with next-generation titania nanotubes, which can be attributed to homogeneous distribution of reactive sites directly in contact with the parent titania. A mechanism for sensor response and in situ functionalization will be presented.

In Chapter 6, the focus shifts from cobalt to gold functionalized titania nanotubes. Light assisted sensing of the biomarkers using Au-TNA will be demonstrated in this chapter. Gold nanoparticles, functionalized on TNA using an electroless deposition technique, couples plasmonic behavior of Au with slow photon behavior of TNA under visible light illumination, to yield significantly enhanced sensor response over Co-TNA and *i*Co-TNA. Two different schemes illustrating the sensing mechanism have been presented.

Chapter 7 extends the electrochemical detection capabilities of the TNA-based sensing platform to investigate the sensing of breath biomarkers from other diseases as well. Nickel functionalized TNA was utilized to detect the four major VOCs obtained

from the breath of colorectal cancer patients, which have recognition capabilities greater than 90%.

Chapter 8 mainly covers the second research objective stated in the previous section. This chapter presents the sensor element integration into the hardware and subsequent testing of the resultant sensor systems in the application environment. The sensor response was recorded upon exposure to actual breath from TB patients, and compared with response to vapor of VOB mimics. The presence of the biomarkers was further confirmed by GC-MS analysis using solid phase microextraction fiber.

In the final chapter of the dissertation, the results from all the above chapters have been summarized and conclusions stated regarding the techno-economic feasibility of the proposed TNA sensor for use in the actual POC environment. In addition, some future studies possible in this direction to develop a smart sensor system with enhanced sensitivity have been presented as well.

1.6 References

1. World Health Organization. Diagnostics for tuberculosis: Global demand and market potential. (2006).
2. UNITAID. Tuberculosis: Diagnostics Technology and Market Landscape. 4th Edition (2015).
3. S. Haldar, S. Chakravorty, M. Bhalla, S. De Majumdar and J. S. Tyagi, *J Med Microbiol*, **56**, 1356 (2007).
4. K. R. Steingart, V. Ng, M. Henry, P. C. Hopewell, A. Ramsay, J. Cunningham, R. Urbanczik, M. D. Perkins, M. A. Aziz and M. Pai, *Lancet Infect Dis*, **6**, 664 (2006).
5. Y. R. Smith, D. Bhattacharyya, S. K. Mohanty, and M. Misra, *J. Electrochem. Soc.*, **163** (3), B83-B89 (2016).

6. D. Bhattacharyya, Y. R. Smith, S. K. Mohanty, and M. Misra, *Mater. Res. Express*, **2**, 025002 (2015).

7. NICE. Tuberculosis: clinical diagnosis and management of tuberculosis, and measures for its prevention and control. London: National Institute for Health and Care Excellence. (2011).

8. Updated guidelines for using interferon gamma release assays to detect mycobacterium tuberculosis infection. *MMWR*, **59,** 1‑25 (2010).

9. World Health Organization. Guidelines on the management of latent tuberculosis infection. (2015).

10. M. Pai, C. M. Denkinger, S. V. Kik, M. X. Rangaka, A. Zwerling, O. Oxlade, J. Z. Metcalfe, A. Cattamanchi, D. W. Dowdy, K. Dheda, and N. Banaei, *Clin Microbiol Rev*, **27,** 3‑20 (2014).

11. Z. Dezemon, C. M. Muvunyi and O. Jacob, *Int. Res. J. Bacteriol.*, **1**, 1 (2014).

12. K. Dheda, C. E. Barry, G. Maartens, and C. Town, Tuberculosis: *The Lancet*, **6736**, 1–17 (2015).

13. E. L. Corbett, C. J. Watt, N. Walker, D. Maher, B. G. Williams, M. C. Raviglione, and C. Dye, *Arch Intern Med*, **163**, 1009-21 (2003).

14. R. N. van Zyl-Smit, A. Binder, R. Meldau, H. Mishra, P. L. Semple, G. Theron, J. Peter, A. Whitelaw, S. K. Sharma, R. Warren, E. D. Bateman, and K. Dheda, *PLoS One*, **6,** e28815 (2011).

15. M. Cruciani, C. Scarparo, M. Malena, O. Bosco, G. Serpelloni, and C. Mengoli, *J Clin Microbiol*, **42,** 2321‑25 (2004).

16. K. R. Steingart, M. Henry, V. Ng, P. C. Hopewell, A. Ramsay, J. Cunningham, R. Urbanczik, M. Perkins, M. A. Aziz, and M. Pai, *Lancet Infect Dis*, **6,** 570‑81 (2006).

17. A. Whitelaw, J. Peter, H. Sohn, D. Viljoen, G. Theron, M. Badri1, V. Davids" M. Pai, and K. Dheda, *Eur Respir J*, **38,** 1393‑97 (2011).

18. S. E. Dorman, *Clin Infect Dis*, **50**, S173-S177 (2010).

19. K. Dheda, M. Ruhwald, G. Theron, J. Peter, and W. C. Yam. *Respirology*, **18,** 217‑32 (2013).

20. World Health Organization. The use of molecular line probe assay for the detection of resistance to second-line anti-tuberculosis drugs. (2013).

21. WHO. Xpert MTB/RIF implementation manual. Geneva: World Health Organization, (2014).

22. M. Barnard, N. C. Gey van Pittius, P. D. van Helden, M. Bosman, G. Coetzee, and R. M. Warren. *J Clin Microbiol*, **50,** 3712‑16 (2012).

23. J. G. Peter, G. Theron, R. van Zyl-Smit, A. Haripersad, L. Mottay, S. Kraus, A. Binder, R. Meldau, A. Hardy, and K. Dheda, *Eur Respir J*, **40,** 1211‑20 (2012).

24. S. D. Lawn, K. Dheda, A. D. Kerkhoff, J. G. Peter, S. Dorman, C. C. Boehme, and M. P. Nicol, *BMC Infect Dis*, **13,** 407 (2013).

25. J. Minion, E. Leung, E. Talbot, K. Dheda, M. Pai, and D. Menzies, *Eur Respir J*, **38,** 1398‑405 (2011).

26. M. Phillips, R. N. Cataneo, R. Condos, G. A. Ring Erickson, J. Greenberg, V. La Bombardi, M. I. Munawar, and O. Tietje, *Tuberculosis*, **87**, 44-52 (2007).

27. M. Phillips, V. Basa-Dalay, J. Blais, G. Bothamley, A. Chaturvedi, K. D. Modi, M. Pandya, M. P. R. Natividad, U. Patel, N. N. Ramraje, P. Schmitt, and Z. F. Udwadia, *Tuberculosis*, **92**, 314–320 (2012).

28. M. Syhre and S. T. Chambers, *Tuberculosis*, **88**, 317-23 (2008).

29. M. Syhre, L. Manning, S. Phuanukoonnon, P. Harino, and S. T. Chambers, *Tuberculosis*, **89**, 263-6 (2009).

30. World Health Organization. Tuberculosis Fact Sheet. (2013).

31. Kalorama Information. World Market for ID Diagnostic Tests. (2013).

32. TB Alliance. Economic Impact of TB. http://www.tballiance.org/why/economic-impact.php

33. C. Denkinger, Target Product Profiles for Next Generation TB Diagnostics. FIND. (2014).

34. D. Bhattacharyya, Y. R. Smith, S. K. Mohanty, and M. Misra, *J. Electrochem. Soc.*, **163**, B206-B214 (2016).

35. K. D. G. Van de Kant, L. J. T. M. van der Sande, Q. Jöbsis, O. C. P. van Schayck, and E. Dompeling, *Respir. Res.*, **13**, 117 (2012).

36. M. Zhou, Y. Liu, and Y. Duan, *Clin. Chim. Acta*, **413**, 1770–1780 (2012).

37. S. Meinardi, K. B. Jin, B. Barletta, D. R. Blake, and N. D. Vaziri, *Biochim. Biophys. Acta - Gen. Subj.*, **1830**, 2531–2537 (2013).

38. C. S. J. Probert, F. Ahmed, T. Khalid, E. Johnson, S. Smith, and N. Ratcliffe, *J. Gastrointest. Liver Dis.*, **18**, 337–343 (2009**)**.

39. J. Li, Y. Peng, and Y. Duan, *Crit. Rev. Oncol. Hematol.* **87**, 28–40 (2013).

40. A. J. Saleh Ahammad, Y. H. Choi, K. Koh, J. H. Kim, J. J. Lee, and M. Lee, *Int. J. Electrochem. Sci.*, **6**, 1906–1916 (2011).

41. Bott, R. WHO Global Tuberculosis Report 2015, 1–192 (2015).

42. R. McNerney, B. A. Wondafrash, K. Amena, A. Tesfaye, E. M. McCash, and N. J. Murray, *BMC Infect. Dis.*, **10**, 161 (2010).

43. J. Haar, *Spec. Chem. Mag.*, **30**, (2010).

44. N. Queralto, A. N. Berliner, B. Goldsmith, R. Martino, P. Rhodes, and S. H. Lim, *J. Breath Res.* **8**, 027112 (2014).

45. Y. R. Smith, D. Bhattacharyya, S. K. Mohanty, and M. Misra, *J. Electrochem. Soc.*, **163**, B83–B89 (2016).

46. R. Moos, K. Sahner, M. Fleischer, U. Guth, N. Barsan, and U. Weimar, *Sensors*, **9,** 4323–65 (2009).

47. G. F. Fine, L. M. Cavanagh, A. Afonja, and R. Binions, *Sensors*, **10,** 5469–502 (2010).

48. M. Arafat, B. Dinan, S. A. Akbar, and A. Haseeb, *Sensors*, **12**, 7207–58 (2012).

49. A. Kolmakov and M. Moskovits, *Annu. Rev. Mater. Res.*, **34**, 151–80 (2004).

50. B. Mishra, P. Ghildiyal, S. Agarkar, and D. Khushalani, *Mater. Res. Express*, **1**, 025005 (2014).

51. Y. R. Smith, R. S. Ray, K, Carlson, B. Sarma, and M. Misra, *Materials*, **6**, 2892–957 (2013).

52. X. Wang, C. Zha, C. Ji, X. Zhang, L. Shen, Y. Wang, A. Gupta, S. Yoriya, and N. Bao, *Mater. Res. Express*, **1**, 035031 (2014).

53. K. Lee, A. Mazare, and P. Schmuki, *Chem. Rev.*, 114, 9385–454 (2014).

54. O. K. Varghese, D. Gong, M. Paulose, K. G. Ong, and C. A. Grimes, *Sensors Actuators B*, **93**, 338–44 (2003).

55. K. Chen, K. Xie, X. Feng, S. Wang, R. Hu, H. Gu, and Y. Li, *Int. J. Hydrog. Energy*, **37**, 13602–9 (2012).

56. E. Sennik, Z. Colak, N. Kilinc, and Z. Z. Ozturkrk, *Int. J. Hydrog. Energy*, **35**, 4420–7 (2010).

57. Z. Wen and L. Tian-mo, *Physica B*, **405**, 564–8 (2010).

58. Z. Wen, L. Tian-Mo, and L. De-Jun, *Physica B*, **405**, 4235–9 (2010).

59. H. F. Lu, F. Li, G. Liu, Z-G. Chen, D-W. Wang, H-T. Fang, G. Q. Lu, Z. H. Jiang, and H-M. Cheng, *Nanotechnology*, **19**, 405504 (2008).

60. P. M. Perillo and D. F. Rodriguez, *Sensors Actuators B*, **171**, 639–43 (2012).

61. Y. Kwon, H. Kim, S. Lee, I-J. Chin, T-Y. Seong, W. I. Lee, and C. Lee, *Sensors Actuators B*, **173**, 441–6 (2012).

62. Z. Wen and L. Tian-mo, *Physica*, **405**, 1345–8 (2010).

63. S. Banerjee, S. K. Mohapatra, M. Misra, and I. B. Mishra, *Nanotechnology*, **20**, 075502 (2009).

64. H. Jayamohan, Y. R. Smith, B. K. Gale, M. Misra, and S. K. Mohanty, IEEE Proc. Sensors (Baltimore, MD, 3–6 November), 1–4 (2013).

65. R. S. Ray, B. Sarma, S. Mohanty, and M. Misra, *Talanta*, **118**, 304–11 (2014).

CHAPTER 2

OPTIMIZATION OF TiO_2 NANOTUBE MORPHOLOGY FOR MAXIMUM SENSOR RESPONSE TO VOLATILE ORGANIC BIOMARKERS

2.1. Introduction

One-dimensional, highly ordered TiO_2 nanotube arrays are large bandgap semiconductors with high surface-to-volume ratio facilitating efficient charge transfer with negligible recombination. Owing to the unique electrical, optical, and thermal properties of titania nanotubes, it has found use in several applications ranging from solar water splitting for hydrogen generation, supercapacitors, sensors, and solar cells, to microfluidic photocatalytic degradation of organic and biological water contaminants.[1]

It is important to note that anodized titania nanotubular arrays have been widely used in a variety of sensing applications, especially gas- or vapor-based sensing. In the past, researchers have demonstrated the use of titania nanotubes for hydrogen sensing, both at room and elevated temperature,[2-5] while amorphous TiO_2 nanotube arrays have been used as low-temperature oxygen sensors.[6] Gas sensing properties of titania nanotubes through electrochemical response to ammonia at room temperatures have been shown by Perillo and Rodriguez.[7] Detection of volatile organic compounds (VOCs) represents a significant portion of the gas sensing capabilities of titania nanotube arrays.

Titania nanotube arrays have exhibited superior ethanol[7,8] and formaldehyde[9] sensing properties to most one-dimensional nanostructured oxides. A SnO_2 – TiO_2 composite oxide sensor doped with silver has been used for sensing volatile organic compound gas such as ethanol, methanol, acetone, and formaldehyde.[10] It is evident that titania nanotube arrays (TNA) synthesized by electrochemical anodization of titanium foils[11,12] offer a robust substrate to functionalize with metals and/or metal hydroxides, which have a high binding affinity for the VOCs of interest. Functionalized titania nanotube arrays have been used for sensor detection of a plethora of VOC analytes such as the explosive triacetone triperoxide[13] and environmental pollutants such as trichloroethylene.[14] Recently, we explained the mechanism for amperometric detection of methyl nicotinate vapors using TNA functionalized with cobalt hydroxide.[15]

However, it is imperative to optimize the TNA morphology in order to maximize the sensor response to the VOC vapors. TiO_2 nanotubes developed with variable diameter and thickness for ethanol sensing at room temperature exhibited relatively poor sensitivity and sluggish response and recovery. [7] On the other hand, ethanol and methanol sensing investigated with TiO_2 nanotubes with varying nanotube morphology achieved by variation of applied potential, temperature, and the type of electrolytes exhibited relatively poor response magnitude.[16] These instances of poor sensitivity, meager response magnitude, and sluggish response could have been avoided by prior optimization of the titania nanotube structure.

A lot of research has been carried out in an endeavor to tweak the nanotube morphology to suit the application requirements. Broadly, the evolution of the self-ordered titania nanotubular array can be categorized under different generations

determined predominantly by their synthesis methods. The conventional first-generation TNA synthesized in acidified fluoride solution with mechanical stirring yielded nanotubes of 30-80nm diameter and 400-500 nm length in 45 minutes.[17] A similar acidified fluoride solution aided by ultrasonication gave rise to second-generation nanotubes characterized by well-ordered, compact, and robust morphology and with dimensions similar to the first-generation tubes achieved within 20 minutes.[18] It is important to note that acidic solution resulted in stunted nanotube growth due to higher etching rates. The third-generation nanotubes employed sonoelectrochemical anodization techniques using neutral organo-fluoride solutions, resulting in smooth, tunable nanotube dimensions varying from 20-200 nm diameter and 0.5-50 μm length over 30-90 minutes duration.[19] The fourth-generation nanotubes comprise TiO_2-metal composites (TiO_2 – MOx / M(OH)x) synthesized by the one-step in-situ anodic functionalization method in metal-organo-fluoride electrolyte with achievable dimensions ranging from 20-150 nm diameter and 0.5-15 μm length over 30-90 minutes duration.[20,21] Further, highly ordered, double walled,[22] hierarchical,[23] Y-branched,[24] and light assisted anodic[25] TiO_2 nanotubes have been successfully synthesized using simple electrochemical anodization techniques. In a recent study, nanoarchitectured arrays of straight, conical, dumbbell, and tilted shaped TiO_2 nanotubes revealed interesting, tunable surface plasmon resonance behavior when coated with Ag and Au nanoparticles.[26] Electrochemical tuning of titania nanotube morphology in inhibitor type electrolytes was examined through potentiostatic anodization carried out in three different electrolytes, over a broad voltage range from 2 to 200V in 0.1–48 wt% HF concentrations and different electrolytic compositions for anodization times ranging from 5s to 70 h.[27] The study suggested wide tunability in

lateral dimensions and aspect ratio of TiO_2 nanotubes by systematically varying the anodization voltage and electrolyte composition. Similar conclusions were echoed in other studies as well.[28,29] It is evident that although researchers have successfully modified the titania nanotube morphology, not much literature is available documenting the geometrical optimization for sensing applications. Only previously, Hazra *et al.*[30] had attempted to judiciously control the titania nanotube structure to enhance its alcohol sensing properties. They had suggested that the pivotal parameters responsible for controlling the nanotube structure include (i) concentrations of oxygen vacancy (Vo) of the nanotubes, (ii) nanotube radius, (iii) tube wall thickness, (iv) wall separation, and (v) tube length.

In this chapter, we present the optimization of the two most critical attributes of TiO_2 nanotubes viz. oxygen vacancy concentrations (Vo), and nanotube wall thickness for maximum sensor response to electrochemical detection of tuberculosis volatile organic biomarkers using cobalt functionalized TNA. Although variation of other mentioned parameters were examined as well, their effect on sensor response was considered not significant enough to be reported.

2.2 Experimental

Titania nanotubes were synthesized by electrochemical anodization of titanium foils (0.1016 mm thick, ESPI metals, G1 grade).[25] Titanium foils were cut into 1.5 x 1.5 cm coupons and were hand-polished with emery paper. Subsequently, the coupons were degreased by sonicating in an acetone-isopropanol (50% v/v each) mixture for 30 minutes. After rinsing with DI water, the coupons were anodized in a fluorinated (0.5

wt% NH_4F) ethylene glycol solution in a teflon beaker under constant stirring at 60 rpm using a two-electrode configuration. The Ti coupon served as the anode and Pt foil as the counter electrode (Agilent E3647A DC power source) with electrode separation maintained at 3cm throughout the process.

It is known that variation of anodization voltage and time leads to change in nanotube diameter and length, respectively.[29] Hence, anodization was carried out for 1 hour at 30, 40, and 60V in a solution containing 3% water to observe the effect of diameter on VOB sensing. As expected, there was no significant effect on the sensor response. Subsequently, TNA was synthesized at 30V for different lengths of time (1, 2, 4 hours) to vary the nanotube length. Due to lack of any observable change in sensor response, morphological and sensor response results from variation in nanotube diameter and length have not been reported here. For further considerations, nanotubes were synthesized at 30V for 1 hour.

Previous reports have indicated that the concentration of the oxygen vacancies in the titania nanotubes has been determined by altering the electrolyte composition.[30] Hence, the electrolyte composition of the anodization bath was varied between 0.5, 3, and 10 wt% water to investigate the effect of the oxygen vacancy content on the sensor response. The resultant titania nanotubes ($TNA_{OV0.5\%}$, $TNA_{OV3\%}$, $TNA_{OV10\%,}$ repectively) were characterized by Mott-Schottky measurements at 1000 Hz alternating frequency in 0.1M aqueous NaOH electrolyte solution to determine the concentration of the charge carriers. Results indicated that maximum sensor response was achievable when anodization was carried out in a solution containing 3% water. Thus, the effect of the variable nanotube wall thickness on sensor response was examined by synthesizing

nanotubes at 10 (TNA_{10C}), 25 (TNA_{25C}), and 50˚C (TNA_{50C}) using the optimized electrolyte composition of 96.5 wt% EG + 3 wt% water + 0.5 wt% NH_4F at 30V for 1 hour. To restrict the growth of the nanotubes to the side facing the counter electrode, the back side of coupons was masked with a kapton tape. Post anodization, the coupons were rinsed with deionized water, and stored overnight under vacuum at 110 ˚C. Subsequently, the anodized coupons were annealed in a tube furnace at 500 ˚C (ramp up at 2.8 ˚C/min from 25 ˚C) for 2 hours in oxygen atmosphere to render crystallinity to the titania lattice.

Cobalt functionalization of titania nanotubes array (TNA) was achieved by incipient wetting impregnation (IWI) method wherein annealed TNA coupons were immersed in 0.1 M $CoCl_2$ (Alfa Aesar) solution in ethanol and sonicated for 30 minutes in an ultrasonic bath and dried overnight under vacuum at 110 ˚C. The resultant cobalt functionalized TiO_2 nanotube array (Co-TNA) sensors were used for electrochemical detection of the tuberculosis VOBs.

Morphological examination (surface and cross section) of the TNA and Co-TNA was performed using a field emission scanning electron microscope (Hitachi S-4800 SEM) with a tungsten filament-based field emission gun at 3 kV accelerating voltage and 15 µA emission current. Energy dispersive x-ray spectroscopic (EDS) analysis was performed using an Oxford (X-Max) EDAX detector attached to the SEM. EDS analysis was carried out at 20 kV accelerating voltage and high probe current. The AZtecEnergy acquisition and EDS analysis software synchronized with the X-Max detector was used mapping and spectral analysis.

The electrochemical detection of the four biomarker vapors viz. methyl nicotinate, methyl p-anisate, methyl phenylacetate, and o-phneylanisole was carried out in a custom

built sensing chamber as described in our previous work.[25] A two-electrode potentiostat system (Gamry Reference 600) was used such that the working electrode had electrical connections on the Co-TNA surface while the counter electrode was connected to the unanodized titanium metal side. Nitrogen gas (UHP grade) at 200 sccm (standard cubic centimeters per minute) was used as the carrier gas and bubbled through a 10 mM biomarker solution in ethanol. The resultant vapor was delivered to the sensing chamber. A low bias (based on cyclic voltammetry studies, not shown) was applied and a potentiostatic (I–t) run was carried out to test the sensor response. Preliminary cyclic voltammetry tests determined the bias voltage for each biomarker. Prior to introducing the analyte or the target biomarker vapor, the sensor was allowed to stabilize under nitrogen flow for ~100 seconds. Upon achieving maximum current when exposed to the biomarkers, the analyte vapor was discontinued and nitrogen was reintroduced into the sensing chamber, until the current decreased gradually and became steady. Sensing experiments were carried out at ambient room temperature. Control tests were run with ethanol.

2.3. Results and Discussion

2.3.1 Effect of Varying Water Content during Anodization

2.3.1.1 Effect on nanotube morphology. The FESEM images as shown in Figure 2.1 reveal the surface morphology of the grown anodic layers of three TiO_2 samples with variable oxygen vacancies ($TNA_{OV0.5\%}$, $TNA_{OV3\%}$, $TNA_{OV10\%}$). In the presence of very low water content (0.5 wt% water), a fiberlike nonuniform TiO_2 surface was formed where the wall connections between the individual nanotubes were not distinguishable.

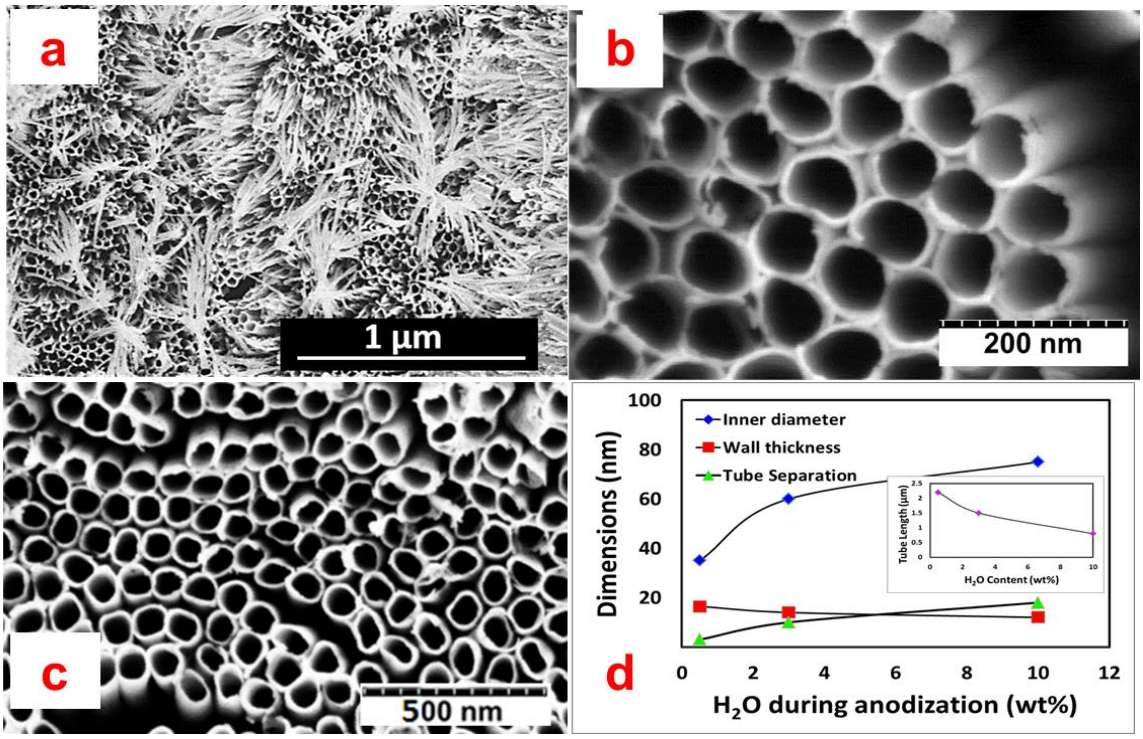

Figure 2.1. SEM micrographs (a-c) illustrating the variation in TiO_2 nanotube morphology when the water content in the anodization bath was varied (a) 0.5 wt%, (b) 3 wt%, (c) 10 wt%.. and (d) the variation in dimensions such as inner tube diameter, wall thickness, and tube separation as a function of water content in anodization bath.

There is visible evidence of a sporadic oxide layer on the surface of $TNA_{OV0.5\%}$ that must have grown during the initial stages of synthesis.[31] This indirectly affects the subsequent nanotube formation. Such sporadic patches were removed significantly in the case of $TNA_{OV3\%}$ (3 wt% water), indicating the formation of both wall-connected and wall-separated TiO2 nanotubes (Figure 2.1b). In the case of $TNA_{OV10\%}$ (Figure 2.1c), wall-separated and ordered TiO2 nanotube array formation is evident where no perceptible coverage of oxide layer is observed. Self-ordered, vertically oriented nanotubes were found to be more prominent in $TNA_{OV3\%}$, and $TNA_{OV10\%}$ compared to those in $TNA_{OV0.5\%}$., where the nanotubes tend to droop. It is also observed that the tube length decreased (from 2.2 to 0.8 µm) slightly from $TNA_{OV0.5\%}$ to $TNA_{OV10\%}$ as the water

content in the anodization bath was increased from 0.5 to 10 wt%.

In order to understand the effect of the varying water content (oxygen vacancy) during the electrolytic anodization on the nanotube morphology and its subsequent effect on the sensor response, we first need to throw some light on the titania nanotube formation mechanism. The titania nanotube formation involves a three-stage mechanism comprising initial oxide barrier layer formation, pore nucleation formation, and steady state nanotube growth. The oxide growth depends on the reaction between Ti metal and water under the influence of an applied potential, whereas oxide dissolution depends on the reaction between the oxide layer and fluoride ions giving rise to soluble titanium fluoride [TiF_6^{2-}]. Thus, it should be noted that the anodic current density during anodization is comprised of two components: the first is current due to the oxidation of titanium at the metal/oxide interface, and the second is current due to the dissolution process at the oxide/electrolyte interface.[32] Although the formation mechanism outlined above for nanotube synthesis is generally accepted, it does not readily explain the driving force for the formation of a tubular morphology over a porous oxide layer or fiber-like structures for that matter. Smith [33] had stated that during the initial stages of anodizing titanium, a moderately soluble barrier layer is formed on the surface, giving rise to a porous oxide film. Oxidation-induced strain compensated by a relatively large flow of cations from the metal, and stress generation due to varying stoichiometry of the oxide layer counteracts the stress developed along the metal/oxide interface, resulting in instability of the perturbed oxide layer.[33,34] Therefore, the initial pore formation mechanism is attributed to instability of the perturbed barrier oxide layer and not due to pitting of the oxide layer from halide species. Upon achieving a critical barrier layer

thickness, the instability of the surface allows the applied electric field to drive the anionic species to the wells of the perturbed surface, where the applied field strength is the highest.[35] A further reduction in the surface energy resulted in an increase in surface instability which is aided by fluoride and hydrogen ions. During the hydrolysis reaction, H^+ ions accumulate to maintain electroneutrality, while F^- ions migrate to the H^+ sites. When a critical concentration is reached in localized regions, dissolution of TiO_2 occurs, resulting in formation of TiF_6^{2-}. Now, in an aqueous electrolyte, pore nucleation can be attributed to both field-assisted ejection of Ti^{4+} as well as chemical dissolution of titania.[36] The dissolution reaction of Ti cations creates negatively charged cation vacancies in the oxide, which migrate to the metal/oxide interface as a result of the potential gradient across the oxide.[37] The presence of metal-cation vacancies near the metal/oxide interface facilitates the ejection of Ti^{4+} to the available vacancy. The grain structure at the electrode/electrolyte interface assumes significance in the context or pore nucleation and subsequent tube formation. A relatively smooth surface enables uniform pore nucleation by even distribution of eclectic field as well as field-induced and chemical etching of the oxide. When the surface is rough or when the water content is varied, the etch rates of various crystal planes will vary across the surface and the grains are comparable in size to the amplitude and spacing of the pores, and the pore formation becomes irregular.

Therefore, when the water content in the electrolyte was varied during anodization, defect or oxygen vacancies (Vo) developed, resulting in stoichiometry-controlled TiO_2 nanotubes. Reduced TiO_2 nanotubes were formed with nonconforming stoichiometric composition due to the restricted supply of water (or the restricted supply

of oxygen) in electrolyte.[38] Such nanotubes with substoichiometric composition can be represented as Ti_nO_{2n-1} (n = 1, 2, 3⋯), as shown in equation 2.1, which leads to the formation of suboxides states of titanium, resulting in higher concentrations of Vo and substandard nanotubular structure formation.[30,39]

$$Ti^{4+} + xO^{2-} \rightarrow TiOx \text{ (sub - oxide)} + 2xe^{-} \quad \ldots(2.1)$$

This can be attributed to the fact that limited water content restricts formation of $[TiF_6^{2-}]$, and thus restricts formation of titania. The fluorine ions have a tendency to directly react with Ti^{4+} and form undissolved $[TiF_6^{2-}]$ due to presence of limited amount of water in the electrolyte. Under this prevailing solution chemistry, it is impossible to form ordered titania nanotubes. Due to differential etch rates and lack of hydroxyl ions, the surface gives the appearance of wall-connected nanotubes with nanofiber or nanograss-like protrusions.[40]

The separation of the pore walls in titana is probably due to the dehydration of titanium hydroxide and radial cation vacancies. It has been shown experimentally that the outer oxide layer exposed to the electrolyte has excess hydroxyl ions compared to the inner oxide layer not exposed to the electrolyte. [41,42] Three ions, namely F^-, O^{2-}, and OH^-, migrate from the electrolyte to the oxide/metal interface. The mobility of these ions is dictated by their respective size and charge strength, as OH^- are larger than F^- and O^{2-} and contain less charge than O^{2-} ions. As a result, the OH^- ions migrate slower than the F and O^{2-} and most likely result in the formation of predominantly $[Ti(OH)_n]^{(4-n)+}$ species on the surface (n = 2-5).[43] Considering a mechanism proposed by Raja *et al.*,[34] where cation vacancy transport in the radial direction leads to cell boundary separation, cation vacancies can migrate along the electric field due to their negative charge. Along the

peaks of the surface, the field strength is not as high. If the cation vacancies are transported radially, vacancies would populate within the area of two neighboring pores. Since the charges are the same, they would repel to maintain an equilibrium distance. To maintain electroneutrality, oxygen vacancies could be generated. If the dissolution of the oxide is much higher than the generation oxygen vacancies at the metal/barrier layer interface, the repelling forces of the cation vacancies could cause separation of neighboring pores. Once the cell boundaries separate, they would become exposed to the electrolyte while forming a thin titanium hydroxide outer layer. Dehydration of titanium hydroxide to titanium dioxide results in a cell volume decrease. Neighboring nanotubes are separated by the volume shrinkage of two neighboring cell walls.

When using electrolytes with very low water content, this limits the amount of OH^- and O^{2-} ions, thereby resulting in the slow and negligible formation of titanium hydroxide, causing slow dehydration at the cell boundary. This results in the volume shrinkage to be continually compensated by the volume expansion of $TiO_2/Ti(OH)_x$ formation. Thus, nanotubes formed in electrolytes containing higher water content are better wall separated.

The predominant effect of the variation in stoichiometry (or V_O) in TiO_2 nanotubes achieved by varying the water contents in the electrolyte during anodization impacts the separation between two adjacent nanotubes. As side effects, it influences the other structural parameters, like tube length, inner tube diameter, and nanotube wall thickness (Figure 2.1). With lowering of the water content, the barrier layer thickness becomes thinner. This results in better ionic conduction, and fast movement of metal/oxide (Ti/TiO2) interface toward metal substrate (Ti), enhancing the TiO2

nanotube lengths.[31,44] In a study by Yin *et al.*,[45] they found the nanotube diameter to increase with increasing water content in ethylene glycol (1-50 vol.%) while keeping all other synthesis variable constant. The larger diameters achieved with higher water content electrolytes is a result of higher OH concentration. This accelerates the formation of titanium hydroxide at the cell walls, and enhances the rates of volume shrinkage during condensation.

2.3.1.2 Effect on sensor response. A perceivable sense of the variable oxygen vacancy concentration in the nanotubes resulting from the different water content in the anodization bath, in terms of a physical quantity, can be directly obtained from determination of the charge carrier density. It is an established fact that TiO2 nanotubes are an n-type semiconductor and possess electrons as majority charge carriers. Mott−Schottky analysis ($1/C^2$ vs potential) was used to determine the carrier density (N_D) of all the stoichiometrically varied (or variable V_O) TiO2 nanotubes ($TNA_{OV0.5\%}$ − $TNA_{OV10\%}$). The slopes of the linear parts of the curves in the Mott−Schottky plot were found to be positive, implying that the samples were n-type semiconductors, as shown in Figure 2.2. Capacitance measurements were conducted according to the following equation 2.2:

$$\frac{1}{C^2} = \frac{2}{N_D e\, \varepsilon_0 \varepsilon_r}\left[(V - V_{FB}) - \frac{kT}{e}\right] \quad \ldots (2.2)$$

where C is the space charge capacitance in the semiconductor, N_D is the carrier density, e is the electronic charge, ε_0 is the permittivity of the vacuum, ε_r is the relative permittivity of the semiconductor, V is the applied potential, V_{FB} is the flat band potential, k is the Boltzmann constant, and T is the temperature. Electrical property (or donor density level) of TiO_2 nanotubes was obtained by electrochemical measurement of the space charge layer capacitance following the relationship (equation 2.3)[46]

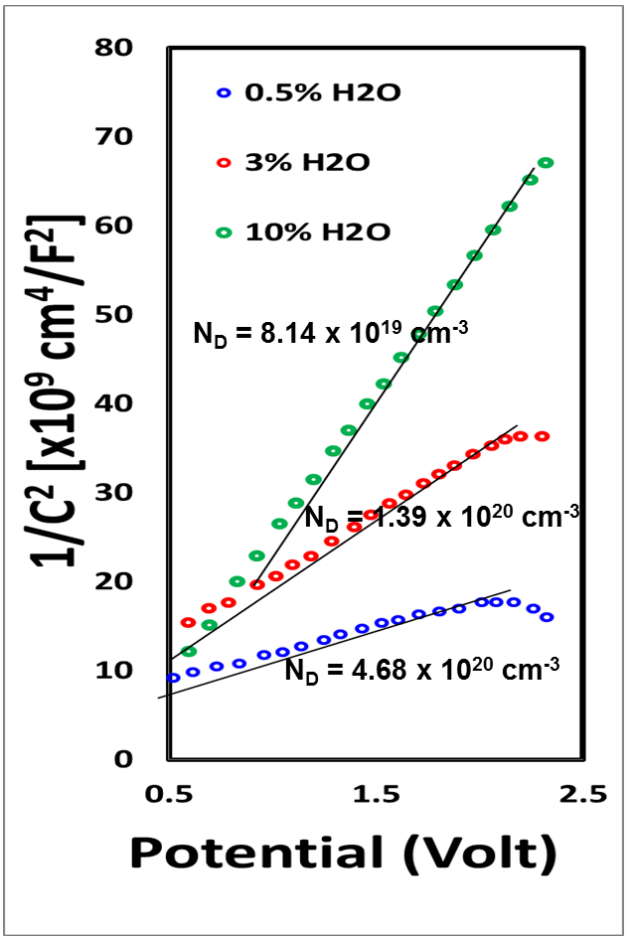

Figure 2.2. Mott-Schottky plots of TiO_2 nanotubes anodized in different electrolytic baths containing 0.5 wt%, 3 wt%, and 10 wt% water, with their corresponding charge carrier densities (N_D).

$$N_D = \left(\frac{2}{e\ \varepsilon_0 \varepsilon_r}\right)\left[\frac{d\left(\frac{1}{C^2}\right)}{dV}\right]^{-1} \quad \ldots (2.3)$$

where $\varepsilon_0 = 8.85 \times 10^{-14}$ F/cm^{-1}, e = 1.6×10^{-19} C, and ε_r of the anatase TiO_2 ($\varepsilon_r = 48$). As revealed from the Mott-Schottky plot in Figure 2.2, all of the three TiO2 nanotubes ($TNA_{OV0.5\%}$ – $TNA_{OV10\%}$) showed n-type conductivity with carrier density of $N_D(TNA_{OV0.5\%}) = 4.68 \times 10^{20}$ cm^{-3}, $N_D(TNA_{OV3\%}) = 1.39 \times 10^{20}$ cm^{-3}, and $N_D(TNA_{OV10\%}) = 8.14 \times 10^{19}$ cm^{-3}.

Figure 2.3 represents the sensor response as the function of water content in the electrolytic bath during anodization ($TNA_{OV0.5\%}$ − $TNA_{OV10\%}$) with exposure to vapors of 10 mM volatile organic biomarkers (methyl nicotinate, methyl p-anisate, methyl Phenylacetate, and o-phenylanisole). Maximum response was recorded for the TNA-based sensors anodized at room temperature in a bath containing 3wt% water. It is evident that $TN_{OV3\%}$ exhibits the best sensing performance in the set, with the highest response magnitude for each biomarker. Researchers have stated in the past that the differences in the magnitude of the sensor response from different biomarkers can be attributed to anomaly in molecular size/molecular weight of the biomarkers in gaseous phase [47-49] and variation in oxidation potential of biomarkers in gaseous phase.[48]

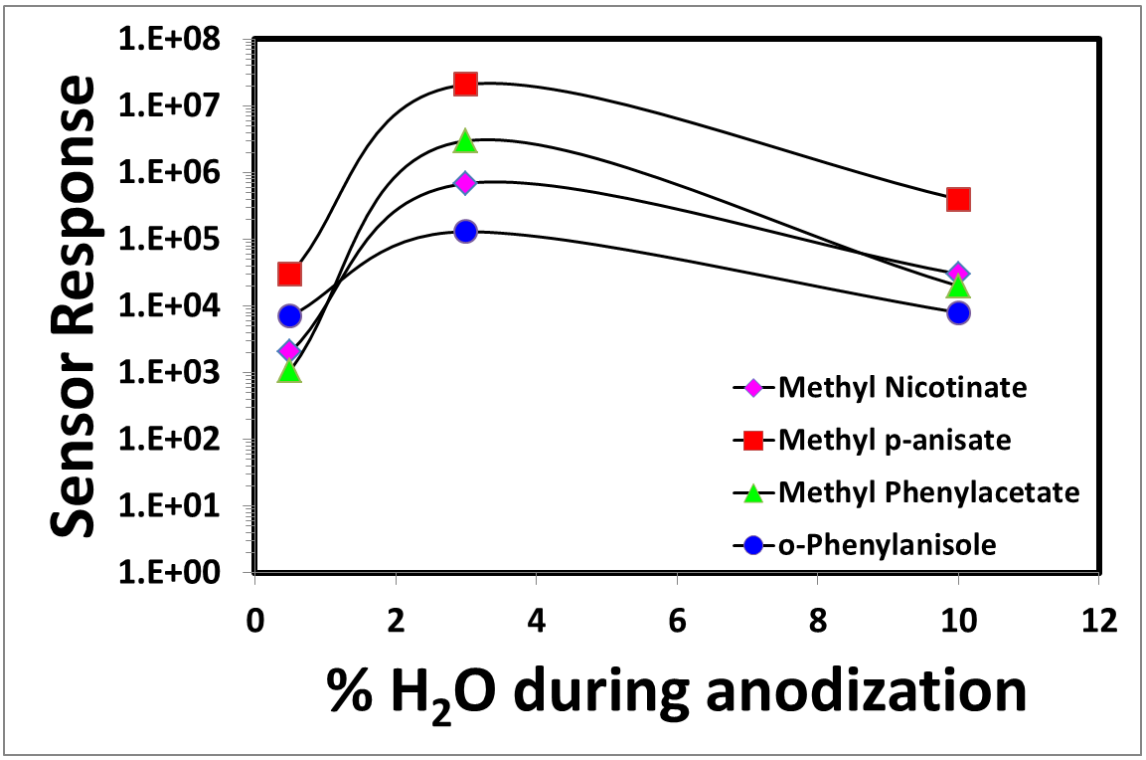

Figure 2.3. Sensor response to the four TB VOBs using cobalt functionalized TiO_2 nanotube array based sensor synthesized in an anodization bath containing different wt% water.

The sensor study exhibited distinctive improvements where appreciably high response magnitude was achieved by judiciously controlling the nanotube parameters through varying the water content in the electrolyte during the anodization process. The trade-off between augmented surface-to-volume ratio and reduced charge carrier density upon increasing the anodization water content is noteworthy. In the case of $TN_{OV0.5\%}$, though the amount of Vo is the highest, extremely poor surface-to-volume ratio resulted into the low response magnitude compared to that of $TNA_{OV3\%}$ and $TNA_{OV10\%}$. The four major factors which control the response magnitude of the semiconducting metal oxide-based gas/vapor sensor are (i) binding interaction between the target gas/vapor species and the semiconducting surface,[50] (ii) effective surface area of the nanotubes providing the available gas interaction sites,[51] (iii) dissociative adsorption of oxygen and biomarker molecules,[52,53] and (iv) required activation energy for the electronic transport (which is related to the barrier potential (qVb) between two grains).[54] Among these parameters, (i), (iii), and (iv) directly depend on the concentrations of Vo in the semiconducting oxide. At the same time, availability of the gas interaction sites can also be enhanced by increasing the surface-to-volume ratio of the sensing layer. Vo-related defect sites/states are the most favorable ones for the adsorption of target species (biomarkers in the present case).[52,55] This is because the binding interaction between O_2 molecules and biomarker molecules is much stronger in such defect sites compared to the defect-free ones. We have demonstrated that O_2 molecules can be dissociated and chemisorbed to the oxygen vacant site (Vo) of the oxide surface with negligible activation energy.[15] As the reducing biomarker vapor comes in contact with the sensing layer, two simultaneous processes take place: adsorption at the active sites and catalytic oxidation enhanced by the activity

of TiO_2.[56,57] In other words, it is adsorbed to the functionalized oxide surface by the dissociative adsorption process and subsequently dehydrogenated by the adsorbed oxygen species. The catalytic activity causes the $O{-}CH_3$ bond to rupture, and the biomarkers can easily be oxidized, thereby releasing free electrons. The released free electrons fills the depleted TiO_2 conduction band and neutralizes the oxygen vacancies, leading to a reduction in the sensor resistance and causing current to rise sharply.

At any particular instant during the sensing operation, the surface coverage of the active sites available for binding to the biomarkers remains almost constant. As the biomarkers are introduced, the response magnitude of a sensor is governed by the availability of the free oxygen vacant sites (Vo). As the biomarkers attach to the sites and get oxidized, they nullify the oxygen vacancies, leading to an increase in electron concentration, resulting in higher electrical conductivity (σ). In the process, the activation barrier which had contributed to the large initial resistivity reduces. As the active sites are used up, the current plateaus out and eventually tend to decrease. A greater concentration of oxygen vacancies implies a lower activation barrier. Thus, it is evident that the required activation energy can be modulated by controlling the concentration of Vo, which in turn is achieved through controlling the amount of water in the electrolyte.[54] Despite the activation energy of electron transport being minimum for $TNA_{OV0.5\%}$ ($TNA_{OV0.5\%} < TNA_{OV3\%} < TNA_{OV10\%}$), the overall response magnitude of $TN_{OV0.5\%}$ is not very promising owing to its relatively poor surface-to-volume ratio.

In the present case, very low (i.e., $TNA_{OV0.5\%}$) water content in the electrolyte resulted in relatively poor surface-to-volume ratio. The $TNA_{OV0.5\%}$ sample showed almost no wall separations, and the $TNA_{OV10\%}$ offered maximum wall separations between

neighboring nanotubes. Eventually, $TNA_{OV0.5\%}$ suffer from poor surface-to-volume ratio of the oxide surface but possess high concentration of oxygen vacancies resulting in poor biomarker sensing performance in terms of response magnitude. On the contrary, $TNA_{OV10\%}$ offers excellent surface-to-volume ratio but does not exhibit the best sensing performance due to the lower concentrations of Vo. The $TNA_{OV3\%}$ sample, owing to the optimum availability of V_O and promising surface-to-volume ratio, offers the best sensing performance at room temperature. Therefore, the processing of the TiO_2 nanotubes warrants the best combination of V_O and surface-to-volume ratio of the nanotube structures to offer promising biomarker sensing performance.

2.3.2 Effect of Temperature during Anodization

2.3.2.1 Effect on nanotube morphology. In the second part of the study, TiO_2 nanotube array was synthesized with variable tube wall thicknesses (TNA_{10C}, TNA_{25C}, and TNA_{50C}). In order to investigate the sole effect of the thickness on nanotube morphology and subsequently on the sensor response, other anodization parameters during the synthesis process were kept fixed, as mentioned in Section 2.2.1. The FESEM micrographs of TiO_2 nanotubes fabricated by anodization at 30V (containing 3wt% water) at 10˚C, 25˚C, and 50˚C are illustrated in Figure 2.4(a-c). An interesting observation indicates that the pore diameter (or outer diameter) of ~60nm is essentially the same for all the nanotubes fabricated at the different temperatures, but the wall thickness changes significantly. Figures 2.4d represents the monotonic decremental nature of tube wall thicknesses with the variations of anodization temperatures (10 to 50 °C), respectively. With decreasing anodization temperature, the wall thickness increases

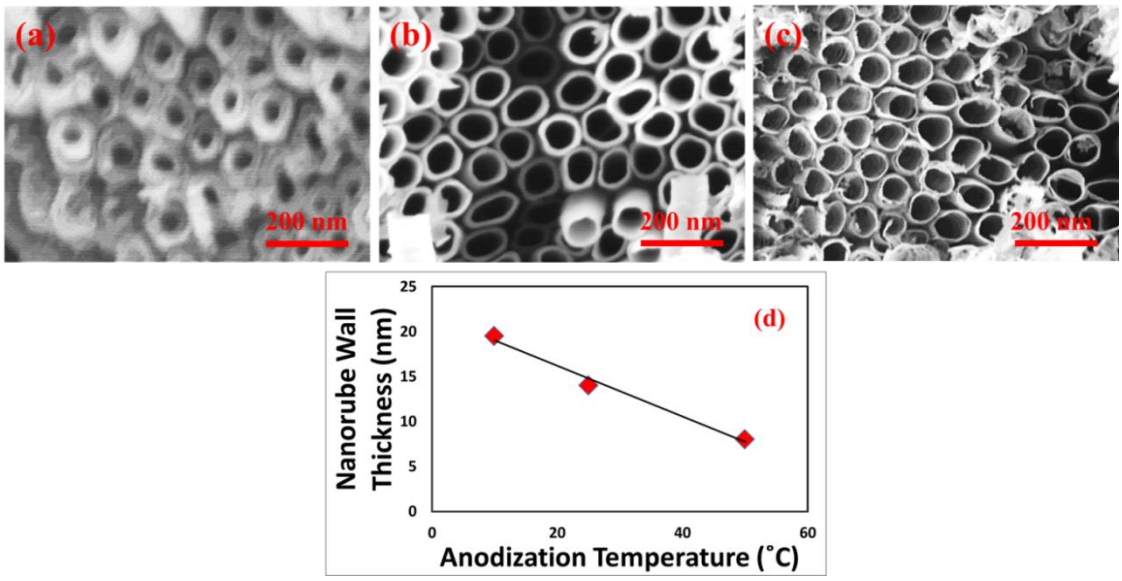

Figure 2.4 SEM micrographs (a-c) illustrating the variation in TiO_2 nanotube wall thickness when the temperature of the anodization solution was varied (a) 10˚C, (b) 25˚C, (c) 50˚C., and (d) plot showing the variation in nanotube wall thickness as a function of anodization temperature.

from ~8nm at 50˚C to ~14nm at 25˚C and ~20nm at 10˚C. Consequently, the voids in both the interpore areas and the tubes become more connected as the temperature is lowered. Therefore, anodizing at very low temperatures can prove to be detrimental towards the sensing performance due to a reduction in surface-to-volume ratio. Grimes[1] had also reported increase in the nanotube length with decrease in anodization temperature. This is particularly not a concern in our case as we had previously stated that variation in tube length does not affect the sensor response.

It is important to note that chemical dissolution and electrochemical etching are critical factors in the growth of the nanotube arrays via anodic oxidation of titanium. Varying the electrolyte bath temperature changes the rate of both etching processes.[1] Further, variation in dissolution rate in the horizontal direction of TiO_2 layer, perpendicular to the tube growth, principally affects TiO_2 nanotube wall thickness. The

dissolution rate depends on the concentration of F− ions in the electrolyte[30], which competes with other ions in the solution bath such as OH^- and H^+, having different ionic radius and charge. As a result, movement of the F- ions is hindered which leads to the dependence of the dissolution rate on two key factors: (i) drift velocity of the F− ions in the electrolyte[30,58] and (ii) rate of diffusion of F− ions through the nanotube wall.[30,45] Hazra *et al*.[30] had explained through the Stokes−Einstein relationship, $D = kT/6\pi\eta\sigma$, (where D is the diffusion coefficient, k is the Boltzmann's constant, T is the ambient temperature, η is the viscosity of the electrolyte, and σ is the diameter of the sphere-like particle), rate of diffusion of F− ions increases with increase in the anodization temperature (T), leading to the higher rate of dissolution. In addition, the viscosity effects become less significant as at higher temperatures, lowering of the viscosity (η) of the electrolyte occurs, enabling enhanced velocity transport of the F− ions in the electrolyte. This is particularly pertinent to our context as the fluorinated ethylene glycol anodization solution we use is fairly viscous at room temperature. Thus, anodizing Ti at a higher temperature causes increased rate of oxide dissolution by F− ions, leading to reduced nanotube wall thickness, and vice-versa, lower anodizing temperatures causes reduced transport velocity of F^- ions, and thicker nanotubes subsequently.

2.3.2.2 Effect on sensor response. Considering the design and fabrication of the TNA vapor-based sensors, it is worthwhile to consider the basis for the remarkable sensitivity demonstrated by the TiO_2 nanotube array sensors, a material architecture that is essentially considered to be all surface and no bulk.[1] The high vapor phase biomarker sensitivity can be attributed to direct chemisorption of biomarker molecules on the

functionalized nanotubes and their subsequent catalytic oxidation being the dominant mechanism leading to the tremendous resistance reduction in the nanotubes.

The biomarker (methyl nicotinate) sensing performance was studied for functionalized TiO_2 nanotubes with variable tube wall thickness (TNA_{10C}, TNA_{25C}, and TNA_{50C}) with optimum stoichiometry (3 wt% water) synthesized at 30V for 1 hour. The response magnitude as a function of nanotube thickness (Figure 2.5) shows the maximum response from sensors fabricated at room temperature (25 °C) with significant variations of response characteristics for different sample. However, the response magnitude reveals an increasing tendency from TNA_{10C} to TNA_{25C}, and then decreases from TNA_{25C} to TNA_{50C} at room temperature exposure to 10mM biomarker concentration.

Though the above mechanism described in the previous section largely demonstrates the efficiency of biomarker-sensing performance for the functionalized TiO_2 nanotube-based sensors, it cannot effectively explain the effect of the wall thickness (t) variations on the biomarker-sensing performance. To illustrate the effect of all the structural parameters (i.e., t, N_D), the role of channels which form in the nanotube wall has been explained.[59,60] As explained by Hazra *et al.*[30], this model considers an individual TiO_2 nanotube as a single resistance (R) with length L and cross-sectional area A. The tube is assumed to have an average free electron density N_D and mobility μ_n. The tube resistance can be represented as:[30]

$$R = \frac{1}{qN_D\mu_n} \times \frac{L}{A} \quad \ldots (2.4)$$

The adsorption of oxygen in air takes place on either side of the nanotube walls, creating an electron depletion region.

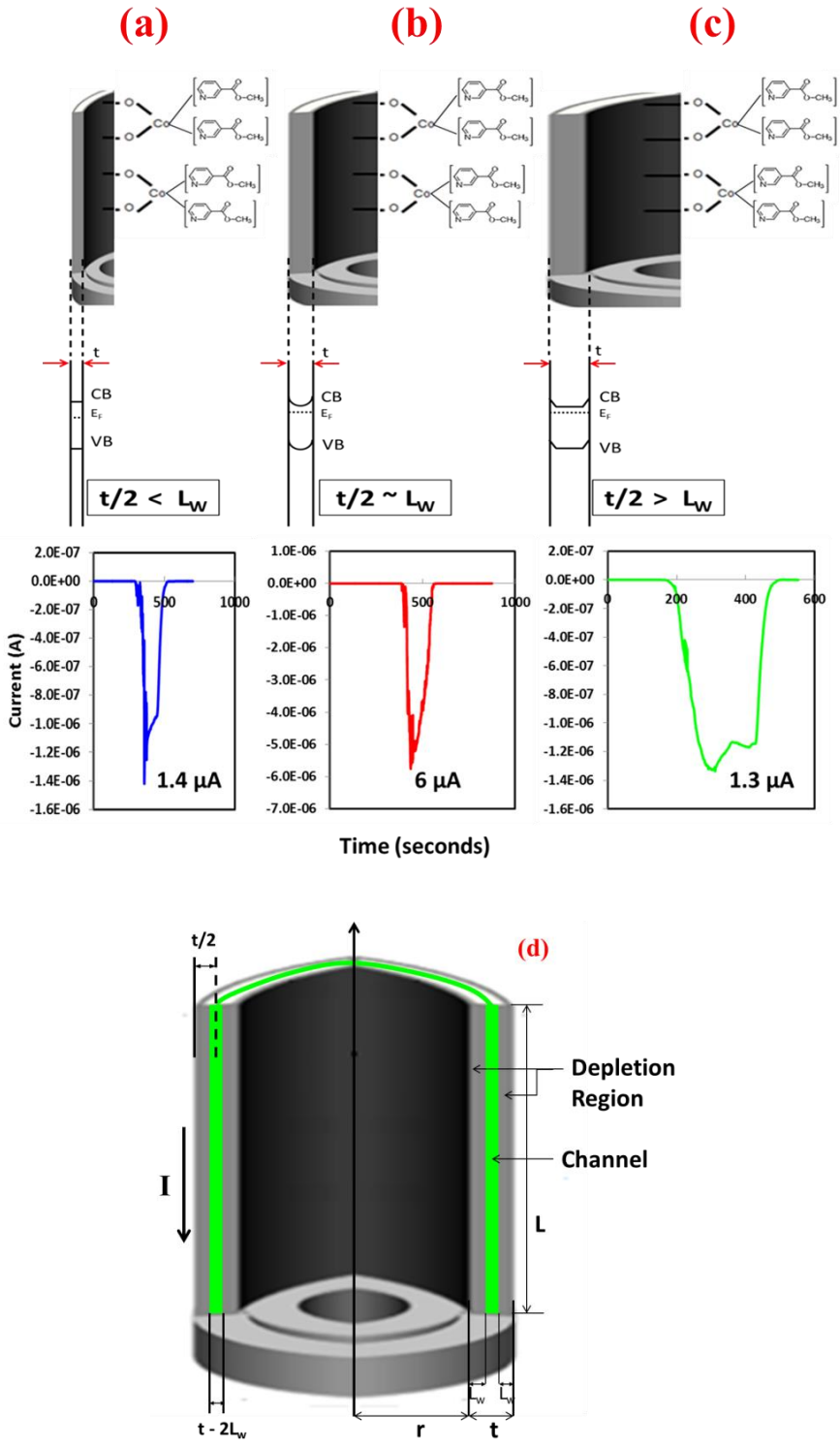

Figure 2.5. Effect of nanotube wall thickness on sensor response to methyl nicotinate vapor (a-c) various nanotube wall thickness compared to Lw. (d) Schematic showing the cross-sectional view of a single TiO_2 nanotube illustrating the depletion region and channel formation in the nanotube walls.

Therefore, in ambient air, the inner and outer surface of the nanotube is depleted, partially due to adsorption of the oxygen species (O^-, O^{2-}, etc.)[15] on the nanotube surface.[15] The conducting channels between the surfaces (inner and outer) have the dimension of ($t - 2L_W$), where L_W is the thickness of depleted region as shown in Figure 2.5d.[61,62] The width of the space charge layer L_W can be given by:

$$L_W = L_D [2eV/kT]^{1/2} \quad \ldots(2.5)$$

where, $L_D = [\varepsilon_0 \varepsilon kT/2q^2N_D]^{1/2}$ is the Debye length, eV is the barrier height, kT is the thermal energy, and N_D the ionized donor density. In metal oxides, the space charge layer extends to a few tens of nanometers depending on the thickness of the film.[63]

It is important to understand that the nanotubular layer is not a flat capacitor. The voltage drop takes place inside the nanotube walls and the space charge region spreads circularly over a few nanometers. With respect to variation in wall thickness and subsequent electron transport properties, band bending is an important phenomenon. In the semiconducting tubular structure, a space charge region with width Lw extends circular in the side walls of the tubes where the band bending extends in half of the tube walls. If the half wall thickness is significantly greater than the width of the space charge layer (i.e., $t/2 > Lw$), the band bending may extend to a few tens of nm throughout the half thickness of the wall in a wide potential range such that there remains a neutral region (or channel) for the charge transport in the middle of the wall.[64] The potential drop difference between the sides of the wall would directly result in separation of charge carriers and prevention of recombination, which is favorable.[65] In this case, there must be a minimal band bending of 50 mV in order to prevent charge recombination.[65] This can be achieved by having an efficient depletion region to accommodate the band bending.

However, if the half wall thickness is shorter than the width of the space charge layer (i.e., t/2 < Lw), flat-band condition exists in the tube wall (Fig. 9b) and band bending can only occur at the bottom of the tubes as the depletion zone goes through the wall and the nanotube remains inactive.[64] This is because thinner wall thickness would result in a lower band bending with the band potential being very close to the flat band potential.[65] Another important point is that the diffusion length of charge carriers in titania is around 10 nm.[65] However, the thin wall thickness would prevent the formation of a large depletion region, and consequently, there would not be enough potential drop across the wall, leading to less separation of the charge carriers. When the wall thickness is less than the diffusion length in titania, which occurs in the case of thin tube walls, there is no electric diffusion layer needed to separate electrons and holes, as the holes simply diffuse through the tube walls to the semiconductor/biomarker vapor interface.[65]

If the nanotube wall half-thickness t/2 is significantly greater than the width of the space charge region L_W, as shown in Fig. 2.5a, oxygen removal by biomarker vapor and subsequent biomarker chemisorption will have little effect on device resistance; hence, high sensitivity cannot be expected. In contrast, when t/2 is comparable to or less than the space charge region, the shift in the electrical resistance on exposure to biomarker vapor can be very high, while a flat-band condition will exist when the wall thickness is less than the width of the space charge region, as described previously. The nanotube array samples showing the highest sensitivity had a wall thickness of ~14 nm, corresponding to the geometry of Fig. 2.5b. Previously, calculations based on equation 2.5 have determined that the depletion width layer is anywhere between 4 – 7 nm.[66] Significant charge separation occurs at a distance of 1-1.5 nm which happens to be the Debye length

for anatase TiO_2 nanotubes.[66] Hence, there is lucid evidence to show that the half thickness of the nanotube synthesized at room temperature is comparable to the width of the space charge region, thereby contributing to enhanced sensor responsivity.

Therefore, considering the conducting channel formation possibility, equation 2.4 can be expressed as

$$R_{(air)} = \frac{1}{qN_D\mu_n} \times \frac{L}{\pi\,(t+2r) \times (t-2L_w)} \quad \ldots (2.6)$$

$$R_{(air)} = \frac{1}{qN_D\mu_n} \times \frac{L}{\pi\,(t+2r) \times (t-2L_D\sqrt{\frac{2eV}{kT}})} \quad \ldots (2.7)$$

$$R_{(air)} = \frac{1}{qN_D\mu_n} \times \frac{L}{\pi\,(t+2r) \times (t-2\sqrt{\frac{\varepsilon_0 \varepsilon \mathrm{kT}}{2q^2(N_D-n_a)}}\sqrt{\frac{2eV}{kT}})} \quad \ldots (2.8)$$

where n_a is the captured electron due to surface adsorption of oxygen species. In ambient reducing vapor (like biomarkers), a fraction of the captured electrons is released (n_g) to the nanotube surface, thereby increasing the channel width ($t - 2L_W$) and lowering the sensor resistance, as shown in equation 2.9

$$R_{(biomarker)} = \frac{1}{qN_D\mu_n} \times \frac{L}{\pi\,(t+2r) \times (t-2\sqrt{\frac{\varepsilon_0 \varepsilon \mathrm{kT}}{2q^2(N_D-n_a+n_g)}}\sqrt{\frac{2eV}{kT}})} \quad \ldots (2.9)$$

Equation 2.8 represents the baseline resistance of the sensor. With decrease in tube wall thickness (t), the increase in baseline resistance of the sensor (R(air)) is not significant as terms associated with the thickness play a major role and mostly stay constant. The rapid decrement of the sensor resistance (R(air)) with increase in V_O content (or increase in

carrier density, N_D) can be correlated with equation 2.9. The response magnitude of the 1D cobalt functionalized titania nanotube-based sensor can therefore be expressed as:

$$Sensor\ Response = \frac{R_{(air)} - R_{biomarker}}{R_{(air)}} = 1 - \frac{R_{biomarker}}{R_{air}} \quad \ldots(2.10)$$

$$Sensor\ Response = 1 - \frac{\left(t - 2\sqrt{\frac{\varepsilon_0 \varepsilon \mathrm{kT}}{2q^2(N_D - n_a)}}\sqrt{\frac{2eV}{kT}}\right)}{\left(t - 2\sqrt{\frac{\varepsilon_0 \varepsilon \mathrm{kT}}{2q^2(N_D - n_a + n_g)}}\sqrt{\frac{2eV}{kT}}\right)} \quad \ldots(2.11)$$

Moreover, the expression of response magnitude in equation 2.11 confirms our earlier observation that there is limited effect of the nanotube length and diameter variations on the sensing performance of the sensor. As evidenced from equation 2.11, the two main factors contributing to the variation in sensor response are nanotube wall thickness (t) and the charge carried density (N_D), which is influenced by the water content of the anodization bath. The response magnitude appears to increase with decrease in the tube wall thickness which conforms to experimental results presented in Figure 2.5.

2.4. Summary

The present work has attempted to optimize the titania nanotube stoichiometry and morphology in order to maximize the sensor response to the volatile organic biomarkers. Results pertaining to variations in nanotube diameter and length have not been presented here due to the lesser impact of these parameters on sensing response resulting in negligible relevance. The interwall connecting points also appear to play a significant role in enabling the ultra-high biomarker sensitivity. The chemisorbed oxygen and its removal by biomarker molecules, as well as chemisorption and oxidation of the

biomarkers at the active sites, regulates the passage of current from nanotube to nanotube. In summary, our studies on the interaction of titania nanotube arrays with biomarkers reveal an unprecedented vapor dependent shift in electrical resistance. The synergetic effect of optimized stoichiometry and geometry, highly active nano-scale surface states and functionalized sites that activate oxygen and biomarker for chemisorption and oxidation, tremendous surface area, and inter-tubular connecting points is believed responsible for the remarkable sensing behavior.

2.5 References

1. C. A. Grimes, *J. Mater. Chem*., **17**, 1451 (2007).
2. O. K. Varghese, D. Gong, M. Paulose, K. G. Ong, and C. A. Grimes, *Sensors Actuat. B-Chem.***, 93** (1), 338 (2003).
3. K. Chen, K. Xie, X. Feng, S. Wang, R. Hu, H. Gu, and Y. Li, *Int. J. Hydrogen Energ.*, **37** (18), 13602 (2012).
4. E. Sennik, Z. Colak, N. Kilinc, and Z. Z. Ozturkrk, *Int. J. Hydrogen Energ.*, **35** (9), 4420 (2010).
5. Z. Wen and L. Tian-mo, *Physica B*, **405** (2), 564 (2010).
6. H. F. Lu, F. Li, G. Liu, Z.-G. Chen, D.-W. Wang, H. T. Fang, G. Q. Lu, Z. H. Jiang, and H. M. Cheng, *Nanotechnology*, **19** (40), 405504 (2008).
7. P. M. Perillo and D. F. Rodriguez, *Sensors Actuat. B-Chem.*, **171-172**, 639 (2012).
8. Y. Kwon, H. Kim, S. Lee, I. J. Chin, T. Y. Seong, W. I. Lee, and C. Lee, *Sensors Actuat. B-Chem.*, **173**, 441 (2012).
9. Z. Wen, L. Tian-Mo, and L. De-Jun, *Physica B*, **405** (19), 4235 (2010).
10 Z. Wen and L. Tian-mo, *Physica B* **405** (5), 1345 (2010).
11. Y. R. Smith, R. S. Ray, K. Carlson, B. Sarma, and M. Misra, *Materials*, **6**, 2892 (2013).
12. K. Lee, A. Mazare, and P. Schmuki, *Chem. Rev.*, **114**, 9385 (2014).

13. S. Banerjee, S. K. Mohapatra, M. Misra, and I. B. Mishra, *Nanotechnology*, **20**, 075502 (2009).

14. H. Jayamohan, Y. R. Smith, B. K. Gale, M. Misra, and S. K. Mohanty, *Proc. Sensors 2013 (Baltimore, MD, 3-6 November 2013) IEEE*, 1 (2013).

15. D. Bhattacharyya, Y. R. Smith, M. Misra, and S. K. Mohanty, *Mater. Res. Express*, **2**, 025002 (2015).

16. N. Kılınç, E. Şennik, and Z. Z. Öztürk, *Thin Solid Films*, **520**, 953 (2011).

17. K. S. Raja, M. Misra, and K. Paramguru, *Electrochimica Acta*, **51**, 154 (2005).

18. S. K. Mohapatra, M. Misra, V. K. Mahajan, and K.S. Raja, *J. Catalysis*, **246**, 362 (2007).

19. S. K. Mohapatra, M. Misra, V. K. Mahajan, and K. S. Raja, *J. Catalysis*, **246**, 362 (2007).

20. Y. R. Smith, B. Sarma, S. K. Mohanty, and M. Misra, *Electrochem. Commun.*, **19**, 131 (2012).

21. Y. R. Smith, D. Bhattacharyya, S. K. Mohanty, and Mano Misra, *J. Electrochem. Soc.*, **163** (3), B1 (2016).

22. S. E. John, S. K. Mohapatra, and Mano Misra, *Langmuir*, **25**(14), 8240 (2009).

23. Y. R. Smith, B. Sarma, S. K. Mohanty, and M. Misra, *Int. J. Hydrogen Energ.*, **38**, 2062 (2013).

24. S. K. Mohapatra, M. Misra, V. K. Mahajan, and K. S. Raja, *Materials Letters*, **62**, 1772 (2008).

25. Y. R. Smith, B. Sarma, S. K. Mohanty, and M. Misra. *ACS Appl. Mater. Interfaces*, **4**, 5883 (2012).

26. D. Bhattacharyya, P. K. Sarswat, M. Islam, G. Kumar, M. Misra, and M. L. Free, *RSC Adv.*, **5**, 70361 (2015).

27. V. C. Anitha, D. Menon, S. V. Nair, and R. Prasanth, *Electrochimica Acta*, **55**, 3703 (2010).

28. S. Yoriya, W. Kittimeteeworakul, and N. Punprasert, *J. Chem. Chem. Eng.*, **6**, 686 (2012).

29. K. N Chappanda, Y. R Smith, S. K. Mohanty, L. W. Rieth, P. Tathireddy, and M. Misra, *Nanoscale Res. Lett.*, **7**, 388 (2012).

30. A. Hazra, B. Bhowmik, K. Dutta, P. P. Chattopadhyay, and P. Bhattacharyya, *ACS Appl. Mater. Interfaces*, **7**, 9336 (2015).

31. M. Yang, W. Liu, J. L. Sun, and J. L. Zhu, *Appl. Phys. Lett*., **100**, 043106 (2012).

32. J. M. Macak, H. Tsuchiya, A. Ghicov, K. Yasuda, R. Hahn, S. Bauer, and P. Schmuki, *Curr. Opin. Solid. St. M.*, **11**, 3 (2007).

33. Y. R. Smith, *PhD Dissertation* (2014).

34. K. S. Raja, M. Misra, and K. Paramguru, *Electrochim. Acta*, **51**, 154 (2005).

35. V. P. Parkhutik and V. I. Shershulsky, *J Phys D: Appl Phys*, **25**, 1258 (1992).

36. D. Regonini, C. R. Bowen, A. Jaroenworaluck, and R. Stevens, *Mater. Sci. Eng. R*, **74**, 377 (2013).

37. J. M. Macak, H. Hildebrand, U. Marten-Jahns, and P. Schmuki, *J. Electroanal. Chem.*, **621**, 254 (2008).

38. P. Roy, S. Berger, and P. Schmuki, *Angew. Chem*., **50**, 2904 (2011).

39. J. Y. Kim, J. H. Noh, K. Zhu, A. F. Halverson, N. R. Neale, S. Park, K. S. Hong, and A. J. Frank, *ACS Nano*, **5**, 2647 (2011).

40. M. Yang, W. Liu, J. L. Sun, and J. L. Zhu, *Appl. Phys. Lett.*, **100**, 043106 (2012).

41. D. Regonini, A. Jaroenworaluck, R. Stevens, and C. R. Bowen, *Surf. Interface Anal.*, **42**, 139 (2010).

42. L. V. Taveira, J. M. Macak, H. Tsuchiya, L. F. P. Dick, and P. Schmuki, *J. Electrochem. Soc.*, **152**, B405 (2005).

43. J. Schmidt and W. Vogelsberger, *J. Solution Chem.*, **38**, 1267 (2009).

44. S. Berger, J. Kunze, P. Schmuki, A. T. Valota, D. J. Leclere, P. Skeldon, and G. E. Thompson, *J. Electrochem. Soc*., **157**, C18 (2010).

45. H. Yin, H. Liu, and W. Z. Shen, *Nanotechnology*, **21**, 035601 (2010).

46. X. Lu, G. Wang, T. Zhai, M. Yu, J. Gan, Y. Tong, and Y. Li, *Nano Lett*., **12**, 1690 (2012).

47. A. Balcerzak, M. Aleksiejuk, G. Zhavnerko, and V. Agabekov, *Thin Solid Films*, **518**, 3402 (2010).

48. M. Kozlov and T. J. McCarthy, *Langmuir*, **20**, 9170 (2004).

49. G. Nabiyouni, A. Barati, and M. Saadat, *Iran. J. Chem. Eng*., **8**, 20 (2011).

50. R. J. Wu, D. J. Lin, M. R. Yu, M. H. Chen, and H. F. Lai, *Sens. Actuators, B*, **178**, 185 (2013).

51. W. An, X. Wu, and X. C. Zeng, *J. Phys. Chem. C*, **112**, 5747 (2008).

52. J. M. Sturm, D. Göbke, H. Kuhlenbeck, J. Döbler, U. Reinhardt, M. V. Ganduglia-Pirovano, J. Sauerzand, and H. J. Freund, Phys. *Chem. Chem. Phys*., **11**, 3290 (2009).

53. O. Lopatiuk, L. Chernyak, A. Osinsky, and J. Q. Xie, *Appl. Phys. Lett.*, **87**, 214110 (2005).

54. A. Rothschild and Y. Komem, *J. Appl. Phys.*, **95**, 63746380 (2004).

55. M. W. Ahn, K. S. Park, J. H. Heo, J. G. Park, D. W. Kim, K. J. Choi, J. H. Lee, and S. H. Hong, *Appl. Phys. Lett.*, **93**, 263103 (2008).

56. X. Yang, X. Wang, C. Liang, W. Su, C. Wang, Z. Feng, C. Li, and J. Qiu, *Catal. Commun*., **9**, 2278 (2008).

57. A. Gazsi, G. Schubert, T. Bánsági, and F. Solymosi, *J. Photochem. Photobiol*. *A*, **271**, 45 (2013).

58. J. Chen, J. Lin, and X. Chen, *J. Nanomater*., 753253 (2010).

59. N. Barsan and U. Weimar, *J. Phys.: Condens. Matter*, **15**, R813 (2003).

60. S. Pokhrel, C. A. Simion, V. Quemener, N. Barsan, and U. Weimar, *Sens. Actuators B*, **133**, 78−83 (2008).

61. N. Barsan, C. Simion, T. Heine, and S. Pokhrel, *J. Electroceram.*, **25**, 11 (2010).

62. M. Hübnera, C. E. Simion, A. Tomescu-Stanoiu, S. Pokhrel, and N. Bârsan, *Sens. Actuators B*, **153**, 347 (2011).

63. H. Ogawa, M. Nishikawa, and A. Abe, *J. Appl. Phys*., **53**, 4448 (1982).

64. P. Pu, H. Cachet, E. Ngaboyamahina, and E. Sutter, *J. Solid State Electrochem*., **17**, 817-828 (2013).

65. A. M. Mohamed, A. S. Aljaber, S. Y. AlQaradawib, and N. K. Allam, *Chem. Commun*.**, 51**, 12617 (2015).

66. R. G. Freitas, M. A. Santanna, and E. C. Pereira, *Electrochim. Acta*, **136**, 404 (2014).

CHAPTER 3

FUNCTIONALIZED ANODIC TITANIA NANOTUBE ARRAY SENSOR FOR ELECTROCHEMICAL DETECTION OF FOUR PREDOMINATE TB VOLATILE BIOMARKERS - PART I: SENSING MECHANISM

3.1 Introduction

Analysis of volatile organic compounds (VOCs) from exhaled breath presents a potential noninvasive, point-of-care (POC) medical diagnostic technique. In recent years, sensor detection of VOC biomarkers has gained significant interest for the early diagnosis of several pulmonary and other diseases. Review articles by van de Kant *et al.* [1] and Zhou *et al.* [2] highlight the clinical use of VOCs identification for improved and accurate diagnoses of pulmonary diseases such as asthma, COPD (chronic obstructive pulmonary disease), lung cancer, and cystic fibrosis, for example. Further, researchers have successfully identified and detected VOC biomarkers from exhaled breath for the diagnosis of chronic kidney diseases,[3] gastrointestinal and liver diseases,[4] breast cancer,[5] and cardiac biomarkers.[6] Among other pulmonary diseases of concern, tuberculosis is a major one, which can potentially be diagnosed via breath analysis. Syhre *et al.* [7] have successfully detected the four prominent biomarkers in the breath of smear positive tuberculosis patients using solid phase microextraction (SPME) fibers.

The majority of studies, which have focused on correlating VOC detection with diseases, have utilized GC-MS or bioassay as the method of biomarker detection. From a POC point of view, the current methods used are not mobile and require time-consuming analysis and trained technicians. Therefore, in an effort to reduce the complexity and detection time, electrochemical detection of volatile organic biomarkers is one approach which has high potential for integration in a hand-held device with rapid detection.

Previously, electrochemical gas sensors have been classified as amperometric, potentiometric, and conductometric based on their mode of operation,[8] although amperometric is more closely related to our methodology. Applying band theory, the n-type and p-type semiconductor sensor response to oxidizing and reducing gases have been explained based on changes in resistance.[9] Owing to high surface-area-to-volume ratio coupled with enhanced chemical and thermal stability which is advantageous in sensing applications, one-dimensional (1-D) nanostructured metal oxides have been widely investigated for potential applications in sensors.[10-12] Nanowires have been examined previously for their role in chemical and biological sensors.[11] 1-D nanotubes, especially titania nanotube arrays (TNA), exhibit good morphological tunability over large length scales[13,14] and have found applications ranging from catalysis to biomedical.[13,15] In the sensing domain, TNA has found use as hydrogen sensor[16-19] while some modifications in terms of functionalization have rendered it useful for detection of formaldehyde,[20,24] oxygen,[21] ethanol,[22-24] ammonia,[22] methanol,[24] and acetone.[24] Previous investigations by our group have demonstrated the successful detection of triacetone triperoxide (TATP)[25] and trichloroethylene[26] vapors using functionalized TNA, in addition to understanding the principle interaction of TATP vapor with metal sensitized

TNA utilizing DFT simulation.[27] Hence, there is ample evidence to support that TNA is a versatile substrate, which has been used extensively for various sensing applications.

In this study, cobalt functionalized TNA were used for the electrochemical detection of methyl nicotinate vapor. Functionalization of the TNA with cobalt was achieved through the incipient wetting impregnation method. The importance of cobalt functionalization has been illustrated from sensor responses and correlated with cobalt loading and oxidation state. Titanium dioxide films synthesized through high-temperature oxidation and functionalized with cobalt were also compared with cobalt functionalized TNA. The ordered TNA was demonstrated to be an effective substrate for cobalt deposition and subsequent biomarker detection over thin titanium dioxide films. Two mechanisms have been proposed to describe the binding of the nicotinate biomarker to cobalt functionalized TNA. The sensing response mechanism has been described in terms of chemical sensitization and band theory. The demonstrated approach for the detection of methyl nicotinate may be extended to other biomarkers by tailoring the TNA surface with compounds that have favorable binding affinities to the analyte.

3.2 Experimental

3.2.1 Synthesis of Titania Nanotubes

Titania nanotubes were synthesized by electrochemical anodization of titanium foils (0.1016 mm thick, ESPI metals, G1 grade).[13] Titanium foils were cut into 1.5 cm x 1.5 cm coupons and polished with emory paper. The coupons were degreased by ultrasonication in an acetone-isopropanol (50% v/v each) mixture for 30 minutes. After rinsing them thoroughly with DI water, the titanium coupons were subjected to

electrochemical anodization at 30 V (Agilent E3647A DC power source) for 1 hour in a teflon beaker under constant stirring at 60 rpm using a Pt foil as a counter electrode. The gap between the cathode and the anode was maintained at 3 cm. Prior to anodization, one face of the coupon was covered with a Kapton tape to enable growth of nanotubes on one surface only. The anodization solution was a fluorinated ethylene glycol solution (0.5 wt.% NH_4F + 2 wt.% H_2O). After anodization, the coupons were rinsed and sonicated in DI water for 20 seconds to remove debris and the glycol solution from the surface. These anodized coupons were then transferred to an oven and dried overnight at 110 ˚C under vacuum. Further, the anodized coupons were annealed in a tube furnace at 500 ˚C (ramp rate of ~3 ˚C/min) for 2 hours in oxygen atmosphere.

3.2.2 Synthesis of Titania Films

Titania films were synthesized by high-temperature oxidation of titanium foil. The titanium foil was cut into 1.5 cm x 1.5 cm coupons and degreased by sonicating in an acetone-isopropanol (50% v/v each) mixture for 30 minutes followed by DI water rinsing. The clean coupons were subjected to oxidation in a tube furnace at 550˚C (ramp rate of ~3 ˚C/min) for 3 hours in oxygen atmosphere to yield high-temperature oxide (HTO).

3.2.3 Cobalt Functionalization

Preliminary screening of candidate metals, which have a high affinity to bind with methyl nicotinate, was carried out using density functional theory, similar to our previous work.[27] A high binding affinity of methyl nicotinate with Co was observed over several

3+ and 2+ metal ions. Cobalt functionalization of TNA and HTO was carried out by immersing the annealed coupons in 0.1 M $CoCl_2$ (Alfa Aesar) solution in ethanol and ultrasonicating for 30 minutes. The cobalt functionalized Co-TNA and Co-HTO were then dried overnight under vacuum at 110˚C.

3.2.4 Characterization

3.2.4.1 SEM. The morphology of Co-TNA and Co-HTO was characterized using a field emission scanning electron microscope (Hitachi S-4800 SEM) with a tungsten filament at 3 kV accelerating voltage and 15 µA emission current. Energy dispersive x-ray spectroscopy (EDS) mapping was achieved using an Oxford EDX detector attached to the SEM. The EDX studies were performed at 20 kV accelerating voltage and high probe current over a 25 µm x 25 µm sample area.

3.2.4.2 XPS. Surface composition and the oxidation states of Co and Ti were analyzed using x-ray photoelectron spectroscopy (Kratos Axis Ultra DLD model). The vacuum in the analyzing chamber was maintained at 3×10^{-10} Torr. The X-ray excitation source was monochromatic Al K_α radiation ($h\nu$ = 1486.6 eV) at 180 W. The survey and high-resolution spectra were acquired at pass energies of 160 and 40 eV, respectively. Spectra were analyzed and all peaks were fitted with CasaXPS software. Charging effects were corrected using the C 1s line at 284.6 eV as an internal reference. Shirley-type background was subtracted from the spectra. Argon ion milling was carried out under gentle conditions to remove the top few nanometers of the sample surface where Ar^+ ions were rastered at 0.4 kV for a total exposure of 3 minutes.

3.2.4.3 Amperometric detection of methyl nicotinate. The detection of methyl

nicotinate vapor was carried out in a custom sensing chamber built out of a 50 ml centrifuge tube with alligator clip connections. One side of each alligator clip was covered with an insulating tape such that one connection was made to the titania surface and the other to the unanodized titanium metal side. A two-electrode potentiostat system was used (Gamry Reference 600). Nitrogen at 200 sccm (standard cubic centimeters per minute) was used as the carrier gas and bubbled through a 10 mM methyl nicotinate solution in ethanol. The resultant vapor was delivered to the sensing chamber and estimated to be ~2 mM analyzed by GC-MS. A schematic diagram of the overall experimental set-up is shown in Figure 3.1. A low bias of -0.5 V (based on cyclic voltammetry studies, not shown) was applied and a potentiostatic (I-t) run was carried out to test the sensor response. The senor was allowed to stabilize under nitrogen flow for several 100s of seconds before any analyte was introduced to the system. After a maximum current is achieved when exposed to the analyte, the analyte is removed and the sensor is exposed to back to nitrogen flow where a decrease in current is observed.

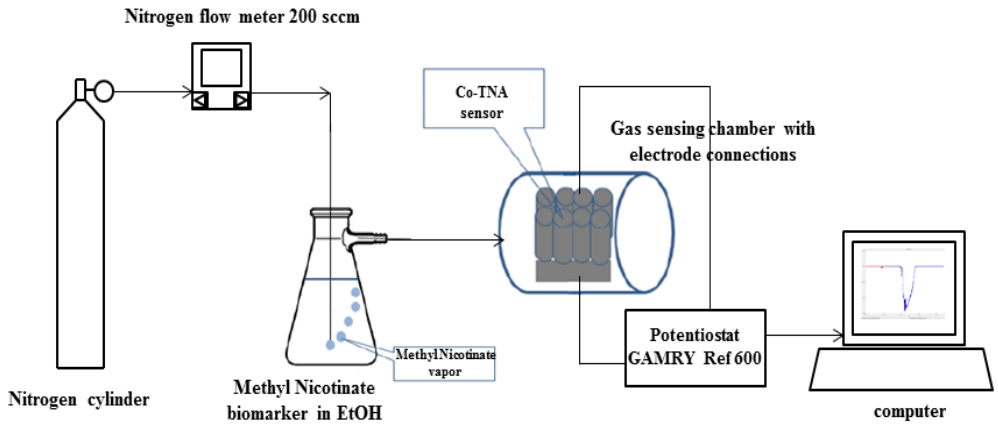

Figure 3.1. A schematic diagram of the overall experimental set-up used for the detection of methyl nicotinate biomarker vapor with cobalt functionalized titania nanotube arrays. Control experiments were run using ethanol only and all the tests were carried out at room temperature.

3.3 Results and Discussions

3.3.1 Surface Morphology and Composition

Scanning electron micrographs as shown in Figure 3.2a-b illustrate the well-ordered nanotubular morphology of TNA as compared to HTO (Figure 3.2c). The highly self-ordered, vertically oriented nanotubes provide for vectorial transport of charges, thereby causing fewer recombination possibilities. The top view reveals ordered arrays of individual tubes having diameters of approximately 53 - 60 nm and an estimated wall thickness of 11 - 14 nm while the length of the nanotubes was estimated to be 1.4 μm (from SEM). The thickness of the TiO_2 film produced by thermal oxidation is estimated to be around 80 – 100 nm. The annealed TNAs are predominantly crystalline anatase phase titania, as discussed in previous reports.[28,29] Also, oxygen annealed TNA exhibits increased resistivity, which can help increase sensitivity in detection of gases. Oxygen scavenges electron from the TiO_2 conduction band, widening its depletion region and contributing to higher resistivity. Scanning electron micrographs, as depicted in Figure 3.2d, reveal precipitates on top of the nanotubes after cobalt functionalization. The presence of cobalt was further confirmed by EDS analysis, as illustrated in Figure 3.3a-d. Analysis through EDS reveals almost no cobalt detected on Co-HTO. Illustrations using scanning electron micrographs and EDS layered images and mapping, as shown in Figure 3.3, further confirm the distribution of cobalt on the surface and walls of the nanotubes in Co-TNA. In comparison, EDS mapping revealed the presence of Co in negligible amount on Co-HTO and was below the detection limit of the EDS system. The results obtained from SEM and EDS characterization confirm that titania nanotubes presents a large surface area for favorable cobalt adsorption in contrast to TiO_2 films.

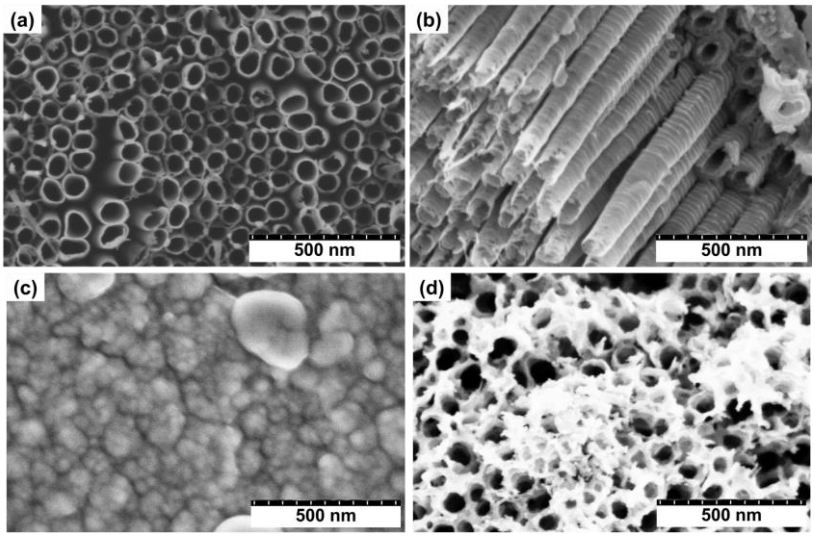

Figure 3.2. : Scanning electron micrographs of plain titania nanostructures showing the top view of the annealed titania nanotubular array (TNA) (a), and side wall view of annealed TNA (b). Scanning electron micrograph of high-temperature titania oxide (HTO) is illustrated in (c) while cobalt functionalized Co-TNA shown in (d) reveals the formation of cobalt hydroxide precipitates on the mouth of the titania nanotubes.

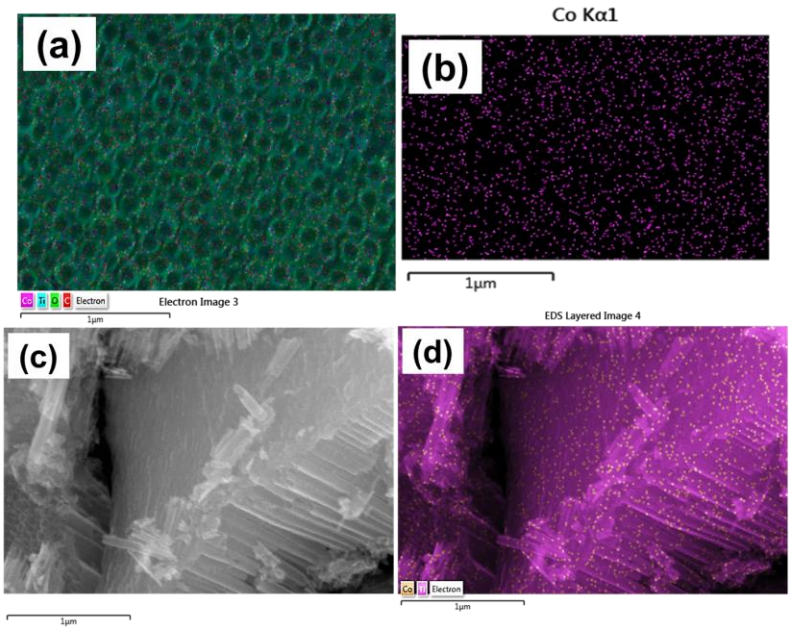

Figure 3.3. Scanning electron micrographs and EDS layered images showing the presence of Co on the mouth and the walls of the nanotubes in Co-TNA. (a) EDS layered image, showing cobalt on the mouth of titania nanotubes. (b) Elemental mapping illustrating uniform cobalt distribution on the mouth of te nanotubes. (c) Electron micrograph of the sidewalls of the nanotubes, (d) corresponding EDS layered image showing cobalt distribution on the nanotubes.

The x-ray photoelectron spectroscopy (XPS) core level spectra of Ti and Co from the Co-TNA are depicted in Figure 3.4 and Figure 3.5, respectively. The Ti 2p level x-ray photoelectron spectra of Co-TNA depict the distinct $2p_{1/2}$ and $2p_{3/2}$ peaks at 464.2 eV and 458.5 eV respectively, with a separation of 5.7 eV between the $2p_{1/2}$ and $2p_{3/2}$ peaks arising from the spin-orbit interaction. These observations are consistent with the peak position and separation for predominantly Ti^{4+} oxidation state. From the Co 2p level x-ray photoelectron spectra, the $2p_{1/2}$ peak is distinctly visible at 797 eV while the $2p_{3/2}$ peak is presented as a multiplet of peaks.

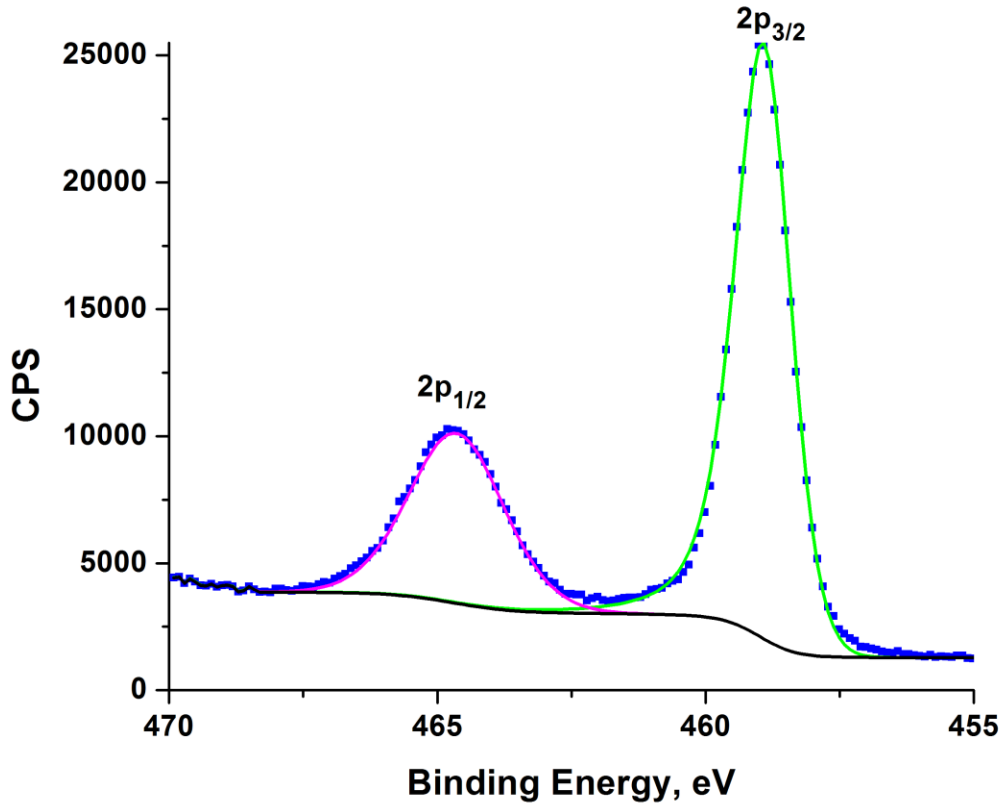

Figure 3.4. Ti 2p level x-ray photoelectron spectra of Co-TNT showing the distinct $2p_{1/2}$ and $2p_{3/2}$ peaks at 464.2 eV and 458.5 eV, respectively, thereby confirming the presence of TiO_2 and the Ti^{4+} oxidation state of titanium.

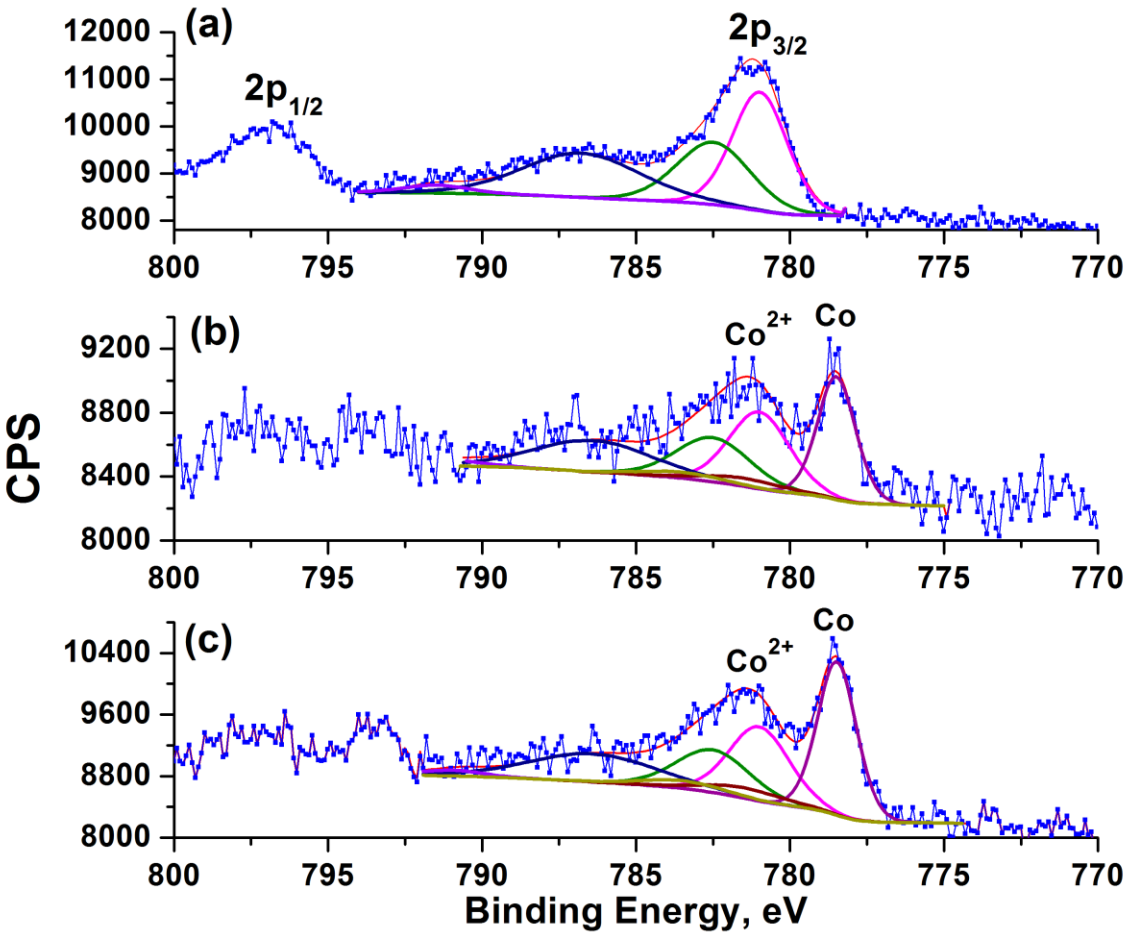

Figure 3.5 Co 2p level x-ray photoelectron spectra of Co-TNT. (a) Unsputtered surface before sensor exposure, (b) argon sputtered surface before sensors exposure, (c) argon sputtered surface after sensor exposure to methyl nicotinate vapor.

The complex nature of the $2p_{3/2}$ peak is due to the spin coupling of the 3d and 2p electrons of cobalt. Peak deconvolution for cobalt compounds were carried out and compared to the reported values by Biesinger *et al.* [30] The native Co-TNA surface reveals that $Co(OH)_2$ (781.5 eV) is the predominant phase present on the nanotubular sensor surface, thereby confirming the Co^{2+} oxidation state of cobalt. Sputtering the surface with Argon ions for 3 minutes, which removed approximately 30 – 50 nm of the top surface layer, was carried out. An XPS spectra of the ion milled sample shows a prominent

metallic cobalt peak at 778.8 eV in addition to the cobalt hydroxide peaks (67% $Co(OH)_2$, 33% Co metal). Quantitative analysis based on the x-ray photoelectron spectra reveals approximately 8-12 wt.% or 3-5 at.% cobalt on the sensor surface. Analysis of the sensor surface after exposure to methyl nicotinate vapor and ion milling, shows a similar spectra as before exposure with ion milling; however, an increase in cobalt metal content is noted (61% $Co(OH)_2$, 39% Co metal). Ion milling-induced reduction of Co^{2+} to metallic Co cannot be entirely ruled out; however, its contribution is rather weak due to the gentle sputtering conditions. The reduction is minimized by the use of low ion beam energy for a short duration of time. The increased cobalt metal amount after exposure of the sensor to methyl nicotnate can be explained by the sensing mechanism (*vide infra*).

3.3.2 Sensor Response to Methyl Nicotinate Vapor

Preliminary studies using cyclic voltammetry methods have indicated cobalt (II) as being a frontrunner for binding methyl nicotinate. The optimum bias voltage was determined to be around -0.5 V for methyl nicotinate using the above-described method. Experimentally, this voltage has consistently delivered the maximum signal during detection. Hence, the amperometric detection of methyl nicotinate using Co-TNA and Co-HTO was carried out at -0.5 V and the result is illustrated in Figure 3.6. The results clearly show that Co-TNA exhibits a change in current, much higher than Co-HTO during detection of methyl nicotinate vapor. The shaded portions of Figure 3.6 show when the sensors surface was exposed to methyl nicotinate vapor. With Co-HTO (Figure 3.6b), the maximum current was approximately -325 nA. In contrast, Co-TNA yielded ~6 μA of current during methyl nicotinate vapor detection.

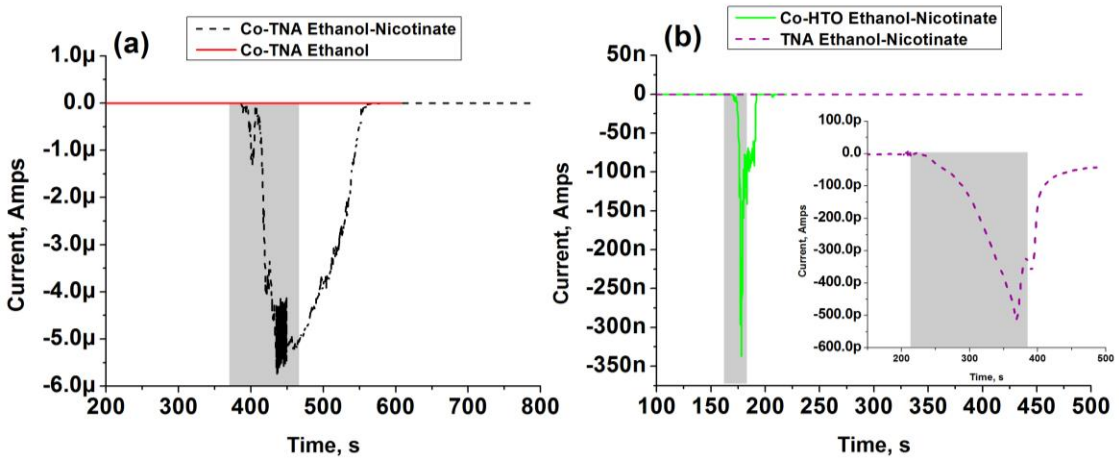

Figure 3.6. Amperometric sensor response to methyl nicotinate vapor (in ethanol) and control tests. (a) Electrochemical detection of methyl nicotinate vapor by Co-TNA as compared to ethanol vapor (control test) showing that the signal is due to the binding of the nicotinate to the metal functionalized titania nanotubes. (b) Electrochemical response to methyl nicotinate vapor by high-temperature titania oxide (Co-HTO) illustrating that the signal is lower than Co-TNA. (inset) Electrochemical response to methyl nicotinate vapor by nonfunctionalized titania nanotube array (TNA) is much lower than Co-TNA, thereby confirming the importance of cobalt functionalization for nicotinate detection. The shaded regions of the plots show when the sensors were exposed to methyl nicotinate vapor.

The sensitivity of the sensor and high affinity of the methyl nicotinate vapor toward Co-TNA is evident from the instantaneous change in current with the introduction of the nicotinate vapor. Control tests for TNA-Co sensor response to ethanol vapor revealed little change in current comparatively, thereby indicating that the current change is predominantly due to the binding of the methyl nicotinate vapor to the cobalt functionalized titania nanotubes. In addition, annealed TNA without cobalt functionalization (Figure 3.6b inset) does not exhibit any significant sensor response (~525 pA), thereby emphasizing the importance of cobalt in methyl nicotinate detection. Initial tests found the detection limit to be ~0.002 mM methyl nicotinate vapor (0.01 mM methyl nicotinate solution). A detailed sensitivity and selectivity (other biomarkers and background VOCs) study is currently underway.

3.3.3 Sensor Response Mechanism

The idea of exchanging metal ions like cobalt to the titania nanotubular surface is due to the presence of a large number of hydroxyl ($Ti(OH)_x$) groups at the surface which has been confirmed by XPS and FTIR analysis.[25,31] Chen *et al.* [31] had proposed that the cell walls of anodic titania nanotubes is composed of a mixture of TiO_2 and titanium hydroxide based on the following reactions:

$$Ti + 2O^{2-} \rightarrow TiO_2 + 4e^- \quad \ldots(3.1)$$

$$Ti + xOH^- \rightarrow Ti(OH)_x + xe^- \quad \ldots(3.2)$$

It has been demonstrated that almost 40% of the surface is covered by hydroxyl groups,[25] which are Brönsted acids and are known to be exchangeable sites. Even though both annealed and as-anodized TiO_2 nanotubes can be used to exchange the metal ions, the latter is preferred for this purpose due to the presence of high-density hydroxyl groups on the TiO_2 surface. The exchange process of the surface hydroxyl proton with candidate metal (Co) ions can be written as:

$$2Ti–OH + Co^{2+} \rightarrow (Ti–O)_2Co + 2H^+ \quad \ldots(3.3)$$

and a representation of the above reaction is illustrated in Figure 3.7.

Cosandey *et al.* [32] had mentioned that gas sensing is based on the changes in the surface or near-surface oxide conductivity. They also stated that such conductivity changes are caused by the formation of a space charge region induced by either gas adsorption or by the formation of oxygen vacancies on the surface. It has been reported that the adsorption of organic molecules on metal cations leads to the oxidation of the organic species.

Figure 3.7 illustrates the binding of methyl nicotinate to Co-TNA.

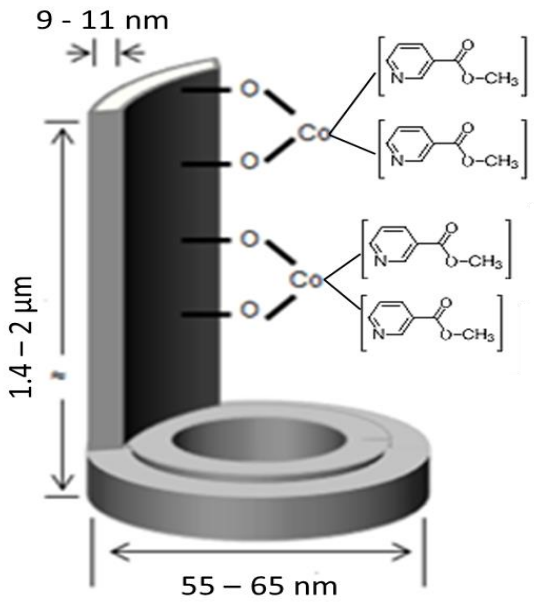

Figure 3.7: A pictorial representation showing the dimensions of the titania nanotubes and the attachment of cobalt to the Brönsted acid sites on the titania nanotube walls. Further, the methyl nicotinate biomarker is attached to the cobalt sites.

For example, Pinnavaia *et al.* [33] observed that Fe(III), Cu(II), and VO^{2+} cations resulted in the oxidation of anisole when adsorbed on the surface. It is also well known that the ability of complex formation and stability of the complex with metal ions is associated with the metal ion's ability to act as an oxidizing agent. Therefore, metal cations can be effectively used for complex formation with volatile biomarkers.

Although studies on the stability of methyl nicotinate on titania or cobalt functionalized titania are not readily available in the literature, the adsorption of methyl nicotinate on the sensor surface is considered stable. Methyl nicotinate is very stable in both aqueous and ethanolic solutions at room temperature.[34,35] Hydrogenation of carboxylic acids over metal oxides generally requires elevated temperatures (>300 ^{o}C). For example, hydrogenation of methyl nicotinate over Cr/ZrO_2 is carried out at 350 ^{o}C.[36]

Both in solution and on the surface of metal oxides, complexation by the anion of weak acids involves the competition of H^+ and the metal center for the anion.[37] In the former case, protons are transferred to the solvent, while in the latter case, they are transferred to surface OH groups, which are important in defining the stability of the surface complexes.[37] Since the sensor surface contains many OH groups (*vide supra*), which are essential in stabilizing surface complexes, stable complexation of methyl nicotinate with the sensor surface may be realized.

The ordered arrays of TiO_2 nanotubes are an excellent support for the metal ions to bind with biomarkers because of their high surface area. When the metal ions participate in the oxidation of the biomarkers, electron transfer occurs from the biomarker to the metal ions, which is then collected through the TiO_2 nanotubes. The nanotube structure has enabled improved charge transport properties and can conduct the electrons with minimal losses.[38,39]

The reaction of methyl nicotinate with Co-TNA can be envisaged as follows. At the cobalt functionalized titania nanotubular surface, methyl nicotinate is oxidized. This leads to the formation of cobalt di-nicotinate on the TNA surface along with the release of two methyl radicals and two electrons (equation 3.4). These electrons flow through the outer circuit to render an observable change in current.

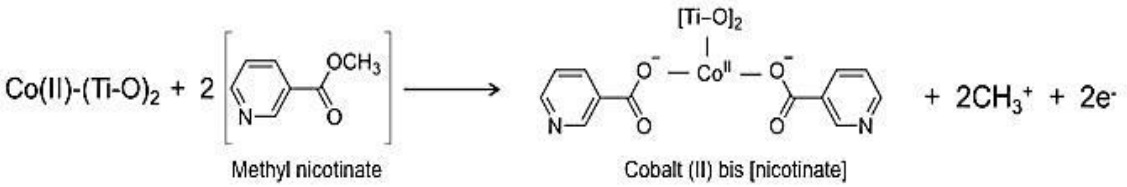

…(3.4)

Cosandey *et al.* [32] had corroborated to the above view and stated that for chemical sensors, the increased selectivity due to addition of metallic clusters can be explained by two mechanisms, chemical sensitization and electronic sensitization. In chemical sensitization, the metal particles act as centers for surface-gas adsorption, which is then followed by spillover onto the oxide surface to react with the negatively charged chemisorbed oxygen. On the other hand, electronic sensitization results in a direct electronic interaction between the oxide surface and metal particles via metal oxidation and reduction processes. In this case, cobalt might form an oxide in the presence of surface adsorbed oxygen ions, resulting in a change in charge carrier concentration of the material.[9] The oxidized metal particles are then reduced in the presence of reducing gases, such as methyl nicotinate vapor, leading to a change in carrier concentration of the semiconductor oxide substrate. As a result, methyl nicotinate will be oxidized to nicotinic acid, while Co(II) itself is reduced to metallic Co. The XPS studies have confirmed the presence of cobalt hydroxide on the surface of Co-TNA (Figure 3.5). The $Co(OH)_2$ reacts with the surface adsorbed oxygen ionic species and is oxidized to CoO_2^-. This can be explained by the following reactions:

$$Co(OH)_2 + 2H^+ + 2e^- \rightarrow Co + 2H_2O \quad \ldots(3.5)$$

$$Co(OH)_2 + 2O^{2-} \rightarrow CoO_2^- + 2OH^- + e^- \quad \ldots(3.6)$$

$$CoO_2^- + 4H^+ + e^- \rightarrow Co^{2+} + 2H_2O \quad \ldots(3.7)$$

During the reaction with methyl nicotinate, the Co(III) is reduced to Co(II). The overall reaction illustrating the oxidation of methyl nicotinate to nicotinic acid and the reduction of Co(III) to Co(II) is illustrated in the following equation:

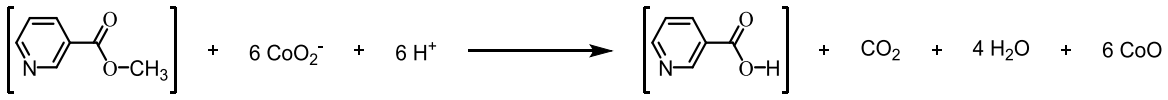

…(3.8)

Similar results were demonstrated by Fine *et al.*[9] Upon interaction with a reducing gas, an increase in conductivity of the material occurs. This explanation fits our scenario wherein titania nanotubes is a well-known n-type semiconductor[40] and methyl nicotinate vapor is a reducing gas. Water molecules form hydroxyl (OH−) ions on the surface, directly introducing electrons that increase the conductivity of an n-type sensor. Further, the role of surface adsorbed oxygen atoms should be discussed in the context of the sensing mechanism. It is well known that titania readily adsorbs atmospheric oxygen[19]. The pre-adsorbed oxygen is strongly electro-negative and gains electrons from the titania surface as the TiO_2 conduction band minimum is higher than the chemical potential of oxygen.[23] This leads to the formation of oxygen ionic species, as described by Kwon *et al.*, [23] Zeng *et al.*, [41] and Wen and Tian-mo [19] and summarized by the following reactions:

$$O_2(gas) \rightarrow O_2(ads) \quad \ldots(3.9)$$

$$O_2(ads) + e^- \rightarrow O^{2-}(ads) \quad \ldots(3.10)$$

$$O^{2-}(ads) + e^- \rightarrow 2O^-(ads) \quad \ldots(3.11)$$

$$O^-(ads) + e- \rightarrow O^{2-}(ads) \quad \ldots(3.12)$$

Thus, surface adsorbed oxygen can act as traps for titania conduction band electrons, leading to a depletion layer or oxygen vacancies near the surface. Cobalt functionalization leading to the formation of cobalt hydroxide precipitates, or simply metallic cobalt (as revealed from XPS studies), causes band bending, which in turn leads to an increase in the energy barrier causing an increase in resistance of the titania substrate.[41] With the introduction of the reducing gas, such as methyl nicotinate vapor, chemical reactions take place between the methyl nicotinate molecules and the pre-adsorbed oxygen ionic species at the cobalt functionalized titania composite surface. As a result, cobalt dinicotinate forms in addition to CO_2 and H_2O and the electrons are released back to the TiO_2 nanotubes. The charge carrier concentration in the walls of the titania nanotubes increases and thickness of the surface depletion layer decreases as electrons are transferred to the conduction band.[23] Consequently, the conductivity increases, which is indicated by the sharp increase in electrical current in the titania nanotubes. The large surface area contributed by the inner and outer walls of the nanotubes presents a high surface-area-to-volume ratio in comparison to titanium dioxide films[23] contributing to a greater response.

The relationship between the energy levels in a semiconductor (i.e., valance and conduction band positions) and the energy levels of the redox potentials (oxidizing or reducing) is of critical importance for favorable charge transfer. Band theory can be applied to explain the sensing and charge transfer mechanism. In a recent study,[42] the oxidation potential of methyl nicotinate in phosphate buffer (pH~7) was measured to be -0.45 V (vs. Ag/AgCl). Figure 3.8 depicts the relationship between the redox potentials (nicotinate/nicotinic acid, Co^{2+}/Co, and Co^{3+}/Co^{2+}) and the energy bands of titania. The

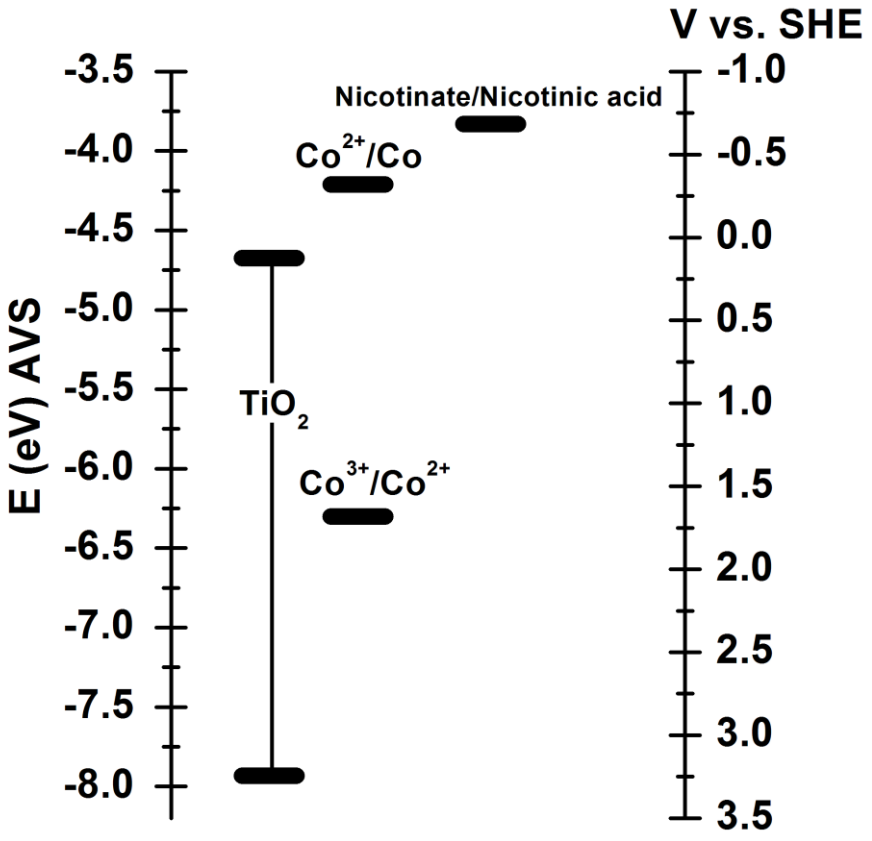

Figure 3.8: Relative valence and conduction band energy levels for TiO_2 as well as nicotinate/nicotinic, Co^{2+}/Co, and Co^{3+}/Co^{2+} redox potentials.

redox potential for nicotinate/nicotinic acid and Co^{2+}/Co are ~0.84 and ~0.46 eV above the conduction band of titania, respectively, whereas the Co^{3+}/Co^{2+} redox couple is essentially halfway between the valance and conduction band energies of titania. It is likely that the observed electrical signal is due to the reduction of Co^{2+} to Co metal (equation 3.5) as donation of electrons from the nicotinate/nicotinic acid redox couple to the Co^{2+}/Co redox couple and subsequent donation to the conduction band of titania is energetically favorable. For the Co^{3+}/Co^{2+} redox couple to donate electrons to the conduction band of titania, a large energy potential barrier must be overcome.

Due to the higher energy barrier, the Co^{3+}/Co^{2+} redox couple is anticipated to proceed slower. This is probably why an increase in Co metal on the surface after exposure of the sensor to reducing methyl nicotinate vapor is observed in the XPS studies (Figure 3.5). It is worth noting, however, that synthesizing TNA in an organic electrolyte (i.e., ethylene glycol) can result in doped carbon. The existence of impurities, crystal defects, and broken bonds at the surface gives rise to surface energy states.[43,44] These surface states are below the conduction band of titania,[45] and would be more energetically favorable for the Co^{3+}/Co^{2+} redox couple to transfer electrons to these surface states than to the conduction band of titania. As a result, it may be possible the current signal is a contribution of both processes.

3.4 Summary

Cobalt functionalized titania nanotube arrays successfully demonstrate application in the electrochemical detection of methyl nicotinate biomarker vapor. Amperometric detection studies of methyl nicotinate vapor confirm the necessity of cobalt functionalization and 1D nanotubular morphology. With regard to the sensor response mechanism, two mechanisms have been proposed for the binding of nicotinate biomarker. One mechanism assumes that when the cobalt metal ions participate in the oxidation of the methyl nicotinate biomarker, electron transfer occurs from the biomarker to the metal ions, leading to the formation of cobalt dinicotinate. The other mechanism proposes that cobalt hydroxide is oxidized to cobalt oxide due to reaction with surface adsorbed oxygen ion species. Thus, cobalt is present as an oxide radical Co(III) causing the oxidation of the methyl nicotinate to nicotinic acid while the cobalt itself is reduced to

Co(II) and subsequently to metallic cobalt. In summary, both mechanisms agree that during the sensing and detection process, methyl nicotinate is a reducing gas, which undergoes oxidation while the cobalt is an oxidative agent, which undergoes reduction. Further, an explanation based on band theory confirms that a reducing gas, such as methyl nicotinate vapor upon interaction with a n-type semiconductor, leads to a decrease in resistance, as indicated by the amperometric studies. The results demonstrated in this study present a robust sensing platform to detect VOC biomarkers and can potentially be tailored and applied to other VOCs of interest.

3.5 References

1. K. D. G. v d Kant, L. J. T. M. v d Sande, Q. Jöbsis, O. C. v Schayck, and E. Dompeling, *Resp. Res.*, **13,** 117 (2012).
2. M. Zhou, Y. Liu, and Y. Duan, *Clinica Chimica Acta*, **413,** 1770-80 (2012).
3. S. Meinardi, K. B. Jin, B. Barletta, D. R. Blake, and N. D. Vaziri, *Biochim. Biophys. Acta*, **1830,** 2531-7 (2013).
4. C. S. Probert, T. Khalid, I. Ahmed, E. Johnson, S. Smith, and N. M. Ratcliffe, *J. Gastrointest. Liver*, **18,** 337-43 (2009).
5. J. Li, Y. Peng, and Y. Duan, *Crit. Rev. Oncol. Hemat.*, **87,** 28-40 (2013).
6. A. S. Ahammad, Y. H. Choi, K. Koh, J. H. Kim, J. J. Lee, and M. Lee, *Int. J. Electrochem. Sc.* **6** 1906-16 (2011).
7. M. Syhre, L. Manning, S. Phuanukoonnon, P. Harino, and S. T. Chambers, Tuberculosis, **89,** 263-6 (2009).
8. R. Moos, K. Sahner, M. Fleischer, U. Guth, N. Barsan, and U. Weimar, *Sensors*, **9,** 4323-65 (2009).
9. G. F. Fine, L. M. Cavanagh, A. Afonja, and R. Binions, *Sensors*, **10,** 5469-502 (2010).
10. M. Arafat, B. Dinan, S. A. Akbar, and A. Haseeb, *Sensors*, **12,** 7207-58 (2012).
11. A. Kolmakov and M. Moskovits, *Annu. Rev. Mater. Res.*, **34,** 151-80 (2004).

12. B. Mishra, P. Ghildiyal, S. Agarkar, and D. Khushalani, *Mater. Res. Express*, **1,** 025005 (2014).

13. Y. R. Smith, R. S. Ray, K. Carlson, B. Sarma, and M. Misra, *Materials*, **6,** 2892-957 (2013).

14. X. Wang, C. Zha, C. Ji, X. Zhang, L. Shen, Y. Wang, A. Gupta, S. Yoriya, and N. Bao, *Mater. Res. Express*, **1,** 035031 (2014).

15. K. Lee, A. Mazare, and P. Schmuki, *Chem. Rev.*, **114,** 9385-454 (2014).

16. O. K. Varghese, D. Gong, M. Paulose, K. G. Ong, and C. A. Grimes, *Sensors Actuat. B-Chem.*, **93,** 338-44 (2003).

17. K. Chen, K. Xie, X. Feng, S. Wang, R. Hu, H. Gu, and Y. Li, *Int. J. Hydrogen Energ.*, **37,** 13602-9 (2012).

18. E. Sennik, Z. Colak, N. Kilinc, and Z. Z. Ozturkrk, *Int. J. Hydrogen Energ.*, **35,** 4420-7 (2010).

19. Z. Wen and L. Tian-mo, *Physica B*, **405,** 564-8 (2010).

20. Z. Wen, L. Tian-Mo, and L. De-Jun, *Physica B*, **405,** 4235-9 (2010).

21. H. F. Lu, F. Li, G. Liu, Z. G. Chen, D. W. Wang, H. T. Fang, G. Q. Lu, Z. H. Jiang, and H. M. Cheng, *Nanotechnology*, **19,** 405504 (2008).

22. P. M. Perillo and D. F. Rodriguez, *Sensors Actuat. B-Chem.*, **171-172,** 639-43 (2012).

23. Y. Kwon, H. Kim, S. Lee, I. J. Chin, T. Y. Seong, W. I. Lee, and C. Lee, *Sensors Actuat. B-Chem.*, **173,** 441-6 (2012).

24. Z. Wen and L. Tian-mo, *Physica B*, **405,** 1345-8 (2010).

25. S. Banerjee, S. K. Mohapatra, M. Misra, and I. B. Mishra, *Nanotechnology*, **20,** 075502 (2009).

26. H. Jayamohan, Y. R. Smith, B. K. Gale, M. Misra, and S. K. Mohanty, *IEEE*, 1-4 (2013).

27. R. S. Ray, B. Sarma, S. K. Mohanty, and M. Misra, *Talanta*, **118,** 304-11 (2014).

28. V. Mahajan, M. Misra, K. Raja, and S. Mohapatra, *J. Phys. D: Appl. Phys.*, **41,** 125307 (2008).

29. Y. R. Smith, R. Gakhar, A. Merwin, S. K. Mohanty, D. Chidambaram, and M. Misra, *Electrochim. Acta*, **135,** 503-12 (2014).

30. M. C. Biesinger, B. P. Payne, A. P. Grosvenor, L. W. Lau, A. R. Gerson, and R. S. C. Smart, *Appl. Surf. Sci.*, **257,** 2717-30 (2011).

31. B. Chen, J. Hou, and K. Lu, *Langmuir*, **29,** 5911-9 (2013).

32. F. Cosandey, G. Skandan, and A. Singhal, *JOM-e*, **52,** 1-6 (2000).

33. T. Pinnavaia, P. L. Hall, S. S. Cady, and M. Mortland, *J. Phys. Chem. C*, **78,** 994-9 (1974).

34. A. Pyka and W. Klimczok, *J. Liq. Chromatogr. Relat. Technol.*, **32,** 1299-316 (2009).

35. B. M. Ross and M. Katzman, *BMC Res. Notes*, **1,** 89 (2008).

36. T. Yokoyama and N. Yamagata, *Appl. Cat. A: Gen.*, **221,** 227-39 (2001).

37. A. D. Weisz, A. E. Regazzoni, and M. A. Blesa, *Croat. Chem. Acta*, **80,** 325-32 (2007).

38. J. R. Jennings, A. Ghicov, L. M. Peter, P. Schmuki, and A. B. Walker, *J. Am. Chem. Soc.*, **130,** 13364-72 (2008).

39. X. Wang, G. He, H. Fong, and Z. Zhu, *J. Phys. Chem. C*, **117,** 1641-6 (2013).

40. W. W. Zhao, Z. Liu, S. Shan, W. W. Zhang, J. Wang, Z. Y. Ma, J. J. Xu, and H. Y. Chen, *Sci. Rep.*, **4,** 4426 **(**2014).

41. W. Zeng, T. Liu, and Z. Wang, *Physica E*, **43,** 633-8 (2010).

42. J. P. Metters, D. K. Kampouris, and C. E. Banks, *J. Braz. Chem. Soc.*, **25,** 1667-72 (2014).

43. H. Gerischer, *J. Electrochem. Soc.*, **125,** 218C-26C (1978).

44. S. R. Morrison, *Electrochemistry of Semiconductor and Oxidized Metal Electrodes* (New York: Plenum) (1983).

45. Q. Zhang, V. Celorrio, K. Bradley, F. Eisner, D. Cherns, W. Yan, and D. J. Fermin, *J. Phys. Chem. C*, **118,** 18207-13 (2014).

CHAPTER 4

PART II: LIMIT OF DETECTION, SPECIFICITY, AND KINETICS

4.1 Introduction

Exhaled human breath contains thousands of volatile organic compounds (VOCs). The analysis of exhaled volatile compounds is a promising, noninvasive method for studying metabolic, oxidative stress-related, and inflammatory processes.[1] Such endogenous VOCs can be related to the physiological and pathological processes of the whole human body.[2] In some cases, exhaled breath from disease stricken patients contains additional VOCs, which are distinguishably absent in healthy subjects. Disease-specific VOCs, termed as volatile biomarkers, can be identified from exhaled breath for most pulmonary diseases,[3,4] although VOC biomarkers for other diseases such as chronic kidney,[5] liver,[6] and cardiac diseases,[7] and breast cancer[8] have been identified as well. A universal sensing platform with replaceable tailor made sensors will serve well.

A specific disease of interest is Tuberculosis (TB), which remains one of the world's deadliest communicable diseases.[9] Tuberculosis is an infectious disease caused by various strains of *mycobacterium*. Prior studies have shown that various strains of the mycobacteria produce distinct gaseous volatile biomarkers that can be used as a methodology for detecting and identifying the *mycobacterium tuberculosis*[10-13] such

as methyl phenylacetate, methyl p-anisate, methyl nicotinate, and o-phenylanisole.[10] These compounds were found in *Mycobacterium tuberculosis* and *Mycobacterium bovis* cultures. Researchers were also able to detect TB before the visual appearance of colonies, which could have implications in detection of latent TB infection. Syhre *et al*. in a follow-up publication were able to detect statistically significant differences of methyl nicotinate in the breath of smear positive TB patients when compared to healthy (smear negative) subjects.[11] Analyses in these studies were done using gas chromatography/mass spectroscopy analysis tools. While they are effective in identifying and quantifying complex gas samples, they are expensive, bulky, and not appropriate for point-of-care (POC) diagnostics. Acid fast staining[14] is the most common TB diagnostic method, which is followed by sputum smear microscopy.[15,16] However, this method is often unreliable due to its poor sensitivity. Another method of diagnosis is done via culturing sputum. This method has a much higher sensitivity, but requires a longer assessment time (~ 4-8 weeks). The GeneXpert (currently the 'state of the art' for rapid TB detection) employs nucleic acid amplification techniques for successful detection of mycobacterium tuberculosis with relatively high sensitivity and specificity[17,18] in a short amount of time (~ 90 min.). Although this method has earned wide acclaims, the detection method is undesirable in a POC setting as it involves an expensive, sophisticated, and nonportable instrument. Subsequently, the development of a robust, inexpensive, and POC sensing device is of necessity.

One proposed methodology for POC settings is through the electrochemical detection of specific VOCs biomarkers for TB, i.e., methyl phenylacetate, methyl p-anisate, methyl nicotinate, and o-phenylanisole that are expired from the breath.

Nanostructured metal oxides and hydroxides, namely transitional metals, have been widely investigated for VOC sensing application due to their low cost, robust synthesis, and wide applications. A recent article had emphasized the role of nanotechnology in emerging medical diagnostic trends.[19] The proposed sensing methodology is antibody and label free, utilizing a solid-state sensor based on functionalized 1D TiO_2 nanotube arrays. Titania nanotube arrays (TNA) synthesized by electrochemical anodization of titanium foils [20,21] offer a robust substrate to functionalize with metals and/or metal hydroxides, which have a high binding affinity for the VOCs of interest. Functionalized titania nanotube arrays have been used for sensor detection of an array of analytes such as hydrogen,[22] the explosive triacetone triperoxide,[23] and environmental pollutants such as trichloroethylene.[24] We have demonstrated the amperometric detection of methyl nicotinate vapors using TNA functionalized with cobalt hydroxide[25] as well as applying computational methods to understanding the binding nature between metals and VOBs.[26,27] Our initial study using one biomarker (i.e., methyl nicotinate) demonstrated the proof of concept sensing methodology and proposed sensing mechanism. In this study, the application of cobalt functionalized TNA for electrochemically detecting all four major TB biomarkers is realized and the sensor response magnitude (change in conductivity) and response time is described by Butler-Volmer kinetics.

4.2 Experimental

Synthesis of titania nanotubes have been illustrated in Section 3.2.1 of Chapter 3. Cobalt functionalization of TNA by incipient wetting impregnation (IWI) method has been detailed in Section 3.2.3 of Chapter 3. A schematic of the set-up for TNA synthesis

and Co functionalization by the IWI method is illustrated in Figure 4.1. Random sampling and XPS analysis on several samples was used to optimize the functionalization process such that a consistent 7-8 wt.% Co is achieved.

Morphological examination (surface and cross section) of the TNA and Co-TNA was performed using a field emission scanning electron microscope (Hitachi S-4800 SEM) with a tungsten filament-based field emission gun at 3 kV accelerating voltage and 15 µA emission current. Energy dispersive x-ray spectroscopic (EDS) analysis was

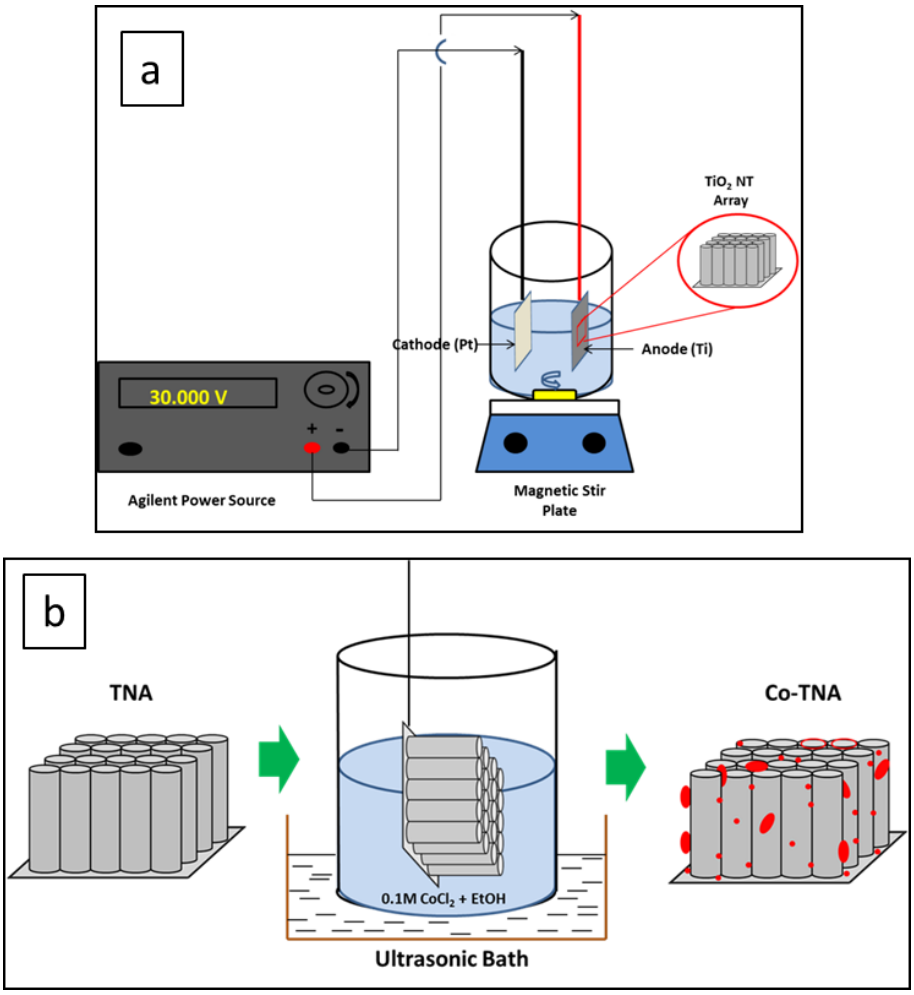

Figure 4.1A schematic of (a) the electrochemical anodization set-up for synthesis of titania nanotube array (TNA) and (b) the incipient wetting impregnation (IWI) cobalt functionalization method.

performed using an Oxford (X-Max) EDAX detector attached to the SEM. EDS analysis was carried out at 20 kV accelerating voltage and high probe current. The AZtecEnergy acquisition and EDS analysis software synchronized with the X-Max detector was used mapping and spectral analysis.

The electrochemical detection of the four biomarker vapors viz. methyl nicotinate, methyl p-anisate, methyl phenylacetate, and o-phneylanisole were carried out in a custom-built sensing chamber as described in our previous work.[25] A two-electrode potentiostat system (Gamry Reference 600) was used such that the working electrode had electrical connections on the Co-TNA surface while the counter electrode was connected to the unanodized titanium metal side. Nitrogen gas (UHP grade) at 200 sccm (standard cubic centimeters per minute) was used as the carrier gas and bubbled through a 10 mM biomarker solution in ethanol. The resultant vapor was delivered to the sensing chamber. A low bias (based on cyclic voltammetry studies, not shown) was applied and a potentiostatic (I–t) run was carried out to test the sensor response. Preliminary cyclic voltammetry tests determined the bias voltage for each biomarker. Prior to introducing the analyte or the target biomarker vapor, the sensor was allowed to stabilize under nitrogen flow for several 100s of seconds. Upon achieving maximum current when exposed to the biomarkers, the analyte vapor was discontinued and nitrogen was reintroduced into the sensing chamber, until the current decreased gradually and became steady. To test the reproducibility of the sensors, each VOB was investigated with 3 randomly selected sensors. The relative standard deviation in sensor response was found to be within ±3%. The sensitivity of the Co-TNA sensor was also examined wherein vapor from biomarker solution of lower concentrations namely 1 mM, 0.1 mM, 0.01 mM,

0.001 mM, and 0.001 mM was passed through the sensing chamber. Sensing experiments were carried out at ambient room temperature. Control tests were run with ethanol. Further, the selectivity of the Co-TNA sensor was demonstrated by passing vapors of methanol, acetone, and benzene.

The I-V characteristics of the Co-TNA sensor were recorded upon exposure to nitrogen and subsequently the volatile organic biomarkers (10 mM), by running a potentiodynamic scan between -2 V and 2 V at a scan rate of 50 mV/s step size using a Gamry Ref. 600 potentiostat.

4.3 Results and Discussion

4.3.1 Co-TNA Sensor Characterization

Ordered arrays of self-aligned vertically oriented titania nanotubes are illustrated in the SEM micrographs shown in Figure 4.2. Figure 4.2a shows the top view of the ordered array of titania nanotubes with the sidewall view shown in the inset. Each nanotube has an outer diameter of ~60 nm with a consistent 12 nm wall thickness, while the length of the nanotubes ~1.5 μm. These dimensions are consistent with that reported in our previous work.[25] Figure 4.2b shows the cobalt hydroxide precipitates on the mouth of titania nanotubes. EDS analysis of Co-doped TNA samples has confirmed the presence of cobalt on the mouth and the walls of the nanotubes (Figure 4.2b inset) whereas XPS revealed that cobalt exists as cobalt hydroxide in the Co^{2+} oxidation state.[25]

4.3.2 Sensor Response to Biomarker Vapors

The optimum bias voltage for amperometeric detection was determined to be -0.5 V for methyl nicotinate, -0.8 V for methyl p-anisate, and -1.0 V for methyl phenylacetate

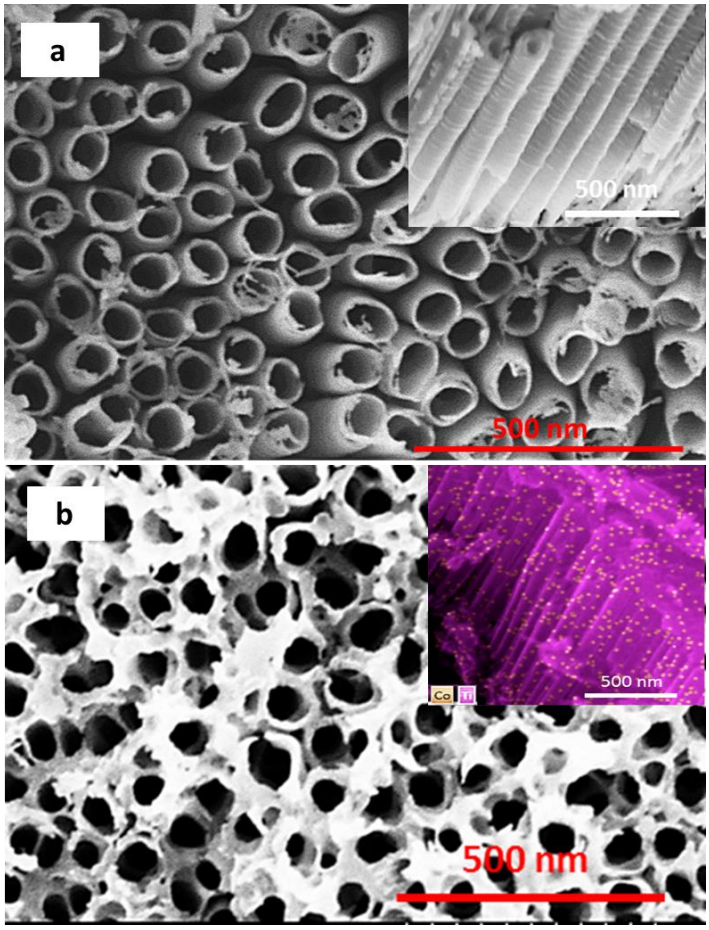

Figure 4.2. SEM micrographs showing (a) the top view of bare TiO_2 nanotubes with the side wall view shown in the inset. (b) SEM micrographs showing the top view of the cobalt functionalized TiO_2 nanotubes, illustrating the cobalt hydroxide precipitates on the mouth of the nanotubes, with the EDS micrograph (inset) revealing the presence of cobalt on the side walls.

and o-phenylanisole, respectively, using preliminary cyclic voltammetry (performed in solution). Co-TNA yielded ~6 μA, ~80 μA, ~30 μA, and ~5 μA of current during vapor phase detection of methyl nicotinate, methyl p-anisate, methyl phenylacetate, and o-phenylanisole, respectively, at their optimized bias conditions.

A typical current-based sensor response from the four biomarkers is illustrated in Figure 4.3. Another noteworthy observation was that in the absence of the biomarker

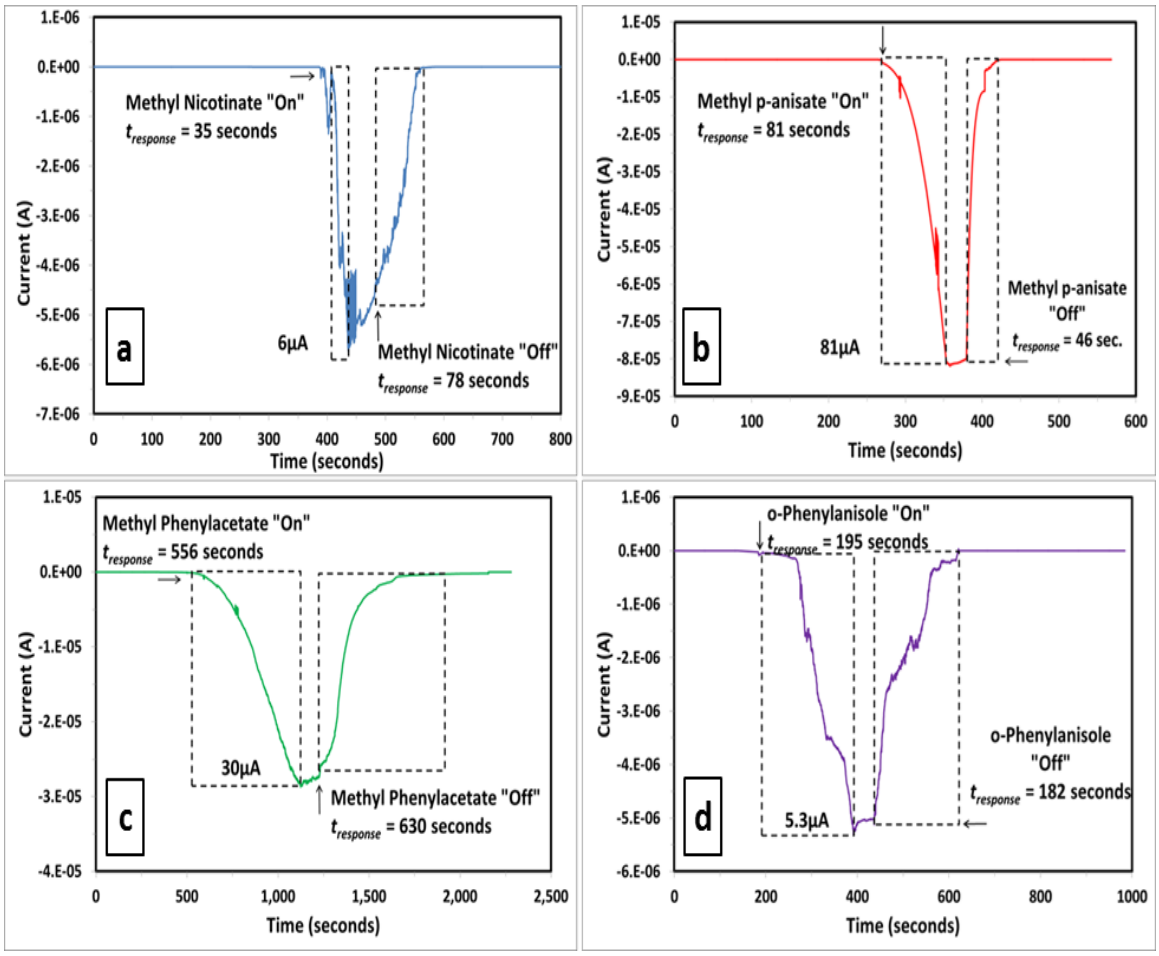

Figure 4.3. Amperometric sensor response to all four TB biomarkers vapor (10 mM in ethanol). Electrochemical detection of methyl nicotinate (-0.5 V) vapor (a), methyl p-anisate (-0.8 V) (b), methyl phenylacetate (-1.0 V) (c), and o-phenylanisole (-1.0 V) (d) at ambient room temperature showing that the signal is due to the binding of the biomarkers to the metal functionalized titania nanotubes. The dotted regions of the plots show the time to reach the maximum current when the sensors were exposed to the biomarker vapor, followed by time to reach baseline current when the vapors were discontinued.

vapors, the current from the sensor upon exposure to the nitrogen gas was of the order of ~pA, which indicates that the sensor is highly resistive in nature. Upon introduction of the biomarker vapors, the maximum achievable current at steady state was usually of the order of ~µA. The signal responses from ethanol vapors were few hundreds of pA (control test). This indicates that the electrical response from the vapors of the individual

biomarkers dissolved in ethanol is at least four orders of magnitude higher than that of the base solvent and that the current change is predominantly due to the binding of the biomarker's vapor to the cobalt functionalized titania nanotubes. Additionally, control tests with nonfunctionalized TNA had yielded negligible change in current upon exposure to the biomarker vapor.[25] The sensor response was calculated based on the following equation:

$$SR = \frac{i_{max,VOC} - i_{N_2,baseline}}{i_{N_2,baseline}} \quad \ldots (4.1)$$

where, $i_{max,VOC}$ is the maximum current achieved when exposed to a VOC biomarker and $i_{N2,\ baseline}$ is the average baseline current achieved when exposed to only nitrogen. To establish the efficacy of Co-TNA as a sensor material, vapor from the individual biomarker solution (in ethanol) of 10 mM concentration was delivered to the sensor to achieve significant electrical response. Based on gas chromatography – mass spectroscopy (GC-MS) characterization of the biomarker vapors, it was found that the actual concentration of the vapor from a 10 mM solution is approximately 2 mM in the sensor chamber. Preliminary tests indicate this concentration to be within range of clinically relevant VOB concentration from exhaled TB patient breath. The sensitivity of the sensor and high affinity of the individual biomarker vapor toward Co-TNA is evident from the instantaneous change in current with the introduction of the vapor. Further, the sensitivity of Co-TNA was examined to determine the limit of detection by exposing the sensor to vapors of the biomarker of lower concentrations. The average sensor response from the range of lower concentrations was still two to three orders of magnitude (~ tens to hundreds nA range) higher than the base current, as illustrated in Figure 4.4. It is evident from the results that the limit of detection of Co-TNA sensor is 0.018 ppm and

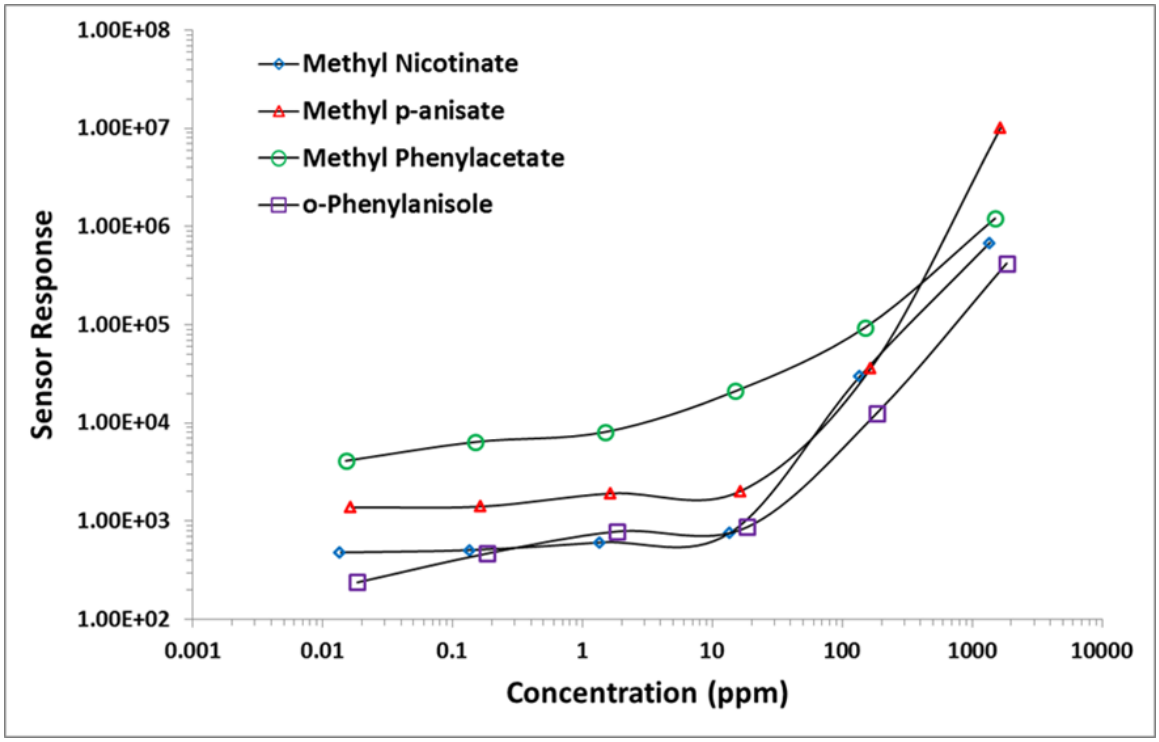

Figure 4.4. Plot showing the effect of concentration of biomarkers on variation of the sensor response (equation 4.1) upon exposure of the Co-TNA sensor. It is evident that the sensor response can be distinguished into two linear regions: 0.01-10 ppm and 10-1000 ppm.

thus, the sensor can be considered extremely sensitive towards all the four biomarkers.

The theoretical lowest detection limit of VOB vapors using a Co-TNA sensor can be estimated as follows:[28]

$$rms_{noise} = \sqrt{\frac{V_x^2}{N}} \qquad \ldots(4.2)$$

$$V_x^2 = \sum (y_i - y)^2 \qquad \ldots(4.3)$$

where rms_{noise} is the root mean square deviation of sensor noise in the relative conductance (or the measured current) of the baseline, y_i is the measured data points in the baseline (i.e., stable baseline with nitrogen gas, before introducing the VOB vapor)

and N is the number of data points in the baseline. The values of y were calculated based on the sensor response from each point relative to the mean baseline current. The detection limit (DL) has been calculated using the relation:[28]

$$DL = 3\frac{rms_{noise}}{slope} \quad \ldots(4.4)$$

As observed in Figure 4.4, the sensor response from biomarkers of varying concentrations comprises two linear regions: 0.01-10 ppm and 10-1000 ppm. The slope was obtained from the linear fit (10-1000 ppm range) of the sensor response of Co-TNA to methyl p-anisate vapor versus concentration plot with a correlation coefficient of 0.984. Since methyl p-anisate exhibited maximum sensor response, calculations were based on the particular vapor and extended to other VOBs as well. The theoretical detection limit of the methyl p-anisate sensing in the vapor phase was estimated to be ~0.62 ppb for the Co-TNA sensor platform.

Results indicate that the experimental limit of detection is approximately 30 times higher than the value predicted from theoretical calculations. The capability of detection of low biomarker concentration with high sensitivity can be considered to be well within the sensing variability for such Co-TNA sensors.

Further, to mimic vapors from human breath, the Co-TNA was exposed to vapors of some common model compounds found in exhaled breath such as methanol, acetone, and benzene. Vapor from solutions of fixed concentration (1000 ppm) of these organics in water was exposed to the Co-TNA sensor. It is important to note here that the concentration of these organics were much higher than that found in breath (which is usually hundreds of ppb). Results indicate that the sensor response for such VOCs is lower than that recorded for the lowest concentration of any biomarker solution. This is

indicative of the fact that the Co-TNA sensor is highly selective towards the TB biomarkers (Figure 4.5).

Understanding the underlying gas sensing principle is critical towards development of better functionalization methods for enhanced sensor response. Pinnavaia *et al.* [29] had stated that metallic cations such as Fe^{3+} and Cu^{2+} facilitated oxidation of anisole, a derivative of one of the biomarkers in our case. The metal ion's oxidizing capability determines the stability of the VOC complex with the metal ions. All four biomarkers are relatively stable in both aqueous and ethanolic solutions.

In addition, the Co-TNA sensor substrate contains hydroxyl groups, which contribute to formation of stable complexes with the organic biomarkers. Cobalt metal

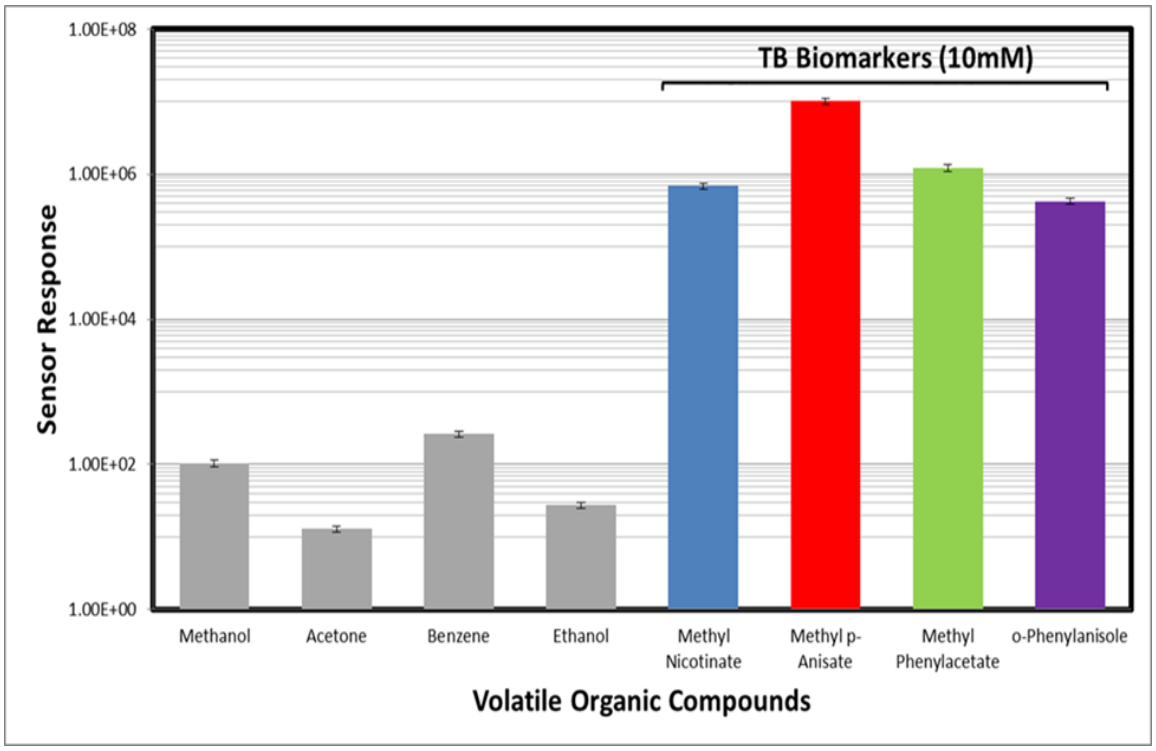

Figure 4.5. Bar graphs showing the comparison of the sensor response upon (equation 4.1) exposure of the Co-TNA sensor to the TB biomarkers (10 mM or ~1400 ppm) and other organic solutions (~1000 ppm), illustrate high sensor selectivity

ions attached to the TNA sensor substrate provide active binding sites for the biomarkers. During oxidation of the biomarkers at the sensor surface, electron transfer occurs from the biomarker to the cobalt ions, which is then collected through the TiO_2 nanotubes. At the cobalt functionalized titania nanotubular surface, the biomarkers are oxidized, which leads to the formation of cobalt complexed species on the Co-TNA surface and two electrons. These electrons flow through the outer circuit to render an observable change in current. The reaction of the four biomarkers with Co-TNA can be envisaged as follows:

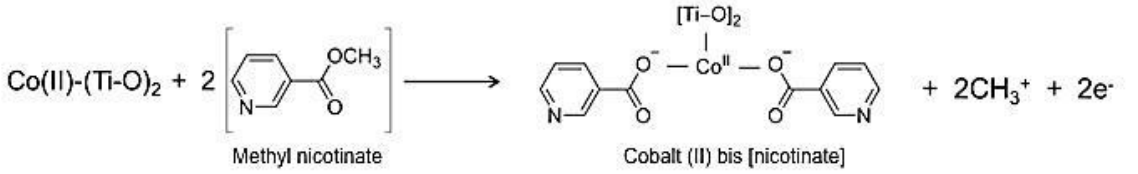

…(4.5)

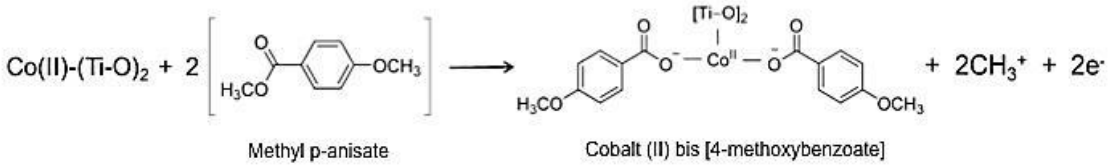

…(4.6)

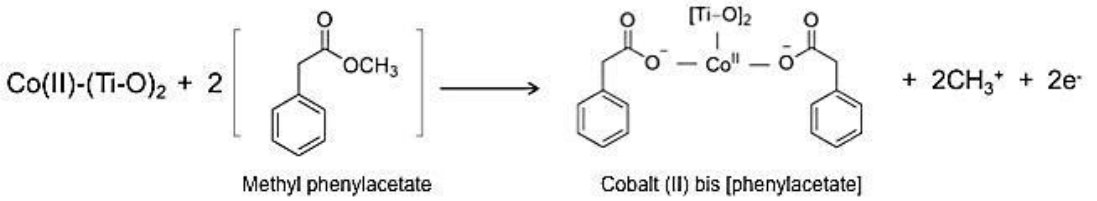

…(4.7)

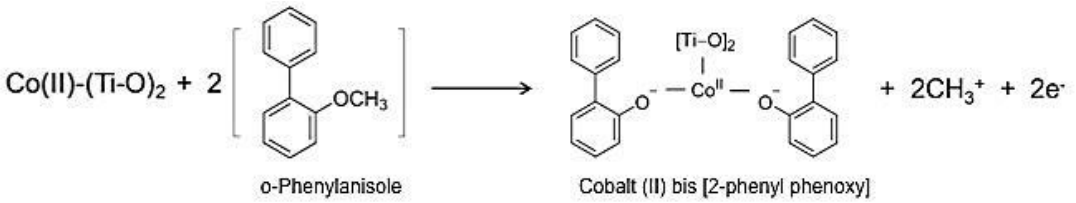

…(4.8)

Weinberg and Weinberg [30] had stated that polycyclic aromatic hydrocarbons proceed by initial charge transfer of the aromatic group where the oxidation follows a mechanism involving loss of two electrons and formation of a cationic species. They had speculated that the reactions may involve discharge of methoxy or methyl radicals which might ultimately form methanol. Further, although they stated that the cationic species discharged could be the methoxide radical, very scant evidence was available to substantiate the claim. They had also shown a reaction scheme where they illustrated that chemically generated methoxy radicals react with aromatic hydrocarbon to provide methanol and benzylic dimers and essentially no methoxylated product was formed. Overall, this supports our proposed reaction mechanism for the interaction of the organic biomarkers (which are essentially aromatic methyl esters) with the cobalt functionalized titania nanotubes. We believe that upon oxidation at the sensor surface, the biomarkers forms benzylic dimers with cobalt along with the release of two electrons and a methyl radical.

The reducing vapors of the biomarker cause partial reduction to metallic cobalt, leading to a change in electron concentration on the Co-TNA substrate. Studies have also stated that that interaction of reducing vapors with n-type TNA substrates results in an increase in conductivity.[31] A better explanation for this case is, surface adsorbed oxygen species scavenge electrons from the conduction band of titana, leading to the formation of oxygen vacancies, or a depletion layer (L_D), which is expressed by:[32]

$$L_D = \left[\frac{2\varepsilon\varepsilon_0}{n_0 e}\right]^{\frac{1}{2}}\left[E - E_{FB} - \frac{k_B T}{e}\right] \quad \ldots(4.9)$$

where ε is the dielectric constant, taken as 42 for TiO_2 (33), ε_0 is the permittivity of vaccum, n_0 is the total carrier concentration, which is ~ 6.5 x 10^{20} cm^{-3} eV^{-1}, E_{FB} is flat band potential, taken as -0.5 V for long nanotubes, [33] e is the carrier charge, k_B is the Boltzmann constant, and T is the absolute temperature. Under these conditions, the depletion width layer is anywhere between 4 – 7 nm. [33,34] Studies have concluded that the maximum sensitivity is achieved whenever the width of the depletion layer is approximately half of the nanotube wall thickness.[32] This is due to the fact that the shift in the electrical resistance upon exposure to a reducing gas can be large when the width of the space charge region is comparable to half of the wall thickness. Significant charge separation occurs at a distance of 1-1.5 nm which happens to be the Debye length for anatase TiO_2 nanotubes.[34] A shorter Debye length determines if the electronic properties are strongly influenced by surface processes. In this conduction regime, Cossandey *et al*.[32] proposed that the sensitivity (S) expressed as the change in conductivity (ΔG) is related to the change in the carrier concentration (Δn) and can be given by:

$$S = \Delta G/G_0 = (\Delta n/n_0)L_D = \Delta I/I_0 \quad \ldots(4.10)$$

where, G_0 is the baseline conductivity and I_0 is the baseline current. This expression is very similar to the one we have used (vide supra) to calculate the sensor response, except we have used change in current (ΔI), which is analogous to the change in conductivity. Also, the titania nanotubes synthesized in our case have a wall thickness of ~12 nm; half the wall thickness is within the range of the width of the depletion layer mentioned

above, which explains the significant change in conductivity upon exposure to reducing VOB vapors.

The charge depletion layer encompasses the entire nanotube, resulting in a flat-band condition.[35] The depleted space charge region attempts to establish kinetic equilibrium between the free electrons and the oxygen vacancies in such a way that the Fermi level shifts from the conduction band edge of titania, causing band bending. As the biomarker vapors are introduced, chemical reactions take place between the biomarkers and the pre-adsorbed oxygen species at the Co-TNA surface. These events result in the formation of cobalt complexes as illustrated in equations 4.5-4.8 and the electrons are released back to the conduction band of TiO_2 nanotubes leading to an increase in charge concentration in tube walls and reduction of the surface depletion layer. Based on band theory, the energy levels of the redox potential of the biomarkers are above the conduction band of titania, as wells as the Co^{2+}/Co redox couple.[25] When the sensor is exposed to the biomarker vapors, electrons are transferred from the biomarker's redox couple to the Co^{2+}/Co redox couple, which subsequently donates electrons to the TiO_2 conduction band, thereby reducing the depletion layer and causing an increase in conductivity, which is reflected by an increase in current. Kolmakov and Moskovits [35] had corroborated to this and based on their observation, we can state that adsorption of a reducing gas leads to reformation of the adsorption sites and redonation of electrons to the titania matrix. Under flat-band conditions, the electron concentration increases, resulting in an increase in the conductivity.[35] Oxidation of VOB vapor by surface adsorbed oxygen is given in equation 4.11.

$$VOB^{vapor} + O^{-2} \rightarrow VOB^{oxidized} + 2e^{-} \quad \ldots(4.11)$$

Transfer of electrons to the Co^{3+}/Co^{2+} redox couple cannot be entirely ruled out. Although the redox potential for this couple is below the conduction band of TiO_2, it can exchange electrons with surface energy states associated with defects and impurities in the titania matrix arising out of incompletely coordinated Ti surface. A reaction mechanism illustrating the interaction of methyl nicotinate biomarker with cobalt functionalized TNA has been enumerated in our previous work [25] and it is envisaged that the other biomarkers follow similar reaction pathways.

4.3.3 Sensor Response Based on Butler Volmer Kinetics

The sensing phenomena have been explained in terms of electrochemical reactions. It follows, then, that electrochemical techniques can be used for further analyses of these phenomena. Careful study and interpretation of the measurements of current-potential relations under controlled conditions can yield important information about reaction rates of the biomarkers at the Co-TNA surface, the propensity for binding to the active sites on the sensor, and other relevant information. Potentiodynamic anodic polarization reveals characterization of the sensor substrate based on the I-V relationship. Such characterization enables better characterization of the anode. This is done because interaction of the biomarkers at the sensor material is predominantly an oxidative reaction. As a result, the electrochemical response can be modeled using Butler Volmer kinetics expressing the Tafel behavior. Solid-state mixed potential gas sensors made of lanthanum manganite/YSZ/terbium yttrium zirconium oxide for CO detection has been mathematically modeled invoking Butler Volmer kinetics.[36] Similarly, a potentiometric hydrogen sensor of Pt coated yttria and zirconia with $CuO/ZnO/Al_2O_3$ catalyst was

modeled by Tan and Tan.[37] Oxygen ionic species are present on the surface of the TiO_2 nanotubes [25,36]. The ionosorbed oxygen contributes to the space charge region and plays an important role in the sensing dynamics.[36]

$$O_2 + 4e^- \rightarrow 2O^{2-} \quad \ldots(4.12)$$

The oxidative reaction of the VOBs vapors occurs as illustrated in equation 4.11. Hence, assuming Butler Volmer kinetics at high overpotentials, the Tafel type behavior can be expressed as follows:

$$i_c = i_{O_2} = i^0_{O_2} \exp\left\{\frac{-4\alpha_1 F\left(E - E^0_{O_2}\right)}{RT}\right\} \quad \ldots(4.13)$$

$$i_a = i_{VOB} = i^0_{VOB} = i^0_{VOB}\exp\left\{\frac{2\alpha_2 F\left(E - E^0_{VOB}\right)}{RT}\right\} \quad \ldots(4.14)$$

where, E is the electrode potential, F is the Faraday constant, R is the molar gas constant, T is the temperature, E^0 is the equilibrium electrode potential, i^0 is the exchange current density, and α is the transfer coefficient. The exchange current density (i^0) is directly proportional to the rate constant k^0, and is frequently used as an important kinetic parameter. At equilibrium, an equal amount of cathodic and anodic current flows and the net current is zero. Although the net current is zero, faradaic activity is still in progress at the electrode surface. Since the exchange current density are related to the kinetic parameter k^0, it can be assumed that they follow the kinetic relationship given by:

$$i^0_{O_2} = -B_1 C^m_{O_2} \quad \ldots(4.15)$$

$$i^0_{VOB} = -B_2 C^n_{VOB} \quad \ldots(4.16)$$

where C represents the concentration of oxygen and VOB vapors and B_1, B_2, m, and n are constants. The above assumption is valid if the exchange current density is proportional

to the active site fractional occupancy θ, i.e., $i^o \propto \theta$. With ionosorbed surface oxygen, some of the vacancies are partially filled. Assuming the surface oxygen coverage is θ', the concentration of unadsorbed chemisorption vacant sites for VOB adsorption is N_s, such that $\theta = \theta' + N_s$. Therefore, the reactions can be rewritten as:

$$O_2 + 4e^- + \theta' \rightarrow 2O^{2-} \quad \ldots(4.17)$$

$$VOB^{vapor} + O^{2-} + N_s \rightarrow VOB^{oxidized} + 2e^- \quad \ldots(4.18)$$

In this sensing system, two electrochemical reactions (equations 4.17, 4.18) co-exist as described above. The mixed potential (E_{mix}) is the potential at which the rate of anodic oxidation of VOB_{vapor} (defined by current i_a) is equal to the rate of cathodic reduction of oxygen (defined by current i_c). The terms "rate" and "current" are used interchangeably since they are directly proportional. The net current can be expressed as the difference between the oxidation and reduction currents, and thus, the current measured with an external device will be zero at the mixed potential E_{mix}.

$$i_{meas} = i_a - i_c = 0 \text{ at } E_{mix} \quad \ldots(4.19)$$

$$i_{meas} = i_{VOB} - i_{O_2} \quad \ldots(4.20)$$

$$i_{meas} = -B_2 C_{VOB}^n \exp\left\{\frac{2\alpha_2 F\left(E - E_{VOB}^0\right)}{RT}\right\} - \left|-B_1 C_{O_2}^m \exp\left\{\frac{-4\alpha_2 F\left(E - E_{O_2}^0\right)}{RT}\right\}\right| \quad \ldots(4.21)$$

$$i_{mix} = i_{VOB} = i_{O_2} \text{ at } E_{mix} \quad \ldots(4.22)$$

The mixed electrode potential (E_{mix}) under equilibrium conditions can be obtained by solving equations (4.13) and (4.14) and is given by:

$$E_{mix} = E_0 + m\frac{RT}{\left(4\alpha_1 + 2\alpha_2\right)F}\ln C_{O_2} - n\frac{RT}{\left(4\alpha_1 + 2\alpha_2\right)F}\ln C_{VOB} \quad \ldots(4.23)$$

$$E_0 = \frac{RT}{(4\alpha_1 + 2\alpha_2)F} \ln \frac{B_1}{B_2} + \frac{2\alpha_1 E^0_{O_2} + \alpha_2 E^0_{VOB}}{(2\alpha_1 + \alpha_2)F} \quad \ldots(4.24)$$

The expression for E_{mix} is similar to the one derived by Kolmakov and Moskovits[36] while describing solid state mixed potential gas sensing. For low concentration of the VOBs, i.e., $C_{VOB} << C_{O2}$, the VOB oxidative reaction occurs at high overpotential while the oxygen reduction reaction occurs at low overpotentials. As a result, the VOB oxidation reaction is mass transport limited. Therefore, the anodic current density can be given by:

$$i^a_{VOB} = 2AD_{VOB}\frac{C_{VOB}}{\delta}F \quad \ldots(4.25)$$

where, A is the electrode area, D_{VOB} is the diffusion coefficient of the VOB vapor, and δ is the diffusion boundary layer thickness. Therefore, the current measured in equation (4.21) is modified and can be expressed as follows:

$$i_{meas} = 2AFD_{VOB}\frac{C_{VOB}}{\delta} - \left| -B_1 C^m_{O_2} \left(\frac{-4\alpha_1 F(E - E^0_{O_2})}{RT} \right) \right| \quad \ldots(4.26)$$

The corresponding mixed electrode potential (E^*_{mix}) coupling the oxygen reduction kinetics and the mass transport limited VOB_{vapor} oxidation kinetics gives:

$$E^*_{mix} = E^0_{O_2} - RT\frac{AD_{VOB}C_{VOB}}{2B_1\delta C^m_{O_2}} \quad \ldots(4.27)$$

Although the possibility of such a case exists, for most of our experiments, the concentration of the VOB vapors were estimated to be higher than the oxygen concentration at the sensor substrate and thus, mass transport limited reaction kinetics is not likely. The conditions prevalent at low VOB concentrations suggest that a highly heterogeneous catalytic oxidation rate on the nonelectrochemically active sites will further lower the concentration of VOBs that reach the electroactive sites, thereby

causing a diminished sensor response. However, it was observed that at high VOB concentration, after prolonged exposure to the biomarker vapors, the current started to decrease slightly. Similar behavior was observed during on/off cycles as well, when the sensor response was maximum during the first cycle and reduced substantially over subsequent cycles. This observation is likely due to a reduction in active sites.

At high overpotential regions, the Butler-Volmer equation (equation 4.14) simplifies to the Tafel equation and can be given by (when E >> E_{mix} for anodic reaction):

$$E - E_{mix} = \left(-\frac{RT}{2\alpha_2 F}\, logi^{o}_{VOB}\right) + \frac{RT}{2\alpha_2 F}\, logi_a \qquad \ldots(4.28)$$

or, $$E - E_{mix} = a + b\log(i) \qquad \ldots(4.29)$$

where, *a* and *b* are the Tafel constants. Kinetic measurements of the VOB oxidation reaction in Co-TNA sensors exhibit Butler Volmer kinetics with a linear Tafel slope region, as shown in Figure 4.6. The equilibrium mixed electrode potential (E_{mix}), the cathodic (α_1) and anodic (α_2) transfer coefficients, the anodic and cathodic exchange current density (i_0), and the Tafel constants *a* and *b*, for each VOB and baseline nitrogen are enumerated in Table 4.1. At the mixed potential (E_{mix}), the rate of oxygen reduction is equal to the rate of biomarker oxidation, and this point corresponds to the magnitude of the sensor response expressed in terms of current density. Thus, the anodic Tafel constant *b* determines this magnitude and is expressed in V/decade, where a decade of current is one order of magnitude. Results based on E_{mix} and *b* values indicate that the methyl p-anisate biomarker shows maximum reactivity with the Co-TNA sensor. This corroborates well with the strength of the signal from the Co-TNA sensor upon exposure to the VOB vapors where it was demonstrated that the maximum sensor response was obtained from

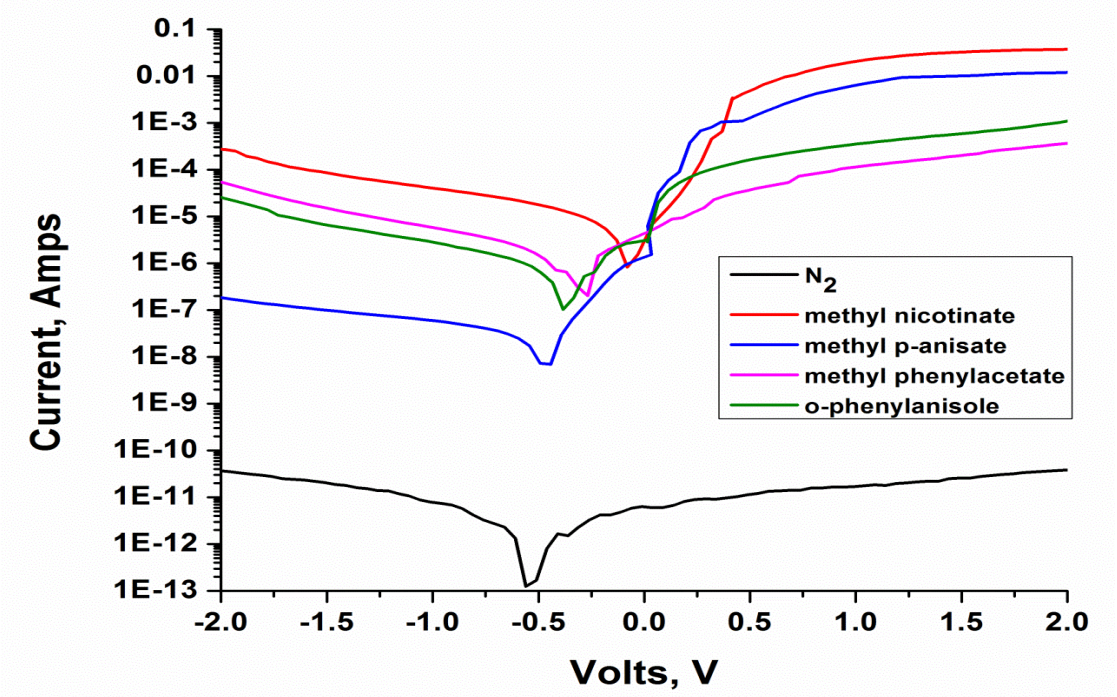

Figure 4.6. Tafel plots of Co-TNA sensor exposed to baseline nitrogen and the VOBs at a concentration of 10 mM in ethanol solution at room temperature (50 mV/s). Calculated Tafel constants are available in Table 3.1.

Table 4.1. Summary of the equilibrium mixed electrode potential (E_{mix}), the cathodic (α_1) and anodic (α_2) transfer coefficients, the cathodic and anodic exchange current density (i_0) and the Tafel constants *a* and *b* for each VOB and nitrogen carrier gas.

	N_2	Methyl Nicotinate	Methyl p-Anisate	Methyl Phenylacetate	o-Phenylanisole
E_{mix} (V)	-0.529	-0.025	-0.422	-0.288	-0.316
α_1 (cathodic)	0.131	0.053	0.053	0.062	0.064
α_2 (anodic)	0.904	0.711	0.685	0.879	0.805
i_o (A/cm^2) (cathodic)	6.90E-14	6.00E-07	8.46E-09	5.60E-07	2.48E-07
i_o (A/cm^2) (anodic)	7.45E-12	8.39E-06	3.57E-06	4.36E-06	6.05E-06
a (V)	-11.128	-5.076	-5.447	-5.361	-5.218
b (V/decade)	1.623	4.880	5.329	2.039	3.299

the methyl p-anisate vapor. For electrochemical reactions described by Butler-Volmer kinetics, the exchange current density i_0 is directly proportional to the rate constant k_0. Ideally, a higher exchange current density indicates faster kinetics. The oxygen reduction reaction is a four-electron process and is expected to have a lower value of rate constant than the biomarker oxidation reaction. A comparison of the anodic and cathodic exchange current densities indeed indicates that the oxygen reduction kinetics (of the order of $\sim 10^{-7} - 10^{-9}$ A/cm^2) is much slower than the VOB oxidation kinetics (of the order of $\sim 10^{-6}$ A/cm^2). Further, from the anodic i_0 values, it is evident that the methyl nicotinate vapor has the fastest reaction kinetics. This corroborates well with experimental results too which show that the sensor response time for methyl nicotinate is the shortest (Figure 4.3). Methyl nicotinate biomarker has the fastest reaction kinetics and, concurrently, has the lowest sensor response time. As the concentration of methyl nicotinate biomarker in the breath of TB patients is higher as compared to other biomarkers, rapid detection of the same is advantageous. Additionally, it is important to note that the anodic exchange current density of nitrogen carrier gas is of the order of $\sim 10^{-12}$ A/cm^2 and is indicative of the fact that nitrogen being an inert gas does not take part in the reaction and the sensor response can solely be attributed to the interaction of the biomarker vapors with the sensor substrate.

4.4 Summary

In this chapter, we have successfully demonstrated the application of titania nanotubular array (TNA) functionalized with cobalt through an incipient wetting impregnation method as a viable sensing platform for electrochemical detection of

prominent tuberculosis biomarker vapors. Sensing of the biomarker vapors was carried out in amperometric mode and the sensor response was calculated from the change in current upon exposure to the VOB vapors. In addition to its selectivity towards the biomarkers over other organics, the sensor exhibits adequate sensitivity in detecting low concentration of the VOB vapors. The width of the depletion layer is comparable to half of the nanotube wall thickness, thereby contributing to its enhanced sensitivity. Further, the sensor response was examined through Butler Volmer reaction kinetics. Experimental investigation of the Tafel plots of the Co-TNA sensor upon exposure to the VOB vapors revealed that the methyl p-anisate biomarker exhibits maximum reactivity towards the sensor and is well in agreement with the electrochemical signal response based on change in conductivity (current). The Co-TNA sensor presents a robust and inexpensive sensing platform for rapid detection of TB biomarkers.

4.5 References

1. A. Bikov, Z. Lazar, and I. Horvath, *J Breath Res*, **9**, 034001 (2015).
2. H. Haick, Y. Y. Broza, P. Mochalski, V. Ruzsanyi, and A. Amann, *Chem. Soc. Rev.*, **43**, 1423 (2014).
3. K. D. van de Kant, L. J. van der Sande, Q. Jobsis, O. C. van Schayck, and E. Dompeling, *Respir Res*, **13**, 117 (2012).
4. M. Zhou, Y. Liu, and Y. Duan, *Clin Chim Acta*, **413**, 1770 (2012).
5. S. Meinardi, K. B. Jin, B. Barletta, D. R. Blake, and N. D. Vaziri, *Biochim Biophys Acta*, **1830**, 2531 (2013).
6. C. S. J. Probert, I. Ahmed, T. Khalid, E. Johnson, S. Smith, and N. Ratcliffe, *J Gastrointestin Liv Dis*, **18**, 337 (2009).
7. A. J. S. Ahammad, Y. H. Choi, K. Koh, J. H. Kim, J. J. Lee, and M. Lee, *Int J Electrochem Sci*, **6**, 8 (2011).

8. J. Li, Y. Peng, and Y. Duan, *Crit Rev Oncol Hematol*, **87**, 28 (2013).

9. World Health Organization, *Global Tuberculosis Report 2014*, (2014).

10. M. Syhre and S. T. Chambers, *Tuberculosis*, **88**, 317 (2008).

11. M. Syhre, L. Manning, S. Phuanukoonnon, P. Harino, and S. T. Chambers, *Tuberculosis*, **89**, 263 (2009).

12. M. Phillips, R. N. Cataneo, R. Condos, G. A. Ring Erickson, J. Greenberg, V. La Bombardi, M. I. Munawar, and O. Tietje, *Tuberculosis*, **87**, 44 (2007).

13. M. Phillips, V. Basa-Dalay, G. Bothamley, R. N. Cataneo, P. K. Lam, M. P. Natividad, P. Schmitt, and J. Wai, *Tuberculosis*, **90**, 145 (2010).

14. Z. Dezemon, C. M. Muvunyi, and O. Jacob, *Int. Res. J. Bacteriol.*, **1**, 1 (2014).

15. S. Haldar, S. Chakravorty, M. Bhalla, S. De Majumdar, and J. S. Tyagi, *J Med Microbiol*, **56**, 1356 (2007).

16. K. R. Steingart, V. Ng, M. Henry, P. C. Hopewell, A. Ramsay, J. Cunningham, R. Urbanczik, M. D. Perkins, M. A. Aziz, and M. Pai, *Lancet Infect Dis*, **6**, 664 (2006).

17. N. T. Nhu, D. Heemskerk, D. A. Thu do, T. T. Chau, N. T. Mai, H. D. Nghia, P. P. Loc, D. T. Ha, L. Merson, T. T. Thinh, J. Day, N. Chau, M. Wolbers, J. Farrar, and M. Caws, *J Clin Microbiol*, **52**, 226 (2014).

18. A. N. Zeka, S. Tasbakan, and C. Cavusoglu, *J Clin Microbiol*, **49**, 4138 (2011).

19. R. Satvekar, B. Tiwale, and P. SH, *Med. Chem.*, **4** (2014).

20. Y. R. Smith, R. S. Ray, K. Carlson, B. Sarma, and M. Misra, *Materials*, **6**, 2892 (2013).

21. K. Lee, A. Mazare, and P. Schmuki, *Chem. Rev.*, **114**, 9385 (2014).

22. S. Joo, I. Muto, and N. Hara, *J. Electrochem. Soc.*, **157**, J221 (2010).

23. S. Banerjee, S. K. Mohapatra, M. Misra, and I. B. Mishra, *Nanotechnology*, **20**, 075502 (2009).

24. H. Jayamohan, Y. R. Smith, B. K. Gale, M. Misra, and S. K. Mohanty, *Proc. Sensors 2013 (Baltimore, MD, 3-6 November 2013) IEEE*, 1 (2013).

25. D. Bhattacharyya, Y. R. Smith, M. Misra, and S. K. Mohanty, *Mater. Res. Express*, **2**, 025002 (2015).

26. R. S. Ray, B. Sarma, S. Mohanty, K. Prisbrey, and M. Misra, *Mater. Chem. Phys.* (2015).

27. R. S. Ray, B. Sarma, S. Mohanty, and M. Misra, *Talanta*, **118**, 304 (2014).

28. N. Gogurla, A. K. Sinha, S. Santra, S. Manna, and S. K. Ray, *Sci Rep*, **4**, 6483 (2014).

29. J. Pinnavaia, P. L. Hall, S. S. Cady, and M. M. Mortland, *J Phys Chem*, **78**, 994 (1974).

30. N. L. Weinberg and H. R. Weinberg, *Chem. Rev.*, **68**, 449 (1968).

31. G. F. Fine, L. M. Cavanagh, A. Afonja, and R. Binions, *Sensors* **10**, 5469 (2010).

32. F. Cosandey, G. Skandan, and A. Singhal, *JOM-e*, **52**, 1 (2009).

33. C. A. Grimes and G. K. Mor, *TiO2 Nanotube Arrays*, p. 358, Springer US (2009).

34. R. G. Freitas, M. A. Santanna, and E. C. Pereira, *Electrochim. Acta*, **136**, 404 (2014).

35. A. Kolmakov and M. Moskovits, *Ann. Rev. Mater. Res.*, **34**, 151 (2004).

36. F. H. Garzon, R. Mukundan, and E. L. Brosha, *Solid State Ionics*, **136-137**, 633 (2000).

37. Y. Tan and T. C. Tan, *J Electrochem Soc*, **141**, 461 (1994).

CHAPTER 5

IN-SITU ANODIC FUNCTIONALIZATION OF TITANIA NANOTUBE ARRAYS FOR ELECTROCHEMICAL DETECTION OF TB BIOMARKER VAPORS

5.1 Introduction

Sensor detection of specific volatile organic biomarkers (VOBs) in breath directly associated with a disease presents itself as a rapid, noninvasive, point-of-care (POC) medical diagnostic technique. Endogenous VOBs can be related to the physiological and pathological processes of the whole human body.[1,2] Recent review articles[3-5] highlight the clinical use of identifying volatile organic compounds (VOCs) in patients' breath for improved and accurate diagnoses of pulmonary diseases such as asthma, chronic obstructive pulmonary disease, lung cancer, and cystic fibrosis, for example.

As has been revealed earlier, Tuberculosis (TB) is an infectious disease caused by various strains of *mycobacterium*, and is arguably one of the most devastating infectious diseases in the world today.[6] Some studies have indicated that various strains of mycobacteria produce distinct VOBs that can be used as a methodology for detecting and identifying the mycobacterium[7,8] and this is further augmented by the ability to detect statistically significant differences of methyl nicotinate in the breath of smear positive TB patients when compared to healthy, smear negative subjects.[9] While these methods are

effective and established as the "gold standard" in identifying and quantifying complex gas samples, the method is, however, expensive, not POC friendly, and requires trained personnel in a controlled laboratory setting. More interesting methods to detect TB VOBs have been investigated such as through the use of trained honeybees to detect low levels of TB VOBs[10] or trained African giant pouched rats [11,12] to sniff out patients with active TB. Such methods demonstrate the efficacy of using VOBs associated with TB in exhaled breath as a robust method to screen TB patients.

One-dimensional nanostructured titanium dioxide materials, in particular titania nanotubes synthesized via anodization, have been studied extensively for their application in catalysis, biomedical, and gas sensing.[13,14] For sensing applications, andodized titania nanotube arrays (TNA) have mainly been applied for oxygen and hydrogen detection as well as VOCs such as alcohols,[15-20] explosive triacetone triperoxide (TATP),[21] and trichloroethylene vapors[22]. Recently, we have demonstrated the application of using cobalt functionalized TNA (via incipient wetness impregnation method) for the electrochemical detection of methyl nicotinate[23] and p-anistate,[24] as well as computational methods to understand the binding nature between metals and VOBs of interest.[25,26] Our initial studies indicate TNA to be a versatile substrate, which can be used extensively for various sensing applications. Sensing of the four biomarkers using TNA functionalized with cobalt by the incipient wetting impregnation (IWI) method has been demonstrated in Chapter 4.

A synthesis methodology for next-generation titania nanotubes has been developed, which is a method to functionalize/dope titania nanotubes in situ during the anodization process.[27] During anodization, the anionic dopant species in solution are

driven to the titanium/titania anode where they are oxidized and coupled with the as-formed titanium oxide layer. This approach has been also been used to dope several other oxygen containing metal anions with titania nanotubes by other groups as well.[28] Although the previous methods resulted in nanotube-type morphology, the order was not high and limited in oxide thickness. This is a result of an aqueous anodization bath with low pH.[14] In this investigation, we demonstrate that in situ functionalization of cobalt metal anions is achievable using an organic-based anodization electrolyte. The higher dielectric constant of ethylene glycol over water enables a more ordered and high-aspect ratio nanotube morphology. The application of next-generation, or in situ functionalized, titania nanotubes as a sensor has yet to be fully explored. In this study, detection of four prominent TB VOBs is demonstrated and shows enhanced signal response and time compared to incipient wetness functionalization method.

5.2 Experimental

5.2.1 Synthesis of Titania Nanotubes Array (TNA)

The procedure for the synthesis of titania nanotubes has been explained in details in Section 3.2.1 of Chapter 3. Cobalt functionalization of TNA by incipient wetting impregnation (IWI) method has been detailed in Section 3.2.3 of Chapter 3 and is hereafter referred to as Co-TNA.

5.2.2 Synthesis of In Situ Functionalized TNA (*i*Co-TNA)

The same synthesis procedure is adopted for in situ functionalization (referred to as iCo-TNA) with the exception of the electrolyte composition. For this, the electrolyte composition consisted of ethylene glycol, 0.5 wt.% CoF_2 + 0.5 wt.% HF + 2.5 wt.% H_2O.

The same post anodization and annealing procedure was followed for these samples as well. For comparison, TNA was also functionalized with cobalt via incipient wetness method (Co-TNA) similar to our previous report.[23]

5.2.3 Characterization

The morphology was characterized using a field emission scanning electron microscope (Hitachi S-4800 SEM) with a tungsten filament at 3 kV accelerating voltage and 15 μA emission current. A JEOL 2800 high-resolution transmission electron microscope with dual EDS detector was used for lattice imaging and *in situ* identification of the elemental composition. A Schottky-type electron gun at 200 kV accelerating voltage was used for high-resolution imaging. Preliminary beam and aperture alignments and selected area diffraction (SAD) were carried out using the Hamamatsu camera. High-resolution images including the lattice spacing were obtained through the Gatan ultra scan camera at 1.5 – 2 million x's magnification. Elemental spectra were obtained in the STEM mode using the dual EDS (Energy dispersive X-ray Spectroscopy) detector. UV-vis diffuse reflectance was performed on a UV-3600 Shimadzu UV-Vis-NIR spectrophotometer.

X-ray diffraction (XRD) was carried out using a Rigaku Miniflex XRD (CuKα = 1.54059 Å) from 2θ = 20 to 60 degrees with a step size of 0.015 degrees and dwell time of 0.5 degrees/min. Surface composition and the oxidation states of Co and Ti were analyzed using x-ray photoelectron spectroscopy (Kratos Axis Ultra DLD model). The vacuum in the analyzing chamber was maintained at 3×10^{-10} Torr. The X-ray excitation source was monochromatic Al K_α radiation (hν = 1486.6 eV) at 180 W. The

survey and high-resolution spectra were acquired at pass energies of 160 and 40 eV, respectively. Spectra were analyzed and all peaks were fitted with CasaXPS software. Charging effects were corrected using the C 1s line at 284.6 eV as an internal reference. Shirley-type background was subtracted from the spectra.

Amperometric detection of all biomarker vapor was carried out in a custom sensing chamber. One side of each alligator clip was covered with a masking tape to prevent short-circuiting between the contacts. The iCo-TNA coupons with one side having in situ Co functionalized titania nanotubes and the other side as the titanium metal were used in the two electrode sensor system and were connected to the working electrode and the counter electrode of a potentiostat (Gamry Reference 600). Nitrogen at 200 sccm (standard cubic centimeters per minute) was used as the carrier gas and was bubbled through a 10 mM VOB (methyl Phenylacetate – 1500 ppm, methyl p-anisate – 1660 ppm, methyl nicotinate – 1370 ppm, and o-phenylanisole – 1840 ppm) solution in ethanol. A schematic diagram of the overall experimental set-up is shown in our previous work (23). Using this experimental set-up, the concentration of VOB vapor was estimated in the sensor chamber using a solid-phase microextraction fiber and GC-MS analysis, and estimated to be 275 ~ 360 ppm (~2 mM of VOB). The sensitivity of the sensor was carried out by subsequent dilution of an ethanolic 10 mM (1370 ppm) solution of methyl nicotinate. A low bias (based on cyclic voltammetry studies, not shown) was applied and a potentiostatic (I-t) run was carried out to test the sensor response. Control experiments were run using ethanol only and all the tests were carried out at room temperature. For each of the four biomarkers, three iCo-TNA sensors were examined and each sensor was exposed to the VOB vapor three times. The reported sensor response towards each VOB

is the most statistically significant representation. The sensor response from the iCo-TNA sensors at each concentration level of the VOBs had a standard deviation of 0.10 ~ 0.15.

Sensor response and sensitivity comparisons were made with a Co-TNA sensor to demonstrate the superior performance of *i*Co-TNA.

5.3 Results and Discussion

Field emission scanning electron micrographs were collected to examine morphology of TNA and iCo-TNA (Figure 5.1). Plain TNA samples were found to have an inner diameter, nanotube length/oxide thickness, and wall thickness of 67.3±8.0 nm, 1.87±0.1 μm, and 6.5±0.9 nm, respectively.

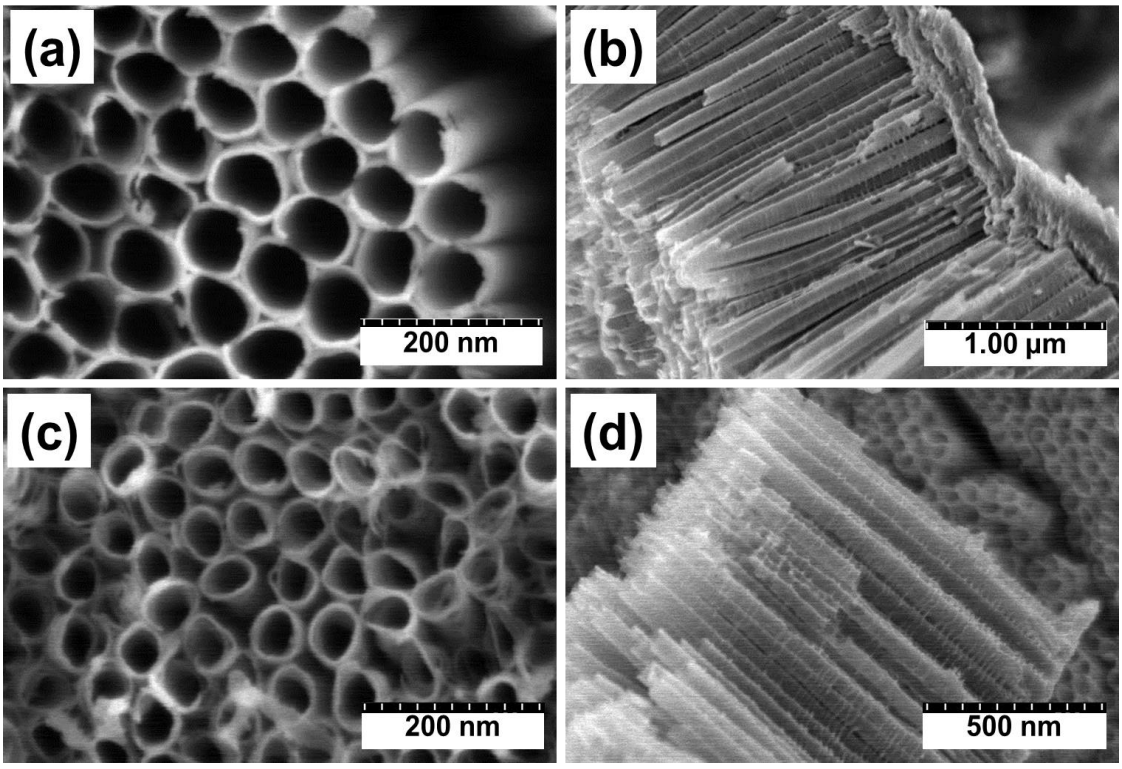

Figure 5.1. Field emission scanning electron micrograph images of (a, b) TNA and (c, d) iCo-TNA.

Nanotube dimensions for iCo-TNA were observed to have an inner diameter, nanotube length/oxide thickness, and wall thickness of 41.7±4.5 nm, 1.25±0.08 μm, 8.13±1.4 nm, respectively. We observe that the addition of cobalt to the electrolyte results in narrower diameter and shorter length nanotubes with increased wall thickness. It is interesting to note that, despite differences in the nanotube dimensions, the aspect ratio of the nanotubes is the same for both (length/(inner diameter + wall thickness) ≈ 25). It is also worth noting that during anodization of iCo-TNA, the steady-state current density was higher than that of plain TNA. Although the anodic current is comprised of two parts, dissolution at the oxide/electrolyte interface and oxidation of titanium at the oxide/metal interface,[29] the increased current is probably attributed to the oxidation of cobalt species.

The HRTEM image in Figure 5.2 illustrates a portion of a single crystalline titania nanotube. Close examination of the HRTEM image reveals that the lattice fringes have an interplanar spacing of 0.35 nm, which corresponds to the {101} facets of anatase phase titania.[30] Further, the FFT (Fast Fourier Transform) of the image captured gives an idea of the spacing of the atomic planes in the reciprocal space and conforms well to reported values.[30,31] The selected area diffraction pattern (SADP) showed a concentric ring pattern, which suggests that the TiO_2 nanotubes are polycrystalline in nature (*vide infra*, XRD). The innermost ring of the SADP signifies diffraction from the anatase {101} plane of atoms.

The HRTEM image in Figure 5.3a illustrates a portion of a single crystalline iCo-TNA. As expected, the lattice fringe spacing of 0.35 nm further confirms the presence of dominant anatase phase titania.

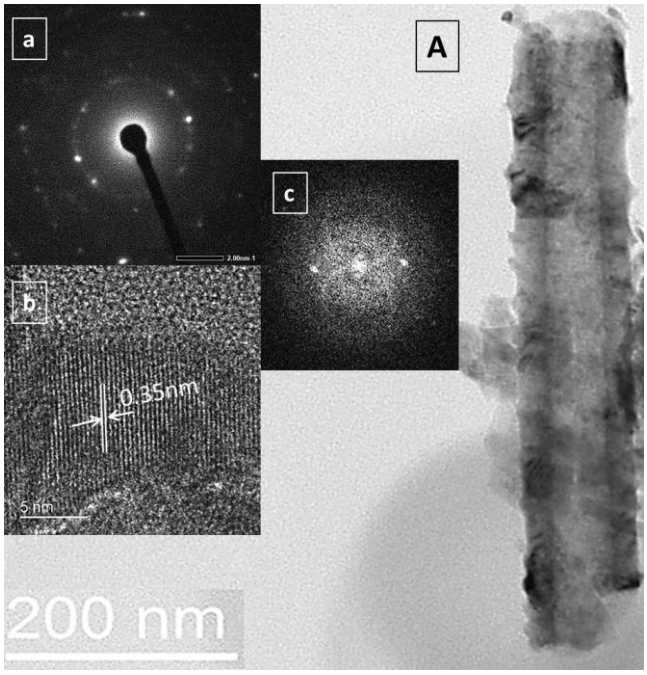

Figure 5.2: High-resolution TEM image of (A) TiO_2 nanotube annealed in oxygen. The insets show (a) selected area diffraction pattern, (b) the lattice spacing, and (c) FFT of the image. The interplanar spacing of ~0.35 nm corresponds to {101} TiO_2 anatase phase.

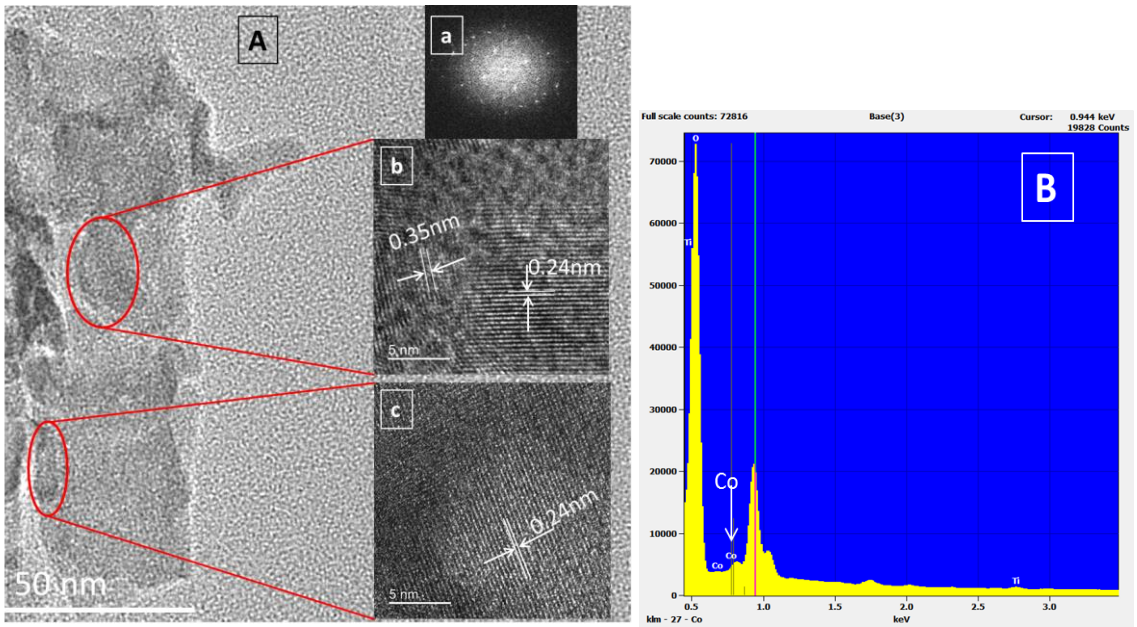

Figure 5.3: High-resolution TEM image of (A) in situ cobalt-doped TiO_2 nanotube. The insets show (a) FFT of the image, and (b, c) the lattice spacing. The interplanar spacing of ~0.24 nm corresponds to the {011} facet of cobalt hydroxide phase while a d-spacing of ~0.35 nm corresponds to {101} TiO_2 anatase phase. (B) Energy dispersive x-ray spectroscopy examination of a single iCo-TNA shows the presence of cobalt.

A closer investigation of walls of the titania nanotube reveal elliptical or oblong shaped particles incorporated into the titania matrix, having an interplanar spacing of 0.24 nm (circled in Figure 5.3A). These dopants are assumed to be cobalt hydroxide, which was confirmed by XPS characterization (*vide infra*). In a study by Liu *et al*.,[32] they report through HRTEM imaging a d-spacing of 0.24 nm for nanocrystalline β-$Co(OH)_2$. The FFT of the image, which is a mirror representation of the SADP, confirms the polycrystalline nature of the cobalt-doped titania nanotubes. It appears the doped cobalt hydroxide was formed with harmonious linkages of the anatase and the cobalt hydroxide facets with excellent alignment and little mismatch among the individual nanocrystals. Energy dispersive x-ray spectroscopy examination of a single iCo-TNA reveals the presence of cobalt (Figure 5.3b); however, the relative intensity of the cobalt peak in comparison to the Ti and O peak was very low, and this can be attributed to the fact that the weight% or atomic% of cobalt on a single nanotube is low. The present results indicate that a uniform distribution of doped Co can be achieved within the titania matrix using this simple process.

X-ray diffraction (XRD) was carried out on annealed samples to determine the crystalline phases of the formed oxide layers. The diffraction patters (Figure 5.4) were analyzed using Rigaku PDXL2 analysis software and indexed with standard JCPDS cards. Both samples show predominate diffraction patterns for anatase (indexed by ■, JCPDS #01-070-7348) and rutile (indexed by ▲, JCPDS #01-076-0318) phase titania, as well as the underlying titanium substrate (indexed by •, JCPDS #00-044-1294). Some subtle differences in diffraction patterns are a marked increase in the Ti {002} diffraction peak ($2\theta = 38.53^{o}$) and an increase in the anatase {004} diffraction peak ($2\theta = 38.02^{o}$)

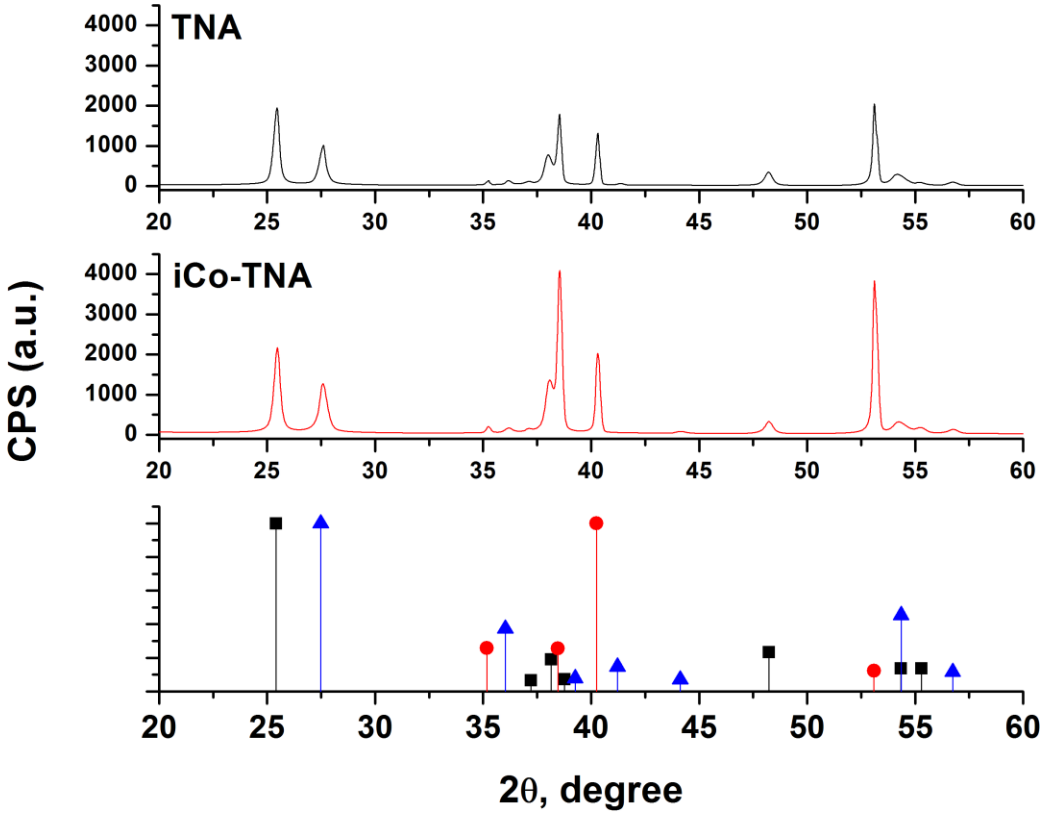

Figure 5.4. X-ray diffraction patterns of (a) TNA and (b) iCo-TNA. (c) The peak indices for anatase (■) and rutile (▲) phase titania, as well as the underlying titanium substrate (•).

for iCo-TNA compared to TNA. As previously mentioned, XPS analysis reveals the dopants to predominantly be $Co(OH)_2$.

Cobalt hydroxide exists in two polymorphs, α and β. The α-$Co(OH)_2$ polymorph is isostructural with hydrotalcite-like compounds that consist of positively charged $Co(OH)_{2-x}$ layers and charge balancing anions (e.g., NO_3^-, CO_3^-, Cl^-, etc.) in the interlayer gallery, while the β-form is a stoichiometric phase with brucite-like structure and consists of a hexagonal packing of hydroxyl ions with Co(II) occupying alternate rows of octahedral sites.[33] As a result, the α-hydroxides have a larger interlayer spacing (7.5 – 8

Å) compared to ~4.6 Å for the β form.[34] The diffraction peaks associated with β-$Co(OH)_2$ are not readily distinguishable from the titania and titanium diffraction peaks as several of them overlap. The increase in the Ti {002} and anatase {004} diffractions may be due to β-$Co(OH)_2$, which has diffraction peaks at $2\theta = 37.92^{o}$ and $2\theta = 38.66^{o}$ corresponding to {101} and {002} planes of β-$Co(OH)_2$ with d-spacing values of 0.232~0.237 nm.[35] It is worth noting that β-$Co(OH)_2$ and Ti are both hexagonal lattice systems. The lattice constants were refined and used to calculate the unit cell volume for each phase, as shown in Table 5.1. A decrease in unit cell volume for both anatase and rutile phase are observed for iCo-TNA compared to TNA. This is attributed to $Co(OH)_2$ present in the titania lattice, which has a smaller unit cell volume (41.067 $Å^3$) and thereby leads to the decrease in lattice cell volume.

The x-ray photoelectron spectroscopy (XPS) core level spectra of Co from the Co-TNA and iCo-TNA are shown in Figure 5.5. From the Co 2p level x-ray photoelectron spectra, the $2p_{1/2}$ peak is distinctly visible at 797 eV while the $2p_{3/2}$ peak is presented as a multiplet of peaks. The complex nature of the $2p_{3/2}$ peak is due to the spin coupling of the 3d and 2p electrons of cobalt. Peak deconvolution for cobalt compounds

Table 5.1. Lattice parameters and unit cell volumes of TNA and iCo-TNA determined from XRD analysis.

	TNA		***i*Co-TNA**	
	anatase	rutile	anatase	rutile
a = b (Å)	3.768	4.591	3.779	4.590
c (Å)	9.470	2.972	9.403	2.957
Volume ($Å^3$)	134.5	62.64	134.3	62.30

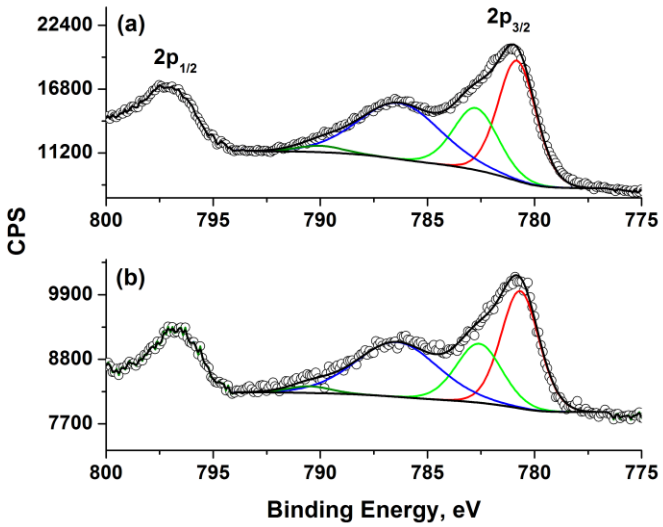

Figure 5.5. A comparison of the Co 2p level x-ray photoelectron spectra of (a) Co-TNA and (b) iCo-TNA.

was carried out and compared to the reported values by Biesinger *et al.* [36] The native Co-TNA and iCo-TNA surface reveals that $Co(OH)_2$ (781.5 eV) is the predominant phase present on the nanotubular sensor surface, thereby confirming the Co^{2+} oxidation state of cobalt. Quantitative analysis based on the x-ray photoelectron spectra reveals approximately 7-9 wt.% or 2.82 - 3.34 at.% cobalt on the iCo-TNA sensor surface. It is evident from the intensity of the peaks at 781.5 eV that the quantity of cobalt in Co-TNA is slightly greater than in iCo-TNA.

The UV-vis diffuse-reflectance absorbance spectra for plain TNA and iCo-TNA are shown in Figure 5.6. From the XRD and HRTEM analysis, it is clear the predominate titania phase is anatase, which has an indirect optical band gap of ~3.2 eV. The band gap of the plain TNA sample was estimated by a Tauc plot (Figure 5.6, inset), and found to have an indirect band gap of 3.27 eV. For iCo-TNA, there is a red shift in the band gap compared to TNA by ~0.15 eV. This shift in band gap implies that cobalt species are

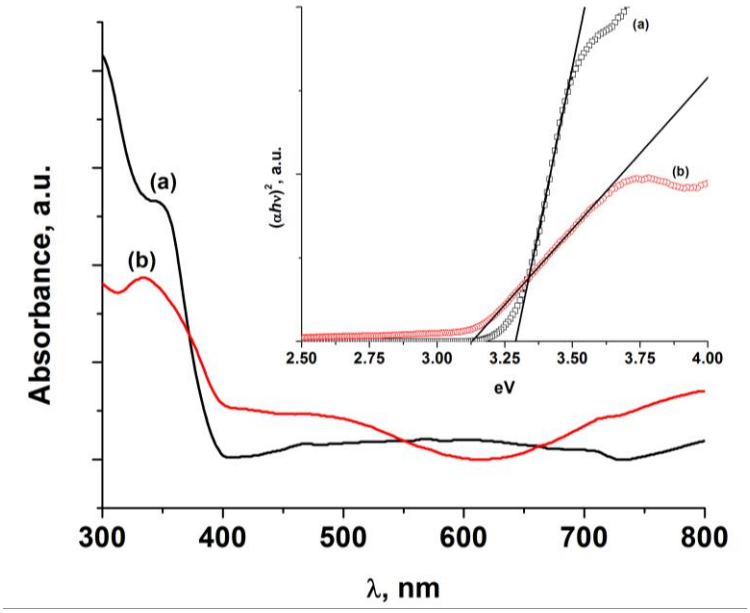

Figure 5.6. Diffuse reflectance absorbance spectra for (a) TNA and (b) iCo-TNA. Inset figure: Tauc plot for indirect band gap transition, showing a red shift in band gap for iCo-TNA compared to bare TNA.

incorporated within the titania matrix, altering the optical properties of the parent titania. If the cobalt species were only on the surface of the titania, the absorbance band edge of TNA would go unaffected and other band gap transitions would be distinguishable. The results of the UV-vis absorbance support the HRTEM analysis that the cobalt species are doped within the parent titania lattice.

Figure 5.7a shows the dynamic electric responses of iCo-TNA to on/off cycles of methyl nicotinate vapor at concentration of ~1370 ppm (10 mM). The iCo-TNA sensor yielded ~100 μA of current during vapor phase detection of methyl nicotinate. The current increases rapidly at the beginning of each pulse when the nicotinate vapor is introduced and decreases rapidly upon removal of the biomarker vapor. The electrical behavior of the iCo-TNA sensor was consistent, reaching the maximum current and

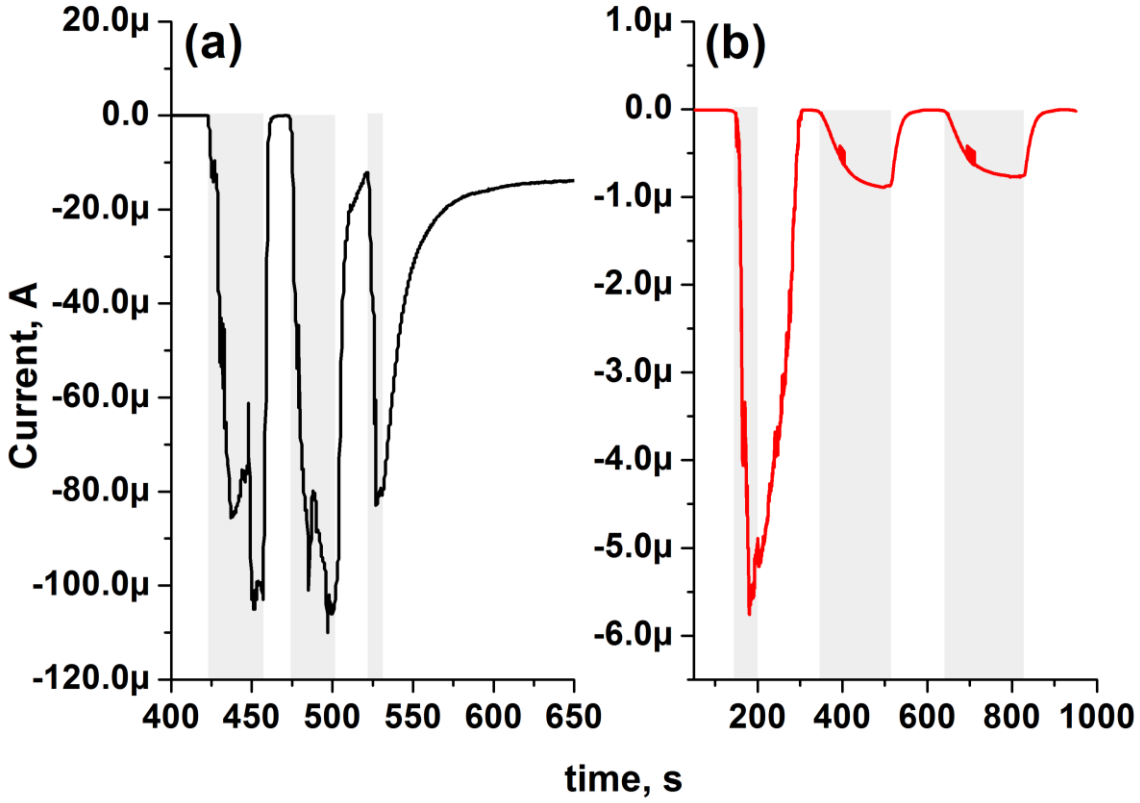

Figure 5.7: Amperometric sensor responses for (a) iCo-TNA and (b) Co-TNA when exposed to 275 ppm of methyl nicotinate vapor. The sensors were held at -0.5 V. The shaded regions of the plots show when the sensors were exposed to vapor.

recovering its original current without much hysteresis after repeated exposures to the biomarker vapor for three cycles. Results indicate that the sensor can be used for three consecutive times before its sensitivity diminishes. In contrast, under the same conditions, the dynamic electric responses from the Co-TNA (Figure 5.7b) sensor functionalized with cobalt using the incipient wetness impregnation method show a maximum current of ~5.5 µA. After the first cycle, the sensor response decays significantly upon subsequent pulsing with methyl nicotinate vapor.

The sensor responses from the other three TB biomarkers using iCo-TNA are illustrated in Figure 5.8. The iCo-TNA sensor yielded ~200 µA, ~60 µA, and ~11 µA of

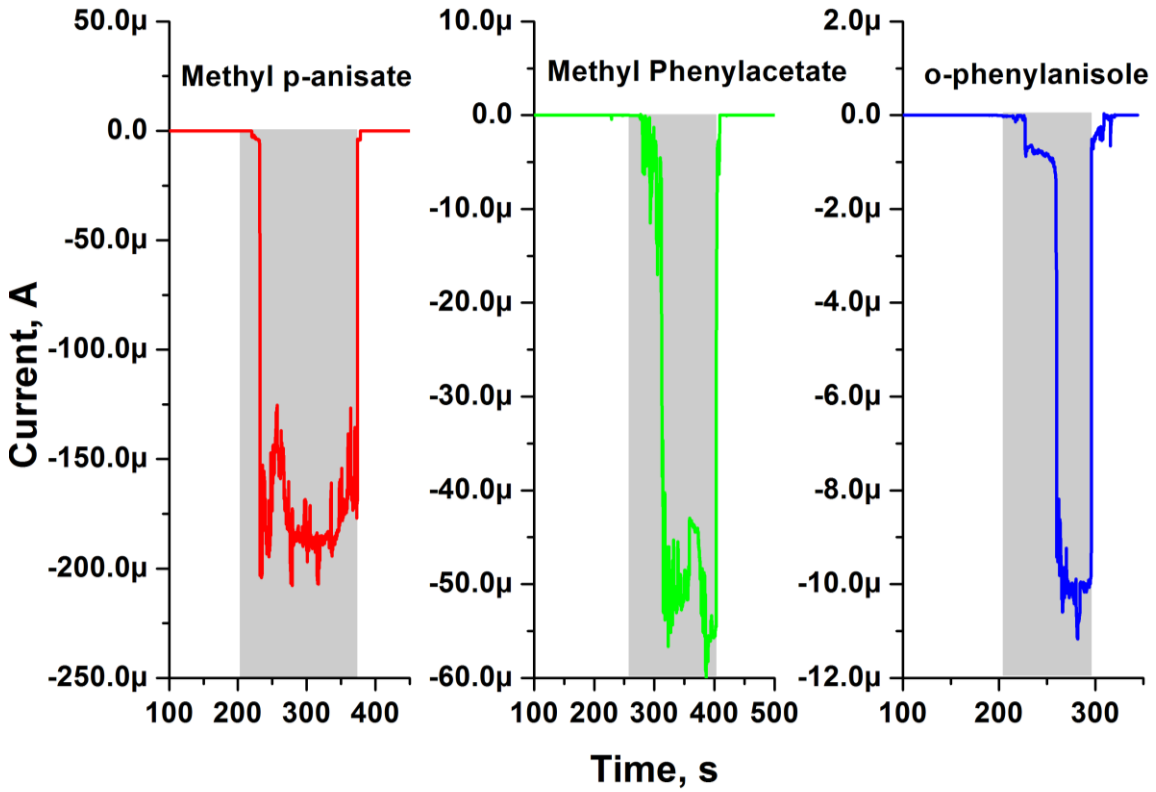

Figure 5.8: Amperometric sensor responses for iCo-TNA when exposed to 275 ~ 360 ppm of volatile organic biomarker vapors. The sensors were held at -0.8, -1.0, and -1.0 V for methyl p-anisate, methyl phenylacetate, and o-phenylanisole, respectively. The shaded regions of the plots show when the sensors were exposed to vapor.

current during exposure to methyl p-anisate, methyl phenylacetate, and o-phenylanisole vapors, respectively. The iCo-TNA was operated at optimized bias conditions of -0.5, -0.8, -1.0, and -1.0 V for methyl nicotinate, methyl p-anisate, methyl phenylacetate, and o-phenylanisole, respectively. The sensitivity of the sensor and high affinity of the individual biomarker vapor toward iCo-TNA is evident from the instantaneous change in current with the introduction of the vapor and rapid decrease in current when the vapors are cut off. The sensitivity of the iCo-TNA and Co-TNA sensors were investigated using methyl nicotinate (Figure 5.9). The sensor response was calculated by:

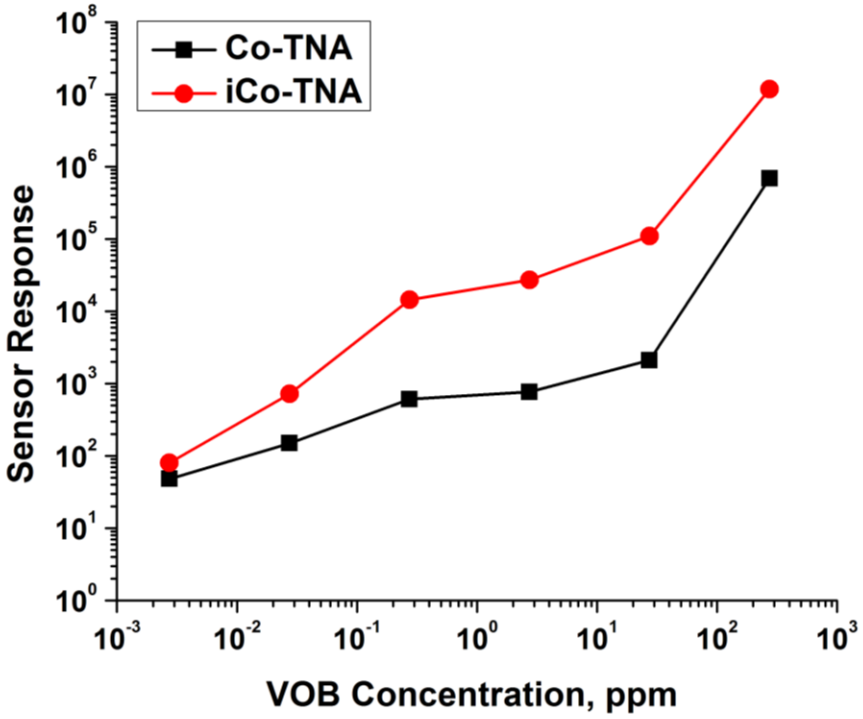

Figure 5.9. Plot showing the effect of concentration of methyl nicotinate vapor on variation of the sensor response for Co-TNA and iCo-TNA sensor.

SR = $(i_{max} - i_{Base})/i_{Base}$ where i_{max} is the maximum current and i_{Base} is the average background current, while the concentration on the x-axis is the estimated concentration in the sensor chamber. The selectivity of the iCo-TNA sensor was also examined by exposure to vapors of some common model compounds found in exhaled breath such as methanol, acetone, and benzene of fixed concentration (1000 ppm). It is important to note here that the concentration of these organics were much higher than that found in breath (which is usually hundreds of ppb). Results indicate that the sensor response for such VOCs is lower than that recorded for the lowest concentration of any biomarker solution. This is indicative of the fact that the iCo-TNA sensor is highly selective towards the TB biomarkers.

5.3.1 Sensor Response Mechanism

The sensing mechanism for Co-TNA in the presence of methyl nicotinate has been discussed in our previous work[23] and it is envisaged to follow a similar mechanism for iCo-TNA. In summary, the reducing vapors of the biomarker can cause partial reduction of the cobalt hydroxide to metallic cobalt, leading to a change in electron concentration. The chemisorbed oxygen on the sensor substrate dissociates to O^- and O^{2-} species by taking electrons from the TiO_2 lattice, leading to formation of oxygen vacancies and resulting in a decrease in the near surface conductivity. Upon exposing the sensor to the biomarker vapors, electrons are transferred from the biomarker to the Co^{2+}/Co redox couple, followed by conduction to the titania conduction band in a cascading fashion. Thus, the oxygen vacancies are filled with electrons causing an increase in conductivity, which is reflected by an increase in current.

Upon removal of the biomarker vapor, the sensor substrate goes back to its original state with oxygen vacancies reappearing on the TiO_2 nanotube surface. The diffusion of vapor molecules into the pores of the films increases the average permittivity, because the empty space is filled with vapor molecules. An increase of the permittivity should cause an increase of the conductivity because the activation energy and height of the potential well barriers are expected to decrease.

It is worth noting the morphological differences between iCo-TNA and Co-TNA in regards to the cobalt hydroxide deposits, as the loading of cobalt species between the two systems is approximately the same. For the Co-TNA sample, the cobalt precipitates are agglomerates of 100~450 nm, whereas the iCo-TNA sensor has cobalt precipitates around 22 nm in size. In a study by Choi *et al.*, [37] they investigated the electron collection

mechanism of TNA with varying layers of homogeneously distributed titania NPs on the TNA surface for dye-sensitized solar cell application. They found that photoinduced electrons generated within the few-nanometer sized titania NPs directly attached to the nanotube wall exhibited direct transport to the nanotube wall (also marked by an increase in cell power conversion efficiency). Increasing the titania nanoparticle layer resulted in random transport of photoinduced electrons with lower power conversion efficiency. A similar mechanism may be applied to our systems in terms of charge conduction and sensor response (Figure 5.10 - Scheme 1). Upon the donation of electrons from the VOB at the reaction sites, for the Co-TNA system, the electron diffusion path is randomized due to the many grain and particle/particle boundaries. In the iCo-TNA sensor system, the reaction sites are in direct contact with the parent titania and direct conduction between the two is envisaged.

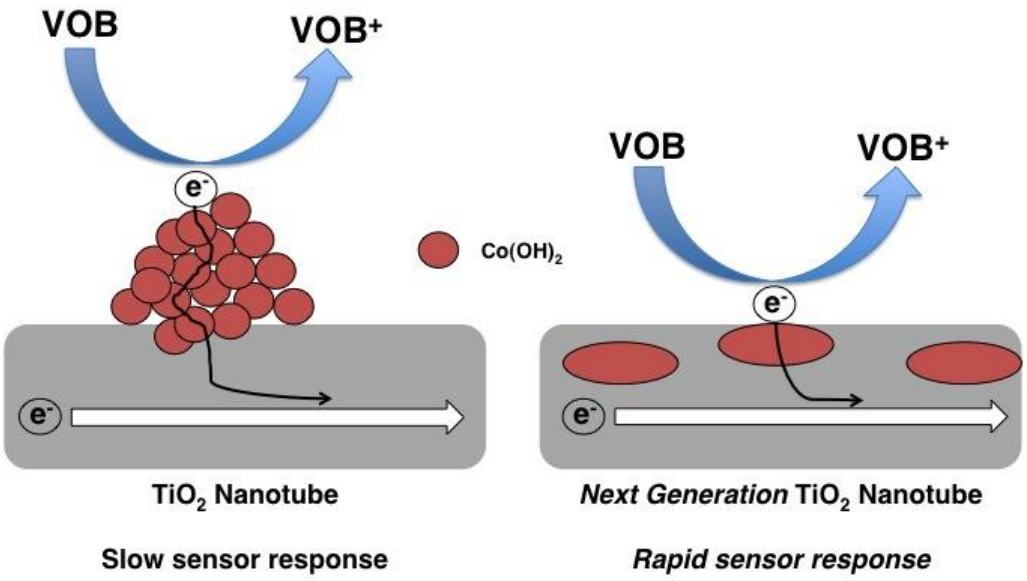

Figure 5.10 (Scheme 1): Comparative depiction of charge migration. Co-TNA electrons have a randomized path, while in iCo-TNA, the electrons have more direct conduction resulting in larger and faster sensor response.

Direct conduction from the reaction site to the parent titania will likely result in a larger sensor response/sensitivity (evident from Figure 5.9) and kinetics (response time). From Figure 5.7, the sensor response times were estimated to be ~26 s for iCo-TNA and ~36 s for Co-TNA, indicating faster reaction kinetics for iCo-TNA over Co-TNA.

5.3.2 *i*Co-TNA Formation Mechanism

It is envisaged that the generalized mechanism for nanotube formation still takes place[14]: (i) initial oxide barrier layer formation; (ii) pitting/nanopore formation; and (iii) steady-state nanotube growth. A recent work by Herbert *et al*. established a quantitative relationship of oxide dissolution and nanoporous film formation on Al and Ti.[38] The mechanism of cobalt functionalization is based on: (i) formation of anionic cobalt complexes in solution; (2) transport of these anionic species to the oxide/electrolyte interface by the applied electric field; (3) precipitation of cobalt hydroxide at the oxide/electrolyte interface. In aqueous solution and in the absence of complexing agents, soluble Co(II) salts form a stable hexaaqua cobalt(II) ion, $[Co(H_2O)_6]^{2-}$. In adding hydrofluoric acid, a ligand exchange occurs where six water molecules are replaced with four fluoride ions, forming an anionic cobalt fluoride species:

$$[Co(H_2O)_6]^{2-} + 4F^- = [CoF_4]^{2-} + 6H_2O \quad \ldots(5.1)$$

The $[CoF_4]^{2-}$ species are driven to the oxide/electrolyte interface by the applied bias. Once these species reach the interface, it is likely they precipitate at the oxide/electrolyte interface and are incorporated within the titania matrix.

$$[CoF_4]^{2-} + 2OH^- \rightarrow Co(OH)_2 + 4F^- \quad \ldots(5.2)$$

It has been shown experimentally that the outer titania oxide layer exposed to the electrolyte has excess hydroxyl ions compared to the inner oxide layer not exposed to the electrolyte.[39,40] The formation of titanium hydroxide can be summarized by the following reactions and subsequent dehydration of $Ti(OH)_x$ to TiO_2:[41,42]

$$Ti \rightarrow Ti^{4+} + 4e^- \quad \ldots(5.3)$$

$$H_2O \rightarrow H^+ + OH^- \quad \ldots(5.4)$$

$$OH^- \rightarrow H^+ + O^{2-} \quad \ldots(5.5)$$

$$Ti^{4+} + xOH^- \rightarrow Ti(OH)_x \quad \ldots(5.6)$$

$$Ti^{4+} + 2O^{2-} \rightarrow TiO_2 \quad \ldots(5.7)$$

$$Ti(OH)_x \rightarrow TiO_2 + (x-2)H_2O \quad \ldots(5.8)$$

Reactions 3-7 represent the possible field-assisted oxidation processes, as the applied electric field controls the rate of ion migration within the metal/oxide interface. In reaction 8, titanium hydroxide is dehydrated to titanium dioxide. This results in a cell volume decrease and is one proposed mechanism for tube separation (41). To date, despite recently improved models describing the formation of porous anodic films, current models do not account for point defects or incorporation of electrolyte species.[43]

It is evident from the electron microscopy analysis (Figures 5.1-5.3) that the wall thickness of the nanotubes is greater for iCo-TNA compared to TNA alone. The increase in wall thickness is attributed to the formation of cobalt hydroxide. Generally, thicker walled TNA are achieved with higher water content electrolytes and are a result of higher OH^- concentration. This accelerates the formation of titanium hydroxide at the cell walls,

and enhances the rates of volume shrinkage during condensation. This has also been further supported experimentally by the addition of ammonium hydroxide to the anodization electrolyte.[41] However, the reason for narrower diameter and shorter oxide length for iCo-TNA compared to TNA is not well understood yet. As mentioned previously, the increase in current density during anodization may be due to the formation of cobalt hydroxide and does not contribute to titania oxide growth, hence the narrower diameter and shorter oxide length compared to TNA.

5.4 Summary

The use of cobalt functionalized next-generation anodized titania nanotube arrays for the electrochemical detection of volatile organic compound vapors associated with the disease tuberculosis is presented. A mechanism for the *in situ* functionalization of cobalt hydroxide is also discussed. Under amperometeric operation and low bias (-0.5 to -1.0 V), the sensor was capable of detecting methyl phenylacetate, methyl p-anisate, methyl nicotinate, and o-phenylanisole vapors with a concentration of 275 ~ 360 ppm. The sensor responses to background and other volatile organics commonly found in exhaled breath were several orders of magnitude lower compared to biomarker responses. When compared to titania nanotubes functionalized with cobalt hydroxide by an incipient wetness method, the *in situ* functionalization method demonstrates greater sensor response, kinetics, and sensitivity attributed to improved charge transport. This approach for detection of volatile organic biomarkers creates a simple, robust, inexpensive, and noninvasive diagnostic platform that can potentially be tailored to detect any disease or physical state of health that exhibits volatile organic biomarkers in exhaled breath with

detectable concentrations.

5.5 References

1. H. Haick, Y. Y. Broza, P. Mochalski, V. Ruzsanyi, and A. Amann, *Chem. Soc. Rev.*, **43**, 1423 (2014).

2. M. Hakim, Y. Y. Broza, O. Barash, N. Peled, M. Phillips, A. Amann, and H. Haick, *Chem. Rev.*, **112**, 5949 (2012).

3. W. Miekisch, J. K. Schubert, and G. F. E. Noeldge-Schomburg, *Clinica Chimica Acta*, **347**, 25 (2004).

4. B. Buszewski, M. Kesy, T. Ligor, and A. Amann, *Biom. Chromatogr.*, **21**, 553 (2007).

5. F. Buljubasic and G. Buchbauer, *Flavour Frag. J.*, **30**, 5 (2015).

6. World Health Organization, *Global Tuberculosis Report 2014*, (2014).

7. M. Phillips, R. N. Cataneo, R. Condos, G. A. Ring Erickson, J. Greenberg, V. La Bombardi, M. I. Munawar, and O. Tietje, *Tuberculosis*, **87**, 44 (2007).

8. M. Syhre and S. T. Chambers, *Tuberculosis*, **88**, 317 (2008).

9. M. Syhre, L. Manning, S. Phuanukoonnon, P. Harino, and S. T. Chambers, *Tuberculosis*, **89**, 263 (2009).

10. D. M. Suckling and R. L. Sagar, *Tuberculosis*, **91**, 327 (2011).

11. G. F. Mgode, B. J. Weetjens, C. Cox, M. Jubitana, R. S. Machang'u, D. Lazar, J. Weiner, J.-P. Van Geertruyden, and S. H. E. Kaufmann, *Tuberculosis*, **92**, 182 (2012).

12. B. Weetjens, G. Mgode, R. Machang'u, R. Kazwala, G. Mfinanga, F. Lwilla, C. Cox, M. Jubitana, H. Kanyagha, and R. Mtandu, *Int. J. Tuberc. Lung Dis.*, **13**, 737 (2009).

13. K. Lee, A. Mazare, and P. Schmuki, *Chem. Rev.*, **114**, 9385 (2014).

14. Y. R. Smith, R. S. Ray, K. Carlson, B. Sarma, and M. Misra, *Materials*, **6**, 2892 (2013).

15. H. F. Lu, F. Li, G. Liu, Z.-G. Chen, D.-W. Wang, H.-T. Fang, G. Q. Lu, Z. H. Jiang, and H.-M. Cheng, *Nanotechnology*, **19**, 405504 (2008).

16. Y. Kwon, H. Kim, S. Lee, I.-J. Chin, T.-Y. Seong, W. I. Lee, and C. Lee, *Sens. Actuator B-Chem.*, **173**, 441 (2012).

17. P. Perillo and D. Rodriguez, *Sens. Actuator. B-Chem.*, **171**, 639 (2012).

18. N. Kilinc, E. Sennik, and Z. Z. Ozturk, *Thin Solid Films*, **520**, 953 (2011).

19. P. Kar, A. Pandey, J. J. Greer, and K. Shankar, *Lab Chip*, **12**, 821 (2012).

20. A. Hazra, B. Bhowmik, K. Dutta, P. P. Chattopadhyay, and P. Bhattacharyya, *ACS Appl. Mater. Interfaces*, **7**, 9336 (2015).

21. S. Banerjee, S. K. Mohapatra, M. Misra, and I. B. Mishra, *Nanotechnology*, **20**, 075502 (2009).

22. H. Jayamohan, Y. R. Smith, B. K. Gale, M. Misra, and S. K. Mohanty, *Proc. Sensors 2013 (Baltimore, MD, 3-6 November 2013) IEEE*, 1 (2013).

23. D. Bhattacharyya, Y. R. Smith, M. Misra, and S. K. Mohanty, *Mater. Res. Express*, **2**, 025002 (2015).

24. Y. Kim, J. Young, D. C. Robinson, G. Jones, M. Misra, and S. K. Mohanty, in *Physics and Technology of Sensors (ISPTS), 2015 2nd International Symposium*, p. 317 (2015).

25. R. S. Ray, B. Sarma, S. Mohanty, and M. Misra, *Talanta*, **118**, 304 (2014).

26. R. S. Ray, B. Sarma, S. Mohanty, K. Prisbrey, and M. Misra, *Mater. Chem. Phys.*, **161**, 1 (2015).

27. Y. R. Smith, B. Sarma, S. K. Mohanty, and M. Misra, *Electrochem. Commun.*, **19**, 131 (2012).

28. R. Hahn, M. Stark, M. S. Killian, and P. Schmuki, *Catal. Sci. Technol.*, **3**, 1765 (2013).

29. M. Misra and K. S. Raja, in *On Solar Hydrogen & Nanotechnology*, L. Vayssieres Editor, John Wiley & Sons, Chichester, UK. (2010).

30. S. K. Mohapatra, N. Kondamudi, S. Banerjee, and M. Misra, *Langmuir*, **24**, 11276 (2008).

31. S. K. Mohapatra, M. Misra, V. K. Mahajan, and K. S. Raja, *J. Phys. Chem. C*, **111**, 8677 (2007).

32. X. Liu, R. Ma, Y. Bando, and T. Sasaki, *Adv. Func. Mater.*, **24**, 4292 (2014).

33. J. Yang, H. Liu, W. N. Martens, and R. L. Frost, *J. Phys. Chem. C*, **114**, 111 (2010).

34. R. S. Jayashree and P. V. Kamath, *J. Mater. Chem.*, **9**, 961 (1999).

35. M. C. Morris, H. F. McMurdie, E. H. Evans, B. Paretzkin, J. H. d. Groot, B. S. Weeks, R. J. Newberry, C. R. Hubbard, and S. J. Carmel, *Nat. Bur. Stand. (U. S.), Monogr. 25, Sec. 15*, 204 (1978).

36. M. C. Biesinger, B. P. Payne, A. P. Grosvenor, L. W. Lau, A. R. Gerson, and R. S. C. Smart, *Appl. Surf. Sci.*, **257**, 2717 (2011).

37. J. Choi, G. Kang, and T. Park, *Chem. Mater.*, **27**, 1359 (2015).

38. K. R. Hebert, S. P. Albu, I. Paramasivam, and P. Schmuki, *Nat. Mater.*, **11**, 162 (2012).

39. D. Regonini, A. Jaroenworaluck, R. Stevens, and C. R. Bowen, *Surf. Interface Anal.*, **42**, 139 (2010).

40. L. V. Taveira, J. M. Macák, H. Tsuchiya, L. F. P. Dick, and P. Schmuki, *J. Electrochem. Soc.*, **152**, B405 (2005).

41. B. Chen, J. Hou, and K. Lu, *Langmuir*, **29**, 5911 (2013).

42. D. Regonini, C. Bowen, A. Jaroenworaluck, and R. Stevens, *Mater. Sci. Eng. R*, **74**, 377 (2013).

43. K. R. Hebert, S. P. Albu, I. Paramasivam, and P. Schmuki, *Nat Mater*, **11**, 162 (2012).

CHAPTER 6

GOLD SENSITIZED TiO_2 NANOTUBES-BASED PLASMONIC SENSORS FOR AMPEROMETRIC DETECTION OF VOLATILE BIOMARKERS

6.1 Introduction

For any gas-based sensor, rapid sensing coupled with enhanced response sensitivity is desirable. Typically 2D metal oxides such as WO_3, MoO_2, ZnO, and TiO_2 have been used for fabrication of chemical sensors owing to their ability to chemisorb organic compounds.[1] In addition, these metal oxide semiconductors possess large band gap and relatively lower dielectric constants, resulting in enhanced quantum characteristics and subsequent better chemical sensing properties. 1D metal oxide nanostructures such as TiO_2 nanotubes act as preferential electron pathways resulting in higher charge collection efficiency, compared to disordered TiO_2 nanoparticles that often suffer higher electron recombination problems. Owing to the unique electrical, optical, and thermal properties of titania nanotubes, it has found use in several applications ranging from solar water splitting for hydrogen generation, supercapacitors, sensors, solar cells, to microfluidic photocatalytic degradation of organic and biological water contaminants.[2] Nanoscopic metallic particles coupled with 1D nanostructures demonstrate exciting catalytic, light scattering, and surface plasmon resonance (SPR)

behavior. Plasmonic nanoparticles such as Ag, Au, etc. in conjunction with titania nanotubes enable the possibility of SPR enhancement and their better usage efficiency over a broader wavelength spectrum.[3] In TNA-based ordered photonic crystal with periodic dielectric structure, slow photons (photons propagating with a reduced group velocity) are observed at a frequency close to the photonic stop band edge.[3] Hence, the coupling of the slow photon region with the SPR region for efficient light harvesting in the UV-visible region can be utilized for enhanced chemical vapor sensing.

With obvious advantages of noble metal nanoparticles such as chemical inertness towards photo-oxidation leading to high stability and SPR properties under visible light illumination, gold nanostructures, either by themselves or immobilized on a sensor substrate, have been reportedly used for sensing applications. Amine terminated gold nanodendrites sensitized with carboxyl terminated quantum dots (AuND-QDs) assembly has been successfully employed for sensing of highly explosive and environmentally detrimental trinitrotoluene (TNT).[4] Arrays of nanoscopic gold tubes within the perfectly cylindrical pores of polycarbonate track-etched membranes (PTM) have been obtained by electroless deposition in a sulfite-based solution containing formaldehyde as the reducing agent.[5] The gold-plated nanoporous PTM functionalized with glucose oxidase enzyme was shown to be useful as a highly sensitive glucose biosensor. In other publications, gold nanotube array electrode demonstrated significant electrooxidative properties in enzyme free amperometric detection of glucose.[6,7] Similarly, arrays of nanoscopic gold tubes synthesized by electroless plating on PTM have been used for amperometric detection of hydrogen peroxide.[8] Guo *et al*. had also synthesized gold nanowire assembling architectures for electrochemical sensing of H_2O_2.[9] One-dimensional Au/α-

Fe_2O_3 nanostructures have been examined as a potential sensor for acetone detection.[10] Kaur and Pal[11,12] demonstrated photocatalytic oxidation of salicylic acid using titania decorated with Au nanoparticles of various sizes and shapes. Hutchings had emphasized on the catalytic properties of gold and mentioned that Au can be a key component of homogeneous and heterogeneous catalysts.[13] He also went on to describe the role of Au in catalytic oxidation of CO, alcohols, and glyecrols. Further, evidence of active oxidative species on Au-TiO2 catalysts has been demonstrated.[14] Au-TiO2 nanotubes composite electrodes have shown efficient immobilization and electrocatalysis of protein macromolecules.[15] Gold nanoparticle modified screen printed carbon electrodes have been used as a highly sensitive sensor for electrochemical detection of methyl salicylate.[16] Hollow Au-Pt and Au-Pd core-shell nanoparticles have demonstrated prominent electrocatalytic properties for ethanol oxidation.[17] Various gold nanostructures or gold supported metal oxide nanomaterials demonstrate interesting properties such as unusual magnetism, optical plasmon peak shift, and enhanced catalytic effect, which can be utilized for electrochemical sensing. Au-ZnO plasmonic nanostructures have exhibited localized SPR, leading to strong field enhancement and resulting in increased room temperature NO sensing and UV photodetection.[18] Similar SPR enhanced alcohol sensor has been fabricated using Ag-WO3 core shell nanostructures.[1]

It is evident that there is limited available literature describing the study of plasmonic behavior of Au-TiO_2 nanotubes in detection of disease biomarkers. Synergistic modifications of electronic and photocatalytic properties of TiO_2 nanotubes can be achieved by implantation of Au atoms.[19] This work explores the VOB sensing applications of visible light driven gold sensitized titania nanotubes. The titania

nanotubes present a robust, self-aligned, and highly ordered substrate conducive for vectorial charge transfer,[20] onto which plasmonic gold nanoclusters are electrolessly deposited for sensing of TB VOBs. The enhancement of photo-induced VOB sensing at room temperature and possible mechanisms have been presented.

6.2 Experimental

Titania nanotubes arrays (TNA) were synthesized by electrochemical anodization of Ti coupons (1.5cm x 1.5cm) in a well-stirred fluorinated ethylene glycol solution (0.5 wt% NH_4F + 3 wt% H_2O) at 30V for 1 hour with platinum counter electrode. The anodized coupons were annealed in a tube furnace at 500 ˚C (ramp up at 2.8 ˚C/min from 25 ˚C) for 2 hours in oxygen atmosphere.

Gold functionalization was achieved through room temperature electroless deposition in a gold thiosulfate – ascorbic acid bath. Electroless plating permits deposition of metals from solutions onto surfaces without the need to apply an external electrical potential. Although $[Au(CN)_2]^-$ has a relatively large stability constant of ~10^{39}, its use is undesirable due to known toxicity, possible degradation of photo-resistive material caused by high alkalinity, and lowered plating rate resulting from accumulation of cyanide ions.[21,22] In applications requiring gold deposition on a substrate with a circuit pattern delineated with a conventional positive photoresist, cyanide ions are known to attack the interface between the photoresist and the substrate, lifting the photoresist and causing extraneous gold deposition under the photoresist. The high alkalinity of the cyanide-based baths is also incompatible with the positive photoresist. For these reasons, noncyanide baths are currently in demand. Gold salts other than cyanide complexes used

for formulating electroless gold baths include chloroaurate(III), Au(I)–sulfite complex, Au(I)–thiosulfate complex, and Au(I)–thiomalate. Researchers have developed environmentally friendly electroless plating solution of chloroauric acid ($HAuCl_4$) and hydrogen peroxide (H_2O_2) for depositing gold film onto (3-aminopropyl)-trimethoxysilane (APTMS) coated glass surface, where APTMS acts as an adhesive reagent to attached the gold nanoparticles.[23] The Au(I)–thiosulfate complex, $[Au(S_2O_3)_2]^{3-}$ has a stability of $\sim 10^{28}$ and ranks just next to the gold cyanide complex whereas the stability constant of the sulfite complex, $[Au(SO_3)_2]^{3-}$ is 10^{10}.[22] It is thus natural that the use of thiosulfate complex has been proposed for formulating electrolytic gold plating baths. Previously, researchers have made an extensive cyclic voltammetric study of the cathodic reduction of $[Au(S_2O_3)_2]^{3-}$ and the anodic oxidation of various reducing agents.[21] They showed that among a number of reducing agents investigated, ascorbic acid is the only compound that is electro-catalytically oxidized at a reasonable rate within the potential range of the reduction of $[Au(S_2O_3)_2]^{3-}$ at a pH between 6.4 and 9.2 and at room temperature. The electroless gold plating bath comprised 0.03 M $Na_3[Au(S_2O_3)_2]$, 0.05 M L-ascorbic acid, and 0.4 M citric acid with the pH adjusted to 6.4 using 1 N NaOH solution. Functionalization was achieved through the incipient wetness impregnation method where the TNA substrates were immersed in the bath for 1.5 hours and subsequently dried in a vacuum oven at 110˚C.

Morphological examination of Au-TNA was performed using a Hitachi S-4800 field emission SEM (at 3 kV and 15 μA) equipped with an Oxford (X-Max) EDAX detector. The oxidation states of Au and Ti were determined through XPS (Kratos Axis Ultra DLD model) using a monochromatic Al Kα excitation source under 10^{-10} Torr

vacuum. CasaXPS software was used for peak fitting while charging effects were corrected using the C1s line at 284.6 eV as an internal reference. X-ray diffraction (XRD) was carried out using a Rigaku Miniflex XRD (CuKa = 1.54059 Å) from 2θ = 20 to 80˚ with a step size of 0.015 degrees and dwell time of 1 degree min^{-1}. The diffraction patterns were analyzed using Rigaku PDXL2 analysis software and indexed with standard JCPDS cards. An UV-Vis-NIR spectrophotometer (Shimadzu UV-3600, Kyoto, Japan) was used to measure the absorbance spectra of TNA and Au-TNA using an external 3-detector system with 32 nm slit width.

The electrochemical detection of the four TB biomarker (10 mM) vapors viz. methyl nicotinate, methyl p-anisate, methyl phenylacetate, and o-phneylanisole were carried out in a custom-built sensing chamber with electrical contacts to the sensor element made using two probes connected with the chamber. Mass flow controllers (MFCs) were used to control the flow rates of carrier (N_2 @ 200sccm) and test gases. A potentiostatic (I–t) run was carried out to test the sensor response using a two-electrode potentiostat system (Gamry Reference 600). SPR assisted plasmonic sensing response was measured using a broad band LED (light emitting diode) light source and was compared to measurements obtained in the dark.

6.3 Results and Discussion

6.3.1 Characterization

SEM micrographs illustrated in Figure 6.1 reveal ordered arrays of self-aligned vertically oriented titania nanotubes. Each nanotube has an outer diameter of ~60 nm with a consistent 12 nm wall thickness, while the length of the nanotubes ~1.5 μm. The

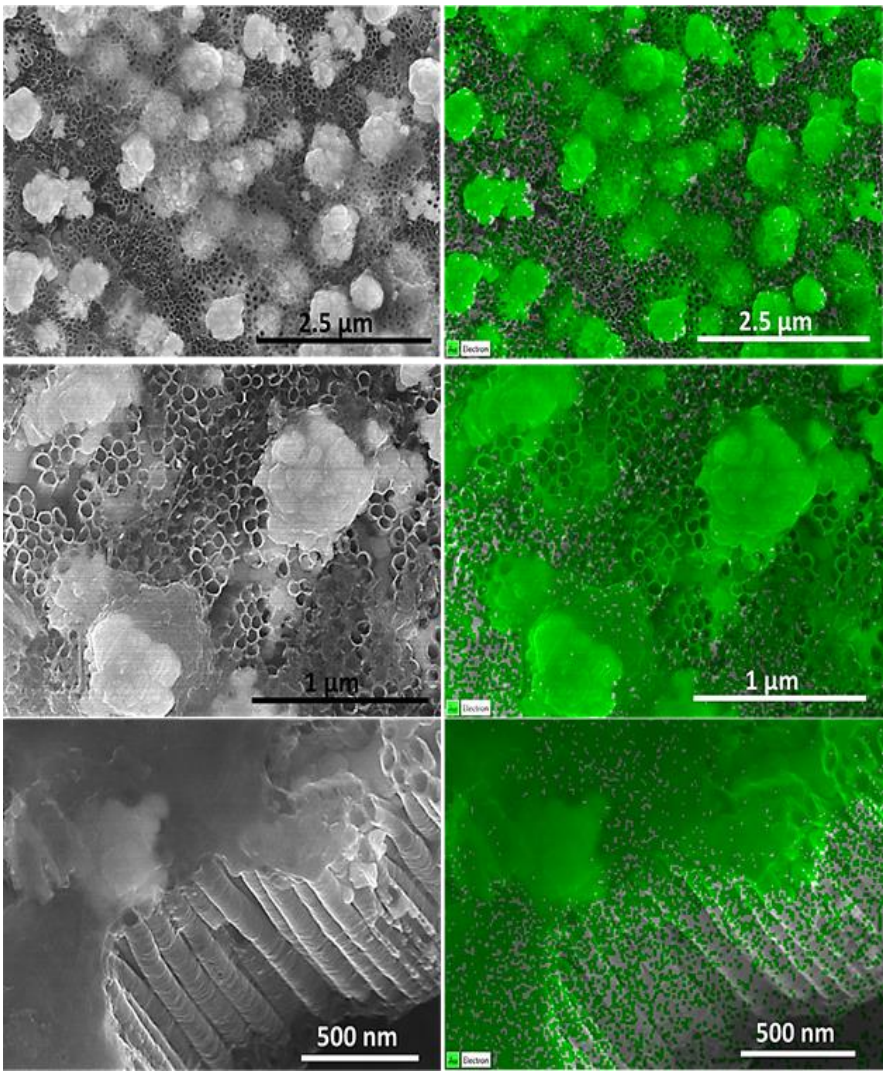

Figure 6.1. SEM-EDS micrographs showing the gold nanoparticles and the larger gold nanoclusters on the mouth and side walls of the nanotubes.

size of Au nanoparticles ranged from 20-50 nm, whereas the Au nanoclusters were 200–450 nm in size. After the Au deposition treatment, the diameter of the tubes remains about the same. However, on the Au-TiO_2 surface, the tubes are covered with Au nanoparticles of different size, aggregating at the pipe orifices. EDS analysis of Au-TNA (Figure 6.2) samples has confirmed the presence of gold on the nanotubes. XPS core level spectra revealed that gold exists in its native state as depicted from the distinct $4f_{5/2}$

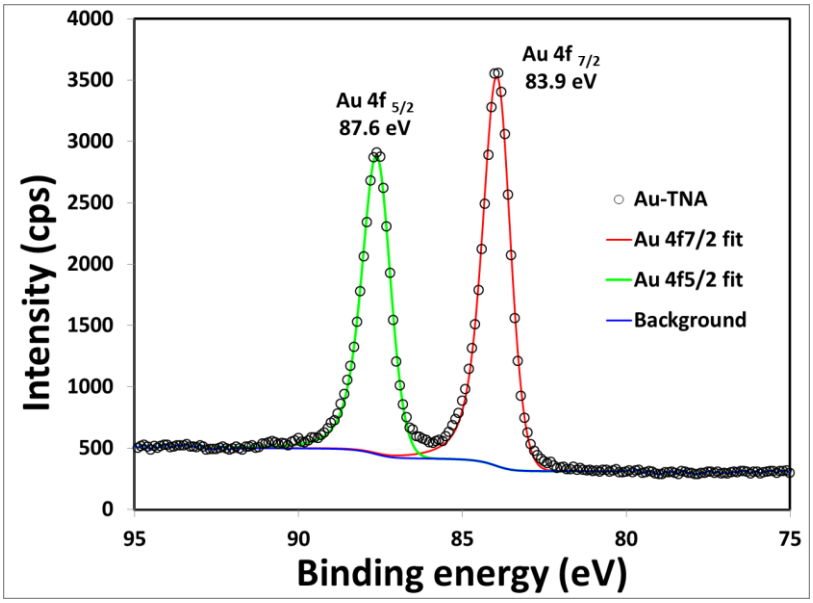

Figure 6.2. XPS core level spectra gold reveals the Au4f5/2 and Au4f7/2 peaks at 87.6 and 83.9 eV, respectively, thereby further confirming the presence of gold in its native oxidation state on the TNA.

and $4f_{7/2}$ peaks at 87.6 and 83.9 eV, respectively, with a separation of 3.7 eV. The Au 4f doublet is caused by spin-orbit coupling arising out of two possible spin states of electrons in p, d, and f orbitals.

Figure 6.3 gives the XRD pattern of the Au-TNA prepared by the deposition-precipitation treatment. It is observed that both the anatase and rutile phases of TiO_2 are preserved in Au-TNA as the annealing treatment was carried out in oxygen atmosphere.[24] In the diffraction pattern, the prominent peaks labelled A at 25.4°, 48°, 62.7°, and 70.9° indicate the presence of anatase crystal phase in Au-TNA and conforms to the anatase peak position in intrinsic TNA, according to previous structural characterizations.[25] Under these preparation conditions, although the TiO_2 nanotubes majorly adopt an anatase crystal structure, some rutile structure is also observed as expected. The labels T and Au represent the reflections from the titanium substrate and different Au

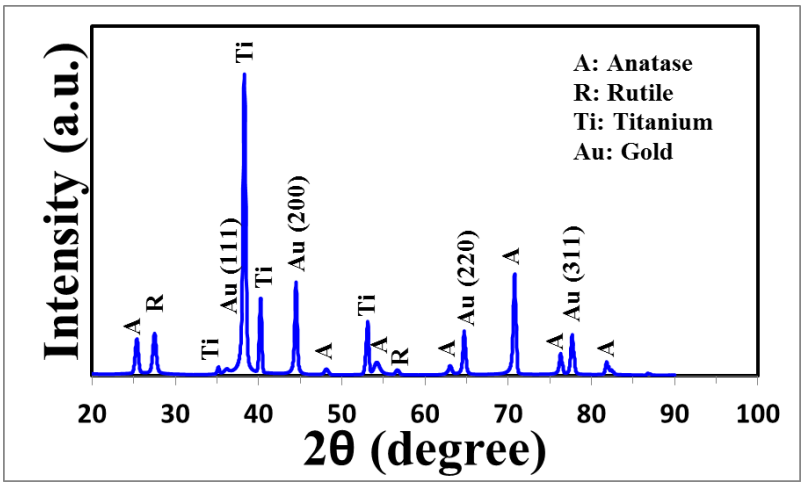

Figure 6.3. XRD pattern of Au-TNA showing the prominent anatase (A) and Au crystal phases along with some rutile (R) phases and Ti peaks from the underlying substrate.

crystallographic planes. It is clearly seen from Figure 6.3 that characteristic gold peaks come into existence in the diffraction pattern observed at 38.2° (111), 44.2° (200), 64.7° (220), and 77.8° (311), respectively. The main Au (111) characteristic peak at 38.2°, which overlaps with the titanium peak at roughly the same position, suggests that small gold nanoparticles of the order ~15 – 30 nm, calculated on the basis of the Scherer formula, are coated onto the anodized TiO2 nanotubes.[24] Other Au peaks pertaining to 200, 220, and 311 planes further confirm the presence of Au nanoparticles of various sizes.

6.3.2 Optical Properties

Diffuse reflectance data from UV-Vis spectroscopy were utilized for band gap energy measurements of Au-TNA and TNA (Figure 6.4). For TNA, a considerable increase in absorbance begins at 390 nm and a shoulder centered at 334 nm appears,

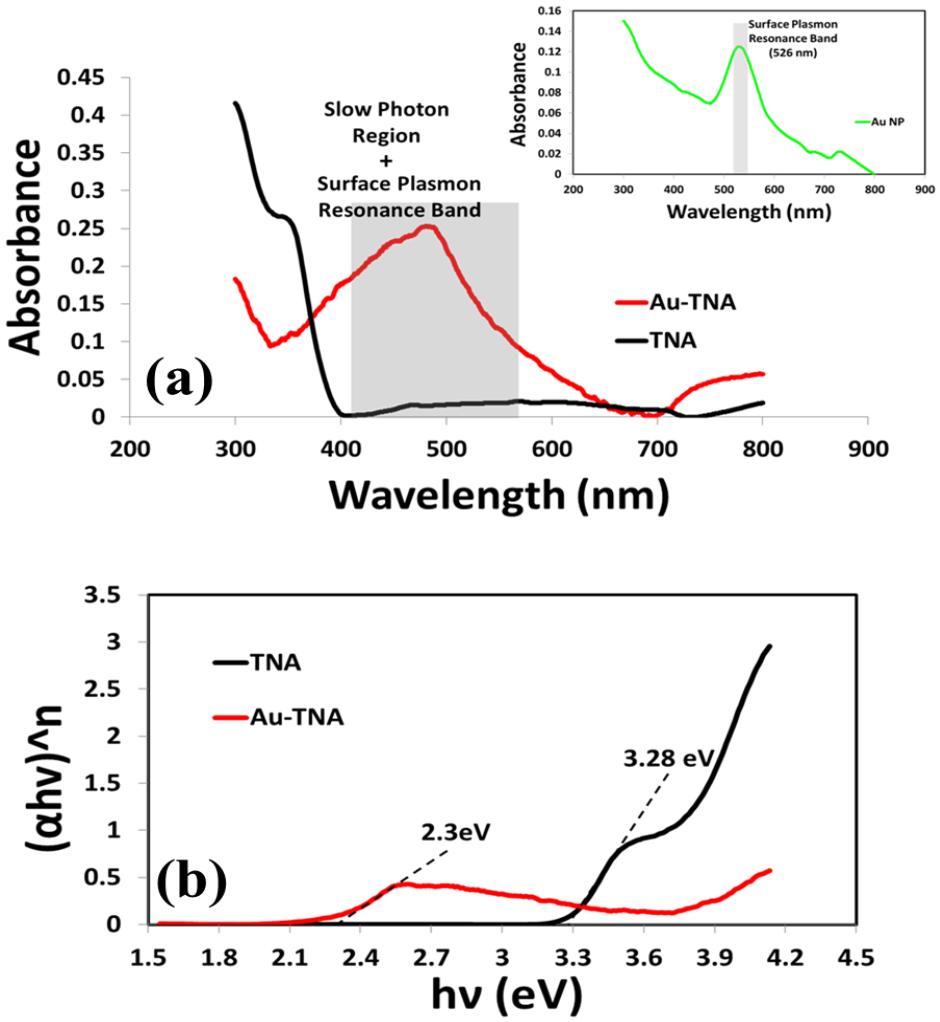

Figure 6.4. Optical properties as revealed from (a) Diffuse reflectance absorbance spectra for TNA and Au-TNA. Inset: absorbance spectra of Au nanoparticles showing the surface plasmon resonance band at 526 nm. (b) Tauc plot for indirect bandgap transition, showing a redshift in bandgap for Au-TNA compared to bare TNA.

corresponding to the band edge absorption. The wavelength, at which the increase in absorbance starts in the annealed samples, indicates the formation of band tail due to incorporation of impurity states. For Au-TNA, the increase in absorbance begins at 690 nm and a peak appearing at 476 nm can be attributed to the coupling of the slow photon effect and LSPR absorption. Au nanoparticles show a strong absorbance peak at ~536nm which is the characteristic LSPR band. In the Tauc plot, the intersection between the

linear fit and the photon energy axis gives the value of the band gap. Figure 6.4 illustrates that TNA has a band gap of ~3.28eV which limits its application to deep UV regions (E_g=3.28eV ≈ λ=380nm), whereas Au-TNA has much lower band gap of 2.3eV which makes it suitable for use in the visible region (E_g=2.3eV ≈ λ=540nm).

The optical absorbance (see Figure 6.4) of the Au nanoparticles coated TiO2 nanotubes increased sharply at a wavelength ~470 nm and this corresponds to the strong intrinsic light absorption of rutile and anatase phase TiO_2 (Eg ~ 3 – 3.2 eV). Systematic examination of the absorbance plots indicates an interaction between surface plasmon of Au nanocrystals and TiO_2 excitons that originates from the exciton-dipole modification, mainly due to surface plasmon local electromagnetic modes.[3,26] Dipole–dipole interaction is not very significant for smaller size Au crystal but can be prominent for larger size Au nanoclusters, as evidenced in SEM images. The broad absorption region between 400–600 nm can be categorized as the 'slow photon region'.[27] In such a substrate, slow photons are observed at a frequency close to the photonic stop band edge. This is due to the fact that at the red edge of the photonic stop band, slow propagation of the light photons takes place with a reduced group velocity owing to the high refractive index of titania. It has been demonstrated that photon density is higher in such a region, when measured in high refractive index medium compared to in air.[27] It is important to note that TiO_2 has higher refractive index ~2.42; hence, the slow photon region and the SPR region (SPR absorption band of freely dispersed gold nanoparticles was found to be ~526 nm, and corroborates well with reported literature values) will be merged (overlapped) due to strong interaction between SPR effect of Au particles and localized photons. This can be attributed to the fact that photon density in the slow photon region is larger in the

high refractive index part (TiO_2 nanotubes) compared to air voids. Such a 'slow photon' effect is advantageous to improve photoelectrochemical (PEC) performance and quantum efficiency, if plasmonic PEC activity is coupled with slow photon effect in SPR region.

The light propagation through TiO_2 nanorods and nanotubes have been previously investigated using FDTD simulations.[28] Due to high contrast between the refractive index and permittivity of TiO_2 and its surrounding medium, such nanotubular architecture can be categorized as a 'potential photonic material'. Such a combination also facilitates the utilization of surface resonances due to interaction of light with the nanotubular morphology. In the work presented here, the titania nanotube wall thickness was consistent between 10-14 nm and thus can be classified as thin walls. Such thin walls act as a subwavelength type Rayleigh scattering medium wherein the wavelength of light is much larger than the wall thickness.[28] Thick walled nanotubes (>20 nm) with a distinct hollow annulus can accommodate guided modes of plane polarized electromagnetic radiation through the walls. On the contrary, for sub-10 nm thin walled titania nanotubes, accommodation of these guided modes are difficult and thus exhibit weaker resonance. Our nanotubes being in the thickness range 10-14 nm exhibit moderate resonance behavior. The resonance behavior can be enhanced by doping plasmonic materials on TiO_2 such as gold nanoparticles, as has been observed. It is also interesting to note though that when thin walled TNA is exposed to plane wave light illumination, the resultant optical field comprises waveguides from the array which are characterized by a combination of slow and fast phase velocity modes, arising from the high permittivity nanotube wall medium and low permittivity air medium present inside the hollow nanotubes, respectively.[28] Although the fast waveguide modes are predominant and

strong, the slow waveguide mode contributes to the slow photon effect, as illustrated through our results. For FDTD simulations, tetrahedral shaped grids of size ~λ/10 were used. For these simulations, a perfectly matched layer boundary condition was applied, in order to avoid reflections that can interfere with actual surface field guided by the nanotube. A waveguide port at a distance of ~200 nm from the top was utilized that acts as a plane wave source. The FDTD simulation of the specular absorbance as a function of wavelength for straight titania nanotubes is shown in Figure 6.5 for incident light polarized along the y-direction.

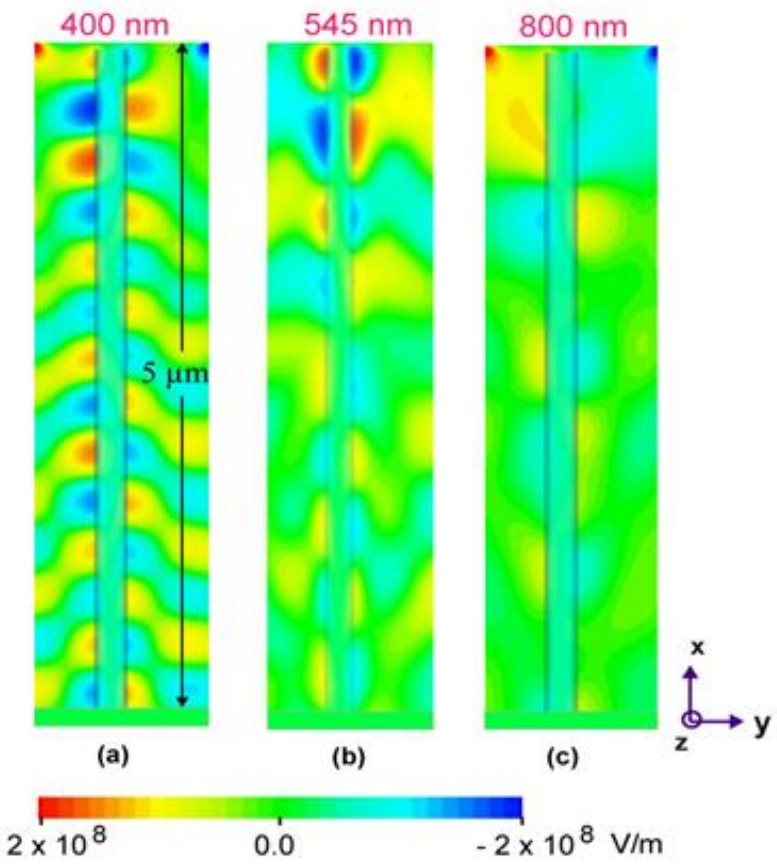

Figure 6.5. FDTD simulated electric field profile in the xy plane of the straight TiO_2 nanotubes at three different wavelengths of incident light (a) λ = 400 nm (b) λ = 545 nm and, (c) λ = 800 nm. The light on the nanotubes is incidence from the top. The inner and outer diameter of the nanotubes is 80 nm and 90 nm, respectively.

Although the titania nanotubes were grown on Ti substrate, it is presumed that the predominant light adsorption is due to the titania nanotubular array only and thus, the simulated absorbance of the nanotube, ignoring the Ti substrate, is presented. The electric field distribution around the nanotubes provides information about the light absorption by the semiconductor material and is determined by the y-component or the dominant component of the electric field. This y-component is oriented parallel to the polarization vector of the incident wave. The FDTD simulations reveal that as expected, the absorbance in the titania nanotube layer is maximum at λ = 400 nm. For wavelengths longer than the electronic bandgap of TiO_2, the absorbance decreases and is very low or negligible at λ = 800 nm. .

6.3.3 SPR Assisted Amperometric Sensing of VOBs

Upon introduction of the biomarker vapors, amperometric detection of the four biomarkers in dark using Au-TNA yielded current in the nA range whereas the maximum achievable current at steady state was usually of the order of ~μA in the presence of visible light illumination (Figure 6.6). Methyl p-anisate exhibits the maximum sensor response (450 μA) whilst o-phenylanisole the minimum (33 μA). The trend remains the same under dark conditions too, although the sensor response was almost 5 orders of magnitude lower than under visible light irradiation. The broad photoresponse of Au-TNA under the visible light is well in agreement with the absorption spectrum of Au-TNA sample, which exhibits a coupling of the slow photon region and SPR. Also, TNA did not exhibit significant current response to the VOBs upon visible illumination. This is expected as the band gap of TNA is much higher than the incident energy.

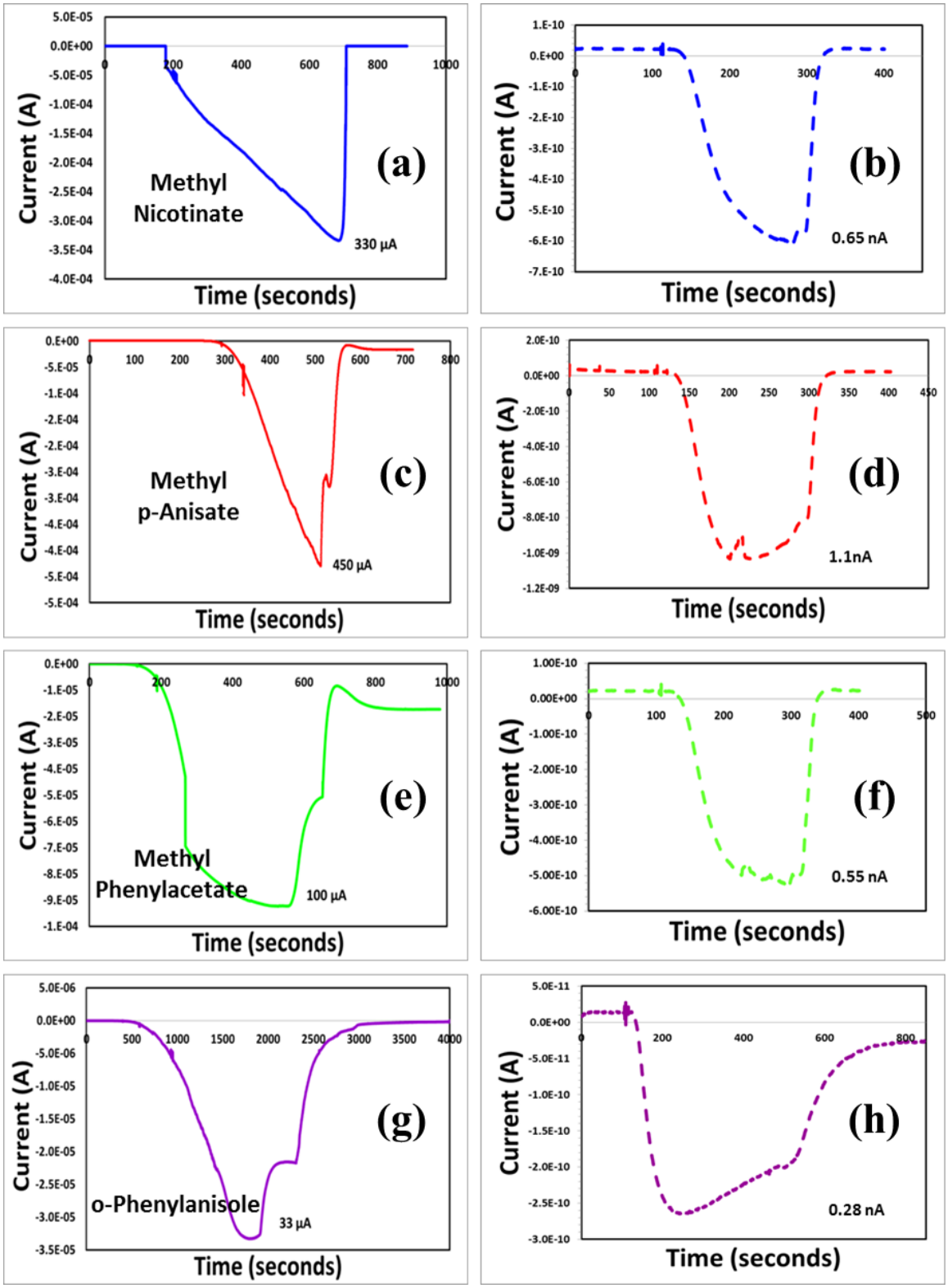

Figure 6.6. SPR assisted plasmonic sensing response (a,c,e,g) measured under visible light illumination and compared to measurements obtained in dark (b,d,f,h) for the four TB biomarkers.

Previously, highly sensitive surface plasmon resonance detection of white spot syndrome virus has been demonstrated using electroless-plated gold films.[29] Kobayashi and Ishii had fabricated sensors of electrolessly deposited gold nanoparticles on glass plates for measuring the dielectric constant of solutions.[30] Additionally, another group applied the Au-doped TiO_2 nanotube array sensor to detect SF_6 decomposed gaseous components.[24] They had mentioned that the charge transfer is important during the processes occurring at the gases/oxide interfaces. According to them, oxygen ions at the TiO_2 boundaries between the grains cause a higher potential barrier, which will block the charge carriers' transfer, leading to a relatively large resistance.[31] This is true in our case too as we observe a base current of the order of pA when nitrogen or air is passed through the sensing chamber. When a reducing gas or an electron donating gas like the biomarker vapors comes into contact with the TiO_2 nanotube sensor, the chemical reaction of the gases and the adsorbed oxygen on the sensor's surface occurs, resulting in a sharp decrease of the adsorbed oxygen. Thereby, the potential barrier of the grain boundary on the surface is reduced, which then contributes to more charge carrier transfers and a decrease in the resistance of the TiO_2 nanotube sensor to obtain the sensing response. This is in addition to electronic perturbations on gold upon interaction with titania nanotubes[32-34] and gold facilitating the increase in oxygen vacancies at the oxide surface[35], both factors contributing to enhanced chemical activity of Au-TNA. Although the mechanism presents a strong and viable argument, it does not explain the SPR effect.

Further, since the TNA substrate contains a mixture of small Au nanoparticles are large nanoclusters, the electronic band structure will play a dominant role over quantum effects in explaining the enhanced sensor response. However, it is a widely known fact

that surface plasmon resonance behavior is prominent only when there exists van der Walls type attractive forces between gold nanoparticles and the TiO_2 nanotubes. Formation of covalent bonds between gold nanoparticles and nanotubes will eliminate the delocalized electrons which are crucial participants in augmenting SPR behavior. In this regard, researchers have demonstrated that ubiquitous van der Waals forces are significant in controlling the interactions between nanoparticles and nanotubes.[36] They stated that adsorption of gold nanoparticles (AuNPs) on nanotubes (NT) obeys a simple quadratic dependence on the nanotube surface area, regardless of the source of AuNPs and nanotubes. Changes in the geometric parameters of the components have pronounced effects on the affinity of nanoparticles for nanotubes, with larger, more polarizable nanostructures exhibiting stronger attractive interactions, the impact of which changes in the following order NT diameter > AuNP diameter > NT length. This successfully explains that in our case too, presumably the gold nanoparticles are strongly bonded by van der Walls forces to the TiO_2 nanotubes, which possess diameter larger than individual Au nanoparticles but less than the larger Au nanoclusters. Both weak and strong van der Walls forces will augment SPR characteristics.

The proposed mechanistic principle of LSPR induced VOB vapor sensing can be illustrated using two schemes, as indicated in Figure 6.7.

This mechanism in Scheme 1 (Figure 6.7a) is described purely by classical physics based on band theory. TiO_2 is a n-type semiconductor which implies that the oxygen vacancies act as electron donors to provide electrons to its conduction band. Oxygen vacancies introduce shallow electron trap states below the conduction band minimum, which plays a major role in charge transport.[37]

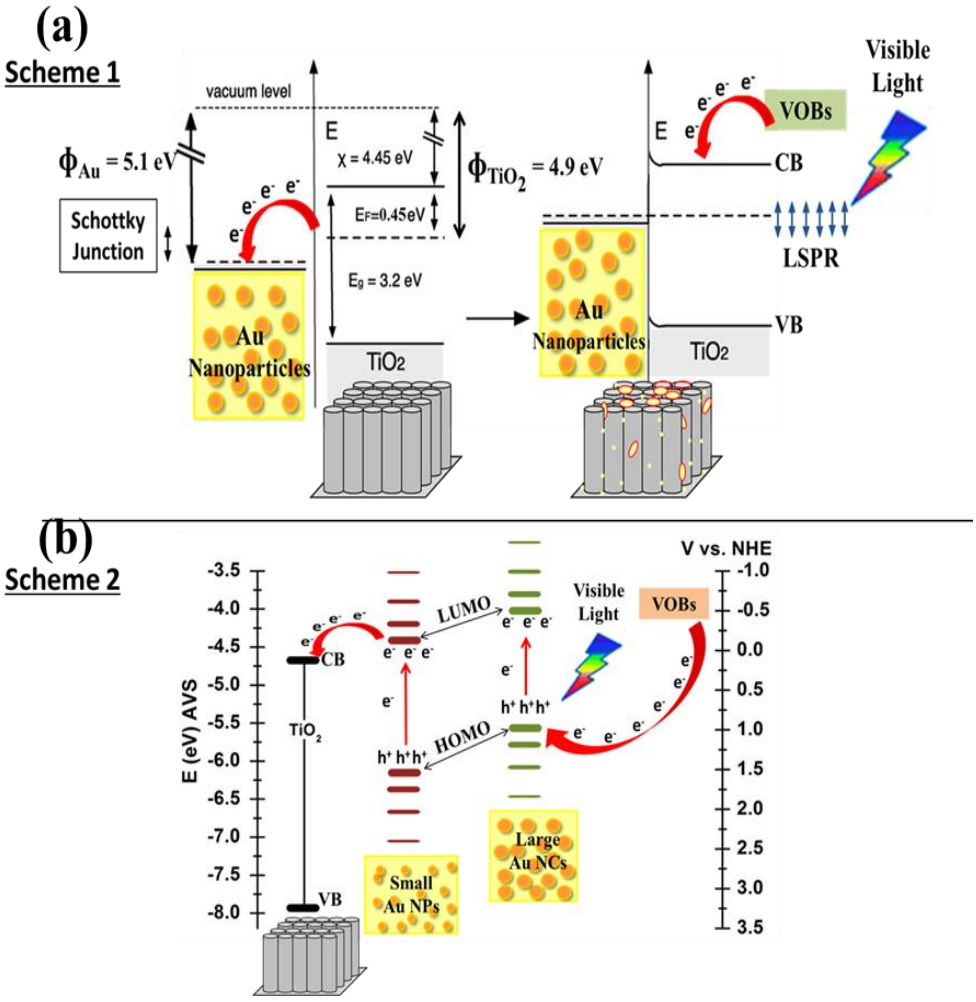

Figure 6.7 The two reaction schemes (a,b) illustrating the SPR assisted biomarker sensing using Au-TNA based sensors.

Further, the work function of TiO_2 nanotubes is 4.902eV in dark and ranges from 4.877 – 4.906 under illumination of varying wavelength (200 – 700 nm).[38] The work function of TNA in the LSPR active region of Au (i.e., ~530nm) is ~4.9eV, which is less than the work function of gold at 5.1eV. As a result, the Au-TNA interface presents a Schottky junction enabling electron transfer from TNA to Au, resulting in an interfacial dipole layer.[1] The induced interfacial potential further lowers work function of Au,

causing band bending and decrease in barrier height. This leads to a negative charge on Au nanoparticles while a depletion region forms in the positively charged TNA surface. In addition, the small Au nanoparticles possess high electron affinity scavenging more electrons from TiO_2. Further, the large surface-to-volume ratio of TNA enables oxygen molecules to be easily absorbed on the surface, creating a broadened depletion layer with a positive space charge region (due to oxygen vacancies + electron capture by Au) with increased resistivity. When the sensor is exposed to reducing atmosphere of the VOB vapors, the electrons from the VOB molecules fill the depleted region resulting in increased conductivity and leading to a large change in current. However, this mechanism is true under dark and illuminated conditions alike. Enhanced sensor response under visible light illumination can be attributed to the LSPR effect caused by Au nanoparticles which behave as nano-antennas under electromagnetic excitation. Au nanoparticles receive excitation energy from electromagnetic radiation and transfer it via the Au-TNA Schottky junction to the TiO_2 surface, leading to collective oscillation of electron density, known as LSPs.[1] As a result of these collective oscillations, narrow concentrated regions of enhanced electromagnetic field strength are formed, which extend from the Au nanoparticles to the TNA surface across the Schottky junction, and contribute to improved sensor responses.

The mechanism in Scheme 2 (Figure 6.7b): is described based on the coupling of the band theory and quantum physics. As in the previous case, the TiO_2 nanotubes array is characterized by the conduction and valence band with a band gap of 3.2eV and surface adsorbed or ionosorbed oxygen species leads to the formation of depletion region (oxygen vacancies). Au nanoparticles act as TiO_2 sensitizers and are characterized by

electron occupancy orbitals such as highest occupied molecular orbital (HOMO) and lowest unoccupied molecular orbital (LUMO). Kogo *et al*.[39] had shown that the lower edge of the TiO_2 conduction band lies at +0.1V (*vs.* SHE) whereas the LUMO of the Au nanoparticles, which is more electronegative than the HOMO by 1.7eV ± 0.4eV, lies around -0.1V (*vs.* SHE) and also stated that the potential of the occupied levels involved in charge separation under visible light shifts negatively as the cluster size increases. Thus, upon visible light irradiation, collective oscillations of the electrons in gold atoms due to the SPR effect excites the electrons in the occupied orbital HOMO to an unoccupied orbital LUMO leading to charge separation which is subsequently injected into the TiO_2 conduction band. The photo-generated positive hole in the HOMO receives an electron from a donor species such as the VOBs resulting in oxidation of the VOBs and preventing electron-hole recombination. Thus, presence of Au nanoparticles facilitates replenishment of the TNA oxygen vacancies under visible light illumination, while simultaneously oxidizing the VOBs.[10] As more electrons are injected into the TiO_2 conduction band, the resistivity decreases and the current increases. Photo-generated electrons contribute to enhanced sensor response under illumination. Small Au nanoparticles enable efficient oxidation of donors and thus provide large photocurrents. On the contrary, large Au nanoclusters are suitable for efficient oxidation of donors with negative redox potentials such as the VOBs. As revealed from the SEM-EDS micrographs, the Au-TNA surface has a mixture of small Au nanoparticles and large Au nanoclusters, enabling efficient oxidation of the VOBs. Thus, a balanced mixture of small Au NPs and large Au NCs facilitates oxidation of the VOB vapors resulting in large currents.

6.4 Summary

TiO_2 nanotubular array (TNA) is a stable and versatile material with high surface area-to-volume ratio that has been widely used for photocatalysis and sensing applications, whereas gold is a known plasmonic material. Plasmonic enhancement of the photoresponsivity is possible in semiconductor–metal nanocomposites in isolated, embedded, or encapsulated form. In this study, we have reported the enhanced visible light photoresponse of LSPR induced VOB vapor sensing at room temperature using Au-embedded-TNA sensors. Two mechanistic schemes – one based on classical physics (band theory) and the other based on the coupling of classical and quantum physics (molecular orbitals) – suggest that augmented sensor response to the four biomarkers based on enhanced photoresponsivity of the sensor is possible.

6.5 References

1. L. Xu, M. Yin, and S. F. Liu, *Sci Rep*, **4,** 6745-51 (2014).
2. C. A. Grimes, *J. Mater. Chem.*, **17**, 1451–57 (2007).
3. D. Bhattacharyya, P. K. Sarswat, M. Islam, G. Kumar, M. Misra, and M. L. Free, *RSC Adv*., **5**, 70361–70 (2015).
4 H. Chen and Y. Xia, *Anal. Chem*., **86**, 11062−69 (2014).
5. M. Delvaux and S. Demoustier-champagne, *Biosens. Bioelectron.*, **18**, 943-51 (2003).
6. S. Cherevko and C. Chung, *Sens. Actuators B*, **142**, 216–23 (2009).
7. Y. Zhou, S. Yang, Q. Qian, and X. Xia, *Electrochem Commun*, **11**, 216–9 (2009).
8. M. Delvaux, A. Walcarius, and S.Demoustier-champagne, *Anal. Chim. Acta*, **525**, 221–30 (2004).
9. S. Guo, D. Wen, S. Dong, and E.Wang, *Talanta*, **77**, 1510–7 (2009).

10. P. Gunawan, L. Mei, J. Teo, J. Ma, J. Highfield, Q. Li, and Z.Zhong, *Langmuir*, **28**, 14090−99 (2012).

11. R. Kaur and B.Pal, *Colloids Surf. A: Physicochem Eng Asp*, **441**,155–63 (2014).

12. R. Kaur and B.Pal, *J. Mol. Catal. A: Chem.*, **355**, 39–43 (2012).

13. G. J. Hutchings, *Catal. Today*, **100,** 55–61 (2005).

14. K. Dumbuya, G. Cabailh, R. Lazzari, J. Jupille, L. Ringel, and M. Pistor, .Catal Today, **181**, 20–5 (2012).

15. G. Zhao, Y. Lei, Y. Zhang, H. Li, and M. Liu, *J. Phys. Chem. C*, **112**, 14786–95 (2008).

16. Y. Umasankar and R. P. Ramasamy, *Analyst*, **138**, 6623–31(2013).

17. H. M. Song, D. H. Anjum, R. Sougrat, M. N. Hedhili, and N. M. Khasab, *J. Mater. Chem*, **22**, 25003-10 (2012).

18. N. Gogurla, A. K. Sinha, S. Santra, S. Manna, and S. K. Ray. *Sci Rep*, **4**, 6483-92 (2014).

19. Y. Zhu, Y. Dai, K. Lai, and B. Huang, *ChemPhysChem*, **14**, 2800–07 (2015).

20. Y. Wen, B. Liu, W. Zeng, and Y. Wang, *Nanoscale*, **5**, 9739–46 (2013).

21. A. M. Sullivan and P. A. Kohl, *J. Electrochem. Soc*, **144**(5), 1686–90 (1997).

22. Y. Okinaka and M. Kato, Electroless deposition of Gold, *Modern Electroplating*, 4th ed.; M. Schlesinger, M. Paunovic, Eds., John Wiley & Sons, Inc., New York,; 483-498 (2010).

23. J. Hu, W. Li, J. Chen, X. Zhang, and X. Zhao, *Surf. Coat. Tech.*, **202**, 2922–2926 (2008).

24. X. Zhang, L. Yu, J. Tie, and X. Dong, *Sensors*, **14**, 19517-19532 (2014).

25. Y. R. Smith, D. Bhattacharyya, S. K. Mohanty, and M. Misra, *J. Electrochem. Soc.*, **163** (3), B83-B89 (2016).

26. E. Khon, A. Mereshchenko, A. N. Tarnovsky, K. Acharya, A. Klinkova, N. N. Hewa-Kasakarage, I. Nemitz, and M. Zamkov, *Nano Lett.*, **11**, 1792–1799 (2011).

27. X. Zhang, Y. Liu, S.-T. Lee, S. Yang, and Z. Kang, *Energy Environ. Sci*., **7**, 1409–1419 (2014).

28. A. Mohammadpour and K. Shankar, *J. Mater. Chem.*, **20**, 8474–8477 (2010).

29. Y. Lei, H. Chena, H. Dai, Z. Zeng, Y. Lin, F. Zhou, and D. Pang, *Biosensors and Bioelectronics*, **23**, 1200–1207 (2008).

30. Y. Kobayashi and Y. Ishii, *J. Nanoparticles*, **2013**, 1–5 (2013).

31. B. J. Choi, D. S. Jeong, S. K. Kim, C. Rohde, S. Choi, J. H. Oh, H. J. Kim, C. S. Hwang, K. Szot, R. Waser, *et al.*, *J. Appl. Phys.*, **98**, 033715 (2005).

32. F. Cosandey, L. Zhang, and T. E. Madey, *Surf. Sci.*, **474**, 1–13 (2001).

33. M. Valden, X. Lai, and D. W. Goodman, *Science*, **281**, 1647–1650 (1998).

34. F. Cosandey and T. E. Madey, *Surf. Rev. Lett.*, **8**, 73–93 (2001).

35. J. A. Rodriguez, G. Liu, T. Jirsak, J. Hrbek, Z. Chang, J. Dvorak, and A. Maiti, *J. Am. Chem. Soc.*, **124**, 5242–5250 (2002).

36. G. A. Rance, D. H. Marsh, S. J. Bourne, T. J. Reade, and A. N. Khlobystov, *ACS Nano*, **4**(8), 4920–4928 (2010).

37. A. Cultrera, L. Boarino, G. Amato, and C. Lamberti, *J. Phys. D: Appl. Phys*, **47,** 015102-09 (2014).

38. G. X. R. Smith, R. Crook, and J. Wadhawan, *J. Phys: Conf Series*, **471**, 012045-48 (2013).

39. A. Kogo, N. Sakai, and T. Tatsuma, *Nanoscale*, **4**, 4217–21 (2012).

CHAPTER 7

INVESTIGATION OF ELECTROCHEMICAL SENSING OF BREATH BIOMARKERS FROM OTHER DISEASES: COLORECTAL CANCER

7.1 Introduction

Recent advances in the field of molecular biology have not only led to an increased understanding of the role played by volatile organic compounds (VOCs) in the metabolic conditions of various diseases but also their potential utilization as unique diagnostic markers for enhanced patient care.[1] The detection of unique VOCs is not an unique idea within itself, but its application as a method of diagnosis is. A noteworthy potential of VOCs lies in the vast array of samples from where they can be extracted. VOCs pertaining to certain diseases can be extracted from urine, serum, and even breath of patients, with each sample type showing certain unique identifying biomarkers for the same disease. Although urine- and serum-based VOCs have been studied in some details, breath-based VOCs have not been looked into much, until recently. Analyses of the data presented in the previous chapters demonstrate the feasibility of utilizing cobalt functionalized titania nanotubes for electrochemical detection of tuberculosis biomarkers derived from breath.[2,3] Research into other diseases have revealed the importance and increased accuracy of breath-based VOCs as diagnostic biomarkers, whether it be

gastrointestinal or liver conditions[4], kidney[5], breast and lung cancer[6], and so on. Analysis of breath specimens for biomarkers of Plasmodium falciparum infection has revealed the VOCs associated with malaria.[7] In an elaborate study, Peng *et al*.[6] have identified VOCs from lung, breast, prostrate, and colorectal cancer using gas chromatography - mass spectrometry (GCMS). Further, they investigated the ability of a cross-reactive nanosensor array based on organically functionalized gold nanoparticles (GNP) to discriminate between breath VOCs of healthy controls and of patients suffering from lung, breast, colorectal, and prostate cancers. Their arrays of broadly cross-reactive GNP sensors were ideally suited to trace the cancer odor prints directly, without identifying the constituent VOCs. But in reality, the different cancer types mentioned have distinct odor prints comprising succinctly distinct VOCS. Hence, it is evident that the GNP-based sensor suffers from selectivity and specificity issues. From a point-of-care diagnostic standpoint, specificity, selectivity, and sensitivity are critical attributes of the sensing platform. Developing a VOC-based sensing platform for rapid detection of any cancer type disease can significantly impact screening of patients at an early stage, which can otherwise prove to be life threatening. The prognosis of a cancer patient improves considerably if the disease is discovered at an early stage.[8,9] Given that colorectal cancer (CRC) is the second leading cause of cancer-related death in Europe and the third in the USA, the quest continues for novel noninvasive screening systems with the potential for high patient compliance and low cost that have an equivalent sensitivity/specificity to colonoscopy, for early detection of colorectal cancer and precursor adenomatous polyps.[10-12]

Arasaradnam *et al.* [13] highlighted the importance of VOCs in the urine of patients

with colorectal cancer and the potential they hold for future noninvasive techniques in this area. However, pertinent to our research interests, recently, Altomare *et al.* [14] have identified fifteen VOCs as potential biomarkers exisiting within the breath of colorectal cancer patients using GC-MS techniques. Among all the VOCs identified within this study, five VOCs viz. cyclohexane, methylcyclohexane, 1,3-dimethylbenzene, 1,2-pentadiene, and decanal demonstrated a recognition capability greater than 90%.

The capabilities of electrochemically-based vapor sensors in this type of setting are highly contingent on the effect of functionalization of an inert but stable substrate base. Metal oxides that are used in gas sensing purposes allow for the surface absorption and desorption of certain gases facilitated by electron transfers on the film surfaces. To increase gas sensitivities and detection, it has been reported by several groups that the adjustment of TiO_2 with certain metallic depositions can alter the band gap of it, allowing for greater conductivity patterns. To that effect, it has been reported by Bhattacharyya *et al.* [2] that TiO2 in a crystalline anatase phase confers greater mechanical strength and stable base for such catalytic processes. It was further reported that the utility of TiO_2 based gas sensors lays in their applicability in high and low temperature settings due to the versatility in the morphology of the surface of the TNA.[15] With a high surface area-to-volume ratio,[2,3] corrosion resistance,[16] and tenacious mechanical characteristic, it is possible to increase the susceptibility of these sensors by functionalization. However, prior to examining the biomarkers using TiO_2 nanotubes, it is imperative to determine the functionalization element which can facilitate catalytic oxidation of the biomarkers. Cyclohexane showed one of the highest selectivity index values and ability to distinguish healthy and cancer patients. The catalytic oxidation of cyclohexane and similar

hydrocarbons has been of great interest for its application in the industrial sectors. Adipic acid, a product of such oxidative processes, is a vital component in the synthesis of Nylon-6 and Nylon-66. [17] Several techniques to achieve this have been developed as a result. For instance, Alshammari *et al.*[17] have reported their success in direct catalytic conversion from cyclohexane to adipic acid with nano-gold catalysts, while Sarkar *et al.*[18] have reported conversions at room temperature using deposited copper nanoparticles on Cr_2O_3 substrate base. Hybridized substrate bases of WO_3/V_2O_5 with a generic oxidant H_2O_2 have also been used in this catalysis.[19] Photocatalytic conversion of cyclohexane to adipic acid has also been reported as a more green method of synthesis with the utilization of TiO_2 functionalized with iron, nickel, and gold.[20] Gaur *et al.*[21] had demonstrated catalytic oxidation of 1,3-dimethylbenzene using activated carbon fiber impregnated with nickel. In addition, Yolcular and Olgun [22] had shown that Ni/Al_2O_3 catalysts exhibit activity in dehydrogenation of methylcyclohexane for hydrogen production. Using this study as well as the reviewed publication by Hosseini *et al.*,[16] nickel was determined to be a highly active oxidant species capable of the catalytic conversion of biomarkers of interest. This evidence is further supported by the studies of Li *et al.*[23] that have explored the potential of nickel-deposited TiO_2 in a variety of hydrogen sensing purposes. In their study, Ni-TiO_2 catalyst demonstrated very good sensing capabilities of varying concentration hydrogen environments in a wide temperature (25^oC-200^oC) range. Based on this premise, Ni-deposited TiO_2 was used to detect the presence of cyclohexane, methylcyclohexane, 1,3-dimethylbenzene, and decanal vapors in ambient conditions. It is envisaged that a similar TNA based platform tailor made for VOBs specific to certain diseases can prove to be versatile.

7.2 Experimental

The procedure for the synthesis of titania nanotubes have been explained in details in Section 3.2.1 of Chapter 3.

Annealed TiO_2 nanotubes were electroplated with a 0.5M $NiCl_2$ solution at room temperature. The cathodic deposition of Ni ions was carried out at 22.5mA, a current density of 10mA/cm^2 for 1 min. A Pt foil was used as the anodic counter electrode; the two electrodes were held approximately 2.5cm apart. The Ni-deposited TiO_2 nanotubes were then rinsed with DI water and left to dry overnight in a VWR oven at 110^{o}C in vacuum.

The morphological characteristics of the TNA and Ni-deposited TNA were analyzed with a Hitachi S-4800 SEM consisting of a tungsten film of accelerating voltage of 5.0kV and an emission current setting of 15μA. In addition to the SEM, an attached Oxford EDX detector provided energy dispersive x-ray spectroscopic (EDS) analysis of the corresponding SEM images. These were done at 20 kV accelerating voltage on a 25x25 μm area.

XPS studies using Kratos Axis Ultra DLD model were used for the determination of the surface composition and characteristics of Ni and Ti. The vacuum inside the analysis chamber was held at a constant 3 x 10^{-8} Torr. A monochromatic AlK_α radiation at 180W and hν = 1486.6eV was used as the x-ray excitation source. The spectra were obtained at passing energies of 160 and 40eV and were analyzed with the aid of CasaXPS software. The C 1s line at 284.6eV was used as the standard reference for all the peaks.

X-ray diffraction (XRD) was carried out using a Rigaku Miniflex XRD (CuKa = 1.54059 Å) from 2Theta = 20 to 80 degree with a step size of 0.015 degrees and dwell

time of 1 degree min -1. The diffraction patterns were analyzed using Rigaku PDXL2 analysis software and indexed with standard JCPDS cards.

The catalytic oxidation of the four CRC biomarkers for its detection was carried out in a customized sensing chamber such that one connection (working electrode) was made to the Ni-deposited TNA side while the other was made to the unanodized face of the coupon. A GAMRY Reference 600 two-electrode based potentiostat was used during these experiments. For biomarker vapor to be introduced into the sensing chamber, nitrogen gas at 200sccm (standard cubic centrimetres per minute) was bubbled through the solution of the biomarker mimics. Varying concentrations of biomarkers (all dissolved in ethanol) were used in these experiments (0.1, 1, 10 mM). From preliminary cyclic voltammetry studies, the bias voltage that allowed for maximal interaction between nickel and the individual VOBs were determined. At the respective voltages, sensor response tests were carried out. During the tests, for the first 100 seconds, only nitrogen gas (no biomarker) was flown to allow for a maximum current value to be established, followed by exposure to biomarker vapors. When maximum current with the analyte was observed, the biomarker was disconnected and the sensor was exposed to only nitrogen gas again where a drop in the current was visible. All of the experiments were conducted at room temperature.

7.3 Results and Discussion

7.3.1 TNA Surface Characterization

Scanning electron micrographs show that the TNA (Figure 7.1) is organized into regularly sized and ordered nanotubes. A top side view indicates the tubes having a

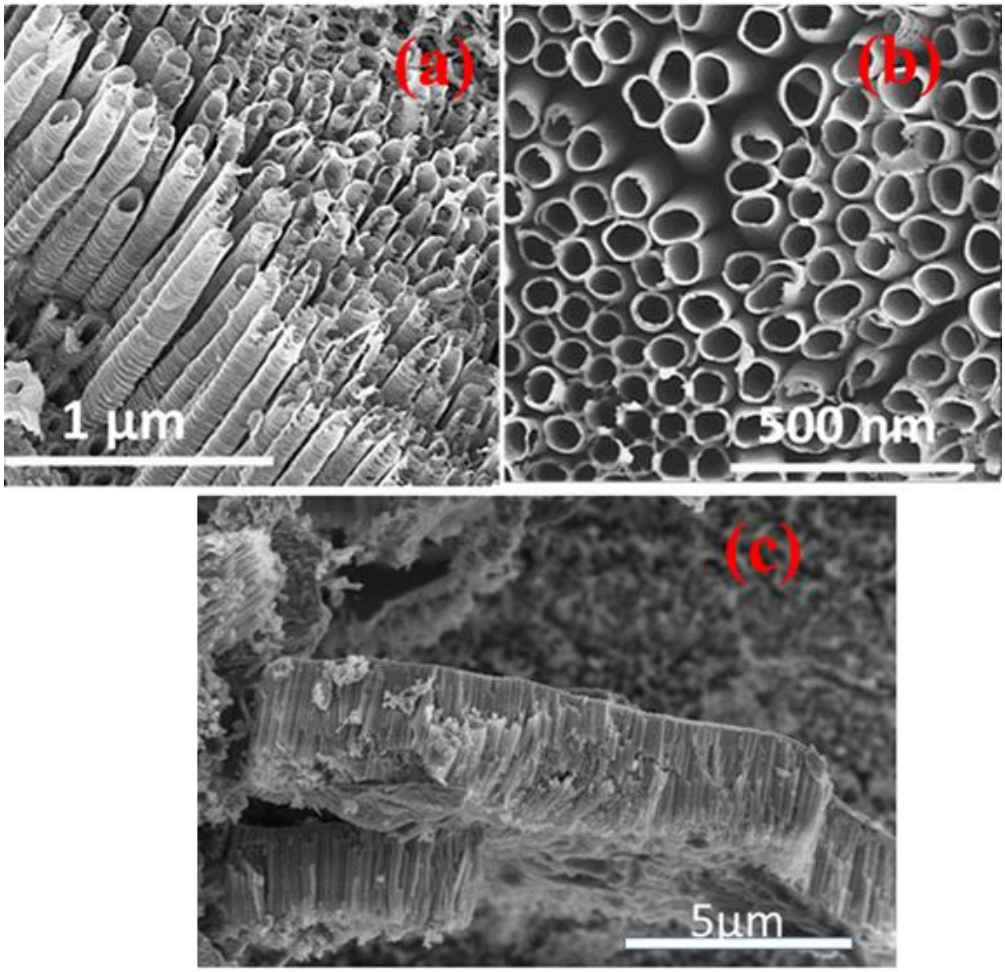

Figure 7.1. SEM micrographs of highly organized, vertically oriented TiO_2 nanotubular array (a) side wall view, (b) top view, and (c) an island chunk of TNA lying on the mouth of the nanotubes.

diameter of approximately 55-60nm and a wall thickness of approximately 14nm. From side views of the nanotube array, it is estimated that the length of the nanotubes ranges from 1.2 - 1.5µm. As discussed earlier, the TNA film showed a presence of primarily anatase phase titania[2] which in combination with annealing in an oxygen environment showed greater resistivity, a vital quality for such electrochemical detection. Scanning electron micrographs of Ni-deposited TNA (Figure 7.2) showed depositions of nickel as globules on the TNA surface.

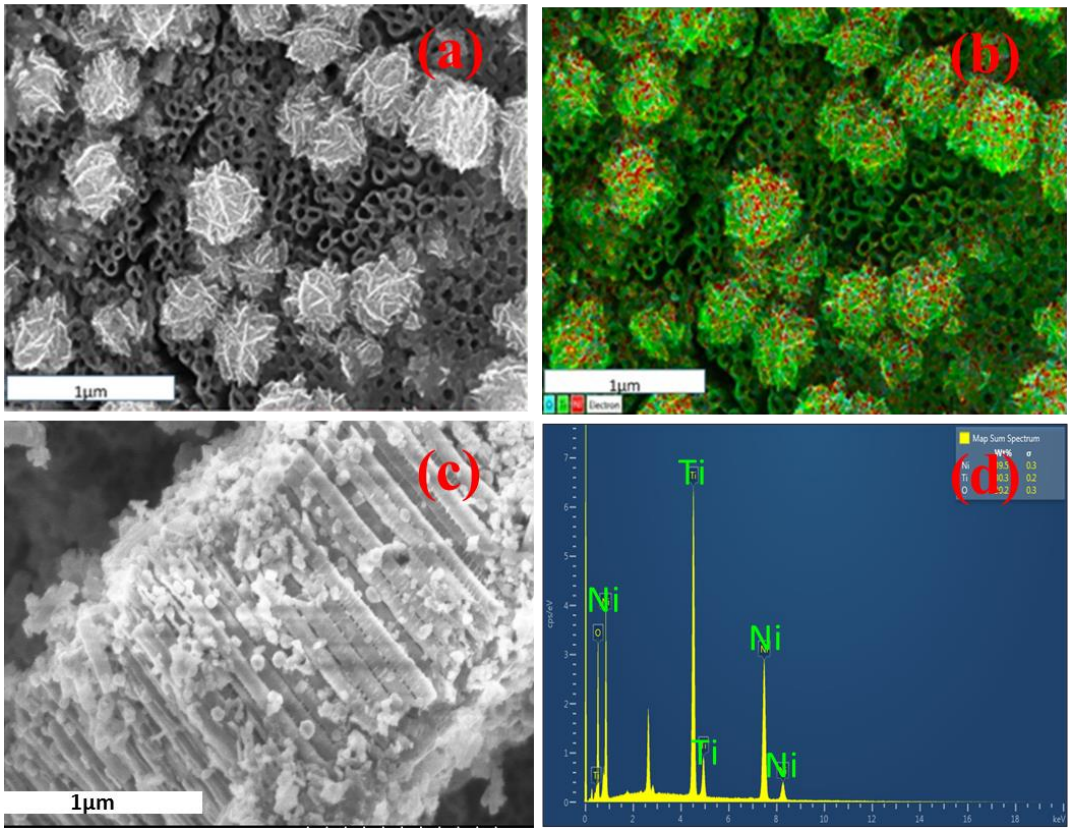

Figure 7.2 SEM image of (a) electrodeposited Ni on TNA, (b) EDS micrograph confirming the presence of Ni globules on TNA, (c) Ni globules present on the side wall of the nanotubes, (d) EDS spectrum further confirming the presence of Ni.

The globules range anywhere from 0.4 - 0.6 µm in diameter and can be seen to be relatively homogenously distributed. Lateral cross-sections reveal that smaller, individual particulates of nickel fit within the openings of the tubes. It is assumed that electroplating of nickel favors congregation of the particulates into globules rather than individual particles on the surface. This confirmation is well suited for sensory purposes due to the higher surface area that is now available for interaction with biomarkers. EDS mapping of the SEM images (Figure 7.2b) reveals that the globules consist of titanium, nickel, and oxygen with their approximate weight distributions as 47.0%, 26.8%, and 26.2%, respectively.

XPS studies of the electroplated Ni on TNA have revealed the existence of Ni as $Ni(OH)_2$ globules on the surface (Figure 7.3). A general survey of the sample shows numerous peaks with prominent ones for nickel and oxygen. Oxygen's 1s peak is observable at 532eV. In the case of nickel, there are two prominent peaks of interest: $2p_{1/2}$ at 872eV and $2p_{3/2}$ at 855eV. Not only are these values well established in the literature but Wu *et al.* [24] have also concluded that these energy values correspond to $Ni(OH)_2$. There is a gap of 17eV between the peaks of interest which indicates that the Ni 2p peak has significant split spin-orbit components. A small, almost imperceptible gap exists between the 2p and $2p_{3/2}$ peaks, but due to spin coupling and overlay of similar energy orbitals on the nickel atom, they appear to be as one peak. Near the lower end of the spectrum, 3s and 3p peaks (0 - 100eV) are also visible, but due to their low energy values and minor peak sizes, these are assumed to be not participating during the progression of the reaction.

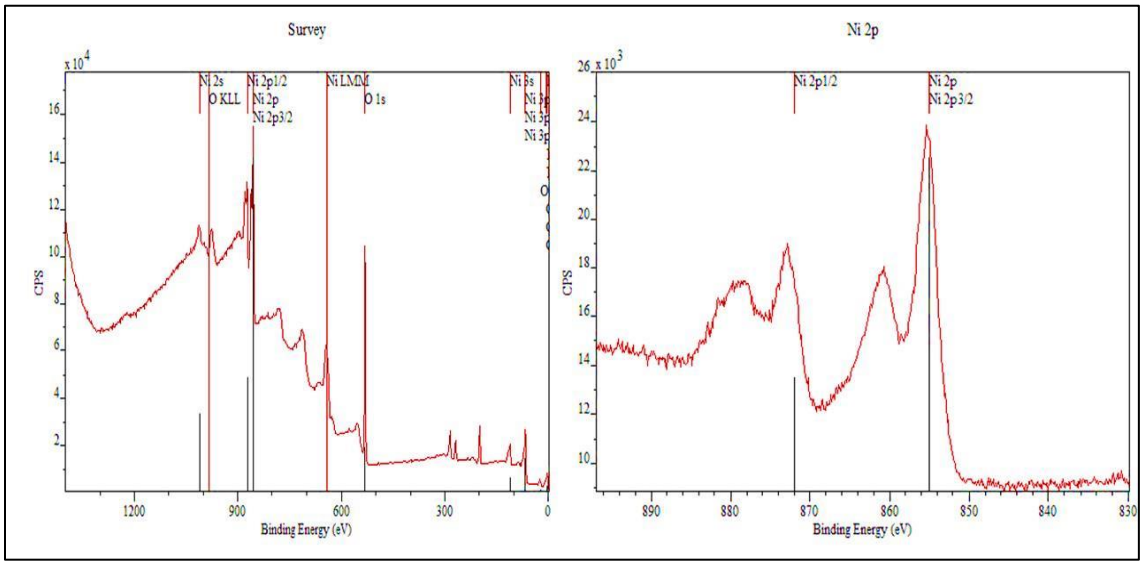

Figure 7.3 XPS spectra of Ni-TNA (left) General survey of the sample shows numerous peaks with prominent ones for nickel and oxygen. Oxygen's 1s peak is observable at 532eV. (right) XPS spectra of Ni shows two prominent peaks of interest: $2p_{1/2}$ at 872eV and $2p_{3/2}$ at 855eV.

7.3.2 Detection of CRC Biomarkers with Ni-TNA Sensor

The ability of nickel to act as a strong binding agent to the biomarkers was determined from cyclic voltammetry studies. From the same studies, the optimal voltage for the reaction between nickel and the individual biomarkers was found (cyclohexane: 1V, 1,3-dimethylbenzene: 1.4V, methylcyclohexane: 1.55V, and decanal: 1.45V, respectively). These bias voltages have been observed to produce the maximum current signal. From Figure 7.4, it can be observed that as compared to nitrogen, when the sensor is exposed to the individual biomarkers, there is sharp and rather rapid increase in current. For a 10mM concentration of cyclohexane, the peak current output was recorded as 1.45 mA (Figure 7.4).

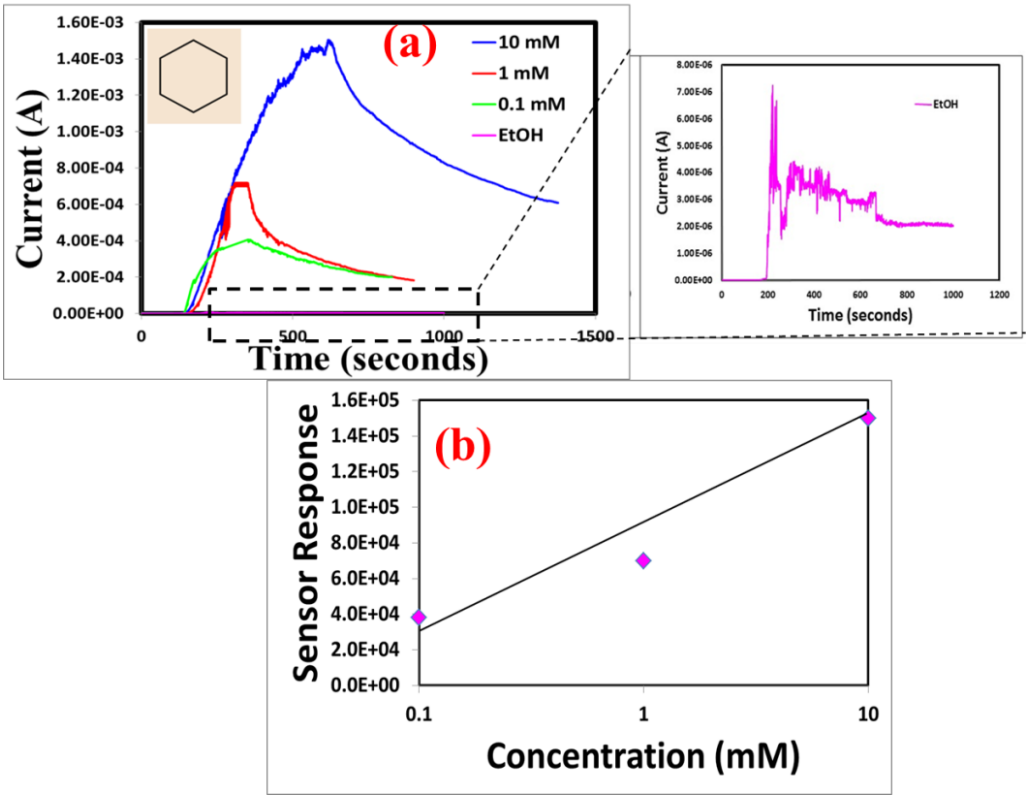

Figure 7.4 Sensor response of Ni-TNA to (a) vapors of cyclohexane (inset) sensor response to ethanol. (b) linear relationship between sensor response and concentration.

As the concentration was decreased by factors of 10, a corresponding decrease in the maximum current recorded was noted; vapors from 1mM solution gave a response of ~700 µA while a current of 392µA was obtained from 0.1 mM solution. Since ethanol was the solvent in which this biomarker was dissolved, the reaction binding affinity of nickel to ethanol was also measured as the sensor control response. Compared to cyclohexane, the maximum current observed for ethanol was <3 µA, a significantly lower value. This is indicative of the fact that the large current peaks observed during the experiments were due to exposure of the sensor to cyclohexane exclusively and a successive drop in current was observed when the flow of cyclohexane was discontinued.

The maximum current response from 10 mM methylcyclohexane was ~21 µA while a maximum current of ~45µA was obtained from vapors of 10 mM solution of 1,3-dimethylbenzene. Decanal vapors from 10 mM solution in ethanol delivered a maximum current of ~1mA. The current response from these vapors decreased monotonically as the concentration was reduced from 10 mM to 1 mM and subsequently 0.1 mM (Figure 7.5). Further investigation is required to determine the vapor phase concentration of the biomarkers reaching the sensor substrate.

7.3.3 Reaction Mechanism

From SEM and EDS analysis of Ni-plated TNA, it was found that the TNA surface was littered with globular $Ni(OH)_2$ complexes. Since the solution in which electroplating had been conducted was aqueous $NiCl_2$, a possible equation for the reaction which explains the formation of nickel hydroxide is follows:

$$NiCl_2 + 2H_2O \rightarrow Ni(OH)_2 + 2HCl \quad \ldots(7.1)$$

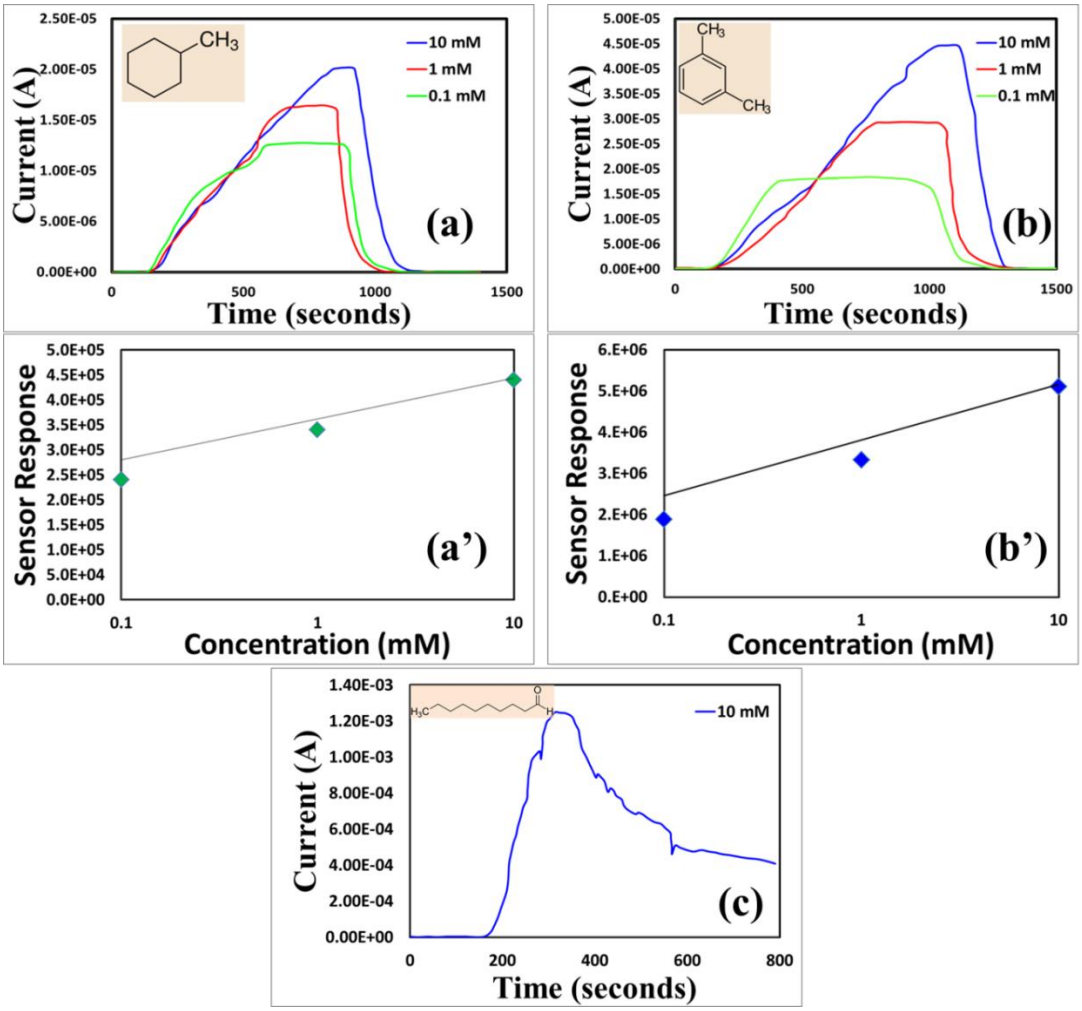

Figure 7.5 Sensor response of Ni-TNA to vapors of (a,a') methylcyclohexane, (b,b') 1,3-dimethylbenzene, and (c) decanal.

This is further supported by XRD studies of the sensor (Figure 7.6) where it can be observed that that anatase TiO_2, Ti, and Ni have separated peaks. Overlapping of Ni and Ti peaks can be observed at 2θ 53^o and 77^o, however, because of their distinct existence, and Ni does not get integrated within the lattice of the TiO_2 nanotube array. This is of great importance in regards to the reaction between $Ni(OH)_2$ and the biomarkers. Also, it is evident from the diffraction pattern that majority of $Ni(OH)_2$ is present in the β phase while only one peak exists for α- $Ni(OH)_2$.

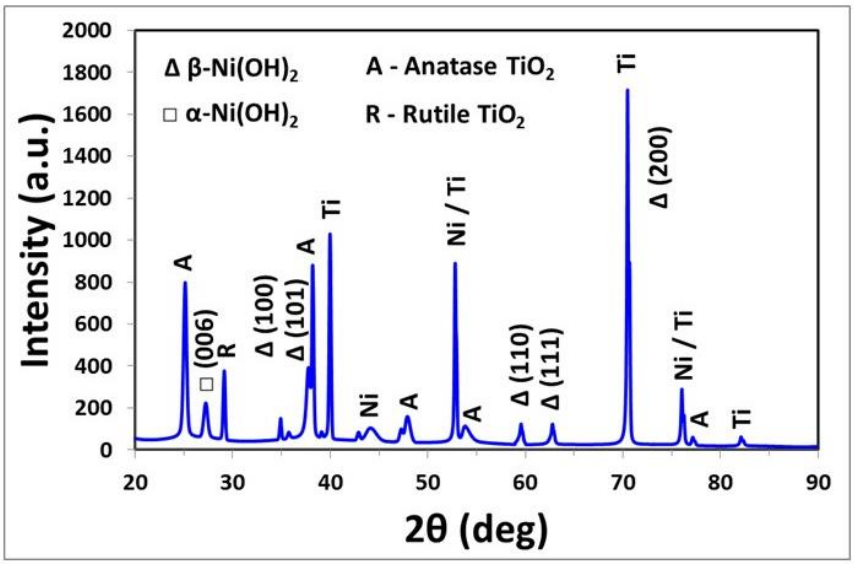

Figure 7.6. XRD pattern of Ni-TNA with 2θ ranging from 20˚ to 90˚.

It has been well reported and corroborated [2,25,20] that gas sensing capabilities of sensors are based on oxide conductivity adjustments that occur on the surface or near the surface of sensors as a consequence of gas adsorption or the formation of complexes. In the case of organic species like cyclohexane, it is the formation of complexes that is the primary mechanism for detection. We have previously reported success in the formation of a complex between Co^{2+} ions and biomarker methyl nicotinate in a similar procedure.[2] In both cases, the presence of metal ions is not only crucial for the stability and formation of complexes but also the ability to act as oxidizing agents in these reaction mechanism.

From previous discussions of various methods of cyclohexane oxidation, there are two reaction mechanisms by which the conversion of cyclohexane to adipic acid is facilitated. [19] In both of the reactions, whether it be the direct conversion to adipic acid, or the formation of the intermediate product cyclohexanol and cyclohexanone, [19] the

creation of the cyclohexyl radical is of great importance. To that effect, Ide *et al.* [20] have reported in their photocatalytic experiments that the synthesis of this intermediate radical on TiO_2 is carried out by the direct interaction of cyclohexane with either the valence band hole of TiO_2 or a combination of the valence band hole and its reduction of an OH^- group. It is well known that TiO_2 is an n-type semiconductor and being as such, the interaction of valence band holes and cyclohexane will be minimal. This is supported from our cyclic voltammetry studies (not shown) where it was found that functionalization of TiO_2 was required for the detection of cyclohexane since TiO_2 within itself was an inadequate oxidizing agent in electrochemical settings. However, the formation of $Ni(OH)_2$ complexes on the surface of the TNA, more specifically the OH^- groups, was crucial in this reaction. The presence of OH^- groups on the surface increase the general conductivity of n-type sensors. This fact is supported by our previous studies that have reported not only the utility of OH^- as great Brönsted-Lowry acids but also their defining role in the stability of these organometallic complexes. Because of the presence of OH^- on the TNA surface, the formation of a stable complex with cyclohexane vapor is possible.

The reaction between the $Ni(OH)_2$ complexes and cyclohexane can be envisaged in equation 7.2. Due to the nickel functionalization of the TNA, cyclohexane gets oxidized and creates a nickel cyclohexyl complex with two cyclohexane molecules attached to one nickel atom (Figure 7.7).

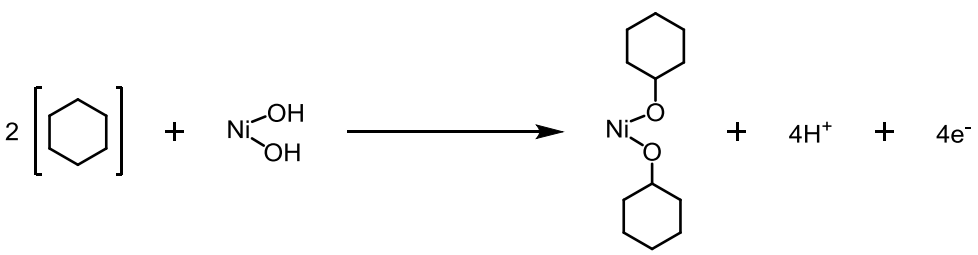

…(7.2)

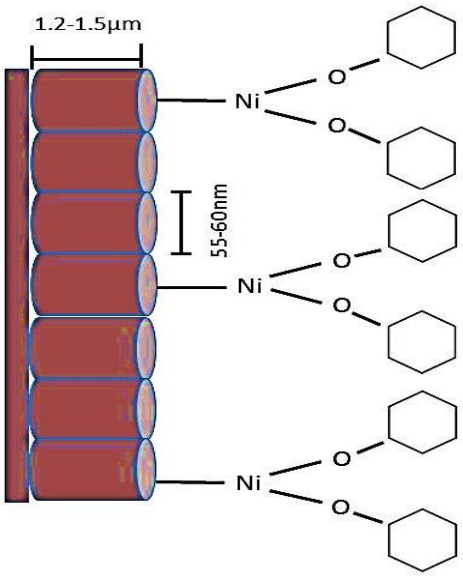

Figure 7.7. Schematic diagram showing the formation of the nickel cyclohexyl complex on the TNA.

The high current response, indicative of a strong interaction between nickel and cyclohexane, is well corroborated by the reaction mechanism shown above. Not only does the efficiency of binding follow a 1:2 ratio of nickel to cyclohexane, but the unique characteristics of TiO_2 nanotubes in electron transfer and atmospheric oxygen adsorption make it a suitable and highly favourable reaction. In the case of the former, as reported by Bhattacharya *et al.*, [2] the structure of these nanotubes provides not only stability and increased surface area of the interaction between the metal ions and cyclohexane but the tubular structure also enables greater electron transfer between the biomarker and the metal ions during the oxidative interaction with minimal losses. As to the adsorption of atmospheric oxygen, this characteristic of TiO_2 is vital in the steps following the synthesis of this radical complex that allow for the formation of the intermediates

mentioned above. [19,20] This is supported by the studies of Ide *et al.* [20] that have reported the importance of the superoxide anion that plays a role in the formation of cyclohexanone and cyclohexanol. TiO_2 generates this superoxide anion by donating its electrons to the ambient atmospheric oxygen that is present during the progress of this reaction. The following equations reported by Bhattacharya *et al.* [2] show how this may be possible:

$$O_2\ (gas) \rightarrow O_2\ (ads) \rightarrow O^{2-}\ (ads) \rightarrow 2O^{-}\ (ads) \rightarrow O^{2-}\ (ads) \qquad ...(7.3)$$

Oxygen vacancy (Vo)-related defect sites/states are the most favorable ones for the adsorption of target species[26,27]. This is because the binding interaction between oxygen molecules and organic molecules is much stronger in such defect sites compared to the defect-free ones. O_2 molecules can be dissociated and chemisorbed to the oxygen vacant site (Vo) of the oxide surface with negligible activation energy.[26,28] It is speculated that once the nickel-cyclohexyl complexes have been created, the superoxide anion is responsible for the direct conversion of the cyclohexyl radical to cyclohexanone and cyclohexanol. This is corroborated by the sensor response graphs (Figure 7.4a) that show a remarkably slow decrease in current after the discontinuation of cyclohexane vapour flow. This is indicative of the possibility that less and less cyclohexyl radical is available for reduction back to cyclohexane. The current signal that has been reported during this experiment may be a result of this reaction mechanism.

Similar reaction mechanisms have been envisaged for the interaction of Ni with other biomarkers as well (equation 7.4-7.6). The reaction with 1,3-dimethylbenzene and methylcyclohexane shows that the organic molecules doubly and triply complexes with

nickel hydroxide, respectively. As a result, effectively more active sites are occupied by a single organic molecule and fewer active sites are thus available for other unreacted molecules. The maximum current response to 10 mM of the respective vapors is also in the same order: 45 μA for 1,3 dimethylbenzene, and 21 μA for methylcyclohexane. As the reducing gas/vapor comes to contact the sensing layer, it is adsorbed to the oxide surface by the dissociative adsorption process and dehydrogenated by the adsorbed oxygen species. Decanal is a straight chain molecule and attaches to a single molecule. Therefore, in addition to not providing any steric hindrance, more active sites are available for unreacted species to form nickel complexes. This results in a higher current response (~1 mA) to 10 mM vapors of decanal in comparison to the previous two recently discussed. Further, catalytic activity of TiO_2 enhances the dissociation possibility of the aldehydes (decanal) at the oxide surface. By the effect of TiO_2 catalyst, aldehyde gets converted to a secondary alcohol. In alcohols, O−H bond scission becomes faster, and alcohols can easily be dissociated and dehydrogenated into different alkoxy fragments.[15] These species are adsorbed to the TiO_2 nanotube surface occupying two active defect sites according to the following reaction (equation 7.4).[26] Because of the capture of free electron to the oxide surface, sensor resistance decreases effectively.

$$RCHO(vapor) \rightarrow ROH(vapor) + O^-(ads) \rightarrow [RO]^-(ads) + OH(ads) \quad \ldots(7.4)$$

where R represents the alkoxy group. Subsequently, the adsorbed alkoxy fragments recombine with the adsorbed hydroxyl ions and form the molecular alcohols, releasing a free defect site following the reversible process as[26]:

$$[RO]^-(ads) + OH^-(ads) \rightarrow ROH(vapor) + O(ads) \quad \ldots(7.5)$$

Two adsorbed hydroxyl groups then react with each other and release water and a free electron (offering a free defect site) following the reaction:

$$OH^-(ads) + OH^-(ads) \rightarrow H_2O + O(ads) + e^- \quad \ldots(7.6)$$

The adsorbed alcohol (ROH) molecules can also be directly oxidized or dehydrogenated by the surface-adsorbed oxygen releasing free electrons (offering free defect sites) to the oxide surface that effectively reduces the sensor resistance of the n-type TiO_2 nanotube array as.[15]

During room temperature sensing, adsorption of the alkoxy group on the nanotube surface strongly depends on the availability of the oxygen vacant sites and the surface coverage of the alkoxy groups.[26,28] At any particular biomarker concentration, when surface coverage of the alkoxy groups is almost constant, response magnitude of a sensor is principally dominated by the availability of the free oxygen vacant sites (Vo).

Thus, we observe that the magnitudes of the amperage sensor response of Ni-TNA to the four CRC biomarkers are pertinent to the reaction mechanism proposed for each.

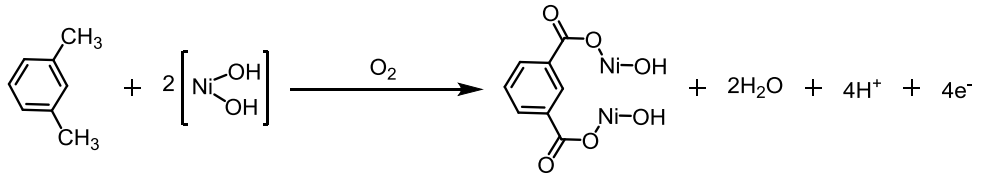

…(7.7)

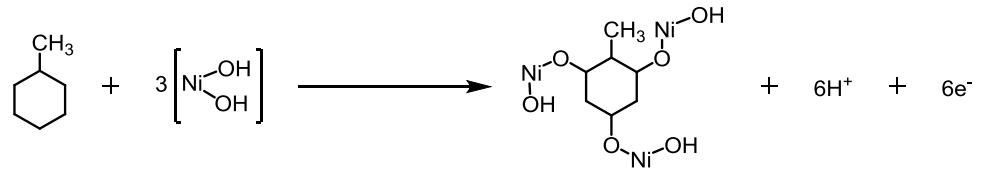

…(7.8)

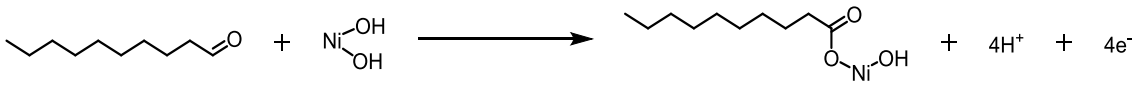

...(7.9)

6.4 Summary

Nickel functionalized TNAs have proven themselves to be strong contenders in the detection of cyclohexane vapour. Cyclic voltammetry studies as well as galvanostatic experiments demonstrate the necessity of not only precise morphology of the TNA array but also the presence of nickel as $Ni(OH)_2$ for the detection of these vapours. To account for the sensor response recorded, a reaction mechanism has been proposed. The mechanism assumes the role of $Ni(OH)_2$ as a catalytic oxidizing agent capable of oxidizing cyclohexane with a combine force of the valence band holes of TiO_2 and the reduction of the radical OH^- groups. This leads to the formation of a complex between nickel and the cyclohexyl radicals that is then possible further oxidized by the superoxide anion generated by TiO_2 by reducing atmospheric O_2 gas with the conduction valence band. This study establishes cyclohexane as a reducing gas capable of amperometic detection with aid of nickel as an oxidizing agent and provides a platform for future exploration in the field of VOCs and the implications of cyclohexane detection in biomedical diagnostics. Further studies are currently in progress for the detection of other VOCs implicated in colorectal cancer.

6.5 References

1. M. Phillips, J. Herrerab, S. Krishnanb, M. Zainb, J. Greenberg, and R. N. Cataneo, *J Chromatography B*, **729**, 75–88 (1999).

2. D. Bhattacharyya, Y. R. Smith, M. Misra, and S. K. Mohanty, *Mater. Res. Express*, **2**(2), 025002 (2015).

3. Y. R. Smith, D. Bhattacharyya, S. K. Mohanty, and M. Misra, *J. Electrochem. Soc.*, **163** (3), B83-B89 (2016).

4. C. S. Probert, T. Khalid, I. Ahmed, E. Johnson, S. Smith, and N. M. Ratcliffe, *J. Gastrointestinal. Liver Disease*, **18**, 337–43 (2009).

5. S. Meinardi, K. B. Jin, B. Barletta, D. R. Blake, and N. D. Vaziri, *Biochim. Biophys. Acta*, **1830**, 2531–7 (2013).

6. G. Peng, M. Hakim, Y. Y. Broza, S. Billan, R. Abdah-Bortnyak, A. Kuten, U. Tisch, and H. Haick, *Br. J. Cancer*, **103**(4), 542–551 (2010).

7. A. Z. Berna, J. S. McCarthy, R. X. Wang, K. J. Saliba, F. G. Bravo, J. Cassells, B. Padovan, and S. C. Trowell, *J Infect Dis*., **212**(7), 1120–1128 (2015).

8. F. R. Hirsch, W. A. Franklin, A. F. Gazdar, and P. A. J. Bunn, *Clin Cancer Res*, **7**, 5–22 (2001).

9. K. Kalogerakos, C. Sofoudis, and N. Baltayiannis, *Cancer Ther*, **6**, 463– 476 (2008).

10. O. Kronborg, C. Fenger, J. Olsen, O. D. Jorgensen, and O. Sondergaard, *Lancet*, **384,** 1467‑1471 (1996).

11. D. A. Ahlquist, J. E. Skoletsky, K. A. Boynton, J. J. Harrington, D. W. Mahoney, W. E. Pierceall *et al*., *Gastroenterology*, **119**, 1219‑1227 (2000).

12. M. C. de Haan, R. E. van Gelder, A. Graser, S. Bipat, and J. Stoker, *Eur Radiol*, **21**, 1747‑1763 (2011).

13. R. P. Arasaradnam, M. J. McFarlane, C. Ryan-Fisher, E. Westenbrink, P. Hodges, M. G. Thomas, S. Chambers, N. O'Connell, C. Bailey, C. Harmston, C. U. Nwokolo, K. D. Bardhan, and J. A. Covington, *PloS One*, **9**(9), e108750 (2014).

14. D. F. Altomare, M. Di Lena, F. Porcelli, L. Trizio, E. Travaglio, M. Tutino, S. Dragonieri, V. Memeo1, and G. de Gennaro, *Br. J. Surg.*, **100**(1), 144–150 (2013).

15. A. Hazra, B. Bhowmik, K. Dutta, P. P. Chattopadhyay, and P. Bhattacharyya, *ACS Appl. Mater. Interfaces*, **7**, 9336−9348 (2015).

16. M. G. Hosseini, M. M. Momeni, and M. Faraji, *Electroanalysis*, **22**(22), 2620–2625 (2010).

17. A. Alshammari, A. Köckritz, V. N. Kalevaru, A. Bagabas, and A. Martin, *Appl. Petrochem. Res.*, **2**(3-4), 61–67 (2012).

18. B. Sarkar, P. Prajapati, R. Tiwari, R. Tiwari, S. Ghosh, S. Shubhra Acharyya, C. Pendem, R. K. Singha, L. N. Sivakumar Konathala, J. Kumar, T. Sasakib, and R. Bal, *Green Chem.*, **14**(9), 2600 (2012).

19. P. R. Makgwane and S. S. Ray, *Catal. Commun.*, **54**, 118–123 (2014).

20. Y. Ide, N. Kawamoto, Y. Bando, H. Hattori, M. Sadakane, and T. Sano, *Chemical Communications*, **49**(35), 3652–3654 (2013).

21. V. Gaur, A. Sharma, and N. Verma, *Carbon*, **43**, 3041–3053 (2005).

22. S. Yolcular and Ö. Olgun, *Catal. Today*, **138**(3-4), 198–202 (2008).

23. Z. Li, D. Ding, Q. Liu, C. Ning, and X. Wang, *Nanoscale Res Lett*., **9**(1), 118 (2014).

24. Z. Wu, X. L. Huang, Z. L. Xu, J. J. Wang, H. G. Wang, and X. B. Zhang, *Scientific Reports*, **4**, 3669 (2014).

25. F. Cosandey, G. Skandan, and A. Singhal, *JOM*-e, **52**, 1–6 (2000).

26. J. M. Sturm, D.Göbke, H. Kuhlenbeck, J. Döbler, U. Reinhardt, M. V. Ganduglia-Pirovano, J. Sauerzand, and H. J. Freund, *Phys. Chem. Chem. Phys*., **11**, 3290−3299 (2009).

27. M. W. Ahn, K. S. Park, J. H. Heo, J. G. Park, D. W. Kim, K. J. Choi, J. H. Lee, and S. H. Hong, *Appl. Phys. Lett*., **93**, 263103 (2008).

28. M. Orzol, I. Martin, J. Kocisek, I. Dabkowska, J. Langer, and E. Illenberger, *Phys. Chem. Chem. Phys*., **9**, 3424−3431 (2007).

CHAPTER 8

ELEMENT INTEGRATION INTO SENSOR HARDWARE AND TESTING OF THE RESULTANT SYSTEMS IN APPLICATION ENVIRONMENT

The development of sensor systems for healthcare diagnostics or any other applications for that matter is a multistep process consisting of sensor element development, element integration into sensor hardware, and testing of the resulting sensor systems in application environments. Of the three steps mentioned, development of the sensor element constitutes the most critical aspect as it governs the sensitivity and specificity of the sensor towards the target of interest, which are disease-specific breath-based VOCs in our case. Having already developed the sensing material and established the sensing mechanism, limit of detection, and specificity of the sensor towards the VOBs of interest for tuberculosis in particular, and colorectal cancer in Chapter 2 through Chapter 6, this chapter is mainly geared towards development of a crude prototype to facilitate the integration of the sensing element into the hardware and subsequent field testing of the prototype in POC type application settings. Thus, production of sensor platform technology which can be flexibly tailored to meet broad application needs and integrated into hand-held devices is required.

These sensor elements must be packaged and integrated with hardware and

software, in order to be implemented for POC applications. Considerations related to application requirements and environments must be considered during the design phase of the sensor systems. Fundamental hardware design considerations include minimizing size, weight, power consumption, and minimum wired communication interfaces. Operational considerations such as the sensor operating temperature, capability to withstand changes in the sensor environment, and durability of the sensor system have strong roles to play in the viability of a sensor system to meet the requirements of a given application. Further, extensive testing of the resulting sensor systems in relevant environments for extended duration to determine the sensor life is a necessary step prior to long-term implementation. These tests are not simply of the sensor element or supporting hardware, but of the complete end-to-end system. Thus, our sensor system development has been driven by the need to broaden the operational capabilities of the various sensor platforms; to integrate sensors with hardware appropriate for implementation in low-income, resource-poor POC applications; and to test the complete sensor systems in relevant environments over the expected life of the sensors.

This chapter will investigate the extended testing for possible implementation of the functionalized titania (TiO_2) nanotubular array-based VOB sensor integrated into the customized sensing platform for healthcare triaging and diagnostic applications. The relevance of these sensing platforms to the broader program of advancing sensor systems for POC applications will be highlighted. However, prior to using the sensor systems for electrochemical detection of the breath-based biomarkers, standard GC-MS analysis will be performed on the breath samples to verify the presence of the biomarkers, which in-turn will act as a reference for comparison purposes. This will help us in establishing the

full proof accuracy of the sensor in detecting disease VOBs and rule out possible, erratic false-positive signals, if any. This will particularly enable the sensor to cement its place in the competitive market upon commercialization. It is concluded that the development and application of such low-cost, efficient sensor technology is both a multidisciplinary and multistage project involving different technological capabilities and requirements for each stage of the process.

8.1 Gas Chromatography – Mass Spectroscopy Analysis

8.1.1 Method

Prior to the use of Co-TNA sensor for the electrochemical detection of the TB biomarkers indicating its presence or absence in sick or healthy subjects, respectively, solid phase microextraction (SPME) fibers were used to analyze the breath samples.

Solid phase microextraction is a fast, solventless alternative to conventional sample extraction techniques. In SPME, analytes establish equilibria among the sample matrix (VOB solution), the headspace above the sample (VOB vapor), and a polymer-coated fused fiber, which then are desorbed from the fiber to a chromatography column. Since analytes are concentrated on the fiber, and are rapidly delivered to the column, minimum detection limits are improved and resolution is maintained. SPME is compatible with analyte detection by gas chromatography, and provides linear results for wide concentrations of analytes.

First, accurate identification of the retention times and the corresponding peak positions for each of the VOB vapors was achieved using gas chromatography coupled with a mass spectroscopy (GC-MS) (Shimadzu 2010S). It was envisaged that obtaining

the chromatograms at different concentrations would help in establishing a calibration method. To remove volatile contaminants, the fiber was preconditioned for an hour in the hot injector of the GC-MS at 250 ˚C and a chromatogram was recorded as the baseline. Further, 2 ml of known concentrations (1, 10, 100 mM) of individual VOB solutions in ethanol was tested using the fiber. The fiber was introduced through a septum into 50 ml qorpak bottles containing the standard solutions and conditioned for an hour at 35 ˚C (to mimic body temperature). The conditioned fibers were immediately tested through the GC-MS with the temperature of the injector and the transfer line maintained at 250˚C (split less injection 10:1). The column was maintained at 60 ˚C for 2 minutes followed by ramping to 250 ^{o}C over 12.5 minutes. A RTX-5MS column was used having a length of 30 m. The thickness and diameter were 0.25 µm and 0.25 mm, respectively. The carrier gas, Helium flowed steadily through the column at a constant rate of 1.04 ml/min under 60.6 kPa inlet pressure with a total flow rate of 11.9 ml/min. The linear velocity was 37.2 cm/sec while the purge flow was around 0.5 ml/min. For the mass spectroscopy, the ion source temperature was maintained at 200˚C while the interface temperature was 280˚C. The retention time for each biomarker was recorded. The procedure was repeated at different concentrations of each biomarker keeping the method (which contains the analysis parameters) constant. In addition, the SPME fiber was inserted into the sensor setup as well to determine the concentration of the VOBs in the vapor phase reaching the sensor substrate. Hence, in the same experimental set-up (as described in the previous chapters) sans the electrode connections, the fiber was introduced in the sensing chamber and held for 5 minutes followed by testing using GC-MS. After having determined the retention time for each of the four TB biomarkers and having established the calibration

curve to reveal the concentration of the VOBs at the sensor, the presence of the biomarkers in breath of actual TB infected subjects was verified as well. The breath of the TB patients were collected in tedler bags from various countries in the world viz. Uganda, Greece, Vietnam, India, etc. to establish the demographic variability and brought to University of Utah. Breath from a young male and old female infected with TB was also collected to investigate the age and gender factor. The SPME fiber was pierced through the septum in the mouthpiece of the tedler breath bag and conditioned at 35˚C in a MTI oven for 1 hour before being analyzed using the GC-MS with the method established for calibration. Similar measurements were also performed for breath collected from healthy, suspected TB, and drug resistant (DR) subjects.

8.1.2 Results and Discussion

8.1.2.1 Individual VOB analysis. Vapor phase analysis of the VOBs was conducted using an SPME fiber. To determine the concentration of the vapor reaching the sensor surface, a calibration curve was generated exposing the fiber to various concentrations of the individual biomarkers in ethanol and the vapor phase analyzed by GC-MS (Figure 8.1). The chromatograms, normalized against the baseline, reveal a systematic increase in peak height with increase in concentration of the biomarkers. The retention time for the respective biomarkers using the method described in the experimental section was found out to be as follows: methy nicotinate ~6.68 minutes; methyl p-anisate ~8.48 minutes; methyl phenylacetate ~6.96/7.16 minutes; and o-phenylanisole ~9.69 minutes. These values are in close agreement to the retention time observed by Syhre et al. using a similar protocol. Variation in concentration clearly

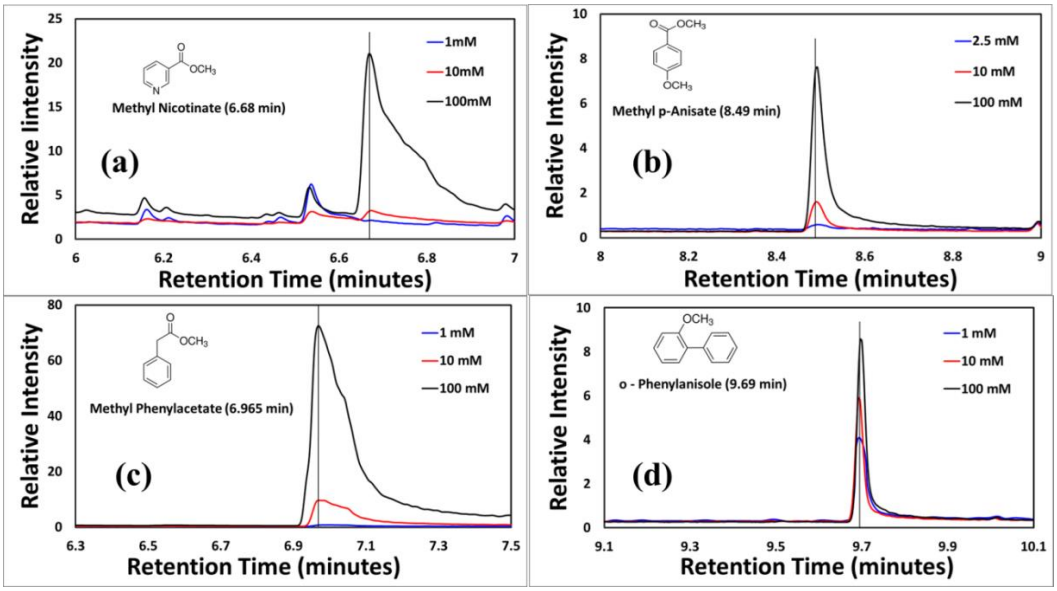

Figure 8.1. The individual biomarkers illustrating the distinct retention time at which they are eluted. (a) methyl nicotinate ~6.68 minutes; (b) methyl p-anisate ~8.48 minutes; (c) methyl phenylacetate ~6.96/7.16 minutes; and (d) o-phenylanisole ~9.69 minutes. The chromatograms, normalized against the baseline, reveal a systematic increase in peak height with increase in concentration of the biomarkers.

indicates a monotonically increasing trend in the peak intensity for the biomarkers at their distinctly, respective retention times. However, in real-life situations, it is practical to assume that all the biomarkers present in breath will be in a mixed state. Therefore, 2 ml of an ethanolic solution with all the four biomarkers (10 mM concentration) mixed together was collected in the 50 ml bottle and equilibrated with the SPME fiber for about an hour. Subsequently, the fiber was analyzed using GC-MS. Results indicated in Figure 8.2 indicate the presence of all the four biomarkers at the respective retention times mentioned earlier. Further, it is interesting to note that the intensity of the VOB peaks from the vapor of the 10mM mixed biomarker solution is equivalent to the intensity of the 10 mM peak obtained from individual biomarkers. This lucidly illustrates that all the four biomarkers are expressed well in the chromatogram when mixed together as they are when examined individually.

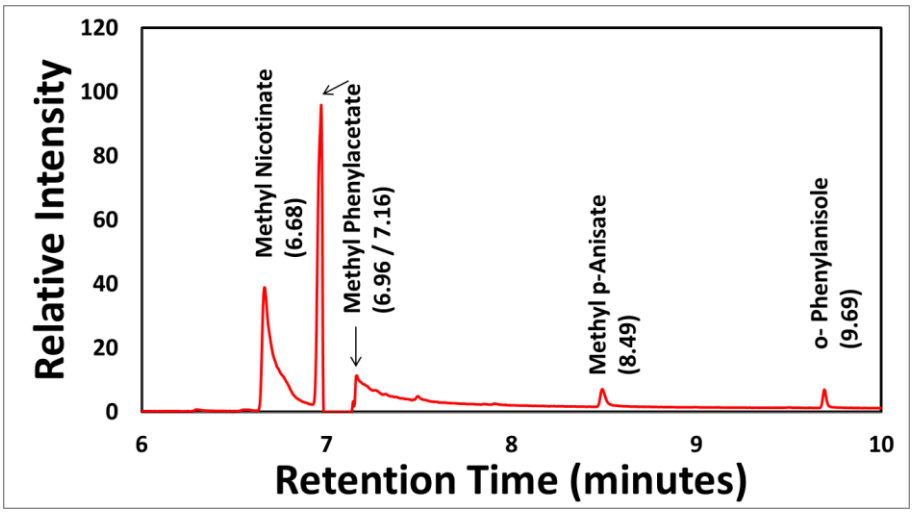

Figure 8.2. Chromatogram obtained from GC-MS analysis of the vapor using an SPME fiber from an ethanolic solution containing 10 mM of all four TB biomarkers mixed together

Interestingly, analysis of the mixed vapor reveals that methyl phenylacetate has a small shoulder-waning peak at 7.16 minutes in addition to the characteristic peak at 6.96 minutes. To determine the concentration of methyl nicotinate in the vapor phase, first a set-up was built in which the methyl nicotinate vapor was passed through the cold trap immersed in liquid nitrogen and the condensate was analyzed by the fiber using the procedure described earlier in this section for obtaining the chromatograms from the standard solutions. The condensate collected over an extended time was analyzed using the GC-MS. The normalized chromatograms (Figure 8.3) reveal that the concentration of the condensate is close to 10mM, which was incidentally the concentration of the parent solution. In this light, it would be too ambitious to assume that the concentration of the vapor reaching the Co-TNA sensor is also 10mM.

It is important to note that although the concentration of the biomarker in solution is ~10 mM, the concentration of the vapor at the sensor is anticipated to be much lower.

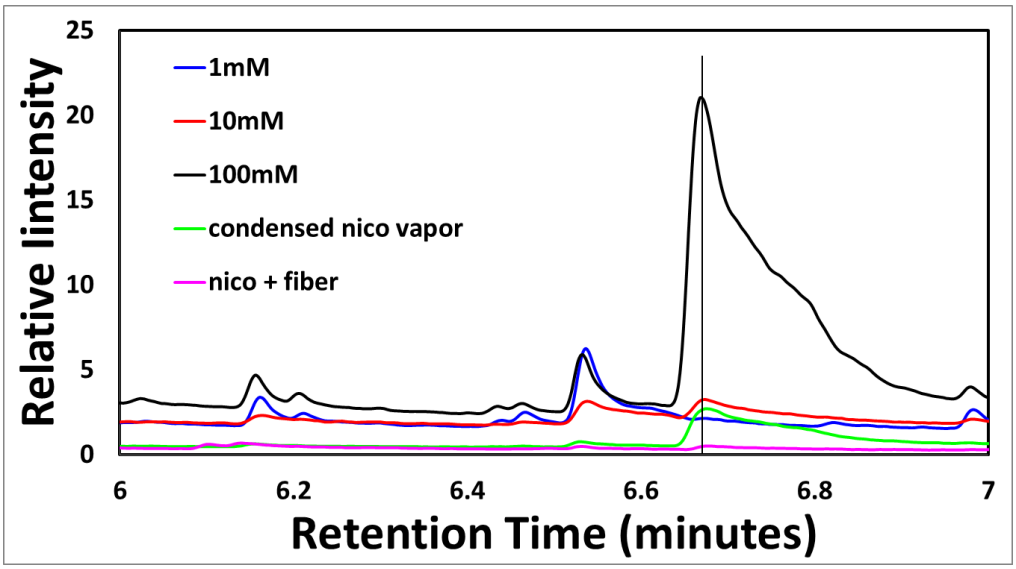

Figure 8.3. Chromatogram of the nicotinate vapor analyzed from the condensate (green) using the cold trap in comparison to that analyzed by the fiber directly (pink). Results indicate that the latter method gives a more probable estimation (2mM) of the concentration of the VOB reaching the sensor substrate.

In a separate experiment, concentration of the VOB vapor reaching the sensor substrate was determined by directly introducing the fiber into the sensing chamber for the duration of exposure of Co-TNA sensor to methyl nicotinate vapor. The chromatogram as recorded from the fiber revealed that the concentration of methyl nicotinate in the vapor phase is much less than 10 mM as expected. A reasonable estimation of the vapor phase concentration based on the calibration obtained previously would be ~2 mM. This gives a clear picture that the concentration of VOBs in the vapor phase actually reaching the sensor is much less than that in the solution. Although the experiment performed with methyl nicotinate is illustrated in Figure 8.3, the other biomarkers showed a similar trend and have not been shown here. Hence, it would not be unreasonable to presume that the Co-TNA sensor is highly sensitive towards small quantities of the biomarkers in the vapor phase.

A crucial observation from the aforementioned results demonstrates that the concentration of the condensate of the vapor collected in the cold trap is almost equal to the concentration of the parent solution, which presents an agreeable argument. On the contrary, the concentration of the nicotinate vapor in the sensing chamber is much lower due to the chemical interactions taking place at the titania nanotube surface. This also indicates that the biomarker is chemisorbed on the titania nanotube surface to some extent, resulting in a lowered measurable concentration of the vapor.

7.1.2.2 Breath analysis. Successful identification determining the presence/absence of the biomarkers can enable rapid screening of suspected cases and is important from an early diagnostic standpoint. After having established the method for accurate identification of the VOB vapors using GC-MS, the research is extended towards clinical study involving actual infected TB patients. Hence, breath samples from patients were collected in tedler breath bags and analyzed by GC-MS at the University of Utah. Prior to using the sensors for electrochemical detection of the breath biomarkers, it is imperative that we verify the presence of these biomarkers in the breath samples. But working with breath biomarkers from actual human subjects is different from VOB vapor mimics and presents with several challenges. People's food habits vary based on demographics and cause difficulties in analysis of breath specimens. Age and gender can also contribute to differences in concentration of VOBs in breath. Further, instances of drug-resistant TB can complicate things a bit. Hence, the following comparisons were made to incorporate the effect of different variabilities: TB patient vs. healthy subject (Figure 8.4); young male vs. old female (Figure 8.5); and TB vs. drug-resistant TB patients (Figure 8.6).

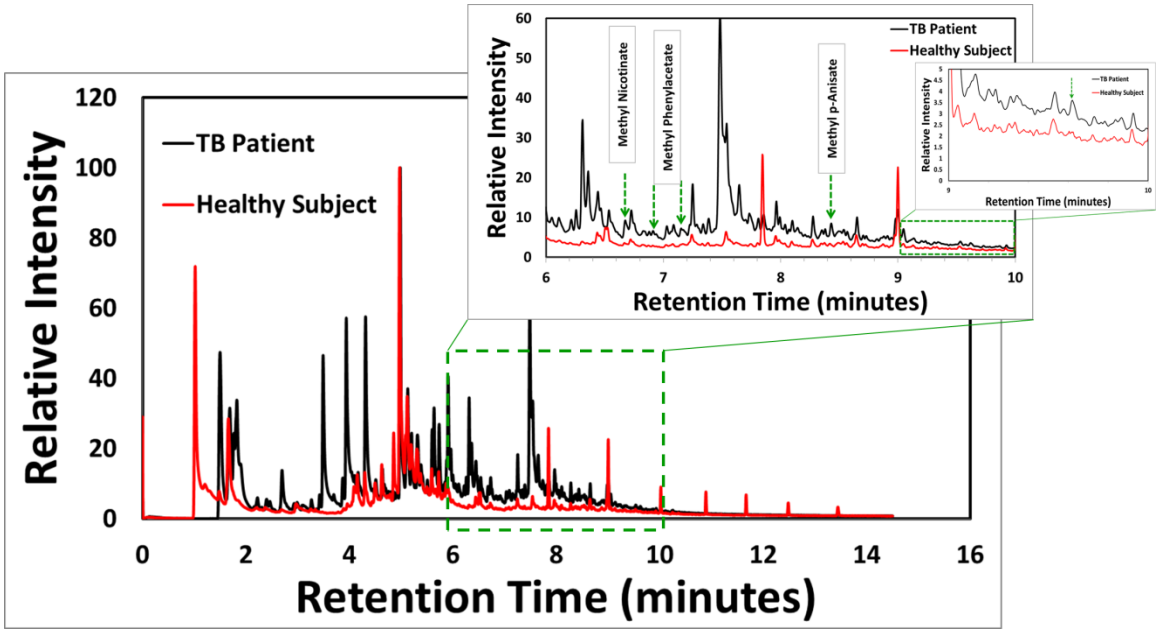

Figure 8.4. GC-MS chromatogram of breath from TB patient and healthy subject. The VOB peaks are succinctly expressed in the TB patient.

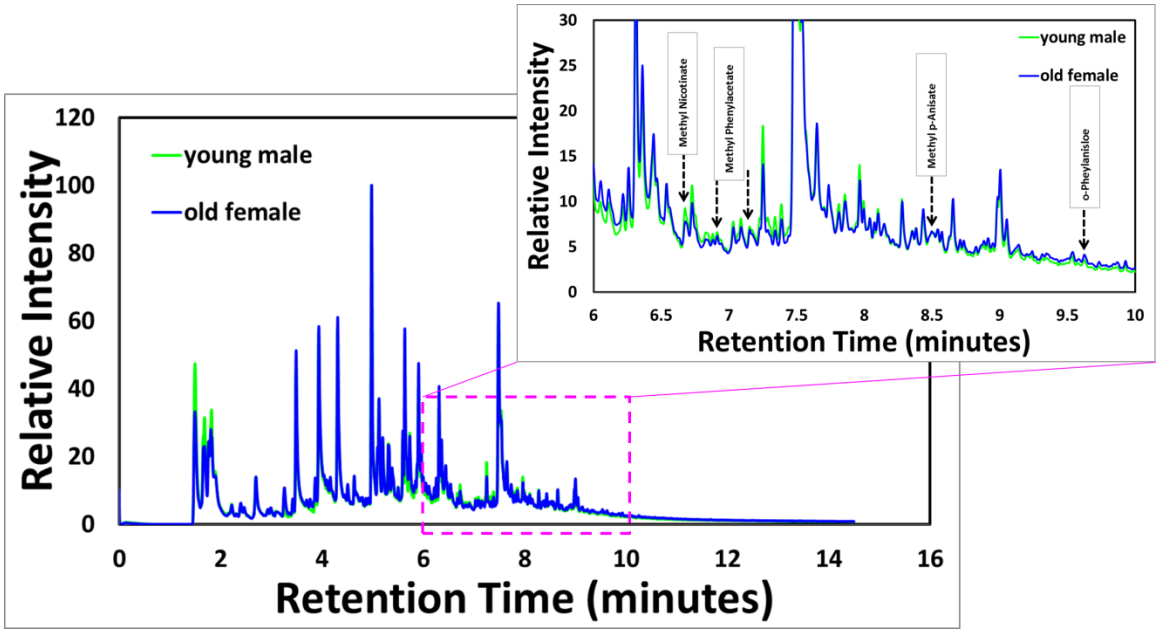

Figure 8.5. GC-MS chromatogram of breath from young male and old female TB patient. The spectra almost overlaps each other with little to differentiate between them.

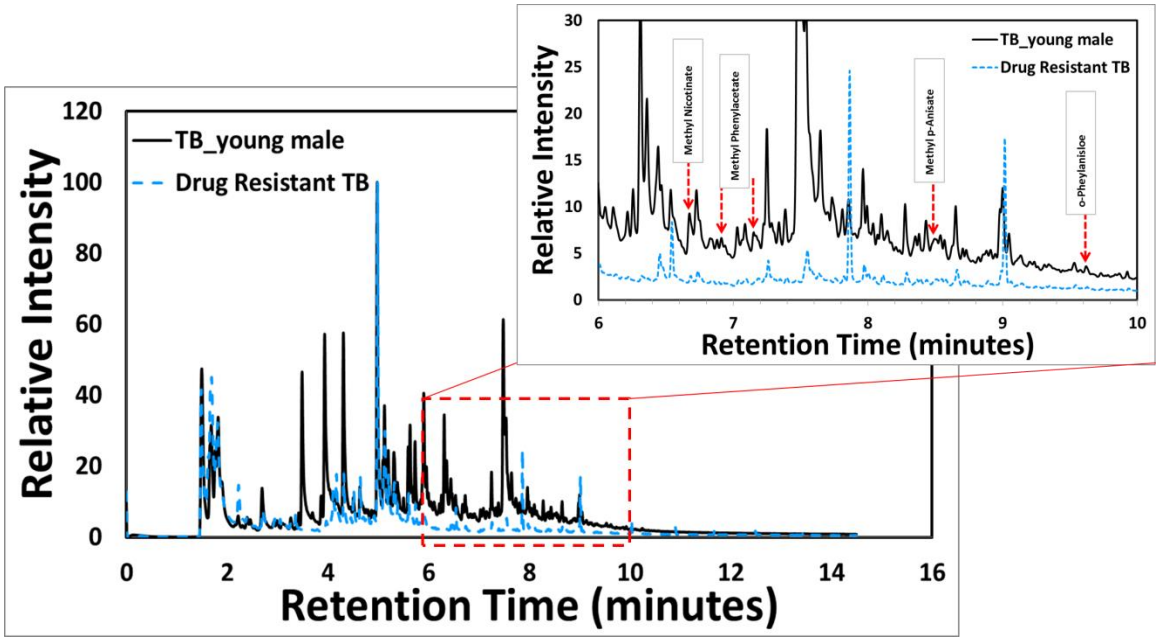

Figure 8.6. GC-MS chromatogram of breath from TB infected young male and drug resistant TB patient. The spectra show small quantities of biomarkers leftover in the breath of drug resistant patient after medication.

Figure 8.4 illustrates that the four specific TB biomarkers are not present in the breath of the healthy subject. This provides confidence in our presumption that the sensor can be expected to be specific towards TB. When it comes to age and gender, the chromatogram spectra for the breath from young male and old female (Figure 8.5) appear to be exactly overlaid on top of each other. The biomarkers from both the patients are quantitatively identifiable and are expected to be detected by the sensor. The breath derived chromatogram comparison between a young male infected with TB and a patient having a drug resistant variant type of the mycobacterium is demonstrated in Figure 8.6. Multi-drug-resistant tuberculosis (MDR-TB) is defined as a form of TB infection caused by bacteria that are resistant to treatment with at least two of the most powerful first-line anti-TB drugs, isoniazid (INH) and rifampicin (RMP). Although the level of the

biomarkers has fallen due to action of the drugs, the biomarkers are still present in identifiable quantities, which gives us hope that MDR-TB patients can be triaged by the proposed functionalized titania nanotube array-based sensing platform. The food habits of people around the world might contribute to variability in the breath VOCs as well. GC-MS-based breath profile analysis for a wide range of population of TB patients covering demographics, age, gender, and MDR type is illustrated in Figure 8.7.

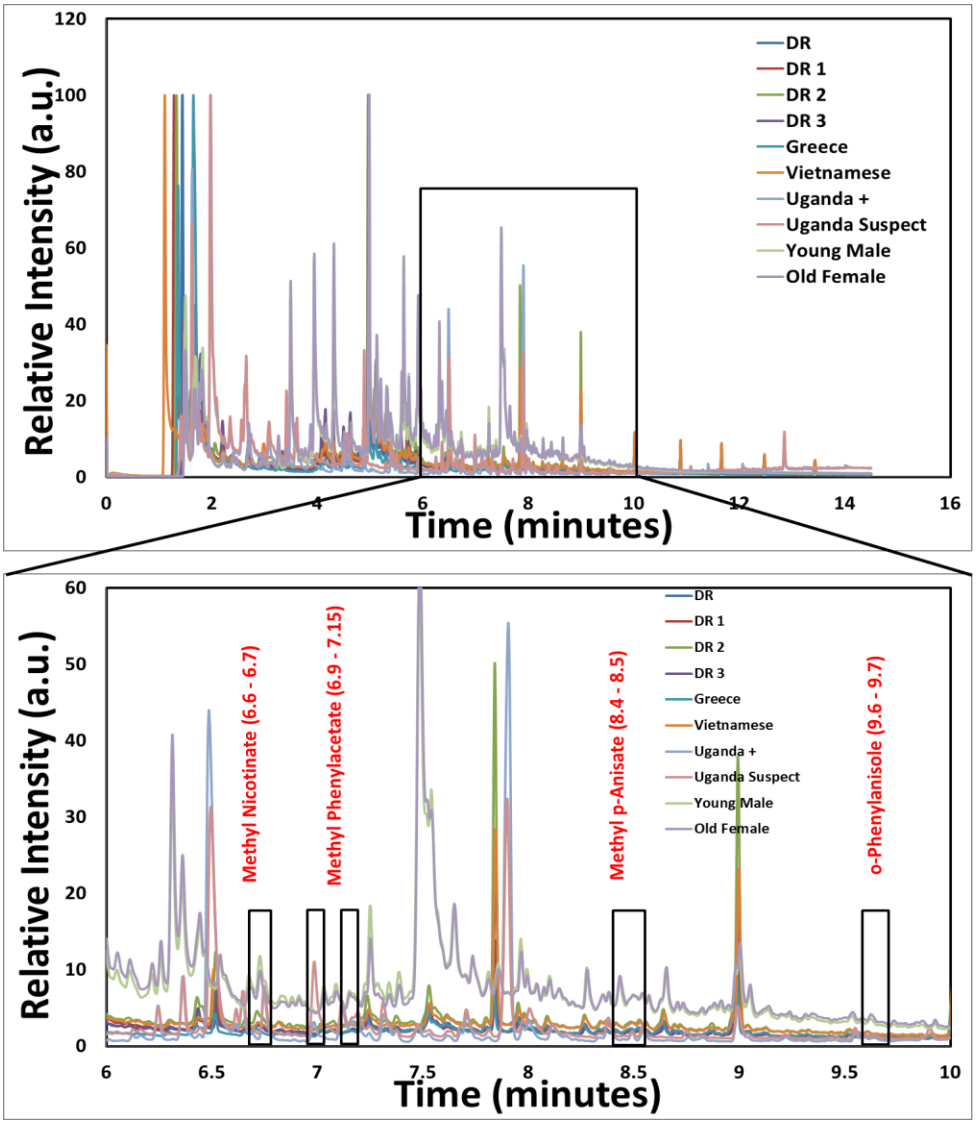

Figure 8.7. Breath profile analysis for a wide range of population of TB patients with the position of the four biomarkers indicated.

It is thus evident from Figure 8.4 through 8.6 and further reinforced in Figure 7.7 that although the four specific VOBs are present in confirmed TB cases throughout the world, their levels vary in the breath form case to case and place to place. The exact reason for the varying VOB levels, though unknown, can be attributed to the severity of the disease or particular food habits. A summary of varying VOB levels measured from confirmed TB cases with patients from different parts of the world is presented in Figure 8.8. Results indicate the VOB levels are particularly higher in patients from South America and Uganda, while are much lower in cases from Europe and Asia. This is not very surprising as researchers have theorized that humans first acquired it in Africa about 5,000 years ago.[1] It spread to other humans along trade routes and to domesticated animals in Africa, such as goats and cows, giving rise to its bovine variants. Sea animals breeding on African coasts are believed to have acquired and carried the disease across the Atlantic to South America.

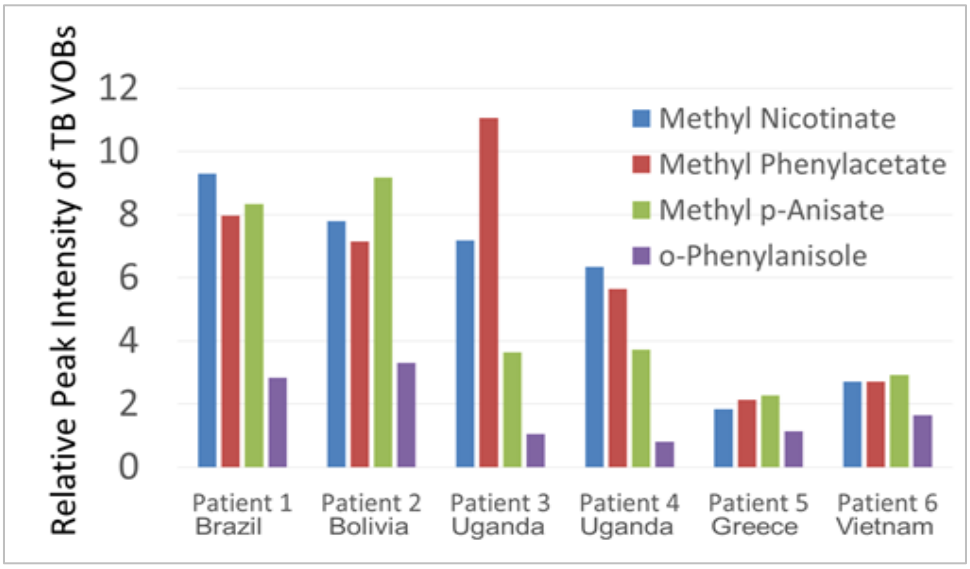

Figure 8.8. Preliminary Results: Levels of TB VOBs measured from confirmed TB cases with patients from different parts of the world.

8.2 Sensor Integration into Hardware

The end-of-phase goal for this project was to develop a novel, low-cost, solid-state functionalized titania nanotube array (TNA)-based sensor which can be integrated into a hand-held device providing portable and noninvasive sensing method with reduced detection time (minutes) and high sensitivity, which is suitable for point-of-care (POC) diagnosis. A schematic cartoon as illustrated in Figure 8.9 envisages that the goal can be realized by integrating the indigenously developed functionalized titania nanotube array (TNA)-based sensor with a portable breathalyzer attachment connected to a display medium such as a smartphone/tablet/or laptop. Although, development of the sensor element is very critical from the standpoint of establishing the sensitivity and selectivity of the sensor, element integration into the hardware plays an important role in determining the overall feasibility and operability of the device. While the sensor element has undergone several evolution steps as demonstrated in Chapter 2 through 6, this chapter focusses our effort on the sensor integration into a customizable hardware. The first-generation optimized Co-TNA sensors achieved by the incipient wetting impregnation method will be used for the first round of clinical study.

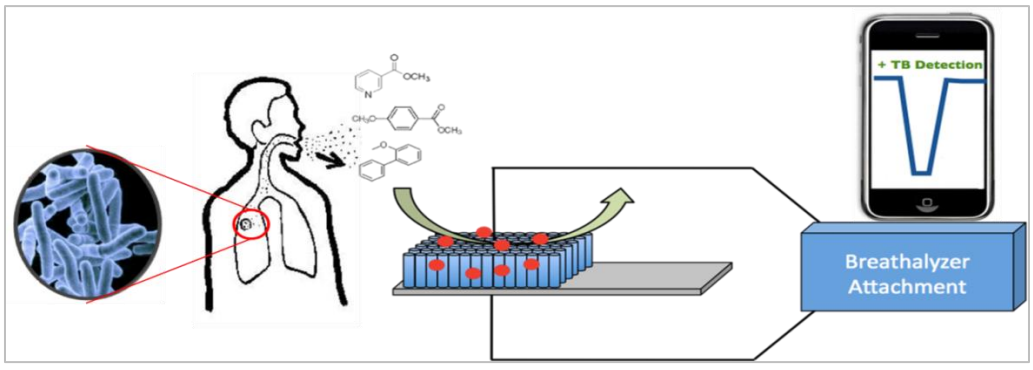

Figure 8.9. Schematic cartoon of the proposed device enabling integration of the sensor element with the hardware.

The individual components comprising the sensing platform are illustrated in Figure 8.10. Various tedlar type breath bags for breath sample collection were supplied by SKC. A Corning 28mm diameter syringe filter (0.2 µm pore) was connected to the bag using Tygon tubing in order to filter out any mycobacterium which might be present in the breath and can potentially soil the sensor upon contact. A SKC GrabAir bag sampler pump with variable flow rate was used to withdraw the breath from the bags and deliver it to the sensing chamber. The design of the customized sensing chamber was conceived in our lab and fabricated using a Makerbot 3D printer. The sensing chamber having dimensions of 3 cm x 3 cm x 2.5 cm has a protruding nozzle like inlet and a tiny outlet. The 4.5 cm long sensor strips were 3D printed as well and was 1 cm (for inserting into sensor port) in width at the base and 1.8 cm towards the top to hold the senor, 1.5 cm x 1.5 cm in dimension. The sensor port having electrical connections was supplied by PalmSens Inc, who also provided the EmStat*MUX8* hand-held potentiostat (Figure 8.11).

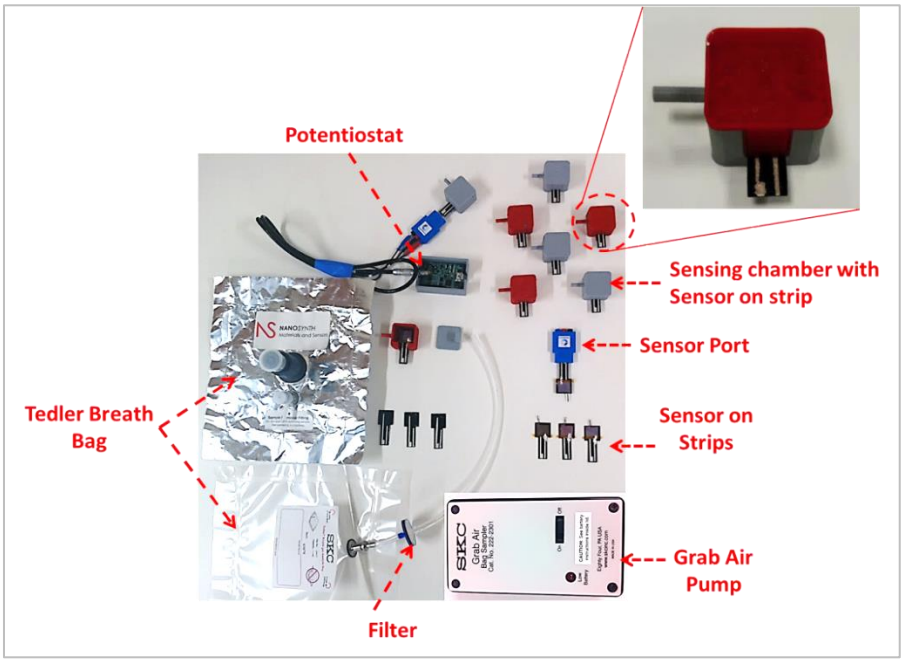

Figure 8.10. The individual components comprising the sensing platform

Figure 8.11. Enlarged view of the sensing chamber housing the sensor on the strips, which is inserted into the sensor port and connected to the potentiostat. (inset) EmStat *MUX8* potentiostat.

For making the electrode connections on the strips on which the sensor is placed, a Silhouette CAMEO electronic cutter was used to cut out a stencil, which was then placed on the sensor strips. Epoxy mixed silver paint was used to fill the vacant areas of the stencil followed by drying at 80˚C on a hot plate for 20 minutes to allow the paint to dry. The working electrode was extended to connect the functionalized titania nanotube side while the reference and the counter electrode was extended to connect the reverse Ti side of the sensor.

The individual components of the sensor were assembled to develop a crude prototype of our proposed sensing platform / device for field testing. An illustration of the complete process flow from patient's breath collection to analysis by the sensing device and subsequent mapping or data tracking is shown in Figure 8.12.

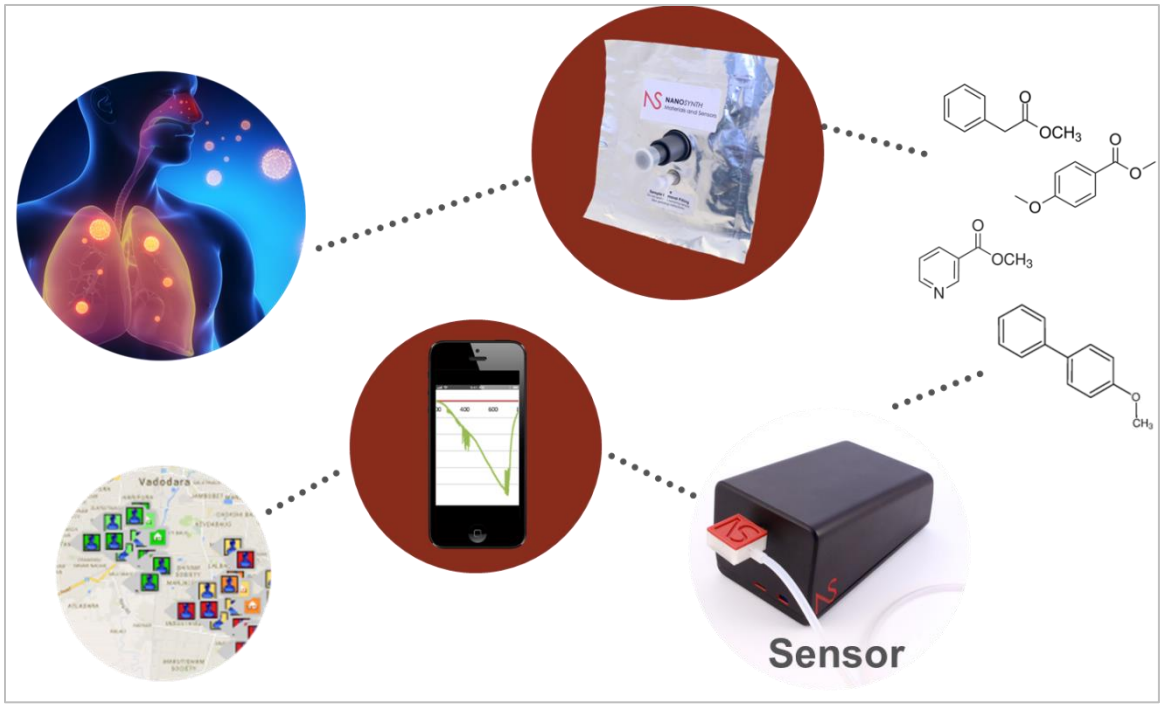

Figure 8.12. Flow chart of the proposed solution for tackling the TB epidemic. This includes collection of patient's breath, analyses by the sensing device, and data tracking.

The TB patient, after being screened positive for the bacterium, has to undergo prescribed medication regimen for almost 6 months and needs to be periodically monitored. The World Health Organization (WHO) mandates that active TB patients have to be tracked continuously for well-being of the patient as well as to prevent spreading the disease. Thus, from a value proposition standpoint, it is proposed the sensor, marketed under the aegis of Nanosynth Materials and Sensors, will be integrated with a data mapping and aggregation platform that combines the screening results with other epidemiological data to allow the tracking of the TB identification efforts. Because the test is fast, we expect to be able to gather real-time information that may be useful in understanding the factors that contribute to the transmission of TB. Some of the more common factors that researchers suspect to affect TB and are currently trying to gather

information about are air pollution and tobacco use. The required data have to be "mined" from databases which is a long and time-consuming process. Real-time data gathering eliminates this problem and allows this potentially relevant information to be immediately accumulated. This data platform will also aid community health care workers in the field by linking data that are not effectively integrated into screening programs such as targeting family members or coworkers who may be infected and clearing them upon a negative screening result. This will allow healthcare workers in the field to know where potentially infected persons live and when a household has been cleared. Work is currently underway to develop and examine the data tracking platform.

7.3 Assessment of Sensing Platform's Response to Breath

Having already established the presence of VOBs in the breath of TB patients using GC-MS in Section 7.1 and having put together a potential sensing platform/device in Section 7.2, this section will investigate the deployment of the device in the field through a pilot study. The purpose of this pilot study is to evaluate the sensitivity, specificity, and convenience of use of a POC breath-based TB screening test as compared to the current standards of care, including sputum microscopy, sputum culture, chest X-ray, and GeneXpert MTB/RIF. The results of the POC TB Breath Test will not be used in the medical decision-making process. The primary objective is to determine an initial estimate of the sensitivity and specificity of a nanotube-based point-of-care test for the screening and diagnosis of active pulmonary tuberculosis. The secondary objective is to collect performance data to guide the design of subsequent studies and to facilitate the necessary marketing approvals from the government and other regulatory agencies. The

collected data will enable us to test and further develop the user interface and mapping platform that will be used in conjunction with the testing sensor based on end-user feedback.

Based on feedback from clinicians and published reports from groups such as the FIND and the WHO, the POC TB Breath Test should meet the following clinical requirements to serve as a screening or triage test: sensitivity: >90%; specificity: >70%; time to result: <15 minutes; sample type: noninvasive, nonsputum; target user: community health worker.

The potential risks to the patients from participation in this pilot study are minimal as the test is a noninvasive test (uses only the patient's breath) and the results will not be used in the patient's medical care. The POC TB Breath Test is a noninvasive breath test with minimal risk to the patient during breath sample collection. Regarding diagnostic testing, each patient received current standard of care TB testing, including sputum microscopy, chest X-ray, and sputum culture (currently considered the 'gold standard' for TB diagnosis). Patients also received testing by GeneXpert, a WHO-recommended cartridge-based nucleic amplification assay for the simultaneous detection of TB and rifampicin resistance. Benefits of this study include the validation of a low-cost and highly portable TB diagnostic test that can potentially be used to screen large amounts of patients and refer them for further care (improving the patient's outcomes and lowering transmission of TB) while improving the use of TB resource utilization by focusing resource-intensive testing on the patients at the highest risk.

Although the POC TB breath test is able to detect all of the target biomarkers in a lab setting and in the small number of patients tested to date, a larger sample of patients

must be tested in order to gain a reasonable estimate of the sensitivity and specificity of the test and to guide future clinical testing. This is the most important part of the chapter as the results obtained from this pilot study will help determining the techno-economic feasibility of the sensing platform. Testing of a larger sample population of patients having active pulmonary TB is currently underway and has not been reported here to avoid conflict of interest issues. Results obtained from a few preliminary testing have been reported here.

Comparisons were made for sensor response obtained from exposure to air, a mixed 10 mM solution of VOB mimics, a healthy subject, a healthy subject's breath spiked with VOB, and a TB patient (Figure 8.13). Preliminary trial-and-error-based testing had showed that at the lowest flow rate setting of the pump, the breath bag can be completely emptied in 13 minutes. A multistep amperometric method was defined such that the sensor was conditioned in air at -0.5 V for 100s, after which the pump was turned on to deliver the vapor to the sensing chamber. A -0.5 V bias voltage was maintained for the next 100 s for detection of methyl nicotinate, after which the bias voltage was held at -0.8 V for 150 s. for detection of methyl p-anisate, and finally at -1.0 V for 430 s for detection of methyl phenylacetate and o-phenylanisole. Results indicate that when the sensor is exposed to air, the current decreases. This is consistent with our previous explanation that air scavenges electron from the conduction band of titania nanotubes, resulting in an increase in its resistance. The sudden spike in current is due to the periodic modulation of the bias voltage as programmed in the method. When exposed to VOB mimics mixed in ethanol, the current increases (μA) as expected, which is confirmed by the slope of the curve. This observation is consistent with our previous explanations that

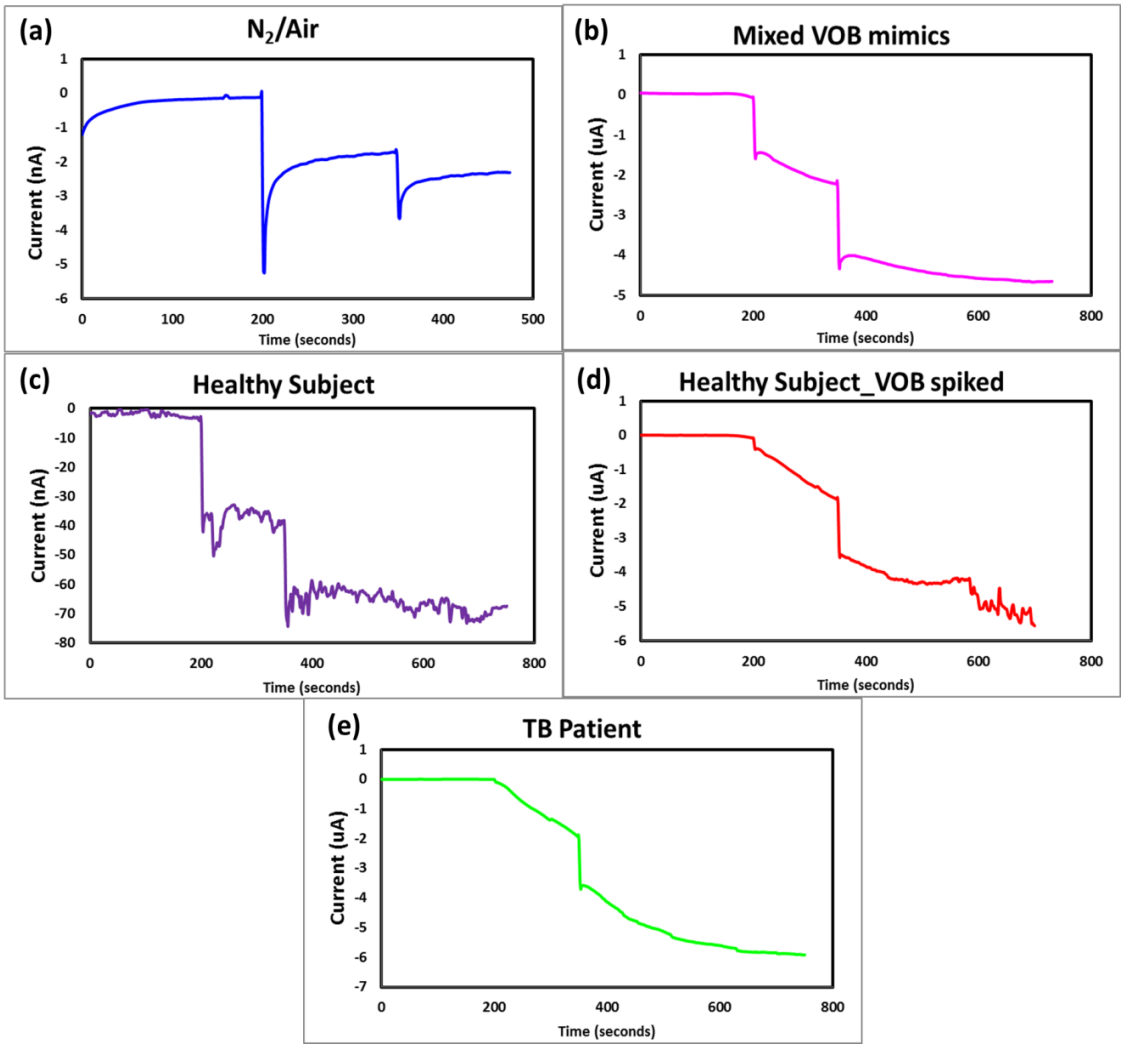

Figure 8.13. Multistep amperometric plots obtained using the TiO_2 nanotube array-based Nanosynth POC device upon exposure to (a) air; (b) 10 mM VOB mimics mixed in ethanol; (c) healthy subject; (d) VOB spiked healthy subject's breath; and (e) TB patient.

showed that the VOBs upon getting catalytically oxidized at the sensor surface donate electrons to neutralize the oxygen vacancies at the titania nanotube conduction band, rendering the nanotubes less resistive and resulting in an increase in current. When the sensor is exposed to the breath from a healthy subject, the current at the designated voltages remains steady (nA) and does not exhibit a slope. This demonstrates that the senor does not react to VOCs commonly found in healthy human being and is somewhat

selective towards the four TB VOBs. Finally, when the sensor was exposed to the breath of a TB patient, the amperometric current profile bore significant resemblance to that of VOB spiked healthy subject's breath profile as well as to the mixed VOB mimic vapor profile. This further proves that the sensor substrate is highly sensitive and selective towards the four TB biomarkers. Thus, based on the successful preliminary testing, the proposed Nanosynth POC TB diagnostic device demonstrated promising potential for upcoming scheduled field testing in a larger population through the pilot study.

8.4 Commercialization Opportunities

Currently, up to 80% of people tested for TB do not have active disease, thereby stretching limited and valuable resources that are used for diagnostic testing. By combining our low-cost and easy-to-use portable sensor with an analytics and tracking platform, the effectiveness of large-scale TB screening efforts can be significantly improved as we can rapidly and efficiently clear patients and narrow the population requiring expensive confirmatory testing. This will enable optimal deployment of diagnostic testing resources to the patients and areas most at risk for the disease, ultimately improving access to care and lowering the transmission rate and disease morbidity even in resource limited settings.

As has been mentioned before, currently, the global TB diagnostic testing is a billion dollar market out of which 65.63% or $676.7M is devoted for TB detection/monitoring alone. Latent TB diagnosis accounts for 34.17% or $352.5M whereas drug susceptibility gets a tiny share of 0.2% or $4.3M (Figure 8.14). In the major segment, i.e., detection and monitoring, the majority of money is currently being pumped

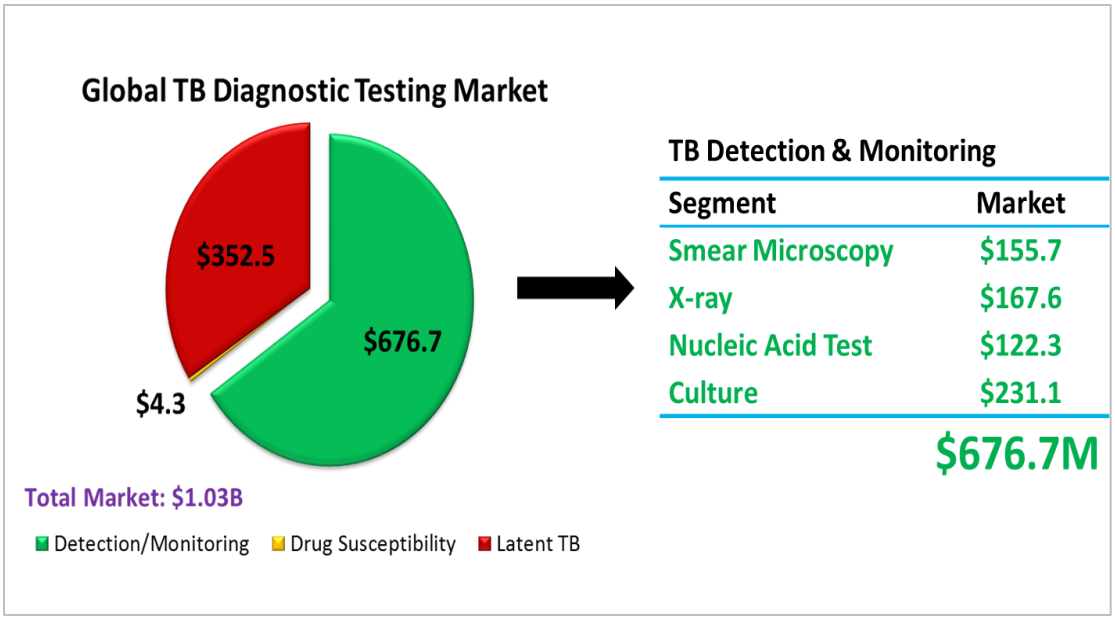

Figure 8.14. Pie chart showing the global TB diagnostic market.

into sputum culture-based testing since it is recognized as the "gold standard" by the industry. However, the sputum culture technique has its own limitation as the outcome can be affected by changes in culture medium and environment. In addition, it is a very time-consuming process. Smear microscopy and x-ray have lower sensitivity, and thus, cannot be very reliable. The nucleic acid amplification-based Gene Xpert has very high sensitivity and specificity with relatively small detection times. However, being a lab-based technique, it is definitely not suitable for POC setting and suffers from high costs. Therefore, the Nanosynth POC TB diagnostic platform has a potential of occupying a major chunk of the TB detection/monitoring market if its viability in terms of its sensitivity and specificity can be proved over time covering a larger sample population. It is envisaged that if the proposed diagnostic platform can prove its mettle and worth, it can revolutionize the TB diagnostic industry through easy-to-use, rapid, POC diagnostic technology with the estimated price being $2-5 per test, whereas the global average is

$15 per test.

8.5 Summary

The chromatograms obtained from the GC-MS analysis of the SPME fibers equilibrated with the VOB vapor from the mimics determined the retention times of the individual biomarkers. This helped in determining the biomarker peaks in the breath of actual TB patients. As revealed from the analysis, the four biomarkers were present in all the TB patients (young, old, male, female, MDR, different countries), albeit in varying quantities.

To examine the VOB vapors and the patient's breath, the first-generation Co-TNA sensor was packaged into a custom made device developed by 3D printing-based rapid prototyping. The sensor showed baseline signal when exposed to air and breath from healthy subject, whereas the spike in signal was observable when exposed to the VOB mimics, healthy subject's breath spiked with VOBs, and ultimately breath from a TB patient. It is anticipated that the sensor will evolve through the developmental stages aided by results from field testing.

CHAPTER 9

CONCLUSIONS

Research and innovation in disease diagnostic technologies can significantly improve the healthcare system and subsequently determine a proper treatment regimen for the infected patients. Tuberculosis (TB) is an extremely life-threatening disease, which, if not detected early, can claim numerous lives. Current diagnostic techniques, although they possess high sensitivity and specificity, are not suited for low-resource point-of-care (POC) settings as they suffer from high costs and portability issues. The need to triage patients at the POC is immense to arrest the spread of the disease. Through our research, we have demonstrated the capability of detecting TB biomarkers from the breath using a TiO_2 nanotube-based sensing platform, as opposed to the more conventional sputum or blood-based diagnostic techniques. Titania nanotubes were synthesized by electrochemical anodization and functionalized using various methods to maximize the sensor response. The salient features of the research have been summarized below.

A systematic approach establishing the favorable combination of stoichiometry and geometry of the cobalt functionalized titania nanotubes for optimizing the biomarker sensing performance has been presented in Chapter 2. Experimental and theoretical evidences suggest that diameter and length of the nanotubes does

not have any significant impact on the sensor response. The water content of the anodization bath influences the concentration of the oxygen vacancies (Vo) in the nanotubes and the tube wall separation which directly affects the surface-to-volume ratio (SVR). The stoichiometry of the nanotubes (Vo) was optimized by varying the water content (0.5 wt%, 3 wt%, and 10 wt%) in the fluorinated ethylene glycol-based electrolyte. The most promising sensor performance in terms of the response magnitude was obtained when anodization was performed in a bath containing 3 wt% water at 30V for 1 hour. This presented an optimal balance of the charge carrier density (analogous to Vo) and surface-to-volume ratio. The extremes had either higher Vo and lower SVR or lower Vo and higher SVR, respectively. The second half of the chapter illustrates the significance of nanotube wall thickness (geometry) on sensor response. The wall thickness of the nanotubes (t) was optimized by varying the temperature (10, 25, and 50˚C) in the fluorinated ethylene glycol-based electrolyte containing 3 wt% water. Results indicated that the anodic sensor synthesized at room temperature having an inherent wall thickness of ~14 nm exhibited the maximum sensor response. This is because the dimension of the half wall thickness (t/2) was equivalent and comparable to the width of the depletion region (Lw). As for anodic coupons synthesized at the extreme condition, they had $t/2<Lw$ or $t/2>Lw$, respectively, and suffered from charge transport properties. Thus, titania nanotubes fabricated using the optimized recipe (96.5% EG + 3% water + 0.5% NH_4F at 30V for 1hr @ 25˚C) yielded maximum sensor response.

In Chapter 3, the electrochemical sensing of the four predominate biomarkers has been discussed in detail. The first part of the chapter describes the semiconductor – biomarker interaction mechanism through electrochemical detection of methyl nicotinate

biomarker vapor. Functionalization of the TNA with cobalt (Co-TNA) was found to be necessary for methyl nicotinate detection. Titanium dioxide films synthesized through high-temperature oxidation and functionalized with cobalt were also compared with cobalt functionalized TNA. The ordered TNA was demonstrated to be an effective substrate for cobalt deposition and subsequent biomarker detection over thin titanium dioxide films. Surface analysis of the cobalt functionalized TNA by XPS studies observed that cobalt deposits exist as cobalt hydroxide on the surface. Exposure of the sensor surface to methyl nicotinate vapor results in the reduction of cobalt hydroxide to cobalt metal on the surface. Two mechanisms have been proposed to describe the binding of the nicotinate biomarker to cobalt functionalized TNA consistent with the XPS studies and band theory. Band theory confirms that a reducing gas, such as methyl nicotinate vapor upon interaction with a n-type semiconductor, leads to a decrease in resistance, as indicated by the amperometric studies.

The second part of the chapter extends the investigation to explain the detection of the other biomarkers as well, with more emphasis on determination of the limit of detection, specificity, and reaction kinetics. Highly ordered titania nanotubular arrays (TNA), functionalized with cobalt using the incipient wetting impregnation method, were utilized as a robust sensing platform for electrochemical detection (amperometric mode) of four prominent tuberculosis volatile biomarkers. The limit of detection of the sensor was determined to be ~0.018 ppm VOBs, with the sensor exhibiting higher selectivity towards the VOBs over other organics commonly found in breath. The sensor response theory modeled using Butler-Volmer kinetics at high overpotentials (Tafel behavior) corroborates well with experimentally derived signal responses. Of the four VOBs

examined, methyl p-anisate exhibits the maximum current response (81 µA), while methyl nicotinate demonstrates the fastest reaction kinetics, or response time (35 seconds). The development of doped 1D nanostructured metal oxide semiconductor-based sensors demonstrates enhanced sensor response with rapid detection times appropriate for POC disease diagnosis.

A new method describing the fabrication of a highly sensitive sensor through a one-step anodization-co-functionalization technique is presented. The synthesis method developed allows for in situ functionalization of titania nanotubes (*i*Co-TNA) with oxygen containing metal species (i.e., $Co(OH)_2$) during anodization. Amperometric detection of volatile organic biomarkers with concentrations of 275 ~ 360 ppm using next generation titania nanotubes functionalized with $Co(OH)_2$ were compared with $Co(OH)_2$ functionalized titania nanotubes via the wet incipient method. Improved sensor response and sensitivity was observed with next-generation titania nanotubes, which can be attributed to homogeneous distribution of reactive sites directly in contact with the parent titania. A mechanism for sensor response and in situ functionalization has also been presented.

In an unprecedented change in the sensing methodology, light assisted sensing of the TB biomarkers using gold functionalized TiO_2 nanotubes (Au-TNA) has been demonstrated. Gold functionalization was achieved through a novel electroless deposition technique using gold thiosulfate in an ascorbic acid bath. The sensor utilizes the synergistic effect of the slow photon region of the nanotubes (due to the high refractive index of titania) and the localized surface plasmon resonance (LSPR) behavior of the gold nanoparticles to enhance charge transport properties under visible light illumination.

Results indicate that the signal response under irradiation is orders of magnitude greater than in dark. Mechanistic schemes based on band theory and molecular orbitals further illustrate the sensing phenomenon. This opens up avenues for further research in this area.

Based on the result of these studies, the performance of the sensors from each study, i.e., Co-TNA, *i*Co-TNA, and Au-TNA, was compared with one another. The response magnitude was obtained using a simple equation to calculate the ratio of the difference between the maximum current (VOB) and base current (air) to the base current and plotted against the four predominate biomarkers, as shown in Figure 9.1. The highest sensor response value was achieved using gold functionalized titania nanotubes equipped with an optimized stoichiometry and geometry.

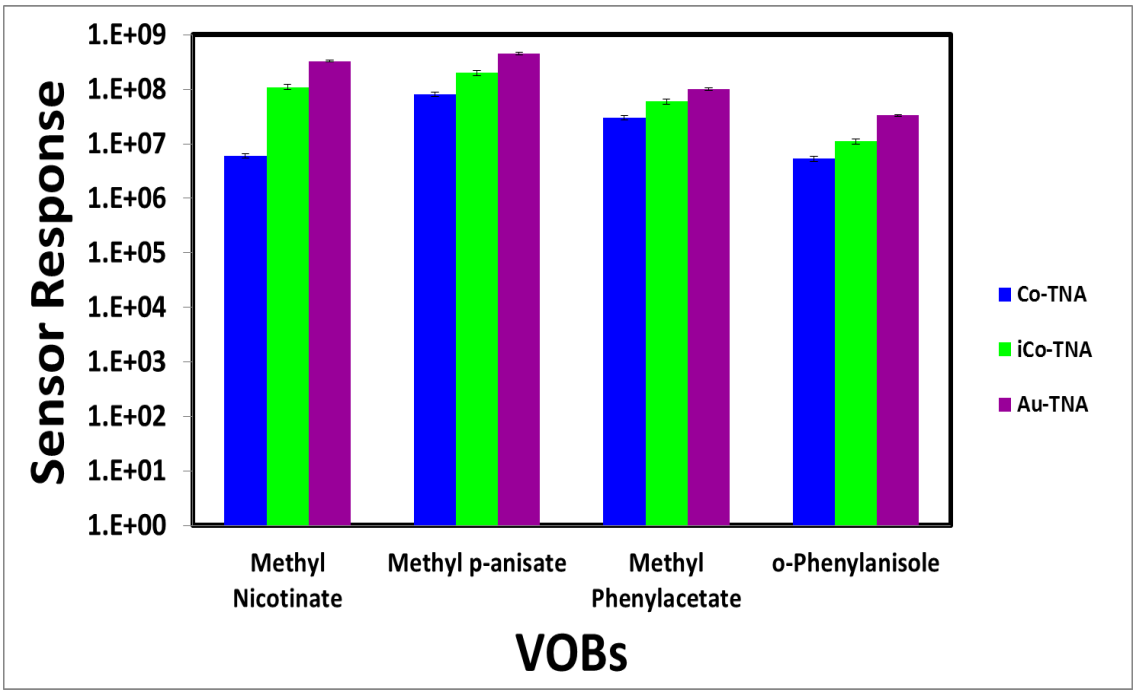

Figure 9.1. A comparison of the Co-TNA, *i*Co-TNA, and Au-TNA sensor performance towards detection of the four TB biomarkers reveals that Au-TNA yields the maximum sensor response.

Having successfully demonstrated the capabilities of cobalt and gold functionalized TiO_2 nanotubes for electrochemical detection of TB biomarkers, the validity of the sensing platform was further verified for detection of other diseases as well. Four prominent biomarkers of colorectal cancer were examined using nickel functionalized titania nanotubes (Ni-TNA). Ni was electroplated on TiO_2 and subsequently used for sensing operations. XPS characterization illustrated $Ni(OH)_2$ on the surface and a similar mechanism proceeds, as described previously for TB biomarkers.

Successful and holistic development of such smart sensor systems for disease diagnostics is a three-step process involving development of the sensor element, element integration into the sensor hardware, and subsequent field testing. Having already gone through the critical stage of sensor development, development of the concept prototype follows. 3D printing-based rapid prototyping was utilized to develop the first set of crude devices housing the sensors, followed by stage-wise refining to obtain a more presentable variant. The as-fabricated devices using first-generation Co-TNA sensors were tested in air, vapors of biomarker mimics, breath from healthy subject, biomarker spiked breath of healthy subject, and finally TB patients. The sensor was successfully able to detect the biomarkers and exhibited exemplary performance. The breath samples were further examined using GC-MS to verify the presence of the biomarkers, which was earlier calibrated using synthetic VOB mimics.

Encouraged by the performance of our sensing platform in its ability to detect TB, we envisage that after having gone through several modifications in its design and having acquired the necessary approvals over the next couple of years, this can be adopted as a

low-cost, hand-held POC sensing device for rapid triaging / screening of TB patients in resource limited settings. Easier said than done, this sensing platform will have to prove itself in various demographic regions, and in varied patient groups (such as children with TB, latent TB, drug resistant TB, HIV+TB, etc.) demonstrating acceptable sensitivity and specificity as per WHO standards. We propose and predict that this sensing technology will compete other technologies in the pipeline for WHO approval (Figure 9.2).

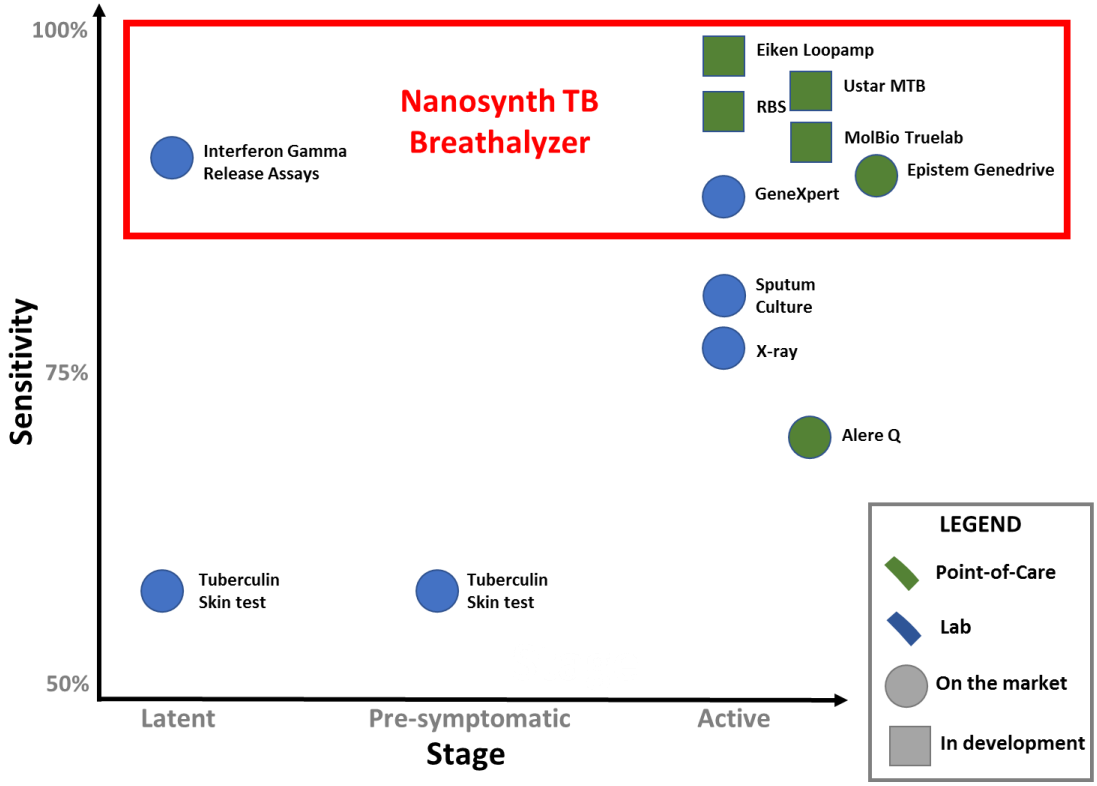

Figure 9.2. Chart showing some of the existing and upcoming TB diagnostic technologies and where the Nanosynth TB Breathalyzer fits in.